UNIVERSITÀ DI PARMA

UNIVERSITÀ DEGLI STUDI DI PARMA

Dottorato di Ricerca in Fisica
Ciclo XXXIV

Epidemic processes on adaptive temporal networks

Coordinatore:
Chiar.mo Prof. Stefano Carretta

Tutore:
Chiar.mo Prof. Alessandro Vezzani

Dottorando: Marco Mancastroppa

ANNI ACCADEMICI 2018/2019 - 2020/2021

Marco Mancastroppa

Abstract

The emergence of new infectious diseases and the persistence of old ones are a major concern for public health. Understanding the fundamental mechanisms driving the spread of epidemics is crucial in order to develop effective control and containment measures. An essential role is played by the mathematical modelling of epidemic processes, based on the detailed knowledge of the structure of the social interactions.

In modelling the spread of epidemics, two levels of coupling between epidemic processes and social interactions must be taken into account. On the one hand, human interactions are continuously rearranged over time, producing a social dynamics which deeply affects the epidemic process. On the other hand, the presence of an epidemic induces adaptive behaviours with which the population responds to the spread of the pathogen, modifying the social dynamics.

A powerful paradigm for considering both these levels of coupling consists in the theory of adaptive temporal networks, in which social interactions are represented by a time-varying network whose evolution is coupled to an epidemic process.

In this thesis, we deal with epidemic processes on adaptive temporal networks, focusing on activity-driven networks, an empirically validated class of networks whose dynamics is determined by the propensity of the nodes to engage interactions over time. These networks can be treated both with rigorous analytical approaches and numerical techniques, allowing the formulation of models for the characterization of the basic mechanisms of adaptive behaviours.

We develop a general formalism for adaptive activity-driven networks coupled to epidemic processes, assuming a change in the nodes activity and attractiveness based on their health status. The epidemic threshold can be estimated analytically, unveiling the crucial role of correlations in the behaviour of individuals between the susceptible and the infected state. The model allows to describe several adaptive behaviours of populations exposed to epidemics, including behaviours observed in the early stages of the COVID-19 pandemic. Inspired by these behavioural changes, we implement two different types of quarantine, comparing their effectiveness and showing the impact of timing in the adoption of measures.

The adaptive formalism proposed can be suitably modified to describe even more complex adaptive behaviours, such as contact tracing which is crucial for controlling SARS-CoV-2 diffusion without disrupting societal activities. We implement contact tracing in its manual (interview-based), digital (app-based) and hybrid protocols. The model highlights an intrinsic difference in contacts exploration: manual tracing performs a stochastic sampling (annealed), while digital tracing performs a

sampling localized on a subpopulation (quenched). Because of this, the manual tracing is robustly more effective than the digital one, even assuming the same probability of tracing a contact. This difference, previously overlooked, is further amplified by the presence of heterogeneity in the individuals behaviour, i.e. superspreaders.

Moreover, in active populations a key property of social interactions is their higher-order nature, due to the formation of social groups and gatherings. In the presence of epidemics, large gatherings can generate superspreading events, thus they must be addressed by control strategies. We implement an epidemic model for the diffusion of SARS-CoV-2 on simplicial adaptive activity-driven networks, in which the interactions are organized in simplices and the tracing is implemented on gatherings. Beside forward and backward tracing, a new tracing mechanism is active in gatherings: the sideward tracing, which occurs laterally exploiting the simplicial structure of interactions. We unveil the relevance of the sideward mechanism in tracing large gatherings, especially in the presence of strategies targeted on them. We implement our model on an empirical dataset of gatherings in a University, suggesting the optimal size of groups to be traced to reach the epidemic control, avoiding the University closure.

Acknowledgements

First and foremost, I am profoundly grateful to my supervisors, Prof. Alessandro Vezzani and Prof. Raffaella Burioni, for their guidance and inspiring mentoring. In recent years, they motivated me to give my best, stimulating the emergence of critical thinking and teaching me to cultivate the passion for physics and complexity. They guided me into the world of research with valuable advices that will help and guide me also in the future. Furthermore, I am also indebted to them for their personal support during these years: their imprint will remain indelible in me.

In these years I had the opportunity to collaborate with amazing people, who contributed crucially to the realization of this work. First of all, I want to thank Dr. Vittoria Colizza for precious discussions and for her unique enthusiasm in research: I would like to thank her and all the members of the EPIcx lab for hosting me in Paris, it was an unforgettable experience from which I learned a lot. I also want to thank Dr. Claudio Castellano for our long and stimulating discussions and collaboration, I really enjoyed it. I would like to extend my sincere thanks to Andrea Guizzo for the fruitful and useful discussions and for our teamwork.

Finally, a special mention to all those who are not directly linked to this thesis, but contributed to generating a fertile environment in which this work originated.

A heartfelt thanks to my family. I express deep gratitude to my parents, for teaching me to be curious and to appreciate knowledge, encouraging me to follow my passions: without their constant support I would not have reached this point, this goal is a little theirs too. I want to also thank my sister for always being close to me, for her constant support and for always being there, ready to provide help or advices.

I thank all my friends for our fantastic time together and for always being close to me during these years, regardless of the distance and despite being overdispersed and delocalized in the world.

Preface

This thesis was mainly developed at the Department of Mathematical, Physical and Computer Sciences of the University of Parma, in collaboration with the Italian National Institute for Nuclear Physics (INFN, Gruppo Collegato di Parma, Sezione Milano Bicocca).

The original research presented in this dissertation is the result of scientific collaborations with the Epidemics in complex environments lab (EPIcx lab) of the Pierre Louis Institute of Epidemiology and Public Health (INSERM, Sorbonne Université) in Paris, and with the Institute for Complex Systems (ISC-CNR) in Rome.

The results discussed in this thesis are based on the following publications:

- Marco Mancastroppa, Raffaella Burioni, Vittoria Colizza, Alessandro Vezzani, *"Active and inactive quarantine in epidemic spreading on adaptive activity-driven networks"*, Physical Review E 102, 020301(R) (2020)
- Francesco Pinotti, Laura Di Domenico, Ernesto Ortega, Marco Mancastroppa, Giulia Pullano, Eugenio Valdano, Pierre-Yves Boëlle, Chiara Poletto, Vittoria Colizza, *"Tracing and analysis of 288 early SARS-CoV-2 infections outside China: a modeling study"*, PLOS Medicine 17(7): e1003193 (2020)
- Marco Mancastroppa, Claudio Castellano, Alessandro Vezzani, Raffaella Burioni, *"Stochastic sampling effects favor manual over digital contact tracing"*, Nature Communications 12, 1919 (2021)
- Marco Mancastroppa, Andrea Guizzo, Claudio Castellano, Alessandro Vezzani, Raffaella Burioni, *"Sideward contact tracing and the control of epidemics in large gatherings"*, arXiv:2110.04742 (2021)

Contents

List of Abbreviations

AD	Activity-Driven
ADA	Activity-Driven with attractiveness
NoPAD	Non-Poissonian Activity-Driven
SAD	Simplicial Activity-Driven
nAD	Node-matched Activity-Driven
eAD	Edge-matched Activity-Driven
NAdwA	Non-adaptive case with attractiveness
NA	Non-adaptive case
CT	Contact Tracing
SSEs	Superspreading events
NPIs	Non-pharmaceutical interventions
APs	Access points

Introduction

Many systems in nature, in our whole physical world, ranging from microscopic to macroscopic scales, and also in human activities, are composed of a large number of elements which interact with each other, producing emergent phenomena, collective and cooperative behaviours: these behaviours cannot be described starting from the single properties of the constituents of the system, but arise from their interactions. The strong interdisciplinary nature of these *complex systems* generated an extremely broad research field, ranging from statistical physics to computer science, from biology to economics [1–4].

Many of these systems can be represented by *networks*, where the vertices represent the elements of the system and the edges connecting them represent the interactions. In several systems the interactions are not static nor fixed in time, but they evolve according to specific temporal patterns: for example, the interactions between neurons, the public transport or the social interactions. Such systems require to explicitly take into account the temporal dimension considering *temporal networks*, whose edges are continuously destroyed and recreated over time, profoundly affecting the topological properties and introducing new temporal features [4–7].

The effect of the network dynamics is even more dramatic considering *dynamical processes* occurring on top of the network: if the time scales of the two processes are comparable, the dynamic process is strongly affected by the network evolution. Indeed, the two dynamics are deeply coupled since the dynamic process occurs along the connections of the network, which evolve on comparable time scales.

The coupling between the two dynamics may be even deeper, since the dynamic process can induce adaptive mechanisms in the underlying network, with which the network adapts to the presence of the dynamic process by modifying its own dynamics. In this case, the temporal dynamics of the interactions and the adaptive coupling with the dynamical process need to be taken into account, by means of *adaptive temporal networks*. Hence, the dynamic on and of the network affect each others: the mathematical treatment of such systems is challenging due to the deep coupling levels and due to the non-trivial effects of adaptive mechanism on the dynamic process [8–10].

This is the case of *epidemic processes on the social interactions network*: the spread of an infectious disease occurs on time scales comparable with that of the social dynamics and, in the presence of an epidemic, the population responds through a series of adaptive behaviours due to symptoms onset, risk awareness and the implementation of control and containment measures. Hence, when dealing with epidemics it is crucial to take into account both the temporal dynamics of the social interactions and the adaptive behaviours induced by the epidemic [8, 11, 12].

Simplified models considering the two dynamics and their adaptive coupling, amenable to analytic control, are fundamental and useful for obtaining insights into the basic mechanisms of adaptive behaviours and for identifying the role played by specific features of the interactions in the epidemic control, such as heterogeneity in

the agents behaviour.

Within this framework, in this thesis we deal with epidemic processes on adaptive temporal networks, in the presence of control and containment measures. We mainly focus on a class of temporal networks, the *activity-driven networks*, which can be treated with rigorous analytical approaches even when considering epidemic processes unfolding upon them [13]. This class of networks shifts the focus from the edges to the nodes: the network properties and dynamics are fully driven by the propensity of nodes to engage interactions, encoded in their activity.

We develop a general formalism for *adaptive activity-driven networks*, in which the adaptive behaviours are modelled with a change in activity and attractiveness due to a change in the health status [14]. The epidemic threshold of the model, i.e. the critical condition for the epidemic to produce a large-scale diffusion, can be obtained analytically, providing insights on the crucial role of correlations in the behaviour of individuals between the susceptible and the infected states. The model can describe several adaptive behaviours in the population, such as disease parties, sick-leave, quarantine: we implement two behavioural changes observed during the early stages of the COVID-19 pandemic, when drastic restrictive measures were implemented. The *active quarantine*, in which the population compensates the loss of links because of quarantine by readdressing its activity towards non-quarantining nodes, and the *inactive quarantine*, in which the loss of activity due to quarantine is not compensated by link rewiring. We compare the two types of quarantine both analytically and numerically, characterizing the effect of link rewiring and highlighting the crucial role of the timing in the measures adoption.

The COVID-19 pandemic significantly impacted the approach to epidemic control: initially it required the quick development of effective containment policies, in order to limit the spread of the pathogen, its consequences in terms of deaths and the overwhelming of the health system [15, 16]; then it required the design of control strategies capable of keeping the population active, in order to avoid the economic, social and psychological consequences of strong restrictions [17, 18]. Furthermore, it provided new data and empirical evidences on the effectiveness of interventions, implemented heterogeneously around the world [19].

During the early stages of the COVID-19 pandemic I carried out a research period at the EPIcx lab of the Pierre Louis Institute of Epidemiology and Public Health (INSERM, Sorbonne Université) in Paris: we analyzed the early data on SARS-CoV-2 transmission, by tracing the first 288 confirmed cases of COVID-19 outside China, collecting all possible information about them and reconstructing the clusters of infection. We built a model for the temporal dynamics in the number of importations, showing the effects of mobility restrictions implemented to contain the spreading. The data collected show the presence of superspreading events and estimate that about 64% of the imported cases went undetected, suggesting a silent transmission of the pathogen, which later gave rise to large outbreaks in many countries [20].

The *contact tracing* proved to be a fundamental strategy for the mitigation of the disease transmission without the disruption of social activity, because of the high fraction of asymptomatic and presymptomatic transmissions of SARS-CoV-2 and thanks to the local nature of the measure [21, 22]. A broad discussion on the effectiveness of manual tracing (interview-based) and on the possibility of enhancing it with digital tracing (app-based) has been opened, aiming to optimize the allocation

of the tracing resources between the different tracing protocols [23–27]. Our work fits in this discussion: we consider an epidemic model for the spread of SARS-CoV-2 on the adaptive activity-driven network proposed, implementing contact tracing on it [28]. We consider the manual and the digital tracing protocols, comparing their effectiveness in curbing the epidemic as isolated protocols and within hybrid protocols. We investigate the effect of contact tracing both on the epidemic threshold and on the active phase of the epidemic: even when the probability of tracing a contact is the same, manual tracing robustly performs better and dominates in hybrid protocols, compared to digital tracing. This is a consequence of an intrinsic difference in the contacts exploration: manual tracing performs a stochastic (annealed) sampling, while the digital tracing performs a prearranged (quenched) sampling, localized on individuals endowed with the app. This difference is further amplified by the presence of superspreaders, i.e. by heterogeneity in the individuals behaviour, who are easily traced manually but are invisible to digital tracing if they have not downloaded the app. This intrinsic difference has been often overlooked and suggests a crucial role of manual tracing in any contact tracing policy.

A further level of complexity in the modelling of social dynamics is due to the *higher-order nature of social interactions*, which typically are organized in groups and gatherings [29, 30], producing potential superspreading events (SSEs) of the epidemic. These events play a crucial role in the spread of SARS-CoV-2, driving the pandemic and suggesting to address them by any control measures [20, 31]. A possible strategy for the control of SSEs, without requiring the complete prohibition of large gatherings, is to implement contact tracing. The role of tracing in gatherings has never been fully investigated, hence we assess its impact within our model, which can be suitably modified implementing simplices of arbitrary size as building blocks. We consider a model for the transmission of SARS-CoV-2 on the simplicial adaptive activity-driven network, with tracing applied on simplices [32]. We show that *forward tracing*, which traces to whom the pathogen is transmitted, and *backward tracing*, which reconstructs from whom the pathogen is transmitted, are augmented by the *sideward tracing*, a third tracing mechanism which occurs laterally by exploiting the simplicial structure of the interactions. This mechanism is crucial in tracing large gatherings, especially in strategies targeted on them. The model is also implemented on an empirical dataset of gatherings collected in the University of Parma, estimating the optimal size of gatherings to be traced to control the epidemic without the closure of teaching and research activities.

In summary, we outlined the main challenging issues that motivated this work: on the one hand the interest in the mathematical modelling of epidemic processes coupled to the social dynamics through complex adaptive behaviours; on the other hand, the interest in a deep understanding of the main epidemic control mechanisms by means of simplified models, amenable of an analytical treatment. In this framework, we model complex adaptive behaviours, understanding their basic mechanisms and the properties of the interactions network that affect their effectiveness.

The thesis is organized in the following way. Chapters 1-3 review the main concepts of epidemic processes on adaptive temporal networks: in Chapter 1 the theory of temporal networks is presented, especially concerning the properties related to the temporal dimension and focusing on the activity-driven networks; Chapter 2 introduces epidemic processes on temporal networks, highlighting the differences with epidemics on static networks; in Chapter 3 the adaptive temporal networks are

presented, highlighting the role of adaptiveness in the presence of epidemics. Chapters 4-6 are the results of original research [14, 20, 28, 32]: in Chapter 4 we present the results of Ref. [14], introducing the general formalism for adaptive activity-driven networks and the specific case of active and inactive quarantine; in Chapter 5 the results of Ref. [28] are presented, by introducing contact tracing and implementing its digital, manual and hybrid protocols on the adaptive activity-driven network; Chapter 6 is based on Ref. [32], it introduces contact tracing on gatherings within the simplicial activity-driven network, also obtaining insights into optimal tracing strategies based on empirical data on gatherings in a University Campus.

Chapter 1

Temporal Networks

In this Chapter we review the *temporal network theory*: we introduce the main fundamental properties of time-varying networks, especially those deriving from the temporal dimension, and we present the main generative models of temporal networks, focusing in particular on *activity-driven networks (AD)*, which constitute the framework in which our work is placed.

1.1 Temporal dimension

Many systems in physics, in nature and in human activities are composed of several interacting elements [1–4]: examples include interactions between proteins, the social interactions, the local and international transport, the internet. These systems are typically characterized by collective and cooperative phenomena, emerging only thanks to the interconnections between the agents of the system and which would not exist considering the single isolated elements. For example, the interactions can be substrates for phenomena, such as diffusive processes, transport phenomena or synchronization processes [1–4]. The study of these collective processes requires a thorough understanding of the structure, topology and properties of the interactions that generate them, in order to identify how the interactions influence the dynamical processes. A natural framework for modelling these systems is graph (or network) theory, in which the elements of the system are described as nodes and the interactions as links between nodes [1, 4].

In many systems, the interactions between elements are not fixed over time, but evolve by being continuously removed, created or changed in intensity. This *temporal dimension* of the topology has often been neglected, by considering only static network in which the interactions between nodes are frozen in time. However, numerous empirical evidences show that many systems are far from being static, the temporal ordering of events is fundamental and cannot be disregarded (e.g. social interactions, public transport connections) [2, 4–7].

This temporal dimension is crucial when considering dynamic processes occurring on the network: if a time-scales separation holds between the dynamics of the network (τ_N) and the dynamics on the network (τ_P), the temporal network can be approximated by a static graph. For example, if $\tau_N \gg \tau_P$, the network evolves slowly (compared to the dynamic process) and the network can be considered static in the quenched approximation; if $\tau_N \ll \tau_P$ the network evolves rapidly (compared to the dynamic process) and the temporal network can be described through the time averaged static network in the annealed approximation. However, if the time scales of the two processes are comparable $\tau_N \sim \tau_P$, the network dynamics and evolution cannot be neglected: the temporal evolution of the structure and link rearrangements may affect the dynamical process.

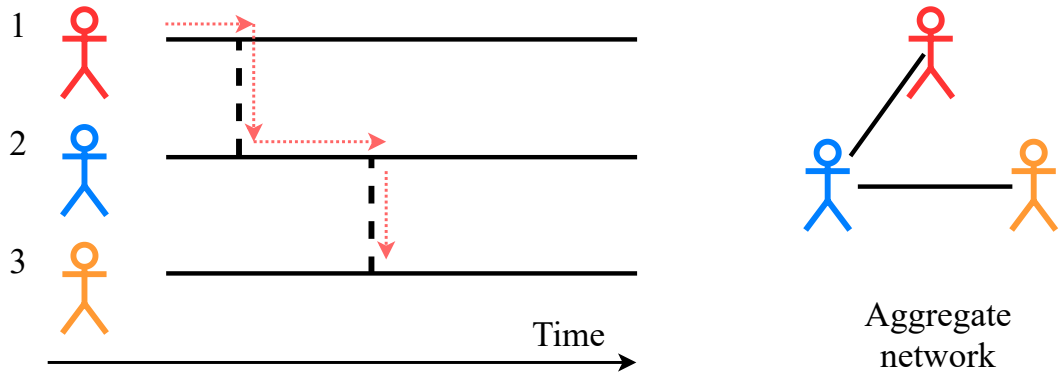

FIGURE 1.1: **The need for the temporal dimension.** Time-varying network made up of three individuals with two contact events and the corresponding aggregate network.

The network evolution can significantly change the behaviour of a dynamical process, this is clearly shown in Figure 1.1. Three individuals compose a time-varying network and two of them have a conversation when there is a vertical line. If individual 1 starts spreading an information, it can reach all individuals (red dashed arrows); however, if individual 3 starts spreading an information, it will never reach individual 1. The temporal dimension introduces asymmetry in the spreading flow, due to the time flow and its direction: aggregating the network would produce a static network in which an information starting from any individual would reach anybody else (see Section 1.3 for more details).

The need to take into account a temporal dimension for the evolution of the network has challenged mathematical understanding and techniques, shifting the focus towards the study of the coupling between the dynamics of and on the network [2, 4–7]. Tools and techniques for the study of these systems derive from statistical physics (which deals with the interactions of many elements), mathematics and computer science, due to the highly interdisciplinary character of this topic.

1.1.1 Examples of temporal networks

Examples of time-varying networks are available in many disciplines and at very heterogeneous temporal and spatial scales.

The classic example is that of communication networks, which can cover two levels: one-to-one communications, such as e-mails [33–35], telephone or instant messages [36], phone calls [37, 38], and one-to-many communications, such as blogs and people's social accounts. Investigating the main topological and temporal features of such networks allow to study and control the spread of computer viruses, information or consensus formation [33, 34, 38].

Similarly, human social interactions constitute a temporal network, which is the substrate for the diffusion of information and also of pathogens: a deep understanding of the social dynamics is essential for controlling the spread of epidemics and information [39]. Extensive access to large-dataset on social interactions networks has been obtained recently through several projects: the first was the Reality Mining project [40], where the proximity of MIT students was recorded using Bluetooth technology. Subsequently, the SocioPatterns project developed a platform for proximity estimation starting from wearable badges with radio-frequency identification devices (RFID). This project allows to obtain data on social dynamics in different settings, such as hospitals, schools and conferences [41–44].

Other notable applications are found in the study of transport networks [45], for example air or urban transport, where the connections between stations and cities evolve over time following the transport schedules. The study of these systems is useful to optimize mobility and transport.

Apart from human activities, many other systems can be represented with temporal networks: in cell biology, the interactome [46], that is the set interactions between molecules in a cell, can be described as a temporal network, where the nodes are proteins (or small molecules) that connect and interact to produce biological functions. Or even the network of protein interactions or gene-regulatory networks can be analyzed as temporal networks [47], in which, for example, the vertices are genes and their interactions correspond to functional relationships, for which a gene influences the transcription of another. Other biological examples concern the network of neuron interactions [48], on different levels ranging from interactions between single spiking neurons to a more coarse-grained level of functional or physiological interactions between areas of the brain.

1.2 Definition and representations

A network can be defined as any system that admits a representation by means of a graph, whose nodes represent the elements that make up the system and whose links represent the interactions among them. A network is static if the links between the nodes of its representation are fixed in time, while it is temporal if they are continuously created, destroyed or modified over time [1, 4].

A *static graph* $\mathcal{G}$ is defined as the pair of sets $\mathcal{G} = (\mathcal{V}, \mathcal{E})$, where $\mathcal{V}$ is the set of nodes and $\mathcal{E}$ the set of links. Each link is defined by a pair of nodes $e = (i, j) \in \mathcal{E}$: the nodes (i, j) are said to be adjacent (or connected) and their order does not matter (in this thesis we focus on undirected graphs). The number of nodes N of the system defines the cardinality of the set $\mathcal{V}$ and denotes the order of the graph $\mathcal{G}$; the number of links M of the system defines the cardinality of the set $\mathcal{E}$ and denotes the size of graph $\mathcal{G}$. The maximum number of possible links is $\binom{N}{2}$ and a graph $\mathcal{G}$ with the maximum number of links is defined complete (or fully connected). Static networks are mainly represented in two ways: the link list and the adjacency matrix. In the link list representation, the graph is represented as a list of pairs of nodes, each corresponding to a link in the graph:

$$\{(u_1, v_1), (u_2, v_2), ..., (u_M, v_M)\}. \tag{1.1}$$

The graph can be also represented by the adjacency matrix $\boldsymbol{A} = A_{ij}$, i.e. a $N \times N$ matrix whose entries are:

$$A_{ij} = \begin{cases} 1 & \text{if} \quad (i, j) \in \mathcal{E} \\ 0 & \text{if} \quad (i, j) \notin \mathcal{E} \end{cases} \tag{1.2}$$

or if the network is weighted the entries of $\boldsymbol{A}$ can assume positive values different from one, which correspond to the weight of the link. This representation suggests the development of matrix analysis theory for the study of static networks, describing key properties of the network through matrix formalism [4]. Moreover, the graph can be also represented by another matrix that is the graph Laplacian $\mathcal{L}_0$:

$$\mathcal{L}_0 = \boldsymbol{D} - \boldsymbol{A}, \tag{1.3}$$

where $\boldsymbol{A}$ is the adjacency matrix and $\boldsymbol{D}$ is the degree matrix, with:

$$D_{ij} = \begin{cases} k_i & \text{if} \quad i = j \\ 0 & \text{otherwise} \end{cases} \tag{1.4}$$

where $k_i = \sum_{j=1}^{N} A_{ij}$ is the degree of the node i, that is the number of links in which i is involved. Analogously to the adjacency matrix, properties of $\mathcal{L}_0$ are able to describe key properties of the graph especially relating to spreading processes on such networks.

Temporal networks can be represented in two ways [4, 7]: the event-based and the snapshot representation (see Figure 1.2). In the event-based representation, the temporal network is described as a sequence of events corresponding to the activation of links between pairs of nodes (see Figure 1.2 - lower panel): thus, the network is represented by a list of time-ordered events:

$$\{(u_i, v_i, t_i, \Delta t_i); i = 1, 2, ...\}, \tag{1.5}$$

where (u_i, v_i) are the nodes involved in the ith event, t_i is the time of the ith event and Δt_i its duration. Generally, the duration of the interactions is very short if compared with the time between two events, therefore hereafter we will consider instantaneous events: this approximation makes numerical simulations and analytical calculations more tractable. In this case the event-based representation becomes:

$$\{(u_i, v_i, t_i); i = 1, 2, ...\}. \tag{1.6}$$

In this representation the time can be both continuous or discretized.

Alternatively, a temporal network can be represented with the snapshot representation (see Figure 1.2 - upper panel), which consists in seeing the network as a sequence of static networks (snapshots):

$$\mathcal{G} = \{G(1), G(2), ..., G(t_{max})\}, \tag{1.7}$$

where t_{max} is the number of snapshots considered. Equivalently, it can be seen as a sequence of adjacency matrices (snapshots):

$$\mathcal{A} = \{\boldsymbol{A}(1), \boldsymbol{A}(2), ..., \boldsymbol{A}(t_{max})\}, \tag{1.8}$$

where $\boldsymbol{A}(t)$ is the adjacency matrix of the static graph $G(t)$. In this representation the time is discretized, however it is possible to introduce an analogous representation continuous in time, by considering tensor analysis. The temporal network can be represented through an adjacency tensor $\mathcal{A} = A_{ij}^{(t)}$ of indices $i = 1, ..., N$, $j = 1, ..., N$ and t:

$$A_{ij}^{(t)} = \begin{cases} 1 & \text{if } i \text{ and } j \text{ are connected at time } t \\ 0 & \text{otherwise} \end{cases} \tag{1.9}$$

This representation highlights the temporal evolution of the network topology and structure, both in continuous and discretized time, moreover it allows to treat network evolution and topology through tensor analysis.

Given a temporal network and given a certain time window $[0, T]$, the static network aggregated on this window is defined as the static network in which a link exists between each pair (i, j) of nodes if in the time window there has been at least an instant t in which they were connected. Clearly the static counterpart of a network

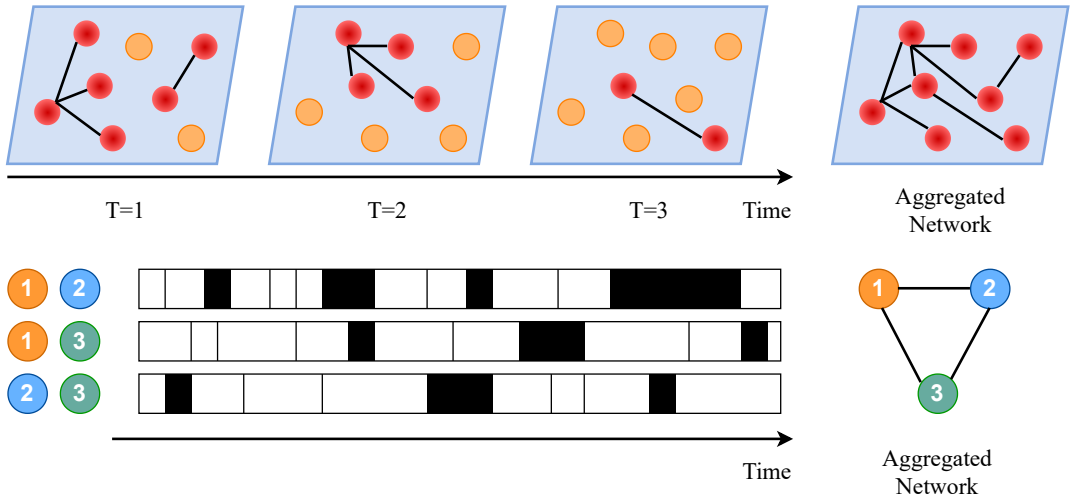

FIGURE 1.2: **Temporal network representations.** In the upper panel a temporal network is displayed in the snapshot representation, highlighting in red the nodes involved in links in each snapshot. In the lower panel a temporal network is displayed through the event-based representation, in which for each link between a pair of nodes the contacts time-line is shown with instant activations event (vertical line) or event with duration (extended bars). Both panels also show the corresponding aggregate network.

loses all temporal information. However, it is possible to keep a partial information, considering a weighted static network, in which each link between pairs of nodes (i, j) is associated with a weight w_{ij} which is the frequency of activation of the link (i, j) in the time window $[0, T]$. In the snapshot representation, the adjacency matrix $\boldsymbol{A}^*$ of the aggregate graph over $[0, T]$ is:

$$\boldsymbol{A}^* = \frac{1}{T} \sum_{t=0}^{T-\Delta t} \boldsymbol{A}(t), \tag{1.10}$$

with $\boldsymbol{A}(t)$ adjacency matrix of the static snapshot at time t and Δt time-step. The term $1/T$ serves as a normalization, so that the matrix element A^*_{ij} represents the frequency of activation of the link (i, j) in the window $[0, T]$. In the aggregate network the temporal information is always lost, but the information on the frequency of connections between pairs of nodes remains, encoded in the weight of the links. In Figure 1.3 it is reported an example of aggregate network for a mobile-phone network [49].

Empirical data of temporal network are usually collected and provided in the event-based version, with discretized time due to technical reasons for data collection [44]: it is possible to pass directly to the snapshot representation, without loss of information, or to perform a coarse-graining, losing some temporal information (see Figure 1.3). Considering a uniform time spacing Δt for all snapshots: all events that occur between time $(k-1)\Delta t$ and $k\Delta t$ are contained in graph $G(k)$, for $k = 1, 2, ...$, which is a static graph aggregated over the period $[(k-1)\Delta t, k\Delta t]$. All the temporal details at time scales lower than Δt are lost and increasing Δt produces greater loss of information: the extreme case is $\Delta t = t_{max}$ in which the aggregate static network over the entire time window is considered.

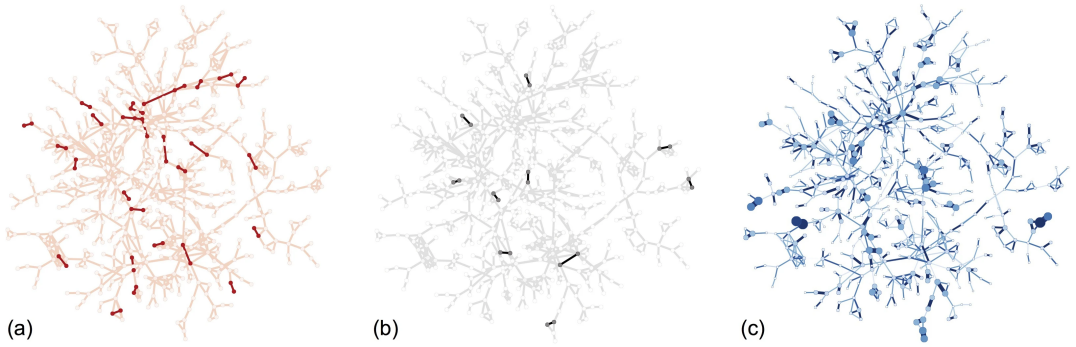

FIGURE 1.3: **Mobile-phone call network.** Dataset of 633986311 time stamped mobile-phone call (MPC), collected during 182 days with 1 second resolution in a European country. The size of the network is $N = 6243322$ connected via $E = 16783865$ links. Panel **a** shows the MPC network involving people in the same town and aggregated over 3 hours. Panel **b** is the same of panel **a**, but on a different time window. Panel **c** shows the total weighted aggregated social network. In all panels, node size and colors indicate the activity of nodes, while edge width and color describe the weight. Image from [49] under CC BY-NC-SA 3.0 license.

1.3 Topological and structural properties

Several topological descriptors can be defined on a temporal network [50], providing information on the structure of the network: these properties can be defined locally (on the basis of connections between a few nodes) or globally (on the basis of connections between many nodes).

A key concept is that of *reachability* of a vertex, that is the possibility of moving from one node to another in the network following the connections. Indeed, the paths that connect pairs of nodes represent the roads to which dynamic processes are bound when evolving on the network.

In a static network $\mathcal{G} = (\mathcal{V}, \mathcal{E})$, a *path* $\mathcal{P}_{i_0,i_n}$ is defined as an ordered collection of $(n+1)$ nodes $\mathcal{V}_\mathcal{P} = \{i_0, i_1, ..., i_n\}$ and n links $\mathcal{E}_\mathcal{P} = \{(i_0, i_1), (i_1, i_2), ..., (i_{n-1}, i_n)\}$, such that $i_\alpha \in \mathcal{V}$ and $(i_{\alpha-1}, i_\alpha) \in \mathcal{E}$, $\forall \alpha$. The path $\mathcal{P}_{i_0,i_n}$ connect i_0 to i_n and its length is n. A node j is said to be *reachable* by another i if there is a path that connects them. This notion in static networks is symmetric (for undirected graph), transitive (both for directed and undirected graph) and time-independent.

When considering temporal networks it is necessary to consider *time-respecting (or temporal) paths* [4, 6, 51]. A node j is reachable by a node i (or is temporally connected) if there is a time-respecting path from i to j, that is a path $\mathcal{P}_{i,j}$ that connects them through temporally ordered events. Indeed, the time flows while the path is executed and the jump from one node to another can only take place on a sequence of link activations that follow one another in time. In the event-based representation this path is defined by the sequence of events:

$$\{(i, v_1, t_1), (v_1, v_2, t_2), ..., (v_{n-1}, j, t_n)\}, \tag{1.11}$$

where $t_i \leq t_{i+1}$ and $i \in [1, n-1]$. The definition in the snapshot representation is analogous, interpreting (v_{i-1}, v_i, t_i) as a link (v_{i-1}, v_i) in the snapshot $G(t_i)$. The time of departure and arrival of the temporal path are t_1 and t_n respectively; the length of the path is estimated both with the number of hops n (spatial) and with its duration $t_n - t_1$ (temporal).

The temporal dimension introduces fundamental modification in the concept of

reachability. The temporal paths and the reachability concept are not symmetrical: indeed, the presence of a temporal path connecting i to j does not imply the presence of a temporal path connecting j to i, due to the constraint on the temporal ordering of links. Moreover, time-respecting paths and the reachability concept are not transitive: the existence of a temporal path connecting i to j and connecting j to k does not imply the existence of one connecting i to k, this happens only if the path i-j is temporally completed before the start of j-k. Finally, time-respecting paths and reachability are time-dependent concepts, due to the temporal nature of the links: a node j can be reachable from i in a certain time window, in which the appropriate links are generated to create the path, and not reachable in a different window.

The set of nodes reachable by a node i over time $t \in [t_1, t_n]$ is called the *set of influence* of i, and the *reachability ratio* is the average fraction of reachable nodes of all vertices [51]. These quantities are relevant since, in the presence of an epidemic, they respectively estimate the set of vertices infectable by an epidemic process if the source of the infection was i and the average infectable fraction not knowing the source of the infection. Also these concepts are time-dependent, given the time-dependence of the reachability concept.

If the temporal information is neglected, the number of paths would be overestimated: in the aggregate network there are paths that cannot be realized in the temporal network, due to the lack of temporal ordering of the link formation. A temporal path is a causal path and therefore it is not allowed to use links in the past, which are present in the aggregate network.

Since a temporal path occurs while time passes, it is possible that the path must wait on an intermediate node before an event occurs and allows it to move to a nearby node: this introduces *waiting times* in the path. This is crucial for diffusion and transport processes: for example, in epidemics it is necessary that transmission occurs before the node heals and waiting times play a key role in this.

In temporal networks it is possible to define a *distance* through the concept of time-respecting path: there exists three possible definitions depending on a different definition of temporal path with the shortest distance [52]. Given a temporal path $\{(i, v_1, t_1), (v_1, v_2, t_2), ..., (v_{n-1}, j, t_n)\}$ from node i to node j, we defined:

1. the *shortest distance* from i to j at time t as:

$$d_{short}(i, j; t) = \min\{n : t_1 \geq t\}. \tag{1.12}$$

   It represents the minimum number of jumps between i and j via a time-respecting path starting after t. This is a topological and adimensional distance measure.

2. the *foremost distance* from i to j at time t as

$$d_{fore}(i, j; t) = \min\{t_n - t : t_1 \geq t\}. \tag{1.13}$$

   It represents the minimum time needed to go from i to j through a time-respecting path, starting to measure time at instant t. This is a temporal measure and has a time dimension.

3. the *travel-time (or fastest) distance* from i to j at time t as

$$d_{travel}(i, j; t) = \min\{t_n - t_1 : t_1 \geq t\}. \tag{1.14}$$

   It is the minimum time necessary to go from i to j, starting to measure the time at the instant t_1 in which the path begins, i.e. regardless of the initial waiting period $t_1 - t$. This is a temporal measure and has a time dimension.

The different distances are useful in different settings: the shorter distance gives information on the topological distance in terms of links, while the two temporal distances give information on how quickly the vertices can reach each other via temporal paths. For example, in public transport the links represent connections between stations: d_{short} will be preferred by passengers interested in minimizing the number of connections; d_{fore} will be preferred by passengers who wants to reach their destination as soon as possible; d_{travel} will be preferred by a passenger who wants to minimize the time spent on public transport. In general, all these distances are highly not symmetric and time-dependent. This is realistic, for example by thinking of the daily and weekly human cycles in communication or transport networks, in which the distance between two individuals/places is changed at different times and days.

For each of the three distances it is possible to define the *average distance* between pairs of nodes:

$$L(t) = \frac{2}{N(N-1)} \sum_{i=1}^{N} \sum_{j=1}^{i-1} d(i,j;t), \tag{1.15}$$

and the *diameter* of the temporal network:

$$D(t) = \max_{i,j \in \mathcal{V}} d(i,j;t). \tag{1.16}$$

These properties provide time-dependent information by estimating the overall evolution of the network over time, presenting dense phases (with small diameter and small average distance) or sparse phases (with high diameter and high average distance). Clearly, the meaning of a small L and D depends on the definition of distance used: for the shortest distance it means a topological dense network, while for temporal distances it means a temporally dense network.

Although they are relevant, distance measures provide global information on the network structure, but they do not provide information on the importance that nodes have in the network structure (local information). Several measures of nodes *centrality* have been proposed, depending on specific process or function of interest that the network must satisfy. These centrality measures can also be defined as time-dependent or time-independent: in the first case they capture changes in the role and importance of a node in the network over time, modelling changes in the relevance of nodes; in the latter they describe the overall importance of a node over a time window.

The simplest measure of the centrality of a node in a static network is the *degree centrality*: the analogue for a node in a temporal network would be total number of events, intended as the formation of links, in which the node has been involved and is a time-independent measure of centrality. It coincides with the degree of the node in the aggregate network and its time-dependent version would be the instantaneous degree of the node $k(t)$.

Another measure of centrality is *closeness centrality* [53], which for a node i is defined as follows:

$$C_C(i,t) = \frac{N-1}{\sum\limits_{j=1; j \neq i}^{N} d(i,j;t)}, \tag{1.17}$$

where $d(i,j;t)$ is one distance, thus $C_C(i,t)$ measures the inverse of the mean distance of i to all other nodes at time t. This centrality is high for nodes that are close

to all the others and it estimates how quickly a node can reach the other nodes on average. Clearly it can be defined in three versions, corresponding to the three choices on the distance.

The closeness centrality of a node would be null if that node were not temporally connected to at least one node: this situation occurs very frequently on temporal networks. For this reason, an increased measure of closeness centrality is defined, the *temporal efficiency* [45]:

$$C_E(i,t) = \frac{1}{N-1} \sum_{j=1;j\neq i}^{N} \frac{1}{d(i,j;t)}, \tag{1.18}$$

where $1/d(i,j;t)$ is defined as zero if there are no time-respecting paths from i to j arriving at time t or earlier. In this way a pair of disconnected nodes contributes with a null term to the centrality, without influencing the other terms.

The degree and closeness centralities consider nodes that are topologically or temporally (depending on the definition of distance used) better connected with the rest of the network: however they neglect vertices that may be poorly connected, but crucial to connect topologically or temporally different regions of the network, behaving as bridges. *Betweenness centrality* was introduced to account this [1, 3, 54]: it measures the fraction of minimum-distance paths that pass through a node, averaged over all starting and ending nodes:

$$C_B(i,t) = \frac{1}{(N-1)(N-2)} \sum_{j=1;j\neq i}^{N} \sum_{j'=1;j'\neq i,j}^{N} \frac{\sigma^i_{jj'}(t)}{\sigma_{jj'}}, \tag{1.19}$$

where $\sigma_{jj'}$ is the number of minimum-distance temporal paths $j \to j'$ over the entire time-window, $\sigma^i_{jj'}(t)$ is the number of minimum-distance temporal paths $j \to j'$ passing through i at time t (i.e. i is reached at time t or earlier and the path does not move to another node before t).

A node with a high betweenness centrality is traversed more by short/fast paths: this is fundamental for transport networks, to estimate the traffic handled by a node, assuming that the number of short/fast paths traversing a node are an approximation of the frequency of use of the node. This information is important to speed up or slow down the transport process: removing a node with high betweenness would temporally disconnect different regions of the network, since it acts as a bridge.

In closeness and betweenness centrality the centrality of a node is defined considering processes in which something moves from a source to a target following a minimum-distance path. Other centrality classes can be defined assuming instead a random diffusion process on the network: in this case a node is central if it is frequently occupied by this process. For static networks this approach leads to matrix-based measures of centrality, such as Katz centrality, eigenvector centrality and the PageRank [1, 3, 4]: generalizations to temporal networks require the use of three-dimensional tensors.

The *PageRank* is defined as the stationary density of a random walk on a node: initially it was proposed for ranking web pages and then it was applied in many other fields, identifying central nodes as the ones which has a high probability to be occupied by a random walker moving on the network [1]. The *TempoRank* is defined as the analogue of the PageRank for temporal networks in snapshots representation [4, 55]. The random walker, in each snapshot, remains on the current node with a certain probability q, even if it can move on neighbouring nodes. The probability of

transition from node i to node j in a snapshot $\boldsymbol{A}(t)$ is defined:

$$T_{ij}(t) = \begin{cases} \delta_{ij} & \text{if} \quad k_i(t) = 0, 1 \leq j \leq N \\ q^{k_i(t)} & \text{if} \quad k_i(t) \geq 1, i = j \\ A_{ij}(t)(1 - q^{k_i(t)})/k_i(t) & \text{if} \quad k_i(t) \geq 1, i \neq j \end{cases} \tag{1.20}$$

where $k_i(t) = \sum_{j=1}^{N} A_{ij}(t)$ is the degree of i at time t, $\sum_{j=1}^{N} T_{ij}(t) = 1$ and the probability for the walker to stay in the node i is $q^{k_i(t)}$, since each edge in the snapshot induces a jump with probability $(1 - q)$. The transition matrix at time t is given by $\boldsymbol{T}(t) = T_{ij}(t)$ and the one-cycle transition matrix for the network is defined as:

$$\mathcal{T}^{tp} \equiv \boldsymbol{T}(t_1)\boldsymbol{T}(t_2)...\boldsymbol{T}(t_{max}). \tag{1.21}$$

Periodic boundary conditions are imposed, i.e. $\boldsymbol{A}(t_1)$ is applied after $\boldsymbol{A}(t_{max})$, and $\boldsymbol{u}$ is defined as an N-dimensional density vector in which the i-th element is equal to the density on node i. The random walker stationary density is given by the solution of the equation:

$$\boldsymbol{u}(t_1) = \boldsymbol{u}(t_1)\mathcal{T}^{tp}. \tag{1.22}$$

Even if the snapshots are applied indefinitely and the dynamics is at equilibrium, the density on each node changes at each snapshot: the stationary density in the usual sense does not apply in a temporal network as the connections continue to evolve. Thus, $\boldsymbol{u}(t_1)$ represents the equilibrium density immediately after $\boldsymbol{A}(t_{max})$ or before $\boldsymbol{A}(t_1)$. The TempoRank is defined as the average of equilibrium density over snapshots:

$$T_R = \overline{\boldsymbol{u}} \equiv \sum_{t=t_1}^{t_{max}} \boldsymbol{u}(t)/t_{max}, \tag{1.23}$$

where $\boldsymbol{u}(t)$ is the stationary density when the observation is made just before applying $\boldsymbol{A}(t)$.

Finally, many more centrality measures have been defined, for example time-independent version of the measures introduced above, eigenvector centrality, running broadcast and receive centrality [4]. Moreover, all definitions of node centrality can be easily redefined for links, identifying central links in the network (local information).

1.4 Temporal properties

The temporal dimension of the network introduces a considerable complexity for the network structure and for topological descriptors, profoundly modifying concepts introduced on static networks. Moreover, additional temporal features, missing in static networks, are introduced peculiarly due to the temporal dimension: the statistics of evolution of interactions and the presence of temporal patterns play a key role in the network properties and for dynamic processes.

1.4.1 Statistical properties of event times

Given a temporal network, a slight modification of the event-based representation presented in Section 1.2 can be considered. Each node (or link) is assigned with the sequence of events associated with it $\{t_1, t_2, ..., t_n\}$, instead of assigning the sequence of events to the entire network. The temporal statistics of these events and

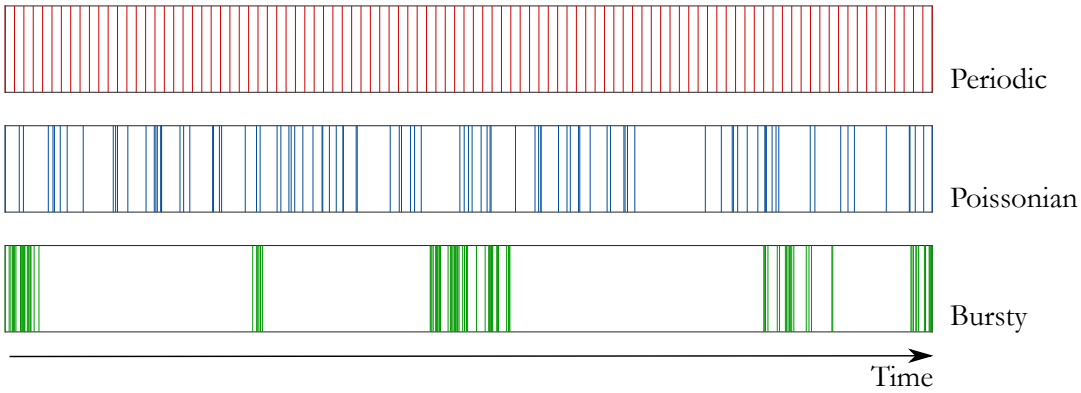

FIGURE 1.4: **Statistics of event sequences.** Periodic $\Psi(\tau) = \delta(\tau - \overline{\tau})$, Poissonian $\Psi(\tau) \propto e^{-\lambda\tau}$ and bursty $\Psi(\tau) \propto \tau^{-\alpha}$ event sequences.

correlations in the timing play a relevant role, for example in the duration of time-respecting paths.

The statistics of the events are regulated by the *distribution of inter-event times*, that is the time elapsed between two successive events involving a node. The i-th inter-event time is:

$$\tau_i = t_{i+1} - t_i. \tag{1.24}$$

Events generated by a Poisson process present an inter-event times distribution $\Psi(\tau)$ which is exponential:

$$\Psi(\tau) = \lambda e^{-\lambda\tau}, \tag{1.25}$$

where λ is the process parameter. This distribution is homogeneous, with light tails and small fluctuations (see Figure 1.4).

Empirical data on many natural (e.g. earthquakes, neuron spiking) and artificial systems (e.g. human communications) show intermittent behaviour that deviates from the homogeneous Poissonian memoryless behaviour, suggesting that the sequence of events is produced by a renewal process rather than a Poisson process [56–60]. This *bursty* dynamic of events consists in alternating periods of strong activity (trains of events) with long periods of inactivity: this can be modelled in general with broad inter-event times distributions, with large fluctuations and heavy tails (see Figure 1.4). For example, a power-law distribution:

$$\Psi(\tau) \propto \tau^{-\alpha}, \tag{1.26}$$

where $\alpha > 0$. This inter-event time distribution shape has been observed in many systems of human activities (see Figure 1.5) estimating $1 \leq \alpha \leq 2.7$ [4, 58, 61].

A good measure of the burstiness of a sequence of events is the *coefficient of variation*, defined as the standard deviation of the inter-event times sequence $\{\tau_i\}$ divided by its average:

$$CV = \frac{\sqrt{\frac{1}{n-1}\sum_{i=1}^{n-1}(\tau_i - \langle\tau\rangle)^2}}{\langle\tau\rangle}, \tag{1.27}$$

where

$$\langle\tau\rangle = \frac{1}{n-1}\sum_{i=1}^{n-1}\tau_i. \tag{1.28}$$

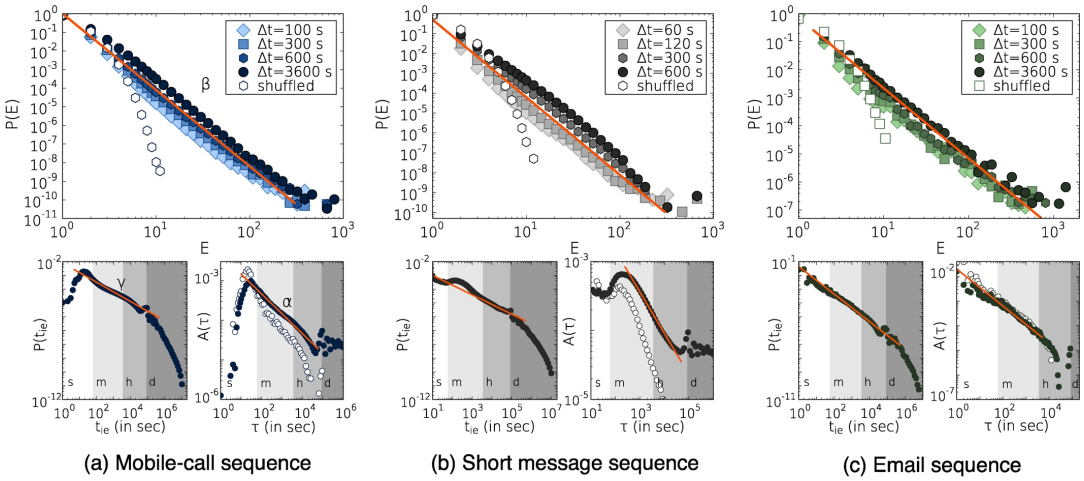

(a) Mobile-call sequence (b) Short message sequence (c) Email sequence

FIGURE 1.5: **Characteristic distributions of human communication event sequences.** In the main panels are plotted the distributions $P(E)$ of the number of events E observed in the same bursty period Δt, with various Δt time-window sizes; in the bottom panels the distributions $P(t_{ie})$ of the inter-event times and the average autocorrelation functions $A(t)$ are plotted. **a** Mobile-phone call dataset for a European operator; **b** text messages from the same dataset; **c** email communication sequences. A comparison can be made with reshuffled temporal sequence, looking at empty symbols. Image from [61] under CC BY-NC-SA 3.0 license.

A periodic process, with $\Psi(\tau) = \delta(\tau - \overline{\tau})$, produces $CV = 0$; the Poisson process, with $\Psi(\tau) \propto e^{-\lambda\tau}$, produces $CV = 1$; a broad distribution $\Psi(\tau)$, on the other hand, produces high values of CV. A normalized version of the coefficient of variation is the *burstiness measure* [60] defined as:

$$B = \frac{CV - 1}{CV + 1}, \tag{1.29}$$

with $-1 \leq B \leq 1$. A periodic process features $B = -1$, a Poissonian process $B = 0$ and an extremely bursty event ($CV \to \infty$) has $B \to 1$. Many empirical systems show values of $CV > 1$ and $B > 0$ [60].

The origin of this temporal statistic in human activities has been much debated [56, 57]: a possible cause could be related to the decision-based queuing process, which humans apply when they need to address multiple tasks and allocate their time and energy in different activities.

The sequences of events can be characterized by even more complex temporal patterns, emerging from *rhythms, cycles or temporal patterns* [36, 62]. For example, human activities are characterized by circadian rhythms and cycles on longer time scales in human activities (e.g. weeks, seasons), which can produce heterogeneity in the dynamics of interactions. An example is the period of inactivity at night or reduced activity on weekends, alternating with periods of high activity during working hours and days.

Realistic temporal networks observed at successive snapshots are typically *correlated*, showing positive correlations even removing the effects of circadian rhymes and periodicities in activities (detrending process). For example, if a node (or a link) has an event at a time t after a short inter-event time, it tends to have a new event after a short inter-event time from t; on the contrary, if the last inter-event time was long, the next one will also be long.

Given a sequence of events of a node (or a link) $\{t_1, t_2, ..., t_n\}$, with a sequence

$\{\tau_i\}$ of inter-event times, a measure of correlations is the *memory coefficient* [60], defined as the sample covariance of adjacent inter-event times:

$$M = \frac{\sum_{i=1}^{n-2}(\tau_i - m_1)(\tau_{i+1} - m_2)}{\sqrt{\sum_{i=1}^{n-2}(\tau_i - m_1)^2 \sum_{i=2}^{n-1}(\tau_i - m_2)^2}}, \tag{1.30}$$

where:

$$m_1 = \frac{1}{n-2}\sum_{i=1}^{n-2}\tau_i, \tag{1.31}$$

$$m_2 = \frac{1}{n-2}\sum_{i=2}^{n-1}\tau_i. \tag{1.32}$$

A positive value of M means positive correlations, as typically observed in realistic datasets [60]. An analogous coefficient can be defined also for the snapshot representation, considering the *temporal correlation coefficient* between two adjacent snapshots [53]:

$$C = \frac{1}{N(t_{max}-1)}\sum_{t=1}^{t_{max}-1}\sum_{i=1}^{N}\frac{\sum_{j=1}^{N}A_{ij}(t)A_{ij}(t+1)}{\sqrt{\left[\sum_{j=1}^{N}A_{ij}(t)\right]\left[\sum_{j=1}^{N}A_{ij}(t+1)\right]}}, \tag{1.33}$$

where t_{max} is the maximum number of snapshots and $0 \leq C \leq 1$. $C = 1$ means that all snapshots are the same, i.e. a static network; C would increase if many links are repeated both at t and $t+1$.

Even more complex correlations can emerge in temporal networks: so far we have considered correlations in the behaviour of a single node or link, however it is possible that an event on a node (or link) increases the probability of another event on another node (or link) soon after. This can easily happen in communication networks for information transmission. Entropy and mutual information concepts can be used to analyze this aspect [63].

We consider a sequence of events for node i, $\{t_1, t_2, ..., t_n\}$, and the corresponding sequence of nodes with which the node i is in contact $\{v_1, v_2, ..., v_n\}$, assuming that a node is adjacent to them one after the other (neglecting simultaneous adjacencies to multiple nodes). The entropy associated with the two sequences of i is:

$$H_i^1 = -\sum_{j=1;j\neq 1}^{N} p_i(j)\log_2 p_i(j), \tag{1.34}$$

where $p_i(j)$ is the probability that the node i is adjacent to j. A node with large degree in the aggregate network and equally connected to the different nodes, will have H_i^1 high. The entropy conditioned by the previous adjacent node is:

$$H_i^2 = -\sum_{j=1;j\neq 1}^{N} p_i(j)\sum_{l=1;l\neq j}^{N} p_i(l|j)\log_2 p_i(l|j), \tag{1.35}$$

where $p_i(l|j)$ is the probability that the node i is adjacent to l knowing that i was adjacent to j in the previous snapshot. H_i^2 measures second-order correlations in

the sequence $\{v_1, v_2, ..., v_n\}$ and estimates the uncertainty on the next adjacent node knowing the previous neighbour. The *mutual information* measures correlations between events on different nodes, and is defined as:

$$I_i \equiv H_i^1 - H_i^2 = \sum_{j,l=1;j,l\neq i} p_i(j,l) \log_2 \frac{p_i(j,l)}{p_i(l)p_i(j)}, \tag{1.36}$$

where $p_i(j,l)$ is the joint probability that the node i is adjacent to the node j and then to the node l immediately after. $I_i = 0$ corresponds to the absence of correlations on different nodes, while $I_i > 0$ presents positive temporal correlations: for many empirical systems $I_i > 0$ has been observed [63].

The event sequence statistics e temporal correlations are very important, as we will see in Chapter 2, for the study of dynamic processes on temporal networks.

1.4.2 Temporal motifs and sub-structures

We have seen global and local topological descriptors of the networks: however, a further fundamental aspect in the study of networks is the identification of intermediate structures (mesoscale) with specific properties for their structure or for their role in dynamic processes, such as highly connected communities or cores. These structures are neither local, since involve several nodes, nor global, since not all nodes are considered: similar structures are observed in temporal networks, by considering temporal cores and meso-structures [6].

In temporal networks can be identified *subgraphs*. Given a subgraph $\mathcal{G}' \subseteq \mathcal{G}_t$ of the complete graph with all links active at time t in the temporal network, the support set $S(\mathcal{G}')$ of $\mathcal{G}'$ is defined as the set of time steps in which $\mathcal{G}' \subseteq \mathcal{G}_t$. A subgraph is said to be *persistent* if it has a support wider than a certain threshold. These types of persistent structures play a fundamental role in diffusive or dynamic processes on the network as well as in the dynamics of the network.

Significant temporal patterns can also be found with *temporal motifs*: a motif is an equivalence class of subgraphs overrepresented in the network (cardinality) with respect to a null model of the network (e.g. with respect to a randomized reference system). This concept can be implemented by considering snapshots of the network at different times and counting the different subgraphs in these snapshots.

These temporal mesoscale patterns are fundamental structure of temporal networks and play a key role in dynamic processes, thus strong efforts have been devoted to the development of tools to detect them [64, 65].

1.5 Temporal networks models

As sketched in the previous Sections, real temporal networks are highly complex, with several properties crucial for their structure, topology and dynamics, and also for dynamical processes occurring on top of them. An enormous work has been directed to the study of empirical temporal networks, however this brings the disadvantage of not obtaining a systematic understanding of the effects of the network temporal structure and properties: to understand this we need generative models and synthetic temporal networks. These allow to explain the emergence of salient properties and to model and investigate specific characteristics of real networks on dynamical processes, by constructing network models with specific and tunable characteristics.

The number of temporal network models proposed has increased significantly recently, here we will present the main models, discussing then in detail the class of models that constitute the framework of this work, i.e. the activity-driven models.

Preferential attachment class of models. The first examples of temporal networks are those generated by the preferential attachment mechanism, which was proposed as a constructive process for networks with heavy-tailed degree distribution [3]. This mechanism is based on the idea that in many real systems the formation of links is not random but occurs preferentially towards nodes with a high number of connections (e.g. web-pages). Hence, the more a node has a high degree k, the higher the node's probability of receiving new links: this mechanism is the elementary generative process for the growth of many networks. For example, in the Barábasi-Albert model the network starts with a core of m_0 connected nodes:

1. at each time-step a new node is added to the network and it engages m links with $m < m_0$ nodes;

2. a node i with degree k_i receives a new link with probability:

$$\Pi[k_i(t)] = \frac{k_i(t)}{\sum_j k_j(t)}, \tag{1.37}$$

   which implements the preferential attachment since $\Pi[k_i(t)] \propto k_i(t)$.

The degree $k_i(t)$ of node i evolves accordingly to $\partial_t k_i(t) = mk_i(t)/[2mt + m_0\langle k\rangle_0]$, where $\langle k\rangle_0$ is the average degree of the initial core. The graph evolves asymptotically towards a stationary state with power-law degree distribution $P(k) \sim k^{-3}$ and the transient graph can be considered as the first example of a temporal network [3].

Stochastic temporal networks. The simplest version of temporal network models is the one in which topological and temporal structures are decoupled [4]. In this network model, a static network is considered (generate with a certain topology) on which a temporal dynamic is defined in the event-based representation, assigning to each link a sequence of events obtained by an inter-event times distribution $\Psi(\tau)$. More complex behaviours can be considered, for example different distributions $\Psi_i(\tau)$ for each link, or correlations in τ assuming a conditional distribution of the inter-event times $\Psi(\tau|\tau_{prev})$. These models allow to tune and investigate the effects of $\Psi(\tau)$ or correlations on the network and on dynamic processes.

Social group dynamics models. Some models have been developed to describe the dynamics of social groups, i.e. the formation of transitory social bonds, such as face-to-face interactions [59, 66]. The main approach is based on defining Master Equations that describe the evolution of the number of people in a group of a certain size and that capture observations such as the fact that the more a node has interacted with a group, the less will abandon it, or that the more isolated an individual is, the less will interact with a group. This produces network models with communities (groups) of strong links, connected to each other via weak links.

Contact network models. Many temporal network models have been proposed to describe the dynamics of strong contacts and the change of partnership, based on the rewiring of an existing static network [67]. The basic idea is to take a static network and select two edges (i, j) and (i', j') with a certain probability at each time step and then replace them with links (i, j') and (i', j) with probability $1/2$ or with (i, i') and (j, j') with probability $1/2$. For example, several models have been proposed that introduce assortativity into the temporal network, through mixing functions

$\phi(i,j)$ [1, 67], which set if the pair is formed or not:

$$\phi(i,j) = 1 - \xi + \xi \frac{k_i k_j}{k_{max}^2}, \tag{1.38}$$

or that introduce disassortativity:

$$\phi(i,j) = 1 - \xi + \xi \frac{(k_i - k_j)^2}{k_{max}^2}, \tag{1.39}$$

with ξ fixing the strength of the mixing pattern and k_{max} fixing the degree upper cut-off. Inspired by this model, several works investigated the stochastic pair-formation network [6].

Null and randomized reference models. To understand the relevance of temporal and structural properties in empirical graphs it is necessary to compare the network with reference models. For static networks the reference network typically considered is the configuration model, since it is obtained by randomly rewiring links of the original network. A similar approach can be obtained for temporal networks, removing all temporal structures and correlations between nodes and links. However, correlations and structures are created on many different (temporal and spatial) scales, thus there is not a single and general method for obtaining a null model of the network. Different randomized models have been developed, in which a specific characteristic of the network is destroyed, in order to identify its single contribution. By selectively turning off specific types of correlation and applying these randomization procedures, it is possible to isolate the role of different topological and temporal properties to the network and to dynamical processes [38, 51]. Randomization procedures can act both on the topological level and on the temporal one [4, 7].

Interval shuffling: For each link, given the sequence of events that characterize it in the original temporal network, the inter-event times are randomly reshuffled keeping the first and last events fixed. This procedure preserves the distribution $\Psi(\tau)$ of inter-event times and the structure of the aggregate network, including the weights of its links. Instead, correlations and causality on each link and between different links are destroyed: this approach can be used to study the effects of the detailed order of events and correlations.

Link shuffling: This approach is based on shuffling the sequence of events across links: the structure of the aggregate network and the weight distribution of the links are conserved, together with the set of sequences of events, while all correlations between links are destroyed.

Random times: For each link, given a sequence of events, the same number of events as the original link are uniformly redistributed on the interval $[0, t_{max}]$. This corresponds to assigning to each link an independent Poissonian process: the effects are the same of the interval shuffling, but also the distribution of the inter-event times $\Psi(\tau)$ is destroyed.

Random link shuffling: This method is the temporal analogous of the configuration model in static networks. It consists in considering sequentially each link: for each edge (i,j) another edge is picked randomly (i',j') and with probability $1/2$ the two links are replaced with link (i,j') and (i',j), otherwise they are replaced with (i,i') and (j,j'), avoiding self-edge or multiple edge. The original sequences of events of the two links are thus randomly reassigned to the two new links. The procedure destroys the structure of the aggregate network and maintains the aggregated distribution of the inter-event times on the links, the distribution of the link weights and

the degree of each node. This approach can be used to study the effect of network topology, assuming that the times of contacts are governed by edges, since after the randomization both the numbers and timings of contacts per nodes will change.

These reference models can be simultaneously applied in order to obtain the combined destruction of various correlations and properties. Finally, many other models for temporal networks have been proposed, a detailed review can be found in [4, 7].

1.6 Activity-driven (AD) models

Many static and temporal network models extensively studied in recent years are connectivity-driven, i.e. they focus attention on links and on topological measures related to them, such as the degree of a node. Recently a new class of temporal network models has been proposed: the *activity-driven models* [13]. This class of models is based on shifting the dynamics from the connections to the nodes themselves: instead of paying attention to the links and the related topological properties, the nodes themselves are considered as central entities for the dynamics of the network and its properties. This is done by assigning to each node i its *activity potential* (also called simply activity) a_i: this parameter measures the propensity of the node to generate links. The activity fixes for each node the dynamics of activation and formation of links in which the node is actively involved.

The idea behind these models is that the dynamic, temporal, topological and structural properties of the network do not emerge from connectivity-driven mechanisms, but rather from the behaviour of the single nodes, which with their dynamics of connections produce specific network characteristics emerging from the collective contribution. The properties of a node do not derive from specific positions in the degree space or from passive attraction mechanisms (as in the preferential attachment mechanism) but rather their properties are encoded in the active behaviour of the node itself.

This model therefore is well suited to describe systems and networks in which connections are guided by the activity of individual: this is the case, for example, of all human activities, such as social interactions, mobile-phone calls, messages, emails, content sharing and use of social networks. The activity-driven models have been used to model time-resolved, empirical large-scale network relating to collaborations between authors of articles in scientific journals, exchanges of messages in the Twitter network and the collaborations of actors [13].

The network is composed of a set of N nodes, each assigned with an activity parameter a_i, distributed with the activity distribution $\rho(a)$. Each node is characterized by an independent activation process and the activity defines the node activation probability per unit of time: in a given time interval Δt the node i is activated with probability $a_i \Delta t$ and generates interactions with other nodes. The average number of active nodes per time unit is $N\langle a \rangle$, where $\langle a \rangle = \int da\, \rho(a)$. The complete network $\mathcal{G}$ is the result of the activation processes of all the nodes, therefore the overall dynamics of the network is regulated by the distribution $\rho(a)$. The dynamics of $\mathcal{G}$ is the following:

1. at the beginning $t = 0$ all the nodes are disconnected and the graph $\mathcal{G}$ is completely disconnected;

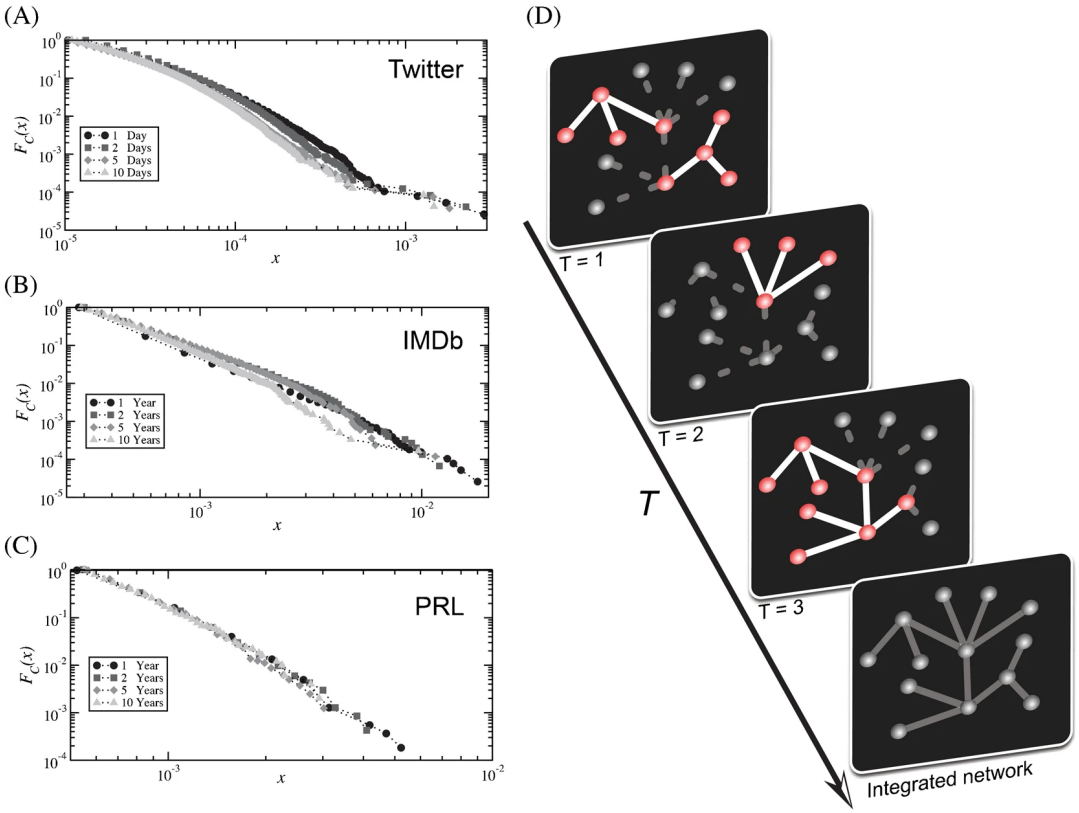

FIGURE 1.6: **Empirical activity distributions and snapshot representation of the AD network.** The cumulative activity distribution is plotted for the network of **a** messages exchanged on Twitter, **b** actors collaborations in movies and TV series (IMBb), **c** collaborations of authors in the journal PRL. In panel **d** the AD network is visualized in the snapshot representation, for $N = 13$ and $m = 3$. Image from [13] under CC BY-NC-SA 3.0 license.

2. each node i fires in the interval Δt with probability $a_i \Delta t$ and generates m links with m randomly chosen nodes. Inactive nodes can still receive connections from other agents;

3. at the next time step $t + \Delta t$ all the links of the network are removed, assuming that the interactions last Δt. Then the process is iterated from point 2.

The model is discrete in time, with time-step Δt, however it can also describe a continuously time-evolving network: in that case $\Delta t \to 0$, the process is continuous, the interactions are instantaneous and the activity sets the activation rate of a node. A sketch of the temporal dynamics is represented in Figure 1.6 in the snapshot representation. Hereafter we fix $\Delta t = 1$, without losing generality.

The activity-driven model obtained is random and Markovian, with successive snapshots independent. Indeed the interactions are without memory and uncorrelated, since the activations of nodes occur independently between each other, without correlation with previous activations and the agents contacted do not depend on previously connected nodes.

The model produces a light-tailed and homogeneous inter-event times distribution on each node [13]. The generative process of the network produces snapshots at successive discrete times Δt: the time between two successive activations of a node i respects the geometric distribution with probability of success $a_i \Delta t$:

$$\Psi_i(\tau = n\Delta t) = a_i \Delta t (1 - a_i \Delta t)^{n-1}, \tag{1.40}$$

since the probability $\Psi_i(\tau)$ of being activated after a time $\tau = n\Delta t$ from the last activation is the probability of not being activated in the previous $(n-1)$ time-steps and of being activated in the last. Within the limit of a continuous process $\Delta t \to 0$ the distribution becomes exponential and the process is Poissonian:

$$\Psi_i(\tau) = a_i e^{-a_i \tau}, \tag{1.41}$$

with average activation time $\langle \tau \rangle_i = \int d\tau \, \tau \, \Psi_i(\tau) = a_i^{-1}$ and activation rate a_i.

The single activation dynamics define the (aggregated) network structure and also the instantaneous connectivity patterns: indeed the degree distribution can be linked to the activity distribution $\rho(a)$. The topological and evolutionary properties are completely encoded in the distribution of the activity $\rho(a)$ [13, 68–70]. The distribution $\rho(a)$ and the cumulative distribution $F_C(a)$ were also observed to be skewed and highly heterogeneous with heavy-tails in many systems, e.g. interactions on Twitter, mobile-phone call, collaborations in papers of scientific journal such as PRL (see Figure 1.6 and Figure 1.8): this is reasonable since real-world social networks and human activities are characterized by complex properties [13, 70]. Large fluctuations in activity correspond to the presence of different types of individuals who engage different number interactions: this may be due to work activities or personal propensity. Furthermore, it has been shown that this distribution, unlike the degree distributions and other structural properties, is weakly dependent on the time scale on which it is measured.

In this model nodes with many connections emerge because of their high activity and propensity for interactions and not because of an advantageous position in the space of the degree or a passive mechanism of attraction of connections (i.e. preferential attachment). The instantaneous network is typically sparse, mostly composed of stars, made up of the active node and some low-degree vertices, contacted by the active node. The integrated network, on the other hand, is very dense.

This model is analytically tractable: several structural properties have been derived mostly for the aggregate network [13, 68–70]. The integrated network can be considered and it is defined as the union of all the snapshots of the network on the $T+1$ time steps $\mathcal{G}_T = \cup_{t=0}^{t=T} \mathcal{G}_t$. Each active node generates m links and therefore the average number of active links per unit of time is $E_t = mN\langle a \rangle$, so the average degree per unit of time is:

$$\langle k \rangle_t = \frac{2E_t}{N} = 2m\langle a \rangle. \tag{1.42}$$

For large time T and network size N, the degree in the integrated network can be approximated by a continuous variable and agent i will have degree $k_i(T)$ in the integrated network at time T:

$$k_i(T) = N\left(1 - e^{-Tm(a_i + \langle a \rangle)/N}\right), \tag{1.43}$$

which is the number of distinct nodes interacting with i up to time T.

The adjacency matrix of the activity-driven network aggregated per unit of time is:

$$A^*_{ij} = m\frac{a_i + a_j}{N}, \tag{1.44}$$

neglecting the probability that an active node contacts another active node (order $1/N$). Thus the average degree of node i in the aggregate network is:

$$k_i(T) = T\sum_{j=1}^{N} A_{ij}^{*} = m(a_i + \langle a \rangle)T, \tag{1.45}$$

which holds for large N at the order $1/N$. This shows a monotonic relationship between $k_i(T)$ and a_i, since $dk_i(T)/da_i = mT$, which allows to obtain the distribution $P_T(k)$ considering that $P_T(k)dk = \rho(a)da$:

$$P_T(k) \sim \frac{1}{Tm}\rho\left(\frac{k}{Tm} - \langle a \rangle\right). \tag{1.46}$$

The same result can be also obtained formally through a hidden-variable formalism [68, 69]. These results imply that the distribution of the degree in the aggregate network follows the same functional form of the distribution of activity $\rho(a)$. For example, for a power-law distribution $\rho(a) \sim a^{-(\nu+1)}$ with $a \geq a_m$, the degree distribution is $P(k) \sim k^{-(\nu+1)}$; if we consider $\rho(a) = \delta(a - a_0)$ the degree distribution is a Poissonian centred on $\mu \sim 2Ta_0$, with $P_T(k) = e^{-\mu}\frac{\mu^k}{k!}$, which in the asymptotic limit is $P_T(k) \sim \frac{1}{T}\delta(k - Ta_0)$. Empirically, however the two distributions differ: this is due to the aspects that the AD model does not capture, such as memory effects, community, weighted interactions, duration of social interactions (persistence).

Finally, results on the probability $P_i(k,t)$ that a node with activity a_i has degree k at time t have been obtained by applying the Master Equation approach. The discrete time equation for $P_i(k,t)$ is (assuming $m = 1$):

$$\begin{aligned} P_i(k,t+1) =& a_i\frac{N-k}{N}P_i(k-1,t) + a_i\frac{k}{N}P_i(k,t) + P_i(k-1,t)\sum_{j\nsim i}^{N} a_j \sum_{h}^{N}\frac{P_j(h,t)}{N} \\ &+ P_i(k,t)\sum_{j\nsim i}^{N} a_j \sum_{h}^{N} P_j(h,t)\frac{N-1}{N} + P_i(k,t)\sum_{j\nsim i}^{N} a_j + P_i(k,t)\left(1 - \sum_{j}^{N} a_j\right), \end{aligned} \tag{1.47}$$

where $j \nsim i$ denotes the sum over the nodes that have not been yet connected to i. Assuming that only one node is active between two time steps t and $t+1$, that $1 \ll k \ll N$ and in the limit of large times and degrees, continuous equation in t and k can be written:

$$\frac{\partial P_i(k,t)}{\partial t} = (a_i + \langle a \rangle)\left(-\frac{\partial P_i(k,t)}{\partial k} + \frac{\partial^2 P_i(k,t)}{\partial k^2}\right), \tag{1.48}$$

which admits as a solution:

$$P_i(k,t) = \frac{1}{\sqrt{2\pi(a_i + \langle a \rangle)t}}\exp\left(-\frac{(k - (a_i + \langle a \rangle)t)^2}{2t(a_i + \langle a \rangle)}\right). \tag{1.49}$$

Within the large time limit, the solution is reduced to:

$$P_i(k,t) = \delta(k - (a_i + \langle a \rangle)t), \tag{1.50}$$

which allows to simply obtain again the growth of the degree:

$$k_i(t) = (a_i + \langle a \rangle)t. \tag{1.51}$$

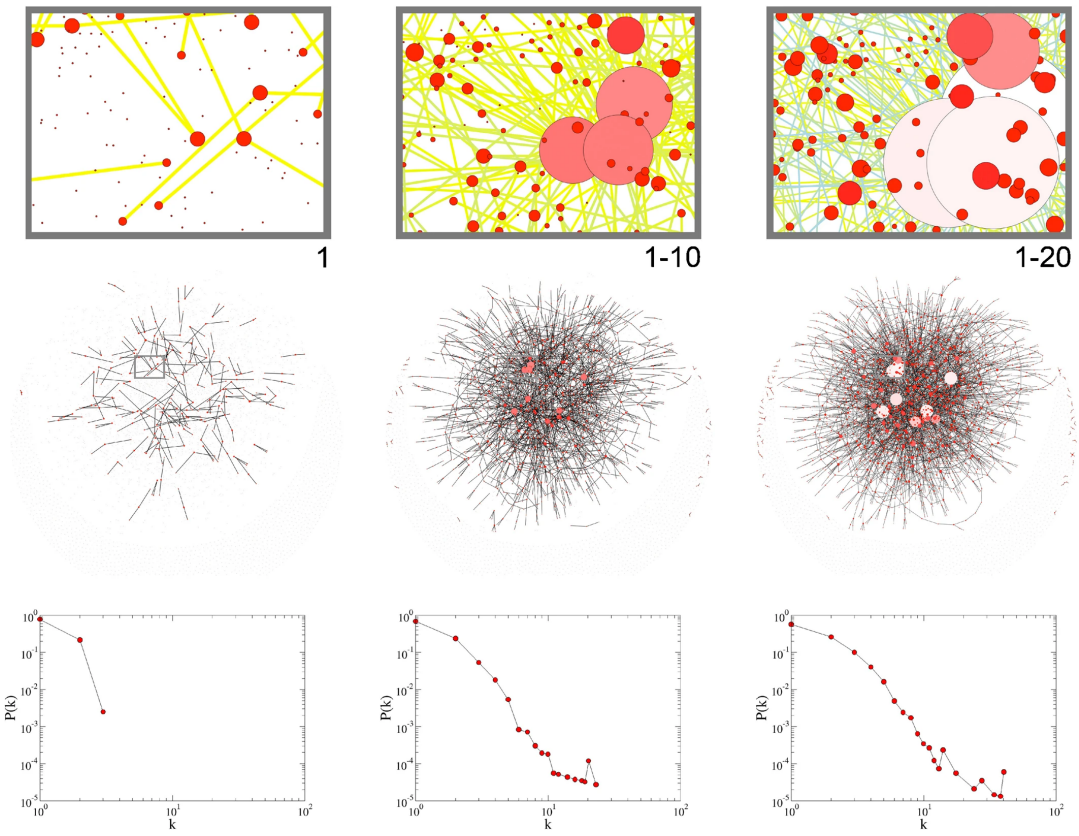

FIGURE 1.7: **AD network and degree distributions.** An example of the AD network is visualized considering different time windows for aggregation: one time-step, 10 time-steps and 20 time-steps. The network is obtained for $N = 5000$, $m = 2$, $a = \eta x$, $\rho(x) \sim x^{-\nu}$ with $\nu = 2.8$ and $x \in [10^{-3}, 1]$. The color and the size of vertices are proportional to their degree. In the lower panels the degree distributions of the aggregate networks are shown. Image from [13] under CC BY-NC-SA 3.0 license.

In Figure 1.7 the aggregated AD network is shown for different aggregation time-window and the corresponding degree distribution is plotted.

The eigenspectrum of the adjacent matrix can be obtained by considering the eigenvalue equation:

$$\boldsymbol{A}^* \boldsymbol{u} = \lambda \boldsymbol{u}, \tag{1.52}$$

where λ is an eigenvalue of $\boldsymbol{A}^*$ and $\boldsymbol{u} = (u_1, ..., u_N)^T$ is the corresponding eigenvector. Substituting the definition of $\boldsymbol{A}$ yields the following equation:

$$m \left(\sum_{i=1}^{N} \frac{a_i}{N} + \sum_{i=1}^{N} a_i u_i \right) = \lambda, \tag{1.53}$$

which allows to determine the eigenvalues:

$$\Lambda_{\pm} = m \left(\sum_{i=1}^{N} \frac{a_i}{N} \pm \sqrt{\sum_{i=1}^{N} \frac{a_i^2}{N}} \right), \tag{1.54}$$

where one is positive, one is negative and the remaining $(N-2)$ eigenvalues are null, since $\boldsymbol{A}^*$ has rank two. The maximum eigenvalue is therefore Λ_+.

As shown, the activity-driven model is extremely interesting and powerful, from

a modelling point of view for the way it is conceived focusing on spontaneous activity of nodes, and from a mathematical point of view for the analytical and numerical tractability. Its advantages are not limited to this, allowing, as we will see in Chapter 2, to couple in a simple way the dynamics of the network with dynamic processes without the need of the time-scale separation approximation.

Clearly the model has some limits mainly related to the lack of empirically observed properties in real systems: for example it does not reproduce bursty contact sequences and memory effects. By taking advantage of the flexibility and simplicity of the AD model, it is possible to modify and extend the original AD model with simple mechanisms, taking into account essential realistic properties.

1.6.1 AD with attractiveness (ADA)

An extension of the AD network is the activity-driven network with *attractiveness* (ADA) [71, 72]. In several networks, the nodes not only generate interactions based on their propensity (activity) but receive links and connections based on their ability to attract links (attractiveness or popularity index) [71, 73, 74], unlike the AD model where all nodes receive them equally. In this model a contact selection mechanism is introduced, which takes into account that some nodes are preferential targets of interactions. This happens for example in social interactions for the popularity of individuals or for their social role, which requires them to be contacted frequently by other individuals, or in information or online communication systems, where celebrities or public media receive a lot of activity.

The model consists in introducing the attractiveness of a node b_i, as a naturally complementary parameter of the activity: the activity defines the propensity of a node to generate social interactions, the attractiveness instead the propensity (voluntary or not) to receive interactions.

In the activity-driven model with attractiveness the network $\mathcal{G}$ is composed of N nodes: each of them is assigned with two parameters the activity a_i and the attractiveness b_i. In general, activity and attractiveness can be correlated and therefore are extracted from a joint probability distribution $\rho(a, b)$. Recent empirical observations show that activity and attractiveness are both power-law distributed and feature an approximately linear correlation [71], e.g. online communities, face-to-face interactions and animal hierarchies [71, 75, 76]. The AD network is the particular case of the ADA network in which the attractiveness of the nodes is the same for all nodes.

The dynamics of the ADA network is identical to that of the AD network, however an active node i chooses the target j the connections with probability proportional to the attractiveness of the node $p_j \propto b_j$, suitably normalized so that the probability of connecting a node is 1. The model thus behaves like a linear preferential attachment, since the number of contacts received by a link in a time window is proportional to its attractiveness, while the total number depends on both activity and attractiveness.

The attractiveness models global popularity, i.e. with respect to the entire population, as opposed to the local reinforcement mechanism where the probability of contact is node-dependent and changes between different nodes (see Section 1.6.2).

The introduction of attractiveness therefore has strong repercussions on the topological structure and on the temporal dynamics of the network: for example positive activity-attractiveness correlations produce strong heterogeneity in the link weights in the aggregate network and produce hubs with a high number of (generated and attracted) links. This will be essential for the study of dynamic processes [72].

1.6.2 AD with memory

In the original AD model, an active node chooses uniformly at random the other nodes to connect: this is clearly an approximation. In empirical networks there are *memory* effects: a node can remember the nodes contacted in the past and generates links preferentially with them (or not) [77, 78]. This is typical of human interactions, in which individuals remember their friends and social circles (e.g. co-workers, family, friends) and can allocate social interactions differently, either by reinforcing a small number of strong interactions, or by exploring new ones. This happens not only in social interactions, but also in online interactions, in work and collaboration networks [79, 80].

The AD model can be extended by introducing memory through a *tie allocation mechanism*, in which the interactions are not random but are concentrated on nodes already connected, through a *local reinforcement mechanism* [49, 70, 81, 82]. This memory process fixes the evolution of the network, producing a non-Markovian dynamics and aging effects, as often observed in processes with memory [4, 83].

Again the basic model is the AD model, however an active node i can allocate their links either by exploring a new connection or by reinforcing one already activated in the past. To implement this mechanism, each node has a memory of the contacts previously made: an active node i, which has already contacted $k_i(t)$ distinct nodes at the time t, connects to a new node with probability:

$$p[k_i(t)] = \left[1 + \frac{k_i(t)}{c_i}\right]^{-\beta_i}, \tag{1.55}$$

or connects a node previously contacted with probability $(1 - p[k_i(t)])$. The β_i parameter sets the memory process: for $\beta_i \simeq 0$ the probability $p[k_i(t)] \simeq 1$ and, regardless of the degree of the node, links with new nodes are always generated; for large β_i instead $p[k_i(t)]$ rapidly decays with $k_i(t)$, modelling cognitive limits and temporal constraints on the number of distinct social interactions an individual can perform. The constant c_i is a characteristic limit on the number of connections that i is able to make before the memory effects are relevant. Empirical estimates of these parameters have been obtained in different networks, such as those of citations, mentions on Twitter and mobile-phone calls, showing strong memory effects ($\beta \sim 0.15 - 1.2$) [49, 70]. In Figure 1.8 the reinforcement curves $p[k]$ are shown for several empirical networks.

For this model it is possible to explicitly write the Master Equation that describes the evolution of the probability $P_i(k,t)$ that the node i has degree k at time t (assuming time-steps $\Delta t = 1$):

$$\begin{aligned} P_i(k,t+1) =& P_i(k-1,t)\left[a_i p_i(k-1) + \sum_{j \nsim i} a_j \sum_{k_j} \frac{p_j(k_j)}{N-k_j} P_j(k_j,t)\right] \\ &+ P_i(k,t)\left[a_i[1-p_i(k)] + \sum_{j \nsim i} a_j \sum_{k_j} \left(1 - \frac{p_j(k_j)}{N-k_j}\right) P_j(k_j,t)\right] \\ &+ P_i(k,t)\left[1 - \sum_j a_j\right], \end{aligned} \tag{1.56}$$

where $j \nsim i$ indicates that the sum is on nodes not yet connected to i and assuming that only one node is active for each time-step. Considering the case of a single

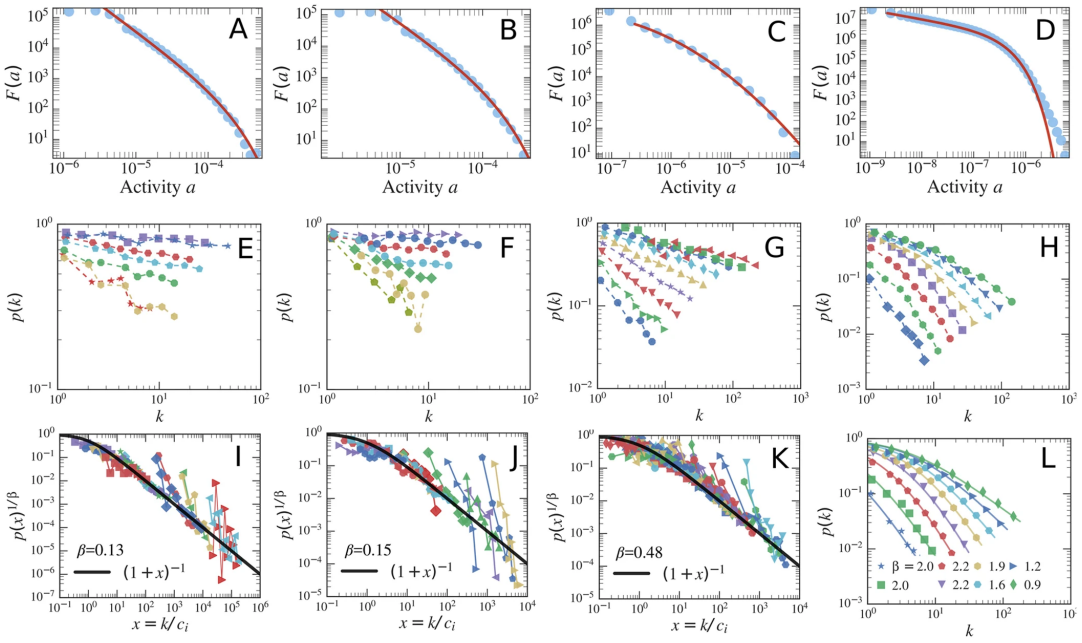

FIGURE 1.8: **Activity distribution and local reinforcement mechanism.** In panels **a-d** the activity distribution is plotted for **a** the collaboration network of authors in PRB, **b** the collaboration network of authors in PRL, **c** the Twitter mentions network (TMN) and **d** a mobile-phone network (MPC). In panels **e-h** are plotted the measured $p_b[k]$ curves for selected nodes classes b, dividing nodes in classes depending on similar number of interactions and cumulative degree distribution, for the **e** PRB, **f** PRL, **g** TMN and **h** MPN datasets. Each data sequence corresponds to a selected nodes class with the average activity of the class increasing from the lower to the upper curves. In panels **i-k** the $p_b[k]$ curves of panels **e-g** have been rescaled with $k \to x_b = k/c_b$ and it is plotted $p_b[xc_b]^{1/\beta}$, with the same β shown on the plot. In panel **l** for the MPN network it is shown the original $p_b[k]$ curves belonging to a single nodes class with their fit, indicating the β_b for each of them falling in $1.0 \lesssim \beta_i \lesssim 2.5$. Image from [70] under CC BY 4.0 license.

exponent β and the conditions $1 \ll k \ll N$, in which k is considered continuous, the asymptotic behaviour can be obtained explicitly:

$$P_i(k,t) \propto exp\left[-A\frac{\left(k - C(a_i,c_i)t^{\frac{1}{1+\beta}}\right)^2}{t^{\frac{1}{1+\beta}}}\right], \tag{1.57}$$

where A is a normalization constant and $C(a_i,c_i)$ is a constant factor that depends on the activity and on the parameter c_i of the agent, respecting the following equation:

$$\frac{C(a,c)}{1+\beta} = \frac{ac^\beta}{C(a,b)^\beta} + \int da'\rho(a')\int dc'\xi(c'|a')\frac{a'c'^\beta}{C(a',c')^\beta}, \tag{1.58}$$

where $\xi(c|a)$ is the probability for a node with activity a to have the reinforcement constant c. An exact solution for $C(a,c)$ is not available, however it can be shown that $C(a,c) \simeq (ac^\beta)^{\frac{1}{1+\beta}}$. Thus, the average degree of a node with activity a and reinforcement constant c evolves over time as:

$$\langle k(a,c;t)\rangle \propto C(a,c)t^{\frac{1}{1+\beta}} \propto (at)^{\frac{1}{1+\beta}}. \tag{1.59}$$

Memory, implemented through a local reinforcement process, has very strong effects

on both $P_i(k,t)$ and on $\langle k(a,t)\rangle$: the parameter β modulates the system's growth and dynamics, fixing the strength of the link reinforcement mechanism. For stronger reinforcement attitude (large β) the growth is slower. In the limit case $\beta = 0$, $C(a) = a + \langle a\rangle$ and the linear growth would be recovered, as in the standard AD model (see Eq. (1.51)) since there are no memory effects and the nodes connect randomly with the other nodes by growing their social circle; in the opposite limit $\beta \to \infty$ each node would create only one link and continue to reinforce it. Real data shows a sublinear growth of $\langle k(a,t)\rangle$ [70].

Moreover Eq. (1.59) connects the degree k of a node to their a for a given time t: given that $k \propto a^{\frac{1}{1+\beta}}$ and knowing the distribution of the activities $\rho(a)$ the functional form of the asymptotic degree distribution $F(k)$ can be determined:

$$F(k)dk \propto \rho(k^{1+\beta})k^{\beta}dk. \tag{1.60}$$

For example, supposing a power-law activity distribution $\rho(a) \propto a^{-\nu}$, we obtain $F(k) \propto k^{-[(1+\beta)\nu-\beta]}$. This relationship between $F(k)$ and $\rho(a)$ is strongly consistent with the distributions observed in real empirical models, obtained from different datasets: this shows that the connectivity pattern depends on the propensity of individuals to participate in social interactions (activities and $\rho(a)$) and on the strength of the reinforcement process towards previous links β. Moreover, the results on $F(k)$ and $\langle k(a,t)\rangle$ are independent of the parameter c distribution.

Analogous results can be obtained considering a distribution of β: in that case the asymptotic growth of $\langle k(a,t)\rangle$ is guided by the minimum value β_{min} [70].

1.6.3 AD with burstiness (NoPAD)

As already extensively described in Section 1.4.1, a fundamental aspect of many systems, especially related to human activities, is a *bursty dynamic*. It is possible to consider a version of the AD model with a *non-Poissonian dynamics* of node activation (NoPAD) [81, 82, 84–86].

The model is analogous to the AD model and evolves similarly, however the activation process of a node is not Poissonian. Each node is assigned with an inter-event times distribution $\Psi(\tau, \xi_i)$, where ξ_i is a parameter that sets the heterogeneity in the agent behaviour (gauging heterogeneity in the activation rate). Thus, each node follows an independent activation process with a dynamics whose statistic is given by $\Psi(\tau, \xi_i)$, following a renewal process. The parameter ξ_i of the node is heterogeneously distributed with $\Phi(\xi_i)$ and fixes the propensity of the node to activate.

Topological properties of the integrated network can be obtained with the general formalism of hidden variables [84]. In this framework, an approximate expression for the degree distribution is:

$$P_t(k) \simeq \sum_{\xi} \Phi(\xi)\chi_t(k - \langle r\rangle_t|\xi), \tag{1.61}$$

where $\langle r\rangle_t = \sum_{\xi} \Phi(\xi) \sum_r r\chi_t(r|\xi)$ is the average number of activation events at time t and $\chi_t(r|\xi)$ is the distribution of the number of activation of a node at time t with heterogeneity ξ. It is sufficient to calculate $\chi_t(r|\xi)$ to obtain the essential structural properties. For example assuming a heavy-tailed distribution:

$$\Psi(\tau, \xi) = \alpha\xi(\xi\tau + 1)^{-(\alpha+1)}, \tag{1.62}$$

with $0 < \alpha < 1$, and a heterogeneous distribution $\Phi(\xi) \propto (\xi/\xi_0)^{-(\nu+1)}$ with $\nu > \alpha$, we get, within the limit $k \gg (\xi_0 t)^\alpha$:

$$P_t(k) \sim (\xi_0 t)^\nu (k - \langle r \rangle_t)^{-(1+\nu/\alpha)}. \tag{1.63}$$

In this way the exponent of the distribution $P(k) \sim k^{-\gamma}$ is linked to that of the distribution of inter-event times α and of heterogeneity ν through the relation:

$$\gamma = 1 + \nu/\alpha. \tag{1.64}$$

In the presence of power-law inter-event times distributions (with exponent $\alpha < 1$), aging effects are introduced, which are not present for Poissonian processes. This can be observed considering the average degree $\langle k \rangle_{t,t_0}$ of the network aged up to time t_0 and then integrated up to $t_0 + t$. It is equal to the number of average activations multiplied by two:

$$\langle k \rangle_{t,t_0} = 2(\langle r \rangle_{t_0+t} - \langle r \rangle_{t_0}), \tag{1.65}$$

and it can be shown that [84]:

$$\langle r \rangle_t \sim (\xi_0 t)^\alpha. \tag{1.66}$$

The sublinear growth ($0 < \alpha < 1$) implies aging behaviours in $\langle k \rangle_{t,t_0}$, resulting in a non-trivial dependence of it on t_0:

$$\langle k \rangle_{t,t_0} \sim [(t_0 + t)^\alpha - t_0^\alpha]. \tag{1.67}$$

So if $t \gg t_0$ then $\langle k \rangle_{t,t_0} \sim t^\alpha \sim \langle k \rangle_t$, i.e. it is independent of the aging time t_0, aging effects and time t_0 are negligible; if $t \ll t_0$, the mean degree decays with t_0 as $\langle k \rangle_{t,t_0} \sim t_0^{\alpha-1}$. This effect can be understood by considering the inter-event time distribution with divergent mean $\alpha < 1$: this distribution is affected by long periods of inactivity. Starting the integration at a random time t_0 we obtain an increased probability of having an integration interval superimposed on the period of inactivity, in which more individuals do not interact. This implies that the average degree decreases with t_0 for $t \ll t_0$. The aging effect is also observed on the $P_{t,t_0}(k)$ which depends not only on the integration window but also on the aging time. This aging behaviour has been observed in several real systems [81, 84].

1.6.4 Simplicial AD (SAD)

In the original AD network, the interactions take place with a star structure, in which an active node contacts m nodes: thus the interaction events are asymmetric, since one node performs m contacts, but the contacted agents receive only one link. This condition is clearly peculiar, because it foresees an individual (active) with a central role in the interactions and other nodes (which receive the link) instead secondary. This can model information transmission systems by mail or messages, but is not able to describe group interactions in which all involved nodes participate similarly (without asymmetry). This is the case of collaborations between authors or actors, social interactions, populations of spiking neurons [87–92]. A network that evolves over time with higher-order interactions between the nodes is required to describe these systems.

The simplical activity-driven model (SAD) is a modification of the AD model, which accounts for higher-order interactions [87]. Indeed the AD model considering $m = 1$ would represent only pairwise interactions; on the contrary, in the SAD model the building blocks are *simplices* of nodes.

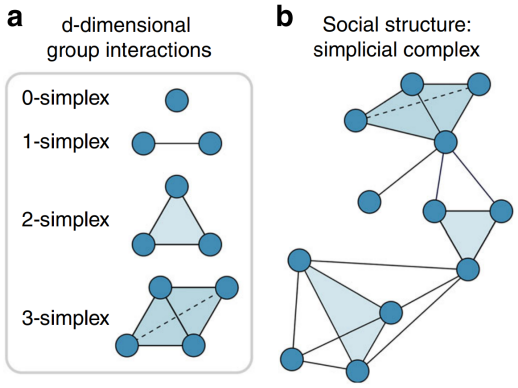

FIGURE 1.9: **Simplicial complexes.** In panel **a** the building blocks of a social system are represented through simplices, which model d-dimensional groups interactions. In panel **b** the simplices are organized in a simplicial complex. Image adapted from [30] under CC BY 4.0 license.

Here we introduce some fundamental definitions for simplicial complexes [29, 30, 87, 91, 93]. A s-simplex (or s-dimensional simplex) σ is a set of $(s+1)$ nodes $\sigma = [v_0, v_1, ..., v_s]$. For example, a 0-simplex is a node, a 1-simplex is the set of two nodes and the link that connects them, a 2-simplex is a triangle consisting of three nodes and the set of all interactions between all of them (see Figure 1.9). A simplicial complex K is a collection of simplices $K = \{\sigma_1, \sigma_2, ..., \sigma_n\}$ such that for every $\sigma \in K$ then all subfaces of σ belong to K (see Figure 1.9). For example if the triangle $[i, j, k] \in K$, it is required that $[i, j]$, $[i, k]$, $[j, k]$, $[i]$, $[j]$ and $[k]$ belong to K. These definitions are trivially respected in the case of group interactions, since in each group interaction foresees all possible sub-interactions. Finally, the d-skeleton K_d of K is the simplicial complex obtained by the union of all the simplices in K with dimension less than or equal to d: for example the 1-skeleton K_1 is the collection of all the links and therefore it is the underlying graph.

The simplicial description of the interactions is extremely powerful because it is accompanied by useful mathematical tools. Simplical complexes can model very regular or highly irregular structures, on them it is possible to define in simple way the Laplacian operators for any dimension and boundary operators that map simplices of different sizes. These operators allow to describe the topology and shape of simplicial complexes.

A set of n-dimensional chains $C_n(K)$ of a simplicial complex K is defined as the formal sum of n-simplices:

$$C_n(K) = \{r_1\sigma_1 + r_2\sigma_2 + ... | r_i \in \mathbb{Z}, \sigma_i \in K_n\}. \tag{1.68}$$

The boundary map ∂_n maps n-dimensional chains $C_n(K)$ to $(n-1)$-dimensional chains $C_{n-1}(K)$ and corresponds to mapping simplices to their edges. Formally:

$$\partial_n : C_n(K) \to C_{n-1}(K) \tag{1.69}$$

$$\partial_n[v_0, ..., v_n] = \sum_{i=0}^{n} (-1)^i [v_0, ..., \hat{v}_i, ..., v_n], \tag{1.70}$$

where the vertex with the hat is omitted. For example a 2-simplex (a complete triangle) is mapped into the alternating sum of its three concatenated links (1-simplex).

The conventional graph Laplacian $\mathcal{L}_0$, defined in Section 1.2, operates on the

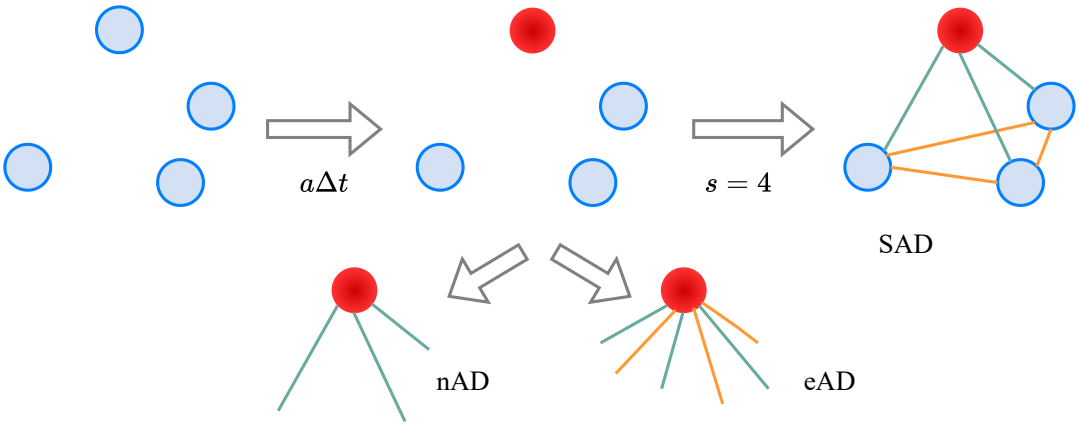

FIGURE 1.10: **Simplicial activity-driven model.** The elementary mechanism of network evolution is represented for the SAD, nAD and eAD models. At each time-step Δt a node activates (red) with probability $a\Delta t$: in the SAD model the node creates a simplex of size s, i.e. a fully connected cluster of s nodes, with $\binom{s}{2}$ interactions between s nodes; in the nAD model the node engages $(s-1)$ interactions with $(s-1)$ distinct nodes; in the eAD model the node creates $\binom{s}{2}$ connections with $\binom{s}{2}$ distinct nodes. In both the eAD and nAD models the interactions are built with a star structure.

nodes of the graph, or on the 0-skeleton, and plays a crucial role in the study of dynamic processes on a network. In the case of a generic simplicial complex, it is possible to define a simplicial (or combinatorial) Laplacian $\mathcal{L}_k$ for each dimension k of the simplices that compose it:

$$\mathcal{L}_k = \partial_{k+1}\partial_{k+1}^* + \partial_k^*\partial_k, \tag{1.71}$$

where $\mathcal{L}_k$ maps $C_k \to C_k$ and is defined through the boundary map. Similarly to the conventional graph Laplacian, the simplicial Laplacian is crucial for the study of dynamic processes on simplicial complexes. While $\mathcal{L}_0$ operates only on nodes and therefore its eigenspectrum is the same for the 1-skeleton and for the simplicial complex, $\mathcal{L}_k$ with $k > 0$ will be very different.

Simplicial complexes can be used to describe social interactions in groups, assuming that a group interaction also implies the underlying pairwise interactions. The SAD model evolution is analogous to the AD model, however when a node is activated it creates an $(s-1)$-simplex, i.e. a clique of size s, which corresponds to a fully connected cluster of s nodes. The others $(s-1)$ nodes participating in the simplex are chosen uniformly at random in the population and in the interactions behave exactly as the active node. Each activation of a node thus produces $s(s-1)/2$ interactions (see Figure 1.10). The size of each active simplex is extracted from the distribution $\Psi(s)$: it allows to model the presence of heterogeneity and fluctuations in the dimension of simplices, as observed in the social dynamics. Group events reasonably involve a number of people that can vary widely depending on the settings, from small groups (e.g. with family or a few friends) to large groups (e.g. sporting events, religious events, university lessons). In general, the distribution $\Psi(s)$ is characterized by being broad and heterogeneous (see Figure 1.11) [87, 89, 92].

The structure of the SAD model can be studied on two levels: on the 1-skeleton, comparing it with the AD model, and on the purely simplicial properties, not comparable to a network approach.

Considering the 1-skeleton, the SAD model can be compared with the AD model

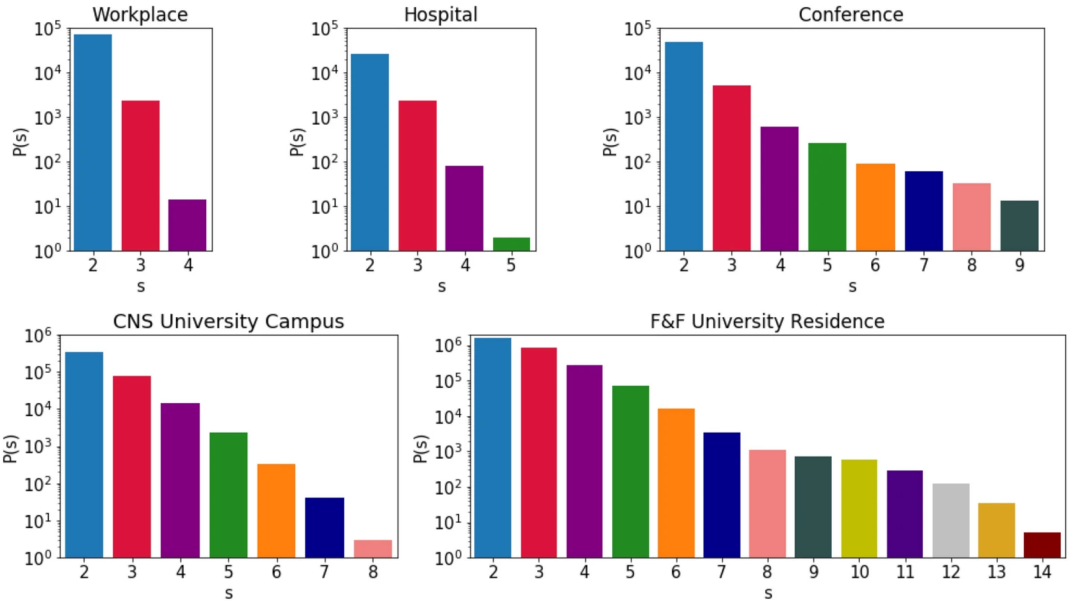

FIGURE 1.11: **Empirical simplex size distributions.** It is plotted, through histograms, the number of human interactions $P(s)$ occurring in simplices of size s in different settings: two university campuses, a conference and a hospital. Image adapted from [89] under CC BY 4.0 license.

by fixing the same number of nodes involved in the activation of an agent (node-matched AD, i.e. nAD) or the same number of interactions (edge-matched AD, i.e. eAD). The activation of a simplex of size s in the SAD model correspond to $m = (s-1)$ in the nAD model, preserving the total number of nodes contacted, and to $m = \binom{s}{2}$ in the eAD model, preserving the total number of links (see Figure 1.10).

For simplicity, a fixed size of simplex size is considered, i.e. $\Psi(s) = \delta(s - \bar{s})$, indicating $\bar{s} = s$. In the SAD model, the number of interactions a node i performs in the time window $[0, T]$ is:

$$\kappa_T(i) = \overline{m} a_i T + \sum_{j \neq i} \frac{\overline{m}^2 T a_j}{N-1} \simeq T(\overline{m} a_i + \overline{m}^2 \langle a \rangle), \tag{1.72}$$

assuming $N \gg 1$ and fixing $\overline{m} = s - 1$. Thus the degree of node i in the aggregate network is the number of distinct nodes contacted:

$$k_T(i) \sim (N-1)\left[1 - e^{-\frac{T(\overline{m} a_i + \overline{m}^2 \langle a \rangle)}{N-1}}\right]. \tag{1.73}$$

It is also possible to obtain the degree distribution, for small k/T and small k/N:

$$P_T(k) \sim \frac{1}{\overline{m} T} \frac{1}{1 - \frac{k}{N-1}} \rho \left[-\frac{N-1}{\overline{m} T} \ln\left(1 - \frac{k}{N-1}\right) - \overline{m} \langle a \rangle\right]. \tag{1.74}$$

$k_T(i)$ depends on $\overline{m}^2$: therefore if the size of the simplex fluctuate through a broad $\Psi(s)$, the fluctuations will strongly affect the aggregate degree. Indeed $k_T(i)$ should be averaged over s and this would produce terms $\langle (s-1)^2 \rangle$, which encode the simplex size fluctuations. This is in contrast to the nAD model, which does not depend on fluctuations, while it is in agreement with the eAD model: this is obvious as what matters for the degree are the interactions produced, which is fixed equal in the SAD

model and eAD.

However, since in the eAD model, $s(s-1)/2$ connections are generated that concern $s(s-1)/2$ nodes, while in the SAD the $s(s-1)/2$ connections concern only $s-1$ nodes, the size of the largest connected component in the SAD model grows much slower than with the eAD model: it grows like in the nAD [87].

From a 1-skeleton point of view the SAD presents similarities and differences with the two considered versions of the AD model. As for the purely simplicial properties, it is possible to study $k_2(i,T)$ defined as the average number of 2-simplices in which node i participated in the SAD model aggregated up to time T:

$$k_2(i,T) = \binom{N-1}{2}\left(1-\exp\left(-\frac{(s-1)(s-2)}{(N-1)(N-2)}T(a_i+(s-1)\langle a\rangle)\right)\right). \quad (1.75)$$

This parameter corresponds to the number of distinct 3-node cliques in which node i participated, which is different (and smaller) from the number of triangles i participated in the 1-skeleton of the aggregated SAD model. This underlines the importance of the simplicial nature of interactions.

Finally, the eigenspectrum of the simplicial Laplacian of the SAD model differs considerably if calculated on the 1-skeleton or on the aggregated SAD simplical complexes: this underlines even more that the SAD model has in itself information that cannot be reduced to only 1-skeleton and differs strongly from the AD model [87].

Other extensions of the AD model have been proposed, for example that bring together burstiness and memory [81], that introduce more network structure through communities [94] or alternative modelization of memory and burstiness [95–97], however here we have focused on those fundamental for our work.

Chapter 2

Epidemic processes

In this Chapter we review the theory of *epidemic processes on temporal networks*: we present a general formalism for epidemic processes on time-varying networks, highlighting the differences with static networks, and we review in detail the main results for *epidemics on activity-driven models*.

2.1 Epidemic models

The mathematical modelling of epidemic processes is an extremely active research field thanks to its strong interdisciplinary nature and its relevance for the humankind. The appearance of new infectious diseases and the persistence of old ones are a strong reason for concern for public health, social welfare and social cohesion. The understanding of the fundamental mechanisms that shape the epidemic spreading is crucial to predict possible developments of epidemics and to guide control and containment policies, in order to minimize and suppress the impact of epidemics [98, 99]. In this framework, an essential role is played by the mathematical modelling of epidemics [99–104], as highlighted and acknowledged during the last major epidemics, such as the H1N1 pandemic, the SARS epidemic and lastly the COVID-19 pandemic (see Figure 2.4). For example, epidemic modelling of COVID-19 allowed to estimate the real extent of the spread of SARS-CoV-2 in the early phases of the pandemic [20, 105], it allowed to predict risk scenarios and to forecast in short-time the trend of epidemic descriptors, such as new infections, deaths and hospitalizations: this allowed policy makers to take decisions on control and containment measures to minimize the health, social and economic costs of the pandemic [16, 106, 107].

A detailed knowledge of contact networks is necessary to obtain outbreak predictions. The availability of large-datasets, the development of computational approaches and mathematical models allowed the implementation of extremely detailed data-driven models to describe the real spread of an epidemic at different spatial and temporal scales [99, 108, 109]. Epidemic models have evolved to structured approaches where population heterogeneity are considered and where spatial structure is taken into account considering sub-populations coupled by travel flows (see Figure 2.1). This meta-population approach is now pushed to the multi-scale framework in which all possible granularities are taken into account, considering cities, states, neighbourhoods, integrating the epidemic model with detailed information on contact networks and on local, national and international transport networks, as well as information on movements obtained through mobile-phone data [3, 99, 104]. In this framework extensive data-intensive computational tools have been developed: an example is the GLEAM (Global Epidemic and Mobility) model [110, 111] (see Figure 2.4).

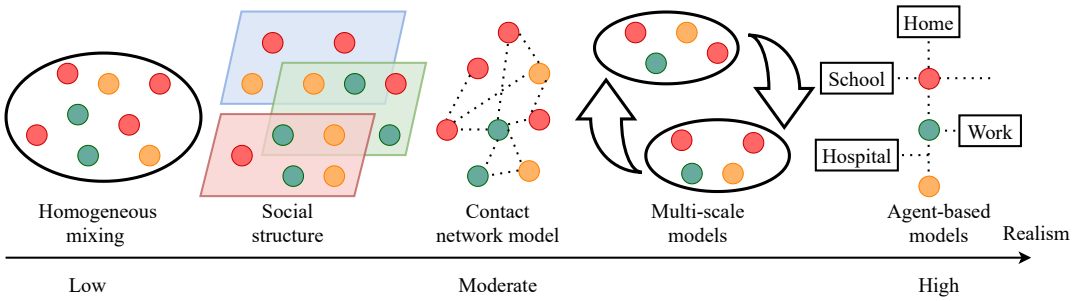

FIGURE 2.1: **Fundamental interaction structures in epidemic models.** Schematic representation of the main structures used to describe interactions in epidemic modelling: nodes represent individuals. From the lowest level of realism to the highest: *homogeneous mixing*, individuals are assumed to interact randomly in a homogeneous way; *social structure*, the population is stratified on the basis of demographic information (e.g. age, social role); *contact network models*, the real pattern of interactions is considered; *multi-scale models*, the population is divided in sub-populations interacting through the mobility and at lower spatial scales homogeneous mixing is assumed; *agent-based models*, the pattern of interactions and mobility of each individual is reconstructed in detail.

These data-driven and data-informed models are essential for developing risk scenarios, for addressing threats and health risks and for developing short-term predictions. However their complexity do not allow to identify the effect of specific properties of the contact network and neither allow to obtain a general understanding of the interplay between the epidemic process and the network dynamics, since these models are strongly data and parameter-dependent [3]. To obtain more general and fundamental results it is necessary to consider simplified models. Although these simplified models are not complete [112], they can provide invaluable information on the fundamental properties of epidemic, by identifying the effects of specific properties of the real networks. The simplification of the real model can be achieved by considering synthetic networks or neglecting network structures, such as hierarchies and heterogeneity. See Figure 2.1 for a detailed description of the main network structures and approaches in epidemic models.

2.1.1 Compartmental epidemic models

In general, epidemics are described through compartmental models, which divide the population into compartments of nodes according to the clinical stage of the disease in which they are or to specific categorization (e.g. immunization, hospitalization). The main compartments considered are the susceptible (S, those who can become infected), the infected (I, those who can infect) and the recovered or removed (R, those who are removed from the chain of infections because recovered or dead). Many other compartments can be introduced to model specific infectious diseases in more detail, such as exposed individuals (E, those who have been infected but are not yet infectious), immunized individuals or hospitalized individuals. Transitions between compartments are regulated by specific mechanisms that define the epidemic model.

In a compartmental epidemic model a node i can be in state $\sigma_i = \{1, 2, ..., \kappa\}$ which corresponds to different health states (compartments) [3]. $X^m(t)$ is the number of individuals in compartment $\sigma = m$ at time t. The dynamics of $X^m(t)$ depends on the specific epidemic model considered: the transition mechanisms between two

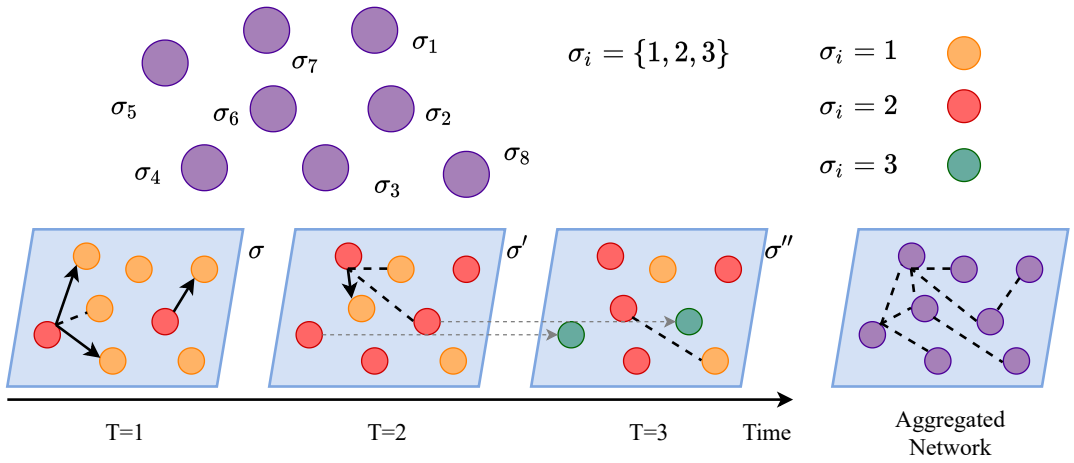

FIGURE 2.2: **Epidemic processes on networks.** We schematically represent a network of $N = 8$ nodes, each described by a dynamic variable σ_i, which can assume three values $\sigma_i = \{1,2,3\}$ (color). In the lower panel a generic epidemic process on a temporal network is represented: the interactions evolve over time according to a snapshot representation and some spontaneous and contact-induced transitions are represented.

different compartments can be *spontaneous*, such as the recovery or loss of immunization, or *induced by contact*, such as infection (see Figure 2.2 for a schematic representation of an epidemic process on a temporal network). A spontaneous transition process can occur with a certain rate from a compartment m to compartment h:

$$X^m \to X^m - 1, \quad X^h \to X^h + 1. \tag{2.1}$$

On the other side, contact processes (or binary interactions) occur through a contact between a node of type g and one of type h, producing or removing a node of type m. Assuming that individuals in each compartment are equivalent and homogeneously mixed, i.e. the probability of interacting with a node of type g at time t is $X^g(t)/N$, the evolution of $X^m(t)$ is:

$$\partial_t X^m(t) = \sum_{h,g} \nu^m_{h,g} a_{h,g} X^h(t) X^g(t)/N + \sum_h \nu^m_h a_h X^h(t), \tag{2.2}$$

where a_h is the spontaneous transition rate for h and $\nu^m_h = -1, 1, 0$ represents the change in the number of individuals in m due to spontaneous process from or to the compartment h, $a_{h,g}$ is the transition rate of the contact process and $\nu^m_{h,g} = -1, 1, 0$ represents the change in the number of m because of the contact between h and g.

We consider here two basic epidemic models: the SIS model (susceptible-infected-susceptible) and the SIR model (susceptible-infected-removed). However, several other models have been implemented, such as the SIRS model, which considers a waning immunity, or the SEIR model, which accounts for a latency period (see Figure 2.3). In all of them, a contact transition is considered $S + I \to 2I$ in which a susceptible individual interacts with an infected one and an infection takes place: thus the transition rate for $S \to I$ depends on the contact pattern and network properties.

The SIS model, provides a mechanism of spontaneous recovery $I \to S$ without immunity (see Figure 2.3). This mechanism allows individuals to be reinfected cyclically, making the model effective in describing endemic infectious diseases (e.g. Influenza-like-illness - ILI).

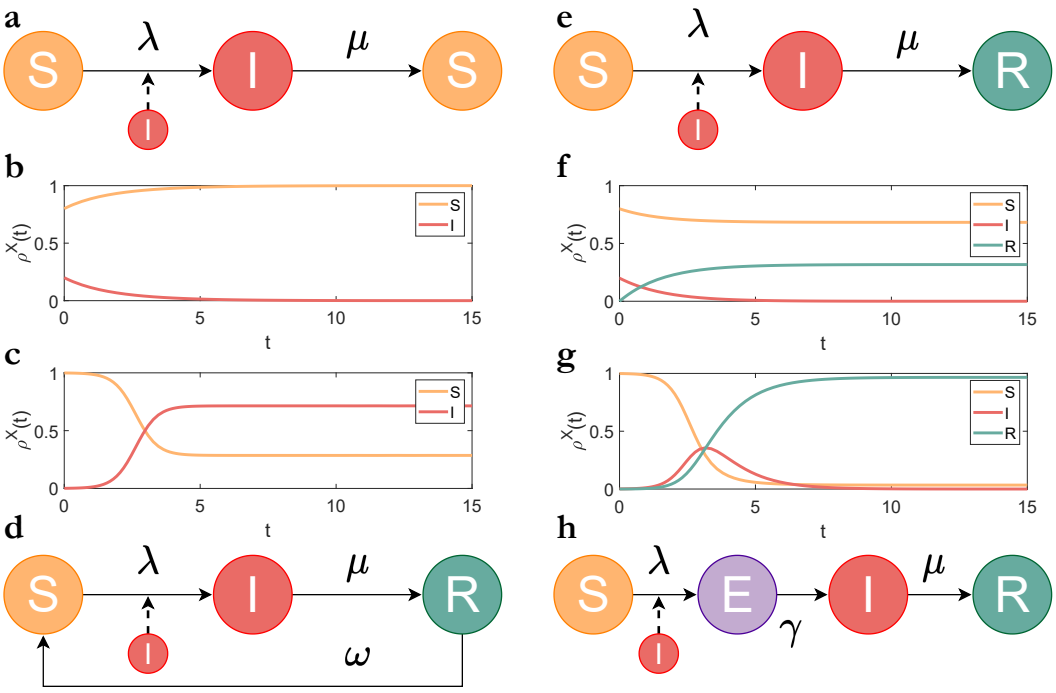

FIGURE 2.3: **Compartmental epidemic models.** Panel **a** shows schematically the SIS epidemic model. In panel **b** we plot the fraction $\rho^S(t)$ of susceptible nodes and the fraction $\rho^I(t)$ of infected nodes as a function of time, for $R_0 = \lambda/\mu = 0.5$, by fixing $\mu = 1$ and initial conditions $[\rho^S(0), \rho^I(0)] = [0.8, 0.2]$. The dynamics are obtained by integrating the Eqs. (2.5) and (2.6). Panel **c** is the same as panel **b** but with $R_0 = 3$ and $[\rho^S(0), \rho^I(0)] = [1 - 10^{-3}, 10^{-3}]$. Panel **e** shows schematically the SIR epidemic model. In panel **f** we plot the fraction $\rho^S(t)$ of susceptible nodes, the fraction $\rho^I(t)$ of infected nodes and the fraction $\rho^R(t)$ of recovered nodes as a function of time, for $R_0 = 0.5$, by fixing $\mu = 1$ and initial conditions $[\rho^S(0), \rho^I(0), \rho^R(0)] = [0.8, 0.2, 0]$. The dynamics are obtained by integrating the Eqs. (2.5) and (2.6). Panel **g** is the same as panel **f** but with $R_0 = 3.5$ and $[\rho^S(0), \rho^I(0), \rho^R(0)] = [1 - 10^{-3}, 10^{-3}, 0]$. In panels **d** and **h** we show schematically the SIRS and SEIR epidemic models respectively.

The SIR model instead predicts a recovery with immunity $I \to R$ (see Figure 2.3), making the model effective in describing infectious diseases with long lasting immunity. All the infected will be removed at a certain stage, thus the epidemic will reach a regime without infected: thus the SIR model do not feature a steady state.

The transitions $I \to S$ and $I \to R$ occur spontaneously after a certain time that the node has spent in the infected state, therefore they do not depend on the interaction network but only on the statistics of recovery, i.e. on the distribution of the infectious periods. This distribution can be obtained from clinical data and typically it is broad and heterogeneous [113, 114]. However, for simplicity a constant transition probability is usually assumed, i.e. a constant recovery rate μ, so that the average infectious period is μ^{-1} and the infectious time distribution is exponential $P_{inf}(\tau) = \mu e^{-\mu\tau}$ (Poissonian recovery process). Throughout this thesis we consider this assumption.

From now on we will consider the following transitions, with the following probabilities for the SIS model:

$$S + I \xrightarrow{\lambda} 2I, \quad I \xrightarrow{\mu} S, \tag{2.3}$$

and for the SIR model:

$$S + I \xrightarrow{\lambda} 2I, \quad I \xrightarrow{\mu} R, \tag{2.4}$$

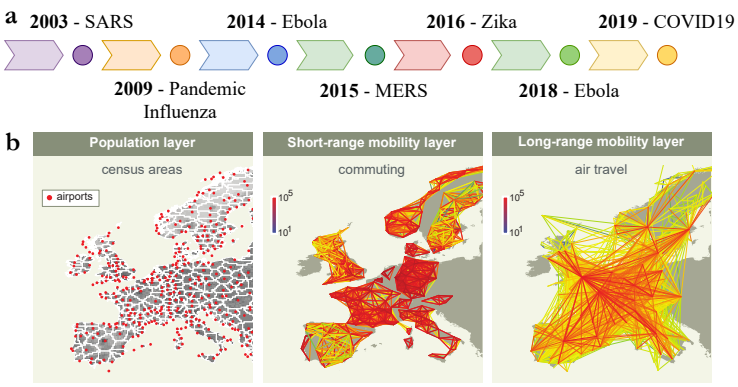

Disease Type	R_0
Measles	12-18
Smallpox	5-10
COVID-19 - δ	5-8
COVID-19 - α	4-5
COVID-19	2.5-3.5
SARS	2-3
HIV	2-5
Pandemic flu	1.5-3.5
Ebola	1.5-3.5

FIGURE 2.4 & TABLE 2.1: **The latest major epidemic outbreaks and their basic reproduction number.** In the table we report the estimated ranges for R_0 of some infectious diseases [99, 115–119]. In panel **a** we show a time-line with the major epidemic outbreaks since 2000. In panel **b** we show the three layers considered by the GLEAM model [110, 111] for modelling epidemics in Europe: the population layer, the short-range and long-range mobility layers. Panel **b** is from [111] under CC BY 2.0 license.

where λ is the infection probability for effective contacts and μ is the recovery rate. The force of infection, i.e. the transition rate for $S \to I$, depends on λ and on the contact pattern, i.e. on the network.

2.1.2 Classical epidemiology

The simplest and classical description of the SIS and SIR models can be formulated in the homogeneous mixing approximation (homogeneous mean-field): all nodes are considered statistically equivalent and the correlations between the node dynamic state $\sigma_i(t)$ are neglected, that is $\langle \sigma_i(t)\sigma_j(t)\rangle = \langle \sigma_i(t)\rangle\langle \sigma_j(t)\rangle$. In this approximation, all nodes have the same properties and feel a mean interaction (mean-field) due to the collective contribution of the other nodes [3, 11]. This approximation is valid in large systems, since it assumes that all nodes interact with each other randomly and therefore are indistinguishable from each other. Under this approximation, we consider the fraction $\rho^\alpha(t) = N^\alpha(t)/N$ of individuals in compartment α. The evolution equations are:

$$\partial_t \rho^I(t) = \lambda \rho^I(t)\rho^S(t) - \mu \rho^I(t), \tag{2.5}$$

$$\partial_t \rho^S(t) = -\lambda \rho^I(t)\rho^S(t) + \chi \rho^I(t), \tag{2.6}$$

where $\chi = \mu$ and $\rho^S(t) = 1 - \rho^I(t)$ for the SIS model, instead in the SIR model $\chi = 0$ and $\rho^R(t) = 1 - \rho^I(t) - \rho^S(t)$. In the initial phases of the epidemic $\rho^I(t \sim 0) \simeq 0$ and therefore, linearizing, the dynamic equations become (both for SIS and SIR models):

$$\partial_t \rho^I(t) \simeq (\lambda - \mu)\rho^I(t), \tag{2.7}$$

with solution:

$$\rho^I(t) \simeq \rho^I(0) e^{(\lambda-\mu)t}. \tag{2.8}$$

In the early phases of the epidemic the fraction of infected individuals is characterized by an exponential phase. If the exponent coefficient is positive the number of cases growth exponentially fast, while if it is negative it decays exponentially fast. In later-time non-linear effects of Eq. (2.5) and Eq. (2.6) become effective and the trend

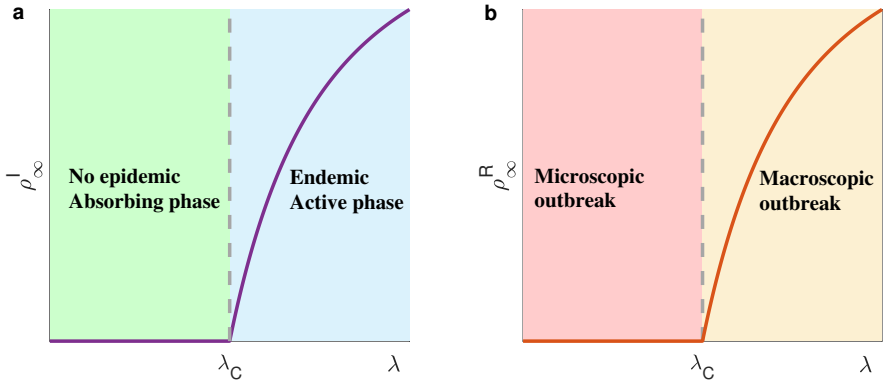

FIGURE 2.5: **Phase diagram of typical epidemic models.** In panel **a** we report the phase diagram of an absorbing-active phase transition, which describes the SIS epidemic model. The order parameter is the epidemic prevalence $\rho^I(t \to \infty) = \rho^I_\infty$. In panel **b** we report the phase diagram of the dynamic phase transition which describes the SIR epidemic model. The order parameter is the epidemic final size $\rho^R(t \to \infty) = \rho^R_\infty$. In both cases the control parameter is the infection rate λ and its critical value is the epidemic threshold λ_C.

is no more exponential (see Figure 2.3). The number of infected increases exponentially if:

$$\lambda - \mu > 0 \Rightarrow r = \frac{\lambda}{\mu} > 1. \tag{2.9}$$

This solution allows to define a key parameter of classical epidemiology: the *basic reproduction number* R_0 [3, 11, 120] defined as the average number of secondary infections produced by an infected individual during the infectious period in a completely susceptible population. If $R_0 > 1$ an infected individual infects on average more than one susceptible individual, suggesting a large-scale propagation; if $R_0 < 1$ an individual generates on average less than a new infected individual, suggesting a receding epidemic. The R_0 value depends on the epidemic model considered (i.e. on the compartments and on the transition rates) and also on the network properties, providing information on the strength of the epidemic both for the pathogen properties and for the features of the interactions pattern on which the pathogen spreads. For example in the homogeneous mean-field approximation of the classical epidemiology $R_0 = \lambda/\mu$ (see Eq. (2.9)). It encodes the idea that the infection process competes with the recovery process: if $R_0 < 1$ the recovery is faster than the infection process and there is no time for infection to spread, while in the opposite case $R_0 > 1$ the infection is extremely effective.

In general the R_0 value can be approximated through mean-field approaches and can be computed from real epidemiological data, with complicated and refined techniques [116]. In Table 2.1 we report the R_0 values obtained for some infectious diseases (see also Figure 2.4). R_0 is a crucial parameter in classical epidemiology, however has some limitations, since it investigate only average infection properties, neglecting heterogeneities which are well known to shape and drive epidemic spreading in real populations [116, 121]. Indeed, typically the number of secondary infections produced by an infected individual is extremely fluctuating, due to the presence of super-spreaders. Several attempts have been proposed to overcome this, even if R_0 is still a crucial epidemic descriptor.

In the SIS model if $R_0 > 1$ the system evolves towards an *endemic* steady state, with a constant finite fraction of infected nodes $\rho^I(t \to \infty) = \rho^I_\infty = 1 - \mu/\lambda = 1 - 1/R_0$ in which individuals are cyclically infected and there is always a fraction

of the population infected (epidemic circulate persistently); if instead $R_0 < 1$ the system evolves towards an absorbing state with all susceptible $\rho^I_\infty = 0$, with epidemic dying out exponentially fast (see Figure 2.3). The SIS model belongs to the Directed-Percolation (DP) universality class, featuring a dynamic phase transition between an absorbing and an active steady state (see Figure 2.5) [11, 122].

In the SIR model if $R_0 > 1$ the system is characterized by an outbreak that infects a finite (macroscopic) fraction of the population $\rho^R(t \to \infty) = \rho^R_\infty \xrightarrow[N\to\infty]{} f$; while if $R_0 < 1$ the epidemic does not spread at large scale, the fraction of infected nodes is negligible (microscopic) and vanishes within the thermodynamic limit $\rho^R_\infty \xrightarrow[N\to\infty]{} 0$ (see Figure 2.3) [3, 11, 122]. The SIR model does not admit a stationary state and its evolution is analogous to the bond percolation (see Figure 2.5) [11, 122].

These results of classical epidemiology detect the presence of a dynamic phase transition: the control parameter is the probability λ of infection (or the effective infection rate $r = \lambda/\mu$), its critical value λ_c (or r_c) is the *epidemic threshold*. The epidemic threshold can be also reformulated in terms of the basic reproduction number R_0, whose critical value is $R^C_0 = 1$, thus in general $R_0 = \lambda/\lambda_C$ (or $R_0 = r/r_C$) provide information on how deeply the system is in the active phase. Moreover, the order parameter depends on the epidemic model: for example, it is the asymptotic fraction of infected individual in the SIS model ρ^I_∞, called *epidemic prevalence*, or the asymptotic fraction of nodes been infected in the SIR model ρ^R_∞, called *epidemic final size*: both are zero below the epidemic threshold, if the epidemic does not spread at large-scales, and are higher than zero above the epidemic threshold, if the epidemic spreads at large-scales (see Figure 2.5).

2.1.3 Epidemics on static networks

The classical epidemiology is based on strong assumptions: it neglects the diffusion of individuals and the spatial scale, which can be introduced with a diffusion term, and Poissonian infection and recovery processes are considered, even if empirical evidence shows heterogeneous time distributions [113, 114]. Moreover, the strongest approximation is the homogeneous mixing, which neglects all the properties of the contact network, its topology, its structure and its eventual temporal dynamics, considering all nodes identical and randomly interacting. This approximation results in obtaining $R_0 = \lambda/\mu$, i.e. $r_C = 1$: however to obtain a more precise estimation of the epidemic threshold and of the epidemic dynamics, we need to relax this assumption, by considering approaches which allow to keep the network structure into account.

An epidemic on a static network can be described exactly through the formalism of the Master Equation, which translates into the Markov chain formalism [123, 124], assuming transitions with constant rates between different epidemic compartments. In a model with N nodes and κ epidemic compartments the system admits κ^N configurations $\sigma(t) = \{\sigma_1(t), \sigma_2(t), ..., \sigma_N(t)\}$: the infinitesimal generator Q of the Markov chain is a matrix κ^N x κ^N and the initial conditions are $\sigma^0(t) = \{\sigma^0_1(t), \sigma^0_2(t), ..., \sigma^0_N(t)\}$. Q and σ_0 are sufficient to obtain the probability $P(\sigma, t)$ that the system is in the configuration σ at time t and all the variables of interest. However, although the Markov chain approach is exact, it allows to obtain results only in very few cases [11]: indeed the method is limited to small N since Q is a matrix κ^N x κ^N, moreover Q is very complex and getting steady-state information from it is quite complicated. Thus, the main analytical results are obtained with mean-field approximations.

We consider the SIS model on an uncorrelated static network with degree distribution $\eta(k)$. A *degree-based mean-field approach* (DBMF) can be applied [11]: the population is divided into classes of nodes with the same degree k and nodes belonging to the same class are treated as statistically equivalent. The probability that a node is in one state is independent of the dynamic state of its neighbours, depending only on its degree k, and $\langle\sigma_i\sigma_j\rangle = \langle\sigma_i\rangle\langle\sigma_j\rangle$. These approach, completely disregard the exact topology of the network, imposing the statistical equivalence of nodes belonging to the same k class: this corresponds to replacing the true adjacency matrix $\boldsymbol{A}(t) = A_{ij}(t)$ with its ensemble average $\overline{\boldsymbol{A}}(t) = \overline{A_{ij}}(t)$ (annealed network approximation). The epidemic dynamics is described by means of the probability $\rho_k^\alpha(t)$ that a node with degree k is in compartment α at time t. Thus, $\sum_\alpha \rho_k^\alpha(t) = 1$ and $\rho^\alpha(t) = \sum_k \eta(k)\rho_k^\alpha(t)$ is the fraction of nodes in compartment α at time t. The evolution equation is:

$$\partial_t \rho_k^I(t) = -\mu\rho_k^I(t) + \lambda k[1-\rho_k^I(t)]\sum_{k'}\eta(k')\frac{k'}{\langle k\rangle}\rho_{k'}^I(t). \tag{2.10}$$

By imposing the stability of the absorbing state it is possible to obtain the epidemic threshold:

$$r_C^{DBMF} = \left.\frac{\lambda}{\mu}\right|_C = \frac{\langle k\rangle}{\langle k^2\rangle}. \tag{2.11}$$

The epidemic threshold (and R_0) strongly depends on the topology and on the structure of the network through the moments of the distribution $\eta(k)$. This shows the need to take into account the heterogeneity and topology of the network: for example a vanishing threshold is obtained when the fluctuations in k diverge (e.g. for a power-law $\eta(k)$ with appropriate exponent).

The *individual-based mean-field approach* (IBMF) [11], assumes that there are no local correlations between the dynamic states of the nodes σ_i, but nevertheless provides a different probability for each node i to be in a state $\sigma_i = x$ at time t. Thus, the probability that a node is in one state is independent of the dynamic state of its neighbours, and $\langle\sigma_i\sigma_j\rangle = \langle\sigma_i\rangle\langle\sigma_j\rangle$. This approach makes use of the classic approximation of the homogeneous mixing on local correlations, but keeps the structure and topology of the interactions, which are still described by the adjacency matrix $\boldsymbol{A}(t) = A_{ij}(t)$ (quenched network approximation). The epidemic dynamics is described by the probability $\rho_i^\alpha(t)$ for the node i to be in the compartment α at time t. The evolution equation in this approximation is:

$$\partial_t \rho_i^I(t) = -\mu\rho_i^I(t) + \lambda[1-\rho_i^I(t)]\sum_{j=1}^{N} A_{ij}\rho_j^I(t), \tag{2.12}$$

where $\boldsymbol{A} = A_{ij}$ is the adjacency matrix of the network. By imposing the stability of the absorbing state, the epidemic threshold is obtained:

$$r_C^{IBMF} = \left.\frac{\lambda}{\mu}\right|_C = \frac{1}{\Lambda_1}, \tag{2.13}$$

where Λ_1 is the maximum eigenvalue of the adjacency matrix. The threshold therefore strongly depends on the network topology through the properties of the adjacency matrix. The estimate of r_C is approximate but it has been observed that it is in very good agreement with results of extensive numerical simulations [11]. The DBMF result is equivalent to the IBMF with an additional approximation: the

detailed network topology is replaced by the annealed one, since considering statistically equivalent all the nodes with the same degree k corresponds to consider the annealed adjacency matrix $\overline{A_{ij}} = k_j k_i / N\langle k\rangle$ and $\rho_k^I(t) = \sum_{i\in k} \rho_i^I / (N\eta(k))$.

Similarly, mean-field approaches can be applied to the SIR model on static networks. For example, in the DBMF approach the SIR epidemic threshold is [11]:

$$r_C^{DBMF} = \frac{\lambda}{\mu}\bigg|_C = \frac{\langle k\rangle}{\langle k^2\rangle - \langle k\rangle}, \tag{2.14}$$

taking into account that in the SIR model a node cannot infect the neighbour who originally infected it, since it will be infected or recovered. Moreover, in some cases is possible to obtain exact results for SIR epidemic model by mapping it to the bond percolation [11].

The r_C values obtained for the SIS and SIR models in heterogeneous networks show that heterogeneity observed in real networks lower the epidemic threshold favouring the epidemic spreading. This is due to the role of hubs in the network, who behave like super-spreaders and drive the epidemic: once the pathogen reaches them it can easily spread among the network.

2.2 Epidemic processes on temporal networks

The results presented in Section 2.1.3 holds for static networks, however the temporal dynamics of the network, as explained in Chapter 1, can profoundly modify the properties of the network and therefore the epidemic spreading. For example, the epidemics propagate along time-respecting paths: by seeding the infection in one node, only its set of influence will be infectable. Moreover, not all the links in the aggregate network are accessible by the real pathogen diffusion, as they may be absent at the time t a node is infected.

Rigorous analytical results on the spread of epidemics on temporal networks have been obtained only recently due to the difficulty of dealing with the coupling between the dynamics of the network and the epidemic process. In the next Section we will present a novel theoretical framework for epidemic processes on arbitrary temporal networks, which represents the first systematic result. Then we will focus on epidemic spreading on activity-driven temporal models, which constitute the natural framework of this thesis.

2.2.1 The infection propagator approach

A general approach to the study of epidemic processes on temporal networks can be obtained by extending the Markov chain approach to temporal networks and by reinterpreting the tensor formalism of multilayer networks [125–127].

Let us consider a static network of N nodes described by an adjacency matrix A, on which a SIS process evolves in discrete time ($\Delta t = 1$). The propagation of the epidemic is described by the probability $p_i(t)$ that the node i is infected at time t, which evolves according to the equation:

$$p_i(t) = 1 - [1 - (1-\mu)p_i(t-1)] \prod_j \left[1 - \lambda A_{ji} p_j(t-1)\right], \tag{2.15}$$

obtained through the Markov chain approach, in the individual-based mean-field approach. The epidemic threshold is $r_C = (\lambda/\mu)_C = \rho(A^\dagger)$, where $\rho(A^\dagger)$ is the spectral radius of the transposed adjacency matrix [11, 125].

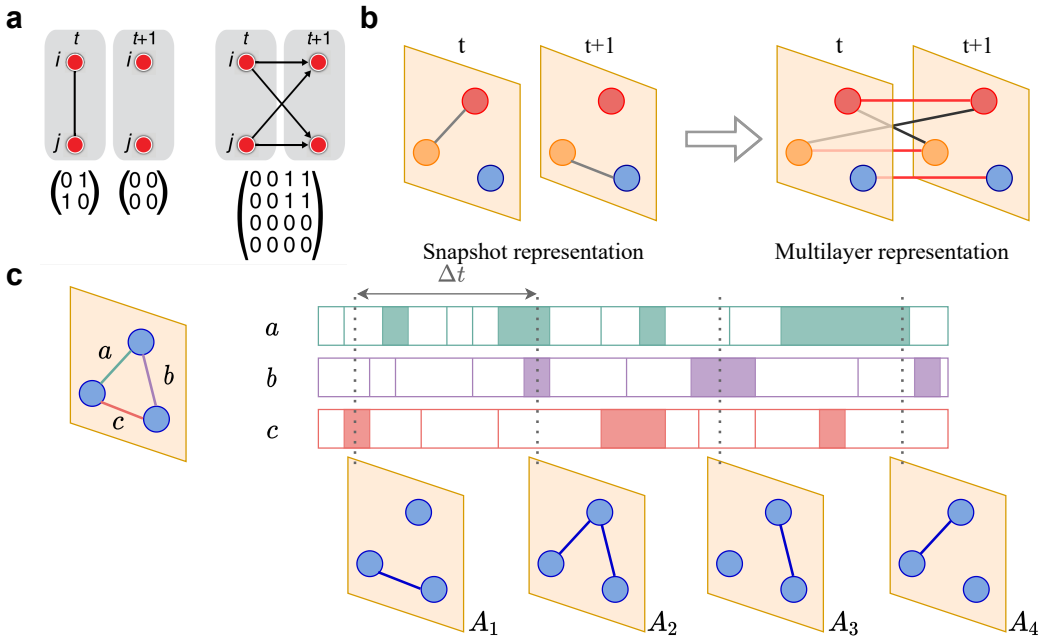

FIGURE 2.6: **Infection propagator approach.** In panel **a** we consider a temporal network of $N = 2$ nodes and we represent it by the snapshot representation and by the multilayer representation. The matrices shown below correspond to the adjacency matrices of the snapshots and the supra-adjacency matrix of the multilayer representation of the network. In panel **b** the same representation is produced for a network of $N = 3$ nodes, colouring the diagonal coupling in red and the non-diagonal coupling in black. In panel **c** we represented a discretization of a continuous-time evolving network. Each connection $\{a, b, c\}$ is activated over time according to the time sequence represented by the coloured bars. The evolution of time is discretized on intervals Δt obtaining a sequence of adjacency matrices $\{A_1, A_2, A_3, A_4\}$ corresponding to the sampled snapshots. Panel **a** is from [125] under CC BY 3.0 license.

This approach can be extended to temporal networks by assuming that the adjacency matrix depends on time $A(t)$ [125]. Considering the adjacency matrix $A(t)$ of the snapshot at time t, the spread of the epidemic is governed by:

$$p_i(t) = 1 - [1 - (1 - \mu)p_i(t-1)] \prod_j \left[1 - \lambda A_{ji}(t-1)p_j(t-1)\right]. \tag{2.16}$$

We assume periodic boundary conditions on the adjacency matrix, with period T, i.e. $A(T+1) \equiv A(1)$: this guarantees the existence of an asymptotic solution of the epidemic dynamics on a generic network, which will be periodic with period T, without limiting the generality of the result.

The epidemic and network dynamics can be described using a multilayer approach (see Figure 2.6), mapping the temporal network to the tensor space $\mathbb{R}^N \otimes \mathbb{R}^T$, in which each node is identified by two indices (i, t), corresponding to the node index and the time considered. The multilayer network is defined assuming:

- **the ordinal (diagonal) coupling term:** each node at time t is connected with itself at time $t + 1$;
- **the non-diagonal coupling term:** if i is connected to j at time t, i.e. $A_{ij}(t) \neq 0$, then i in the layer at time t is connected to j in the layer at time $t + 1$ and similarly j in the layer at time t is connected to i in the layer at time $t + 1$.

The obtained multilayer network has no links in the same layer and therefore is multipartite: connections occur only between two consecutive layers (see Figure 2.6). This new representation of the network encodes all the information necessary to understand the epidemic spreading. The multilayer network can be represented tensorially as:

$$\boldsymbol{A}_{ij}^{tt'} = \delta^{t,t'+1}[\delta_{ij} + A_{ij}(t)], \tag{2.17}$$

and similarly, the tensor associated with the epidemic dynamics can be constructed by coupling the two dynamics:

$$\boldsymbol{M}_{ij}^{tt'} = \delta^{t,t'+1}[(1-\mu)\delta_{ij} + \lambda A_{ij}(t)]. \tag{2.18}$$

The tensor space can be represented with a single index by applying an isomorphism $(i,t) \to \alpha = Nt + i$, with $\alpha \in \{1, 2, ..., NT\}$. This means mapping $\mathbb{R}^N \otimes \mathbb{R}^T$ with $\mathbb{R}^{NT}$, allowing to rewrite the $\boldsymbol{M}$ tensor in matrix form, representing the coupled topology and temporal dimension underlying the epidemic dynamics:

$$M = \begin{bmatrix} 0 & 1-\mu+\lambda A(1) & 0 & \dots & 0 \\ 0 & 0 & 1-\mu+\lambda A(2) & \dots & 0 \\ \vdots & \vdots & \vdots & \vdots & \vdots \\ 0 & 0 & 0 & \dots & 1-\mu+\lambda A(T-1) \\ 1-\mu+\lambda A(T) & 0 & 0 & \dots & 0 \end{bmatrix} \tag{2.19}$$

The non-symmetric nature of this representation preserves the temporal ordering of events and causality, while the weights take into account the transition probabilities of the epidemic model.

The system is described by a vector $\hat{p}_\alpha(\tau)$ which represents the probability for each node to be infected at each time-step t in the interval $[\tau T, (\tau+1)T]$. This state vector thus evolves in space $\mathbb{R}^{NT}$, according to the equation:

$$\hat{p}_\alpha(\tau) = 1 - \prod_\beta [1 - M_{\beta\alpha}\hat{p}_\beta(\tau - 1)]. \tag{2.20}$$

The asymptotic state, periodic with period T, is mapped to the steady state $\hat{p}_\alpha(\tau) = \hat{p}_\alpha(\tau - 1)$, which can be obtained from:

$$\hat{p}_\alpha = 1 - \prod_\beta [1 - M_{\beta\alpha}\hat{p}_\beta]. \tag{2.21}$$

By linearizing the equation around the absorbing state and imposing the asymptotic stability, the condition for the epidemic threshold is obtained [125]:

$$\rho(M^\dagger) = 1, \tag{2.22}$$

where $\rho(M^\dagger)$ is the spectral radius of the transpose of M. The equation gives the critical value $r_C = (\lambda/\mu)_C$ for the absorbing-active phase transition. Moreover, the spectral radius can be simplified as follows:

$$\rho(M) = \rho(P)^{1/T}, \tag{2.23}$$

where

$$P = \prod_{t=1}^{T} (1 - \mu + \lambda A(t)). \tag{2.24}$$

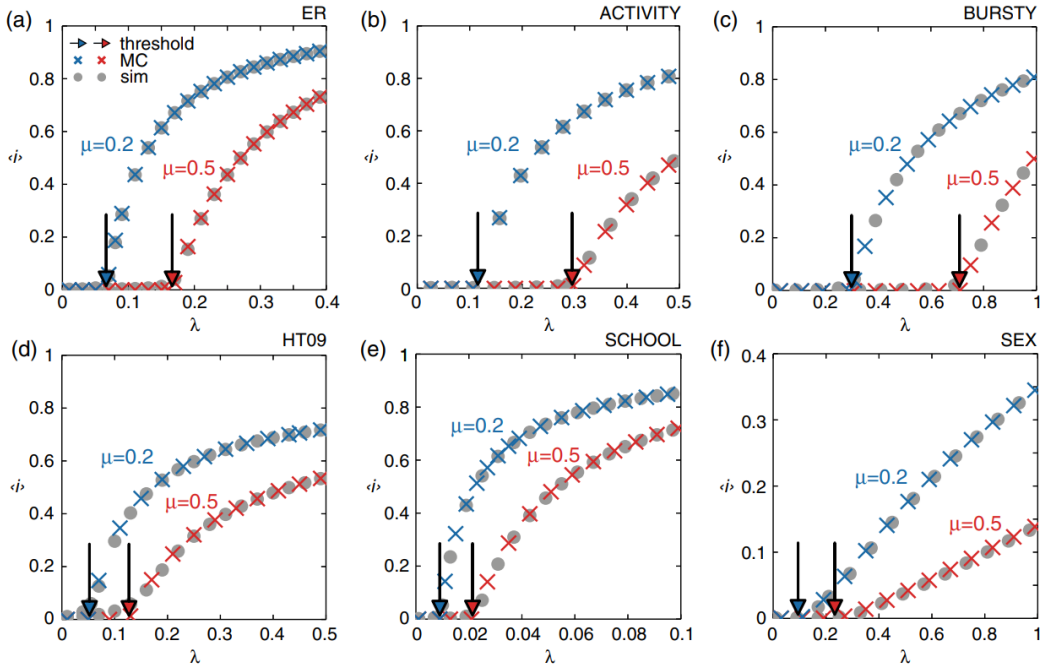

FIGURE 2.7: **Numerical validation of the infection propagator approach.** In all the panels the epidemic prevalence $\langle i \rangle$ is plotted as a function of the probability of infection λ: the cross symbols represent the numerical solutions of Eq. (2.16); the circles represent the numerical simulations of the SIS process; the arrows indicate the analytical estimate of the epidemic threshold obtained from Eq (2.23). In each panel a different temporal network is considered as a substrate for the SIS process: a sequence of random Erdos-Rényi graphs (panel **a**), the activity-driven network (panel **b**), a network with bursty dynamics (panel **c**), an empirical network of face-to-face interactions during a scientific conference (panel **d**), a network of sexual contacts (panel **e**), a network of interactions in a high school (panel **f**). Image from [125] under CC BY 3.0 license.

P is a weighted matrix and can be physically interpreted as the *infection propagator*, which gives the name to this approach thus called the *infection propagator approach* [125, 126]. We consider a time-respecting path between nodes i and j that lasts T time steps and long n jumps (with waiting time $T - n$). The element P_{ij} is the sum over all the time-respecting paths from i to j, from time $t = 1$ to time $t = T$, each weighted with $\lambda^n(1-\mu)^{T-n}$, which is the probability that the infection starting from i at time $t = 1$ pass to j at time $t = T$. Thus P_{ij} represents the total probability that j is infected at time $t = T$ knowing that the infection originated from i infectious at time $t = 1$. P describes the propagation of the infection near the absorbing state (small probabilities) and assuming the absence of interactions between the paths (mean-field).

The infection propagator approach allows to analytically calculate the SIS epidemic threshold, without any assumptions about the topology or dynamics of the network, only assuming the absence of local correlations (mean-field). Moreover, the validity of the approach has been extensively verified for empirical and synthetic temporal networks, considering numerical simulations of the epidemic (see Figure 2.7) and considering limit cases, such as the quenched and annealed regimes [125].

The infection propagator approach has also been extended to consider the impact of immunity [126], showing that the immunity and its duration do not modify

the epidemic threshold, as also already observed in static networks [128, 129]. Indeed, if we consider the SIRS model (see Figure 2.3), i.e. the SIR model with waning immunity $R \xrightarrow{\omega} S$, the equations of the model in the Markov chain approach are:

$$p_i(t) = (1-\mu)p_i(t-1) + (1-p_i(t-1)-q_i(t-1))\left[1-\prod_j(1-A_{ji}(t-1)p_j(t-1))\right], \tag{2.25}$$

$$q_i(t) = \mu p_i(t-1) + (1-\omega)q_i(t-1), \tag{2.26}$$

where $p_i(t)$ is the probability that node i is infected at time t and $q_i(t)$ is the probability that node i is recovered at time t. Linearizing around this state $p_i(t) = q_i(t) = 0$:

$$p_i(t) \approx \sum_j (A_{ji}(t-1) + (1-\mu)\delta_{ij})p_j(t-1), \tag{2.27}$$

$$q_i(t) = \mu p_i(t-1) + (1-\omega)q_i(t-1). \tag{2.28}$$

The equation for $p_i(t)$ no longer depends on $q_i(t)$, thus the immunity does not change the epidemic threshold. The threshold of the SIS model and the corresponding infection propagator are also valid for the SIRS model, independently on the rate ω. Thus:

$$\lambda_C^{SIR} = \lim_{\omega\to 0}\lambda_C^{SIRS} = \lambda_C^{SIRS} = \lambda_C^{SIS}. \tag{2.29}$$

The approach presented is valid only for discrete-time evolving networks, since it is based on representing the network as a multilayer object. When dealing with continuous-time evolving networks this representation is no longer valid: the infection propagator approach can be extended also to the continuous case [127].

Let us now consider a temporal network of N nodes that continuously evolves over time with an adjacency matrix $A(t)$ with $t \in [0, T]$ and that constitutes the substrate for an SIS epidemic model. The network can be discretized with time-step Δt, considering the sequence of snapshots $\{A_1, A_2, ..., A_{T_{step}}\}$, where $T_{step} = \lfloor T/\Delta t \rfloor$ and $A_h = A(h\Delta t)$, which approximates the network with accuracy decreasing with Δt (see Figure 2.6). By applying the infection propagator approach to the discretized network, the epidemic threshold is given by the relation $\rho[P(T_{step})] = 1$ where:

$$P(T_{step}) = \prod_{k=1}^{T_{step}}[1 - \mu\Delta t + \lambda\Delta t A_k], \tag{2.30}$$

is the discrete infection propagator. Starting from these results for the discretized network, it can be obtained the continuous-time limit of P [127], i.e. the *continuous-time infection propagator*:

$$P(t) = \mathcal{T}exp\left(\int_0^t dx[-\mu + \lambda A(x)]\right), \tag{2.31}$$

where $\mathcal{T}$ is Dyson's time order operator, defined as $\mathcal{T}A(t_1)A(t_2) = A(t_1)A(t_2)\theta(t_1 - t_2) + A(t_2)A(t_1)\theta(t_2 - t_1)$, with $\theta(x)$ Heaviside step-function. The epidemic threshold can be obtained from:

$$\rho[P(T)] = 1. \tag{2.32}$$

The infection propagator in general need to be computed numerically due to its complex definition, however it can be obtained explicitly in a closed-form in the *weak communication hypothesis*, i.e. if the adjacency matrix $A(t)$ commutes with the

aggregate adjacency matrix up to t:

$$\left[A(t), \int_0^t dx A(x)\right] = 0, \quad \forall t \in [0, T]. \tag{2.33}$$

This condition allows to state that the ordering of the factors in Eq. (2.31) is no longer relevant and therefore the Dyson operator $\mathcal{T}$ can be removed, obtaining explicitly the infection propagator:

$$P(T) = e^{T[-\mu+\lambda\langle A\rangle]}, \tag{2.34}$$

where $\langle A\rangle = \int_0^T dt A(t)/T$ is the time-averaged matrix, and the threshold becomes:

$$r_C = \frac{\lambda}{\mu}\bigg|_C = \frac{1}{\rho[\langle A\rangle]}. \tag{2.35}$$

This closed relation is useful in those classes of networks which respect weak communication, such as annealed networks, networks whose adjacency matrix depends on time as a scalar function $\langle A(t)\rangle = c(t)\langle A(0)\rangle$ and the original activity-driven network model [127].

The infection propagator approach constitutes a theoretical framework to concisely and analytically describe the epidemic diffusion on arbitrary time-varying networks, allowing the calculation of the epidemic threshold for different epidemic models (e.g. SIS, SIR or SIRS) on dynamical networks both with discrete dynamics and with continuous dynamics, both for synthetic and empirical networks.

2.3 Epidemics on activity-driven models

The activity-driven (AD) models presented in Section 1.6 allow to describe exactly and analytically the spread of an epidemic occurring on top of them, by considering the real dynamics of the links and without the need to consider the aggregate static network or a time-scales separation [13].

We consider here the SIS epidemic model on the original AD network described in Section 1.6 with activity distribution $\rho(a)$. An *activity-based mean-field approach* can be applied, dividing the nodes in classes with the same activity a and assuming that all nodes belonging to the class behave statistically in the same way. Thus, the epidemic is described by the number $I_a(t)$ of infected individuals at time t belonging to the activity class a. The evolution of $I_a(t)$, considering the AD model with discrete time-step Δt, is:

$$I_a(t+\Delta t) - I_a(t) = -\mu\Delta t I_a(t) + \lambda m S_a(t) a \Delta t \int da' \frac{I_{a'}(t)}{N} + \lambda m S_a(t) \int da' \frac{a'\Delta t I_{a'}(t)}{N}, \tag{2.36}$$

where $S_a(t)$ is the number of susceptible nodes in class a at time t, $N_a = I_a(t) + S_a(t)$ is the number of nodes belonging to the activity class a and $N = \int da N_a$ is the total number of nodes. In Eq. (2.36) the first term in the right-hand side accounts for spontaneous recovery, the second term takes into account the probability that a susceptible node with activity a activates and is infected through a connection to another infected node (summing over all activity classes), while the fourth term takes into account the probability that a susceptible node with activity a receives a connection from an active infected node (summing up to all activities).

The equation for the total number of infected nodes $I(t) = \int da I_a(t)$ is obtained by integrating Eq. (2.36) on the activity:

$$I(t+\Delta t) = I(t) - \mu \Delta t I(t) + \lambda m \langle a \rangle \Delta t I(t) + \lambda m \Delta t \theta(t), \tag{2.37}$$

where $\theta(t) = \int da I_a(t) a$, $\langle f(a) \rangle = \int da f(a) \rho(a)$ and the higher-order terms in $I(t)$ and $\theta(t)$ have been neglected, assuming that in the early phase of an epidemic $I_a(t) \ll N_a(t)$ (or considering the system near to the epidemic threshold $r \sim r_C$). To obtain the evolution equation of $\theta(t)$, Eq. (2.36) is multiplied for a and integrate on the activity obtaining:

$$\theta(t+\Delta t) = \theta(t) - \mu \Delta t \theta(t) + \lambda m \langle a^2 \rangle \Delta t I(t) + \lambda m \langle a \rangle \Delta t \theta(t). \tag{2.38}$$

In the continuous-time limit $\Delta t \to 0$ the Eqs. (2.37) and (2.38) are:

$$\partial_t I(t) = -\mu I(t) + \lambda m \langle a \rangle I(t) + \lambda m \theta(t), \tag{2.39}$$

$$\partial_t \theta(t) = -\mu \theta(t) + \lambda m \langle a^2 \rangle I(t) + \lambda m \langle a \rangle \theta(t). \tag{2.40}$$

The Jacobian matrix of the system of equations is:

$$J = \begin{bmatrix} -\mu + \lambda m \langle a \rangle & \lambda m \\ \lambda m \langle a^2 \rangle & -\mu + \lambda m \langle a \rangle \end{bmatrix} \tag{2.41}$$

This J matrix admits eigenvalues:

$$\Lambda_{\pm} = \langle a \rangle \lambda m - \mu \pm \lambda m \sqrt{\langle a^2 \rangle}. \tag{2.42}$$

The epidemic threshold can be obtained by imposing the stability of the absorbing state $(I(t), \theta(t)) = (0,0)$, i.e. by imposing that the maximum eigenvalue Λ_+ is negative, obtaining:

$$r_C^{AD} = \frac{\lambda}{\mu}\bigg|_C = \frac{1}{m} \frac{1}{\langle a \rangle + \sqrt{\langle a^2 \rangle}}. \tag{2.43}$$

The obtained epidemic threshold is exact, as shown with numerical simulations in Figure 2.8, since the model is exactly mean-field: indeed, local correlations are continuously destroyed at each time-step with the destruction of the links.

The approach implemented takes into account the real temporal dynamics of the interactions, describing the real coupling between the dynamics of the network and the epidemic. In particular, the epidemic threshold shows that the spread of the epidemic depends on the natural time scale of the network, i.e. on $\langle a \rangle^{-1}$, and on the heterogeneity and fluctuations in activity encoded in $\rho(a)$, i.e. $\langle a^2 \rangle$. Broad activity distributions produce a lower threshold, because of the presence of very active nodes which, due to the high number of interactions, favour the epidemic. The AD model is able to effectively describe the effect of heterogeneities in the agents behaviour on epidemics.

Moreover, the epidemic threshold and the epidemic prevalence are considerably different considering the integrated network or the real temporal network. This is shown in Figure 2.8: the aggregate network allows the epidemic to spread on links that are not temporally ordered while in the temporal network the epidemic can only propagate along temporally ordered paths, producing a lower threshold and a higher prevalence in the aggregate case [13]. This shows the crucial role of the temporal dimensionality of the network.

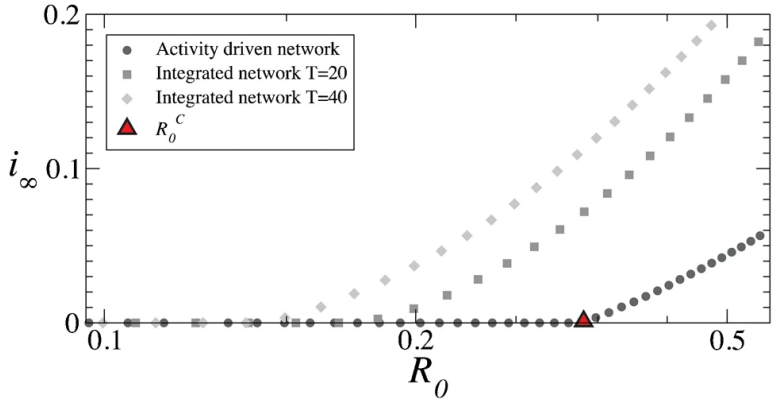

FIGURE 2.8: **SIS epidemic threshold and epidemic prevalence in the AD network.** The epidemic prevalence $I_\infty = I(t \to \infty)$ is plotted as a function of the basic reproduction number R_0. I_∞ was obtained by numerical simulations of the SIS model on a temporal AD network and on two static networks obtained by integrating the temporal network on $T = 20$ and $T = 40$ time-steps. Each point corresponds to an average over 10^2 independent simulations, $N = 10^6$, $m = 5$, $\eta = 10$, $\rho(x) \propto x^{-\nu}$ with $a = \eta x$, $\nu = 2$, $x \in [10^{-3}, 1]$. Furthermore, the epidemic threshold obtained through Eq. (2.43) is highlighted with a red triangle. Image adapted from [13] under CC BY-NC-SA 3.0 license.

Finally, analogous results on the epidemic threshold can be obtained for the SIR model, mapping it to the temporal percolation model on the AD network. In this model the SIS and SIR thresholds coincide as a consequence of the Markov dynamics of the link formation (as shown in Section 2.2.1) [13, 126, 128–130].

2.3.1 Epidemics on AD with attractiveness

In Section 1.6.1 we presented the AD model with attractiveness (ADA), showing how the presence of a popularity index modifies the topological and temporal network properties: this can induce effects on the spread of epidemics [71, 72].

In the ADA network each node is assigned with an activity a and an attractiveness b parameter, drawn from a joint distribution $\rho(a, b)$. An active node i contacts another node j with probability $p_{b_j} = b_j / \langle b \rangle N$, where the denominator is a normalization factor. We consider the SIS epidemic model on the ADA network and we apply an *activity-attractiveness-based mean-field approach*, dividing the population into classes of nodes (a, b) with equal activity and attractiveness: the nodes within the same class are considered statistically equivalent and to be fully described by (a, b).

The epidemics is described by the number $I_{a,b}(t)$ of nodes belonging to the class (a, b) infected at time t. The evolution of $I_{a,b}(t)$ is described by a Master Equation, valid in the limit $N \gg 1$ (i.e. the probability that two nodes have repeated contact with each other can be neglected):

$$I_{a,b}(t + \Delta t) - I_{a,b}(t) = -\mu \Delta t I_{a,b}(t) + \frac{\lambda m}{N \langle b \rangle} S_{a,b}(t) \left[a \Delta t \int da' \int db' b' I_{a',b'}(t) + b \int da' \int db' a' \Delta t I_{a',b'}(t) \right], \tag{2.44}$$

where $S_{a,b}(t)$ is the number of susceptible nodes in class (a, b) at time t, $N_{a,b} = I_{a,b}(t) + S_{a,b}(t)$ is the number of nodes in the class (a, b) and $N = \int da \int db N_{a,b}$ is the total number of nodes. This equation is analogous to Eq. (2.36) of the AD model, but the probability of being contacted for a node of class (a, b) now is $b / \langle b \rangle N$ [72].

The evolution equation for the total number of infected nodes at time t, $I(t) = \int da \int db I_{a,b}(t)$, is obtained by integrating Eq. (2.44) on all classes:

$$I(t+\Delta t) = I(t) - \mu \Delta t I(t) + \frac{\lambda m}{\langle b \rangle} \Delta t [\langle a \rangle \phi(t) + \langle b \rangle \theta(t)], \tag{2.45}$$

where $\langle f(a,b) \rangle = \int da \int db \rho(a,b) f(a,b)$, $\phi(t) \equiv \int da \int db I_{a,b}(t) b$ and $\theta(t) \equiv \int da \int db I_{a,b}(t) a$ and where higher-order terms in $I(t)$, $\phi(t)$ and $\theta(t)$ are neglected, assuming that in the early stages of the epidemic $I_{a,b}(t) \ll N_{a,b}$ (or that the system is near to the epidemic threshold $r \sim r_C$). The Master Equations for $\phi(t)$ and $\theta(t)$ are obtained by multiplying Eq. (2.44) respectively for b and a and then summing on the classes (a,b):

$$\phi(t+\Delta t) = \phi(t) - \mu \Delta t \phi(t) + \frac{\lambda m}{\langle b \rangle} \Delta t [\langle ab \rangle \phi(t) + \langle b^2 \rangle \theta(t)], \tag{2.46}$$

$$\theta(t+\Delta t) = \theta(t) - \mu \Delta t \theta(t) + \frac{\lambda m}{\langle b \rangle} \Delta t [\langle a^2 \rangle \phi(t) + \langle ab \rangle \theta(t)]. \tag{2.47}$$

In the continuous-time limit $\Delta t \to 0$:

$$\partial_t I(t) = -\mu I(t) + \frac{\lambda m}{\langle b \rangle} [\langle a \rangle \phi(t) + \langle b \rangle \theta(t)], \tag{2.48}$$

$$\partial_t \phi(t) = -\mu \phi(t) + \frac{\lambda m}{\langle b \rangle} [\langle ab \rangle \phi(t) + \langle b^2 \rangle \theta(t)], \tag{2.49}$$

$$\partial_t \theta(t) = -\mu \theta(t) + \frac{\lambda m}{\langle b \rangle} [\langle a^2 \rangle \phi(t) + \langle ab \rangle \theta(t)]. \tag{2.50}$$

This system admits a Jacobian matrix:

$$J = \begin{bmatrix} -\mu & \frac{\lambda m}{\langle b \rangle} \langle a \rangle & \lambda m \\ 0 & -\mu + \frac{\lambda m}{\langle b \rangle} \langle ab \rangle & \frac{\lambda m}{\langle b \rangle} \langle b^2 \rangle \\ 0 & \frac{\lambda m}{\langle b \rangle} \langle a^2 \rangle & -\mu + \frac{\lambda m}{\langle b \rangle} \langle ab \rangle \end{bmatrix} \tag{2.51}$$

which has eigenvalues:

$$\Lambda_0 = -\mu, \qquad \Lambda_\pm = \frac{\lambda m}{\langle b \rangle} \left(\langle ab \rangle \pm \sqrt{\langle a^2 \rangle \langle b^2 \rangle} \right) - \mu. \tag{2.52}$$

To obtain the epidemic threshold, the stability of the absorbing state $(I(t), \phi(t), \theta(t)) = (0,0,0)$ is imposed, which corresponds to impose the maximum eigenvalue to be negative $\Lambda_+ < 0$. The epidemic threshold is:

$$r_C^{ADA} = \frac{\lambda}{\mu}\bigg|_C = \frac{1}{m} \frac{\langle b \rangle}{\langle ab \rangle + \sqrt{\langle a^2 \rangle \langle b^2 \rangle}}. \tag{2.53}$$

The obtained epidemic threshold is exact, given that the model is exactly mean-field and Markovian, and this can be proved by extensive numerical simulations based on the lifetime-based method [72]. Moreover, it is valid for arbitrary $\rho(a,b)$: the epidemic threshold strongly depends on the correlations between activity and attractiveness in the behaviour of an individual, encoded in $\langle ab \rangle$, as well as on fluctuations and heterogeneity in activity and attractiveness, i.e. $\langle a^2 \rangle$ and $\langle b^2 \rangle$. By introducing heterogeneity or positive correlations a reduction in the epidemic threshold is always obtained, due to the introduction of hubs who simultaneously activate and

receive many links, acting as super-spreaders [72].

These results show how the introduction of attractiveness in the network, as a new source of heterogeneity, profoundly influences the dynamics of the network and the spread of the epidemic. The epidemic dynamics on the AD network and on the ADA network are profoundly different.

2.3.2 Epidemics on AD with memory

In Section 1.6.2 we presented the AD model in the presence of memory, which introduces aging and non-Markovian effects, showing how memory effects significantly modify the network topology and its dynamics (see Figure 2.9), potentially affecting also the spread of epidemics [49, 83, 130].

We consider the SIS process on the AD network with memory, with N nodes assigned with the activity a drawn from the distribution $\rho(a)$. Each active node can create a new link with probability $p(k_i(t)) = [1 + k_i(t)]^{-\beta}$ or reinforce an old one with probability $(1 - p(k_i(t)))$, where $k_i(t)$ is the degree of the node at time t in the aggregate network and β is the memory parameter. The network is characterized by strong local correlations due to the reinforcement mechanism, thus the mean-field approaches are not exact.

An individual-based mean-field approach can be applied, in which the epidemic dynamics is described by the probability $I_i(t)$ that node i is infected at time t. The Master Equation for $I_i(t)$ is:

$$\begin{aligned}\partial_t I_i(t) = -\mu I_i(t) + \lambda[1 - I_i(t)] \Bigg[& \sum_j a_i [1 - p(k_i(t))] \frac{A_{ij}(t)}{k_i(t)} I_j(t) \\ & + \sum_{j \nsim i} a_i p(k_i(t)) \frac{1}{N - k_i(t) - 1} I_j(t) \\ & + \sum_j a_j [1 - p(k_j(t))] \frac{A_{ij}(t)}{k_j(t)} I_j(t) \\ & + \sum_{j \nsim i} a_j p(k_j(t)) \frac{1}{N - k_j(t) - 1} I_j(t) \Bigg],\end{aligned} \tag{2.54}$$

where $j \nsim i$ indicates a sum on the nodes j not yet connected with i, which at time t are in total $N - k_i(t) - 1$, $A_{ij}(t)$ indicates the element of the adjacency matrix of the integrated network up to time t. The structure of the equation is analogous to that of the AD model, however in this case it is necessary to differentiate whether the link that produces the contagion is an old reinforced link or a new one [83].

The epidemic dynamics strongly depends on the time t_0 at which the pathogen start spreading, since $k_i(t)$ and $A_{ij}(t)$ depend on the evolution time t (see Eq. (2.54)): this produces the emergence of aging effects. If the epidemic begins at large times, the dynamics of the network and memory reached a regime where the formation of new contacts can be neglected, as the connectivity of a node in the integrated network $k_i(t)$ becomes very large and so the probability $p(k_i(t)) \sim 0$. In this regime the dynamic correlations are asymptotically negligible and it is possible to apply a heterogeneous mean-field approximation on $A_{ij}(t)$ by replacing it with its annealed version and obtaining an analytical solution asymptomatically exact. This approximation transforms the individual-based approach into an *activity-based approach*, allowing to consider the probability $I_a(t)$ that a node with activity a is infected at the

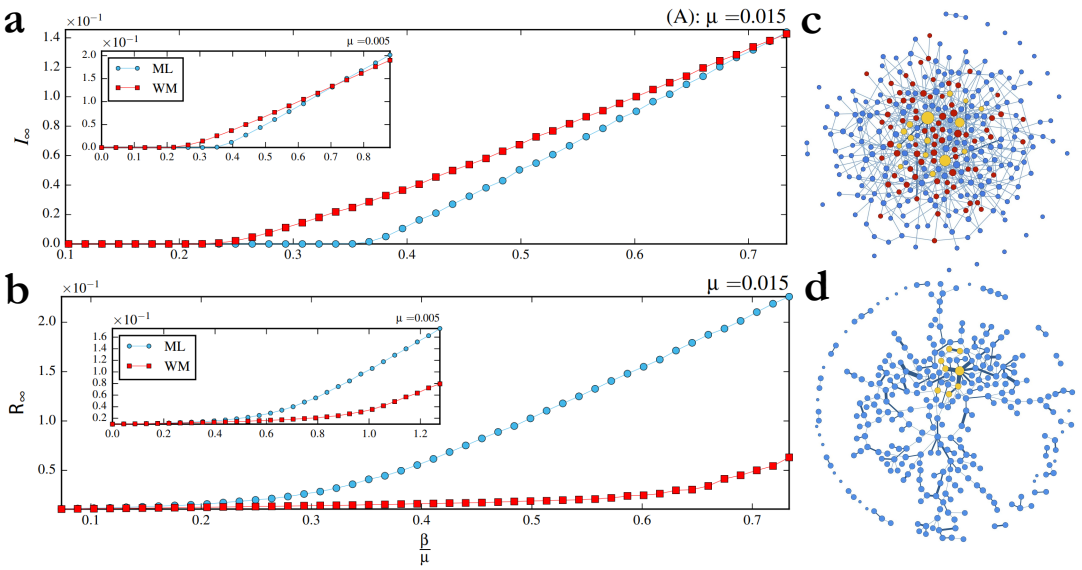

FIGURE 2.9: **The effects of memory on epidemic spreading.** In panel **a** and **b** we plotted respectively the numerical estimation of the epidemic prevalence $I_\infty = I(t \to \infty)$ and the epidemic final size $R_\infty = R(t \to \infty)$ as a function of $\beta/\mu = 2m\langle a\rangle\lambda/\mu$ both in the memoryless case (ML) and in the case with memory (WM). In both panels $N = 10^5$, $m = 1$, $F(a) \propto a^{-\nu}$ with $a \in [10^{-3}, 1]$: each point is the average over 10^2 independent simulations, with initially a fraction 10^{-2} of infected nodes randomly selected. The main plots were obtained for $\mu = 0.015$ and the inset for $\mu = 0.005$. Panel **c** and **d** show a rumour diffusion process (analogous to the SIR model) respectively on the memoryless AD network and on the AD network with memory: the color of the nodes identifies their state, their size represents their degree and the links width represents their weight. Panels **a** and **b** are adapted from [130] under CC BY 4.0 license, while panels **c** and **d** are adapted from [49] under CC BY-NC-SA 3.0 license.

time t and obtaining the mean-field equation [83]:

$$\begin{aligned}\partial_t I_a(t) = -\mu I_a(t) + \lambda[1 - I_a(t)] \Bigg[& \frac{a g(a)}{g(a) + \langle g(a)\rangle} \int da' \rho(a') I_{a'}(t) \\ & + \frac{a}{g(a) + \langle g(a)\rangle} \int da' \rho(a') I_{a'}(t) g(a') \\ & + g(a) \int da' \rho(a') \frac{a'}{g(a') + \langle g(a)\rangle} I_{a'}(t) \\ & + \int da' \rho(a') \frac{a' g(a')}{g(a') + \langle g(a)\rangle} I_{a'}(t) \Bigg],\end{aligned} \tag{2.55}$$

where $g(a) = a/[C(a)]^\beta$, $C(a) = (1+\beta)[g(a) + \langle g(a)\rangle]$ and $\langle g(a)\rangle = \int da \rho(a) g(a)$ (see Section 1.6.2). The explicit dependence on time in the right-hand member is cancelled suggesting that in the large times regime it is as if the epidemic evolves on a static effective graph.

An analytical condition for the epidemic threshold r_C can be obtained, for arbitrary distribution $\rho(a)$ and for arbitrary reinforcement mechanism β, imposing the stability of the absorbing state. However, the complexity of the model does not allow to obtain a closed relation for the epidemic threshold [83]. The mean-field asymptotic approach implemented for the SIS model can be tested through numerical simulations and is also valid for the SIR model, producing the same mean-field threshold [83].

The mean-field epidemic threshold in the presence of memory is always lower than the memoryless model in the large-times limit [83]: this is due to the tie allocation mechanism which amplifies the effects of activity fluctuations. Nodes with high activity a have a high degree $k(t)$, so they are easily involved in interactions both for their activity but also because of the reinforcement mechanism, being part of the social circle of many other nodes: the reinforcement of the links of the social circle favours interactions with hubs and thus the effects of activity fluctuations. This is validated by the fact that by reducing the heterogeneity of $\rho(a)$ the differences with the memoryless model are reduced [83].

An analytical analysis for the epidemic spreading at short-times regime is difficult to obtain since the correlations become relevant due to the finite connectivity of the network, producing pre-asymptotic effects. This regime can be investigated through extensive numerical simulations (see Figure 2.9): in this regime the mean-field approach is not exact and therefore the SIS and SIR epidemic thresholds differ [49, 83, 130].

In the short-times regime, the memory mechanism induces the formation of clusters of nodes with high activity, which tend to explore their social circle, and then nodes with small activity, which tend to explore new connections. This is because nodes with high activity quickly perform a large number $k_i(t)$ of connections and their probability of new connections $p(k_i(t))$ decays rapidly, favouring the reinforcement of the social circle; while nodes with small activity will slowly reach saturation in the social circle dimension, thus exploring new contacts. Clusters become reservoirs of the pathogen in the SIS model, due to the high frequency of connections and reinfections between them, while nodes with small activity slow down the epidemic due to the formation of new links. This can lead to an increase or a decrease in the epidemic threshold compared to the asymptotic regime, depending on the initial conditions and the memory parameter β [83]. On the contrary, in the SIR model, reinfection is not allowed and so the presence of highly connected clusters of highly active nodes also reduces the spread of the epidemic, given that these clusters become immunized. This leads to an increase in the SIR epidemic threshold compared to the asymptotic limit (see Figure 2.9) [83, 130].

These results allow to fully understand the coupling between the dynamics of a network with memory and the epidemic dynamics, explaining contrasting effects of memory and aging on the spread of epidemics.

2.3.3 Epidemics on AD with burstiness

Many results have been obtained recently on the effects of a non-Poissonian network dynamics on epidemic spreading, some observing a slowdown in the spreading, compared to the Poissonian case, while others showing an acceleration (see Figure 2.10) [33, 38, 57, 85, 131, 132].

In Section 1.6.3 we introduced the AD model with arbitrary dynamics of node activation, i.e. with arbitrary distribution of inter-event times $\Psi(\tau)$, showing how the temporal dynamics of interactions affect the network topology and its properties, potentially affecting also the spread of epidemics [85].

We consider the AD model with arbitrary activity distribution $\rho(a)$ and inter-event times distribution $\Psi_a(\tau)$, by fixing $\langle\tau\rangle = \int d\tau\Psi(\tau)\tau = a^{-1}$ and assuming $m = 1$. On this network we consider the evolution of the SIS epidemic model. We apply an activity-based mean-field approach by dividing the population into classes of nodes with the same activity a and considering them statistically equivalent. This

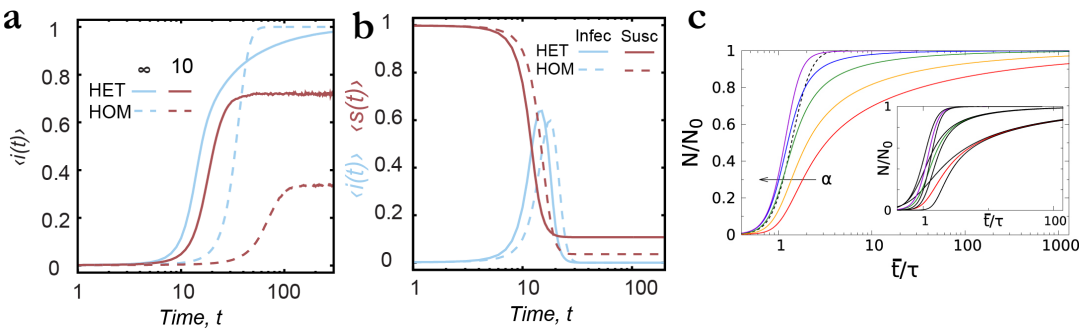

FIGURE 2.10: **The effects of bursty interaction dynamics on epidemic spreading.** In panel **a** the epidemic prevalence $\langle i(t)\rangle$ for the SI epidemic process is plotted as a function of time. In panel **b** the epidemic prevalence $\langle i(t)\rangle$ and the fraction of susceptible individuals $\langle s(t)\rangle$ for the SIR epidemic process are plotted as a function of time, fixing $1/\mu = 5$. In both panels a bursty (HET - $\Psi(\tau) \sim \tau^{\alpha} \exp(-\beta_{HET}\tau)$) and a homogeneous contact pattern (HOM) are considered, and $N = 10^3$, $\lambda = 1$, $\beta_{HET} = 0.001$ and $\alpha = 2$ in panel **a** and $\alpha = 2.5$ in panel **b**. Panel **c** shows the SI fraction of infected nodes as a function of time (where τ is the average inter-event times) for an exponential distribution $\Psi(t) \sim e^{-at}$ (black and dashed curve) and for a power-law distribution $\Psi(t) \sim t^{-(1+\alpha)}$ for $t > t_0$, with different exponents α for different colors. The simulations were conducted by initially randomly infecting a high-grade node, on a Barabási-Albert network with $N = 10^4$ nodes and $\langle k\rangle = 4$. The curves are averaged over $2.5\,10^3$ runs. The arrow indicates increasing values of α, while the inset shows the fluctuations of the curves for some values of α. Panels **a** and **b** are adapted from [132] under Creative Commons Attribution License, while panel **c** is adapted from [131] under CC BY 3.0 license.

approach is correct since the model is exactly mean-field since the reshuffling of the links breaks all local correlations at each time-step.

Given a contact event at time t, the epidemic dynamics is completely described by: $Q_a(t)$ the probability that a node of activity a activates at time t and is infected; $P_a(t)$ the probability that a node of activity a is not active at time t and is infected; $Z_a(t,t')$ the probability that a node of activity a is infected at time t knowing that its last activation occurred at time t'.

The probability $Z_a(t,t')$ evolves over time according to the Master Equation:

$$\partial_t Z_a(t,t') = -\mu Z_a(t,t') + \lambda(1 - Z_a(t,t')) \int da' \rho(a') a' Q_{a'}(t), \tag{2.56}$$

where the first term takes into account spontaneous recovery and the second term takes into account a contagion in which the node of activity a is passively infected by an active infected node, given the definition of $Z_a(t,t')$. Furthermore, Eq. (2.56) admits as initial conditions:

$$Z_a(t',t') = Q_a(t') + \lambda[1 - Q_a(t')] \int da' \rho(a') P_{a'}(t'), \tag{2.57}$$

in which the node can be already infected at time t' (first term) or can be susceptible at time t' and be infected through the contact activated with an infected inactive node (second term). $P_a(t)$ and $Q_a(t)$ can be defined in terms of $Z_a(t,t')$ [85]:

$$Q_a(t) = \int_0^{\infty} Z_a(t, t-\tau') \Psi_a(\tau') d\tau', \tag{2.58}$$

$$P_a(t) = \frac{1}{\int_0^{\infty} d\tau' \int_{\tau'}^{\infty} \Psi_a(\tau'') d\tau''} \int_0^{\infty} d\tau' Z_a(t, t-\tau') \int_{\tau'}^{\infty} d\tau'' \Psi_a(\tau''). \tag{2.59}$$

Eq. (2.56) with initial conditions of Eq. (2.57) can be solved assuming that the system asymptotically reaches a stationary state $(P_a(t), Q_a(t)) \xrightarrow[t\to\infty]{} (P_a^0, Q_a^0)$, in which also the activation dynamics of the nodes has reached a steady state. In this regime it is possible to obtain a condition for the epidemic threshold [85]:

$$\frac{\lambda\langle a\rangle}{\mu} + \lambda\sqrt{\frac{1}{\mu}\int da\rho(a)a\frac{L_a(\mu)}{1-L_a(\mu)}} < 1, \tag{2.60}$$

where $L_a(\mu) = \int_0^\infty d\tau e^{-\mu\tau}\Psi_a(\tau)$ is the Laplace transform of the inter-event times distribution $\Psi_a(\tau)$. This relation is extremely powerful and general, since it provides a closed, analytical and exact condition for the epidemic threshold of the SIS model on AD network with arbitrary activity distribution $\rho(a)$ and arbitrary inter-event times distribution $\Psi_a(\tau)$. In general, the epidemic threshold strongly depends on the functional form of $\rho(a)$ and of $\Psi_a(\tau)$ via its Laplace transform (see Figure 2.10). Furthermore, the validity of the relation was tested through extensive numerical simulations, based on the time-life method, showing excellent agreement [85].

By considering a broad distribution $\Psi_a(\tau)$, it can be shown that temporal heterogeneities, i.e. fluctuations in inter-event times, produce a reduction in the epidemic threshold favouring the spread of the epidemic [85]. On the contrary, the effects of burstiness on the epidemic prevalence are twofold: in low infective systems it favours the epidemic by increasing the prevalence, while in highly infective systems it reduces the average probability of infection, weakening the epidemic [85].

These results show the strong impact of the temporal properties of the network on the epidemic dynamics, especially highlighting the effects of the link formation statistics.

2.3.4 Epidemics on simplicial AD

In Section 1.6.4 we introduced the AD model with simplicial interactions, showing how group interactions profoundly modify the temporal and topological properties of the AD network. The simplicial AD model allows to investigate the effect of higher order interactions on epidemic processes [87].

An epidemic process occurring on a model with simplicial interactions can be characterized by three types of contagion mechanisms [30] (see Figure 2.11):

- **simple contagion:** the contagion occurs through pairwise interactions between susceptible and infected individuals and the infection is caused by a single exposure. This mechanism occurs along the links of the network;
- **complex contagion:** the contagion occurs through pairwise interactions between susceptible and infected individuals and the transmission requires that the susceptible individual entered into contact with two or more infected ones. This mechanism occurs along the links of a network, but only after repeated exposure to multiple infected. The contagion probability depends on the number of previous exposures or on a threshold effect;
- **simplicial contagion:** the contagion occurs through interactions in groups, i.e. through real high-order interactions. With this mechanism an individual can be infected from a group event in which the presence of more than one infected produces a reinforcing effect on the infection. In this case the contagion occurs through multi-body interactions.

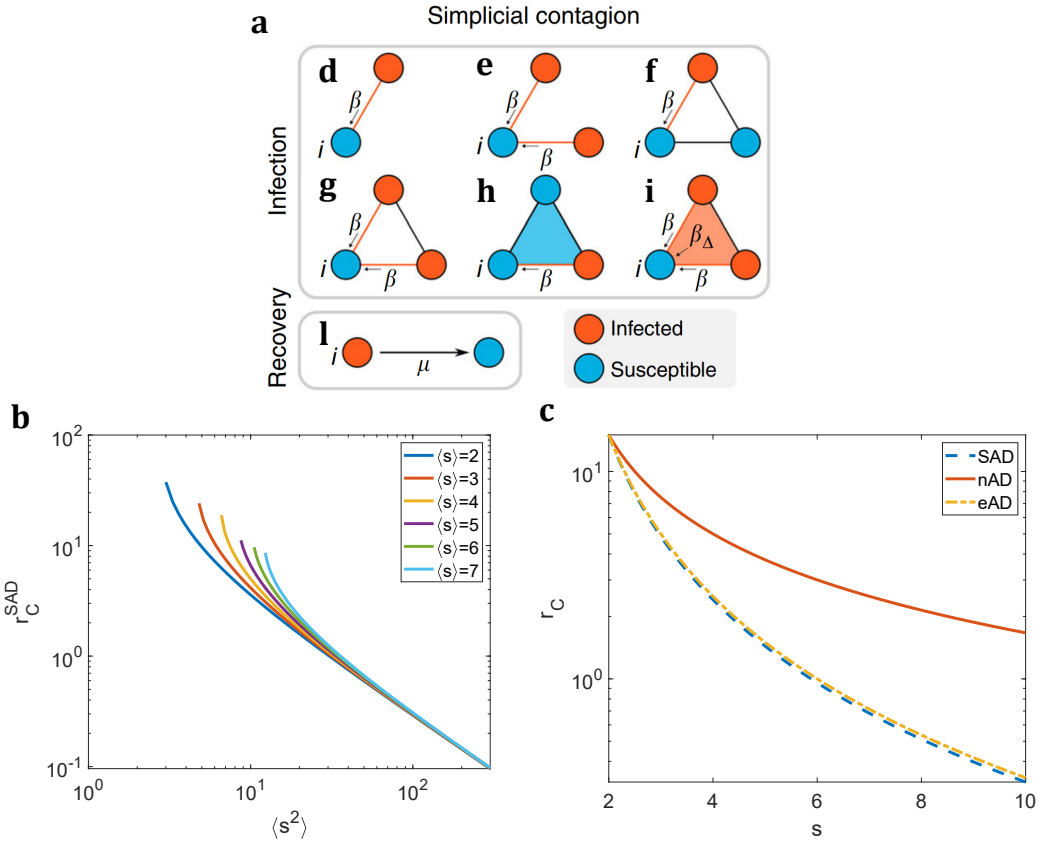

FIGURE 2.11: **Epidemic spreading on simplicial model.** In panel **a** we represent the main infection and recovery (sub-panel **l**) mechanisms that can be activated in a model with simplicial interactions. A susceptible node can be infected with probability β via a *simple contagion* mechanism via links (1-simplices), if it is in contact with one (sub-panels **d** and **f**) or with more infected nodes independently (sub-panels **e** and **g**). The *simplicial contagion* mechanism can also be activated: if a susceptible participates in a 2-simplex with only one infected, then can be infected only through the link (sub-panel **h**); if in the same 2-simplex there are two infected nodes, the susceptible node can be infected independently through the single links (1-face) with probability β and also by a group contagion from the 2-face with probability β_Δ (sub-panel **i**). In panel **b** we plotted the epidemic threshold r_C^{SAD} of the SAD model as a function of $\langle s^2 \rangle$ for different values of $\langle s \rangle$. Panel **c** shows the epidemic threshold r_C for the SAD, eAD and nAD models, as a function of the simplex size $s = \bar{s}$ assuming that $\Psi(s) = \delta(s - \bar{s})$. In panels **b-c** we fixed $\langle a \rangle = 0.035$ and $\langle a^2 \rangle = 0.001$. Panel **a** is adapted from [30] under CC BY 4.0 license.

The three contagion mechanisms described are very general and can describe contagion processes for infectious diseases or information transmission, such as the adoption of an opinion. In the case of infectious diseases, the main active contagion mechanisms are simple and complex contagion (e.g. threshold effects related to viral load), while simplicial contagion is absent given that the exposure to multiple sources of contagion simply multiplies the likelihood of infection but does not produce strengthening with group contagion. On the contrary, if we consider the adoption of an opinion all the mechanisms are active: an individual can be convinced independently by their contacts (simple contagion), by the multiple exposure to contacts with the same opinion (complex contagion), or by participating in a group with a certain number of people with the same opinion (simplicial contagion) who convince them through a group interaction (see Figure 2.11). The complex and

simplicial contagion mechanisms can produce non-trivial effects, profoundly modifying the evolution of the dynamic process and inducing the emergence of new phenomena such as discontinuous phase transitions and bistable regions [30].

Let us now consider the SIS process on the SAD model: nodes interact through simplices and we consider a simple contagion mechanism, in which contagion occurs with probability λ along each link between a susceptible S and an infected I, neglecting the mechanisms of complex or simplicial contagion.

The epidemic dynamics can be described through an activity-based mean-field approach, dividing the nodes into classes of equal activity a, indicating with $N_a = S_a(t) + I_a(t)$ the number of nodes in the class a, with $I_a(t)$ the number of infected nodes at the time t belonging to class a and with $S_a(t)$ the number of susceptible nodes at time t belonging to class a. Thus $N = \int da N_a$ is the total number of nodes in the population and $I(t) = \int da I_a(t)$ is the total number of infected nodes at time t. The size s of an active simplex is drawn from the distribution $\Psi(s)$ and it is independent of the activity of the active node. The evolution of $I_a(t)$ is regulated by the Master Equation:

$$\begin{aligned} I_a(t+\Delta t) - I_a(t) = -\mu \Delta t I_a(t) &+ \lambda \Delta t \int ds \Psi(s) S_a(t) a(s-1) \int da' \frac{I_{a'}(t)}{N} \\ &+ \lambda \Delta t \int ds \Psi(s) S_a(t) \int da' a' \frac{I_{a'}(t)}{N}(s-1) \\ &+ \lambda \Delta t \int ds \Psi(s) S_a(t) \int da' a' \frac{S_{a'}(t)}{N}(s-1) \int da'' \frac{I_{a''}(t)}{N}(s-2). \end{aligned} \tag{2.61}$$

The first three terms on the right-hand side are analogous to that of the AD model, taking into account that at each activation of a node a simplex is formed with $s(s-1)/2$ interactions. The fourth term exploits the simplicial structure of the interactions and describe the case in which a susceptible node with activity a is infected by participating in a simplex, activated by another susceptible node a', in which an infected node a'' also participates. The infection terms in the equation are already linearized in λ (or in $I_a(t)$) and by integrating Eq. (2.61) over the activity the temporal evolution of $I(t)$ is obtained:

$$I(t+\Delta t) = I(t) - \mu \Delta t I(t) + \lambda \Delta t \langle (s-1)^2 \rangle \langle a \rangle I(t) + \lambda \Delta t \langle s-1 \rangle \theta(t), \tag{2.62}$$

where $\theta(t) = \int da I_a(t) a$, $\langle f(a) \rangle = \int da \rho(a) f(a)$, $\langle g(s) \rangle = \int ds \Psi(s) g(s)$ and the high-order terms are neglected, assuming that in the initial phases of the epidemic $I_a(t) \ll N_a$ (or considering the system near the critical point $r \sim r_C$). Similarly, the evolution equation of $\theta(t)$ can be obtained by multiplying Eq. (2.61) for a and integrating over the activity:

$$\begin{aligned} \theta(t+\Delta t) = \theta(t) - \mu \Delta t \theta(t) &+ \lambda \Delta t [\langle s-1 \rangle \langle a^2 \rangle + \langle (s-1)(s-2) \rangle \langle a \rangle^2] I(t) \\ &+ \lambda \Delta t \langle s-1 \rangle \langle a \rangle \theta(t). \end{aligned} \tag{2.63}$$

In the continuous-time limit $\Delta t \to 0$:

$$\partial_t I(t) = -\mu I(t) + \lambda \langle (s-1)^2 \rangle \langle a \rangle I(t) + \lambda \langle s-1 \rangle, \tag{2.64}$$

$$\partial_t \theta(t) = -\mu \theta(t) + \lambda [\langle s-1 \rangle \langle a^2 \rangle + \langle (s-1)(s-2) \rangle \langle a \rangle^2] I(t) + \lambda \langle s-1 \rangle \langle a \rangle \theta(t), \tag{2.65}$$

which admits Jacobian matrix:

$$J = \begin{bmatrix} -\mu + \lambda \langle (s-1)^2 \rangle \langle a \rangle & \lambda \langle s-1 \rangle \\ \lambda [\langle s-1 \rangle \langle a^2 \rangle + \langle (s-1)(s-2) \rangle \langle a \rangle^2] & -\mu + \lambda \langle s-1 \rangle \langle a \rangle \end{bmatrix} \tag{2.66}$$

The eigenvalues of J are therefore:

$$\Lambda_{\pm} = \frac{1}{2}[\lambda\langle s(s-1)\rangle\langle a\rangle - 2\mu \pm \lambda\sqrt{\langle(s-1)(s-2)\rangle\langle(s-1)(s+2)\rangle\langle a\rangle^2 + 4\langle s-1\rangle^2\langle a^2\rangle}]. \tag{2.67}$$

The stability of the absorbing state $(I(t),\theta(t)) = (0,0)$ is obtained by imposing the maximum eigenvalue to be negative $\Lambda_+ < 0$. The epidemic threshold is:

$$r_C^{SAD} = \frac{2}{\langle s(s-1)\rangle\langle a\rangle + \sqrt{\langle(s-1)(s-2)\rangle\langle(s-1)(s+2)\rangle\langle a\rangle^2 + 4\langle s-1\rangle^2\langle a^2\rangle}}. \tag{2.68}$$

where $r = \lambda/\mu$. The epidemic threshold shows the key role played by the simplicial nature of the interactions and by the distribution $\Psi(s)$ of the simplices size, strongly depending on $\langle s\rangle$ and on $\langle s^2\rangle$. If the fluctuations in the simplices size $\langle s^2\rangle$ diverge then, at a fixed average size $\langle s\rangle$, the epidemic threshold vanishes (see Figure 2.10). This analytical result can be verified through extensive numerical simulations [87].

The epidemic threshold r_C^{SAD} can be compared with the threshold of the eAD network (edge-matching AD, where $m = s(s-1)/2$) and of nAD network (node-matching AD, where $m = s-1$), considering also in that case that s is drawn from $\Psi(s)$ at each activation of a node. In that case simply m is replaced by $\langle m\rangle$ [13, 87]:

$$r_C^{eAD} = \frac{2}{\langle s(s-1)\rangle}\frac{1}{\langle a\rangle + \sqrt{\langle a^2\rangle}}, \quad r_C^{nAD} = \frac{1}{\langle s-1\rangle}\frac{1}{\langle a\rangle + \sqrt{\langle a^2\rangle}}. \tag{2.69}$$

Comparing the SAD model with the eAD:

$$\frac{r_C^{SAD}}{r_C^{eAD}} = \frac{\langle a\rangle + \sqrt{\langle a^2\rangle}}{\langle a\rangle + \sqrt{\langle a^2\rangle}\sqrt{\Theta}}, \tag{2.70}$$

where:

$$\Theta = \frac{4\langle s-1\rangle^2}{\langle s(s-1)\rangle^2} + \frac{\langle(s-1)(s-2)\rangle\langle(s-1)(s+2)\rangle}{\langle s(s-1)\rangle^2}\frac{\langle a\rangle^2}{\langle a^2\rangle}. \tag{2.71}$$

Since $s \geq 2$ and $\langle s^2\rangle \geq \langle s\rangle^2$, the ratio r_C^{SAD}/r_C^{eAD} is always larger than 1, implying that the SAD model always features a higher threshold than the eAD model: in Figure 2.11 this result is clearly shown. Indeed, the SAD and eAD models involve the same number of links at each node activation, but in the SAD model the connections are all made between the same s nodes in the simplex, while in the eAD model they are made between $s(s-1)/2$ distinct nodes. This clearly favours the spread of the epidemic in the eAD model compared to the SAD model, as the infection can potentially reach many more distinct nodes and there is a higher probability of connecting an infected node.

Comparing SAD with nAD, the ratio r_C^{SAD}/r_C^{nAD} is always lower than 1: in Figure 2.11 this result is clearly shown. Indeed, the SAD and nAD models involve the same number of nodes at each node activation, but in the SAD model these nodes interact with $s(s-1)/2$ connections in the simplex, while in the nAD model the nodes interact through $s-1$ interactions in a star-like structure. This favours the spread of the epidemic in the SAD model compared to the nAD model.

Let us now consider the particular case of uniform activity $\rho(a) = \delta(a-a_0)$, in this case $\langle a^2\rangle = \langle a\rangle^2 = a_0^2$ and the thresholds becomes:

$$r_C^{SAD} = \frac{1}{\langle s(s-1)\rangle a_0} = r_C^{eAD}, \quad r_C^{nAD} = \frac{1}{\langle s-1\rangle a_0}. \tag{2.72}$$

The epidemic threshold of the eAD model coincides with that of the SAD model, but differs from the nAD one. In this case the different terms in the mean-field equations contribute equally to the infection, independently of the activity of the nodes involved, and only the number of links formed counts: this number is the same for the SAD and eAD model, thus they have the same threshold, but it is different for the nAD model. This is valid only near the critical point where it can be ignored that the eAD model is the SAD model have the same number of links but involve a different number of nodes.

These results show that the topological and temporal differences in the network due to simplicial interactions have a strong impact on epidemic processes, affecting deeply the epidemic threshold [87].

The results presented in the last Sections show that the activity-driven models allow to investigate both analytically and numerically the effect of specific network properties (e.g. memory, burstiness) on epidemic processes, keeping into account the true temporal dynamics of interactions. We presented the main AD models and the effects on epidemic spreading of specific network properties, however further extensions of the AD model have been proposed, for example investigating the effect of communities on epidemics [94], the effects of memory and burstiness in other formulations of the model [95, 97] and the effects of static structures underlying the interactions [96].

Chapter 3

Epidemic spreading with adaptiveness

In this Chapter we review the modelling framework of the *adaptive temporal networks*, a new class of time-varying networks whose evolution is coupled to dynamical processes unfolding upon them. In particular, we show how adaptive temporal networks can describe the spread of epidemics in populations which respond and adapt to the pathogen diffusion.

3.1 Adaptive temporal networks

Historically, the study of dynamic processes and complex networks has been performed with a strict separation between the dynamics on the network and the dynamics of the network, as we have seen in Chapter 1. Recently a lot of interest has been attracted by considering the two dynamics simultaneously and their interplay. Indeed, many complex real systems present a coevolution of the network topology and of the dynamic processes occurring on top of them [8–10, 133, 134]. This coupling can be very deep and can take place on two distinct levels: on the one hand, the dynamics and topology of the network can deeply influence the evolution of a dynamic process, as discussed in Chapters 1-2; on the other hand, the dynamic process can induce adaptive mechanisms in the network, as a response to the presence of the dynamic process, modifying the network evolution and in its topology.

In many complex systems the coupling between the network dynamics and the dynamic process occurs on both levels, since the two dynamics are deeply coupled and interdependent (see Figure 3.1): this produces emergent phenomena that could not be observed otherwise. In this case, the underlying network evolves over time, its evolution influences the dynamic process, which in turn induces adaptive mechanisms in the network, affecting the network topology and evolution through a feedback loop. The framework for describing these systems is that of *adaptive temporal networks (or coevolutionary networks)*, which are dynamic networks whose evolution is coupled to a dynamic process of which they are substrates: see Figure 3.1 for a schematic representation.

Adaptive networks are widely applied across many disciplines, from social to biological science, from physics to epidemiology, from logistics to public transport [8–10]. A simple example is that of the traffic on the road network: the traffic constitutes a dynamic process whose dynamic entities (seen as people or goods) move along the links of the network between the nodes. The topology and dynamics of the network profoundly affect the traffic (for example the flow or density of entities on links or nodes), but at the same time the traffic influences the network. If traffic

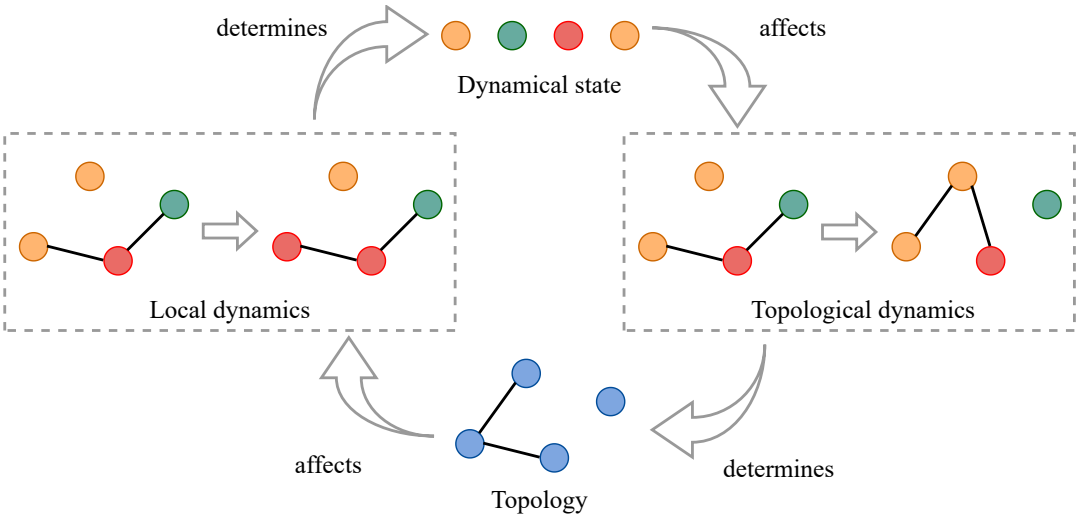

FIGURE 3.1: **Adaptive temporal networks.** We schematically represent an adaptive temporal network and its coupling to a dynamical process through a feedback loop. The network evolution determines the network topology, which affects the dynamical process and its local dynamics; the local dynamics determines the node dynamical state, which affect the topological dynamics through adaptiveness.

jams occur frequently, it is likely that new roads will be built or that a road will be closed, with the aim of loan on the congested road. The same happens in many other artificial networks and transport processes such as power-grids for the transport of electricity and the internet communication network [8], in which links or nodes can be removed to avoid failure or as a consequence of that.

Another simple example is the dissemination of opinions and consensus that takes place on the networks of social interactions. This process is strongly influenced by the structure and dynamics of social interactions and can change the topology of the network, for example by favouring interactions between individuals with the same opinion and breaking the connections between individuals with contrasting views.

Finally, also a population exposed to an epidemic can be described as an adaptive temporal network [8, 11, 12], since the presence of an epidemic induces a wide range of adaptive behaviours in the population, ranging from self-protective behaviours to public interventions, which strongly couple the interaction dynamics to the epidemic [12].

Despite the ubiquity of adaptive networks, a general mathematical modelling is still missing, due to the complexity of the deep coupling between the dynamics. Most of the results are obtained with numerical approaches modelling specific adaptive behaviours. However, some general insights and hallmarks emerged to be shared by many adaptive networks [8–10, 135], such as the formation of complex global topologies, a robust self-organization dynamic and the spontaneous emergence of different classes of nodes.

In the next Section we present the main adaptive behaviours observed in populations exposed to epidemics, showing the main modelling frameworks to describe them.

3.2 Epidemics and adaptive behaviours

Populations exposed to epidemics respond and adapt with a broad set of adaptive behaviours, including public coordinated measures, implemented by healthcare institutions and governments for the control of the epidemic, and personal responses, driven by individual behavioural changes induced by awareness of the epidemic [12, 133, 136]. These adaptive behaviours are implemented on a time-scale τ_A comparable with that of the network dynamics τ_N and of the epidemic process τ_P, since they are induced by the presence of the epidemic: for example, epidemics with long time scales induce behavioural changes over large-time scales through cultural changes (e.g. changes in sexual habits induced by HIV); epidemics with short time scales induce changes extremely faster (e.g. COVID-19, SARS, MERS) [11, 12]. Understanding the mechanisms underlying the response to epidemics is crucial, both for mathematical fundamental reasons and for the optimization of control and containment measures, informing policy makers and health institutions.

Public coordinated interventions include a wide set of measures directly activated on the whole population or on specific classes of individuals [21, 137–141]: these interventions can be pharmaceutical, such as optimized vaccination strategies, or non-pharmaceutical (NPIs). Non-pharmaceutical interventions include a broad set of measures [142], for example interventions at the *personal and environmental level* aiming to reduce the transmission probability by increased hygiene (e.g. sanitation and ventilation) or by the use of protection devices (e.g. face masks). Other NPIs are implemented directly at the *population level*, acting directly on the pattern of contacts, modifying it to reduce community-wide spread. For example, the creation of health cordons for the spatial containment, the promotion of physical distancing, the closure of specific activities (such as schools, universities, restaurants), the implementation of restrictions to the mobility and to gatherings, up to social distancing and extended lockdowns [16, 140, 143–145]. Finally, fundamental NPIs are pursued at the *active-surveillance level*, acting directly on infected individuals and actively searching new infected individuals. For example, a timely testing of suspected cases [106, 146], the mandatory isolation of positive cases and the quarantine of their contacts potentially infected and identified through the timely tracing of contacts.

The type of public measures activated, their intensity and their specific implementation strongly depend on the specific infectious disease [21, 138], on the epidemiological situation, as well as on extremely complex socio-economic factors, since all these measures have significant socio-economic consequences [17, 18, 147].

Self-initiated responses include all the individual adaptive behaviours that emerge spontaneously, without the intervention of public institutions [148, 149]: for example, the reduction of social activity in infected individuals, caused by the appearance of symptoms, and in susceptible individuals, caused by the perception of risk, the creation of disease-party to promote diffusion and gain immunity [150–155]. All these changes in behaviour can derive from the awareness or the fear of the epidemic, from information by the media or by the contacts engaged [12]. Moreover, there exist adaptive mechanisms induced by the epidemic but not directly linked to reducing or promoting the spread of the pathogen, such as the replacement of infected individuals with susceptible peers if they have an essential social role (e.g. teachers or doctors) [156].

These behavioural changes and adaptive mechanisms have been widely observed and documented during the recent COVID-19 pandemic, also thanks to the availability of new tools which allow to systematically investigate the social dynamics during the several phases of the pandemic. For example, the effects of adaptive behaviours

on the social dynamics has been estimated by monitoring the mobility of individuals [20, 144, 157], the use of internet [158] and through data on mobile phones [159, 160] and surveys [161, 162]. This allows the development of models in the various phases of the pandemic, first for containment and then for safe exit strategies, estimating the effects of the public interventions and of spontaneous behaviours in the population [16, 140, 143–145]. In the past these tools were almost absent, however adaptive behaviours have been documented. For example, behavioural changes have been documented during the SARS epidemic of 2002-2004, such as the use of masks, changes in travel habits and the implementation of powerful tracking and containment systems. Further protective behaviours have been observed for HIV, in sexual habits, and for the H1N1 influenza pandemic in 2009 [12]. These protective behaviours have often been accompanied by rarer opposite behaviours, for example with the organization of disease-party (e.g. measles [153], chicken-pox [152], COVID-19 [154, 155], swine-flu [150, 151]) in which people try to get infected to immunize themselves by exposing directly to the pathogen.

Many mathematical models have been developed to describe some of these adaptive behaviours, both to investigate the effectiveness of public control and containment measures and to determine the effects of self-initiated adaptive behaviours. In general, adaptive behaviours can be classified on the basis of several factors [12]:

- **the source of information, which induces the behavioural changes.** It can be *global* or *local*: in the first case, the individual acts on the basis of information available to the entire population, for example broadcast by media, from the government, from local or national health authorities; in the second case the information derives only from the (spatial or social) local neighbourhood of the individual. The difference between global and local information is crucial, since in structured populations information can spread locally in (spatial or social) clusters, profoundly affecting the epidemic (e.g. local clusters of immunized individuals);

- **the type of information, which induces the behavioural changes.** Most of the models can be classified as *prevalence-based* or *belief-based*: in the first case the behaviour of an individual is determined by the number of infected individuals; in the second case, the adaptive behaviours derive from an information not directly linked to the prevalence, for example due to discrepancies between the personal perception of risk and the real epidemiological parameters;

- **the type of the adaptive behaviour induced**. The adaptive behaviour can change the dynamical state of the individual, can induce an increased protection by a change in the node infection probability, or can change the structure of the interaction network on which the pathogen spreads.

The effects of the adaptive behaviours on the epidemic spreading are not only restricted to the protection of the affected nodes but also have strong repercussion on the global epidemic spreading, also in the rest of the population. These effects can be investigated by considering different epidemiological descriptors:

- **the epidemic threshold r_C**, compared to the non-adaptive (NA) case r_C^{NA}. $R_0 = r/r_C^{NA}$ estimates how much the system with $r = \lambda/\mu$ is above the threshold r_C^{NA} in the absence of adaptive behaviours: the effective infection rate r is a fixed parameter of the pathogen (assuming that the pathogen does not change its epidemiological properties), while the epidemic threshold r_C strongly depends on the epidemic model considered, on the pattern of contacts, on its

topology and its dynamics. Thus, the epidemic threshold r_C is affected by control measures and adaptive behaviours, which impact on the topology of interactions, on the dynamics of contacts and on the susceptibility of some nodes. We can define the *effective reproduction number* $R = r/r_C$ which indicates how much the system is above threshold when the adaptive behaviours are implemented. Adaptive behaviours reduce the impact of the epidemic if they increase the epidemic threshold $r_C^{NA} \to r_C$, i.e. if they reduce the reproduction number $R_0 \to R$. The measures can push the system from the active phase into the absorbing phase with a regressive epidemic $R_0 > 1 \to R < 1$, or can reduce significantly the pathogen circulation but maintaining the system is still in the active phase $R_0 > 1 \to 1 < R < R_0$.

- **the asymptotic epidemic prevalence (or the epidemic final size)**. Adaptive behaviours can lower or increase the epidemic prevalence (or epidemic final size) lowering the endemicity (or the total number of infected individuals during the epidemic). In both cases, the transmission of the pathogen would be minimized and thus the costs in terms of hospitalizations, deaths and short/long-term health consequences of the infection;

- **the infection peak**. Adaptive behaviours can lower the height of the infection peak, reducing the instantaneous impact of the epidemic to avoid overwhelming the health system. This can be achieved in two ways: *mild measures* flatten the infection curve $I(t)$ by lowering the peak, widening and slowing it down, effectively producing a similar epidemic final size but over longer times and with lower instantaneous incidence; *strong measures* instead anticipate the infection peak, reduce its duration and its height, immediately stopping the spread of the epidemic also reducing the epidemic final size, by anticipating the epidemic decay.

A large set of mathematical models investigates the effects of adaptive behaviours, dealing with the difficulty of considering the interplay between the dynamics of the network and of the epidemic process, coupled through complex adaptive behaviours, which typically depend themselves on a third dynamic process (e.g. awareness diffusion). Many of them are mainly numerical or are based on some assumption and simplification; only few models consider the coupled dynamics without any assumption on the time-scales of the different processes.

3.2.1 Prevalence-based adaptive behaviours

A first approach to model adaptive behaviour is that to directly modify a compartmental epidemic models by introducing new compartments and new transition processes, modelling self-protective behaviours or protection implemented by control measures [163]. The SIR model (with μ recovery rate and $\beta = \lambda$ infection rate) can be extended by assuming that a susceptible node can adopt a protective behaviour by moving into a new compartment S^F due to the risk perception. Individuals in S^F engage contacts with the rest of the population but with a lower risk of infection (for example by wearing face masks, by keeping a physical distance or by reducing the number of contacts engaged). This is effectively modelled by assuming that for S^F the infection rate is reduced by a factor r_β and therefore:

$$S^F + I \xrightarrow{r_\beta \beta} 2I, \tag{3.1}$$

with $r_\beta \in [0, 1)$ that modulates the level of behavioural change. Then individuals can relax their behaviour $S^F \to S$ returning to behave as previously, due to a reduction in risk perception or a relaxation in the public measures. This relaxation can be mediated by interactions with susceptible or recovered individuals who have not adopted the adaptation measures, in a sort of imitation process with rate μ_F:

$$S^F + S \xrightarrow{\mu_F} 2S, \quad S^F + R \xrightarrow{\mu_F} S + R. \tag{3.2}$$

A wide range of mechanisms can be considered regarding the transition $S \to S^F$, depending on the implementation of the adaptiveness. The simplest case is an adoption of adaptive behaviours with *prevalence-based local information*: susceptible individuals change their behaviour only if they interact with infected individuals, assuming that the more an individual engages interactions with infected nodes, the higher the probability of assuming adaptive behaviours. This corresponds to:

$$S + I \xrightarrow{\beta_F} S^F + I, \tag{3.3}$$

where β_F is the disease awareness acquisition rate. See Figure 3.2 for a schematic representation of the complete compartmental epidemic model with adaptive behaviours. In the homogeneous mixing approximation, the system is described by:

$$\partial_t S(t) = -\beta S(t)\frac{I(t)}{N} - \beta_F S(t)\frac{I(t)}{N} + \mu_F S^F(t)\frac{S(t)+R(t)}{N}, \tag{3.4}$$

$$\partial_t S^F(t) = -r_\beta \beta S^F(t)\frac{I(t)}{N} + \beta_F S(t)\frac{I(t)}{N} - \mu_F S^F(t)\frac{S(t)+R(t)}{N}, \tag{3.5}$$

$$\partial_t I(t) = -\mu I(t) + \beta S(t)\frac{I(t)}{N} + r_\beta \beta S^F(t)\frac{I(t)}{N}, \tag{3.6}$$

$$\partial_t R(t) = \mu I(t), \tag{3.7}$$

where $X(t)$ is the number of individuals in compartment X.

If the infection spreads much faster than the disease awareness $\beta \gg \beta_F$, the model reduces to the SIR model with $R_0 = \beta/\mu$. If the infection spreads much slower than the disease awareness $\beta \ll \beta_F$, the model reduces to the SIR model with $R = r_\beta \beta/\mu = r_\beta R_0$: the adaptive behaviour reduces R_0 by a factor r_β which corresponds to the reduction in the infection rate for S^F. By integrating the Eqs. (3.4) - (3.7) and through numerical simulations we can consider the case in which $\beta \approx \beta_F$, i.e. the intermediate case. In this regime, the adaptive behaviours implemented reduce the epidemic size, weakening the epidemics, and modify the epidemic dynamics by introducing multiple peaks in the evolution of the number of infectious individuals $I(t)$, corresponding to successive waves of infection (see Figure 3.2). Indeed, after the first wave the adaptive behaviours are relaxed with the transition $S^F \to S$, increasing the susceptible population: if at this stage $I(t)$ is not too small and there is a large set of nodes still susceptible, the second wave occurs [163].

The adaptive model features a very rich dynamics, as shown in the phase diagram on the (R_0, β_F) plane shown in Figure 3.2. Different regimes occur varying R_0 and β_F, with a different number of peaks in $I(t)$. This reproduces what was observed during the 1918 pandemic and during the recent COVID-19 pandemic, where consecutive waves were observed due to the alternation of tightening and relaxation of control measures [164].

Another possibility is an adoption of adaptive behaviours with *prevalence-based*

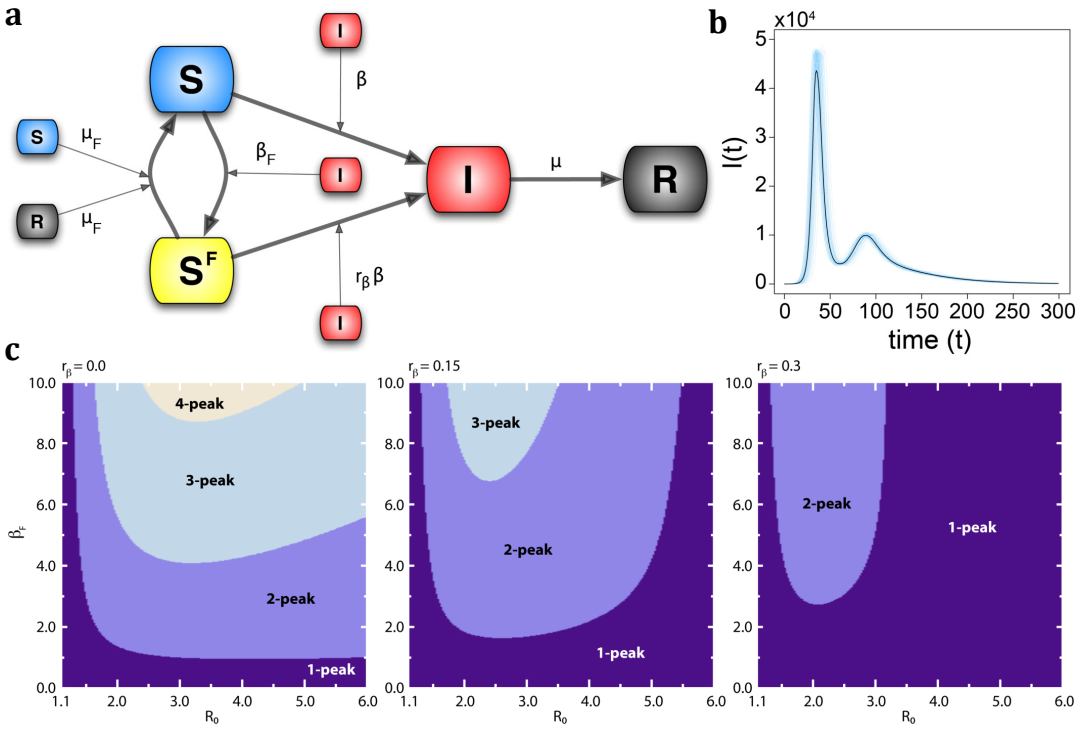

FIGURE 3.2: **Prevalence-based adaptive behaviour with local information.** Panel **a** shows the compartmental epidemic model with prevalence-based adaptive behaviours induced by local information: all transitions are described in the main text. In panel **b** the temporal evolution of the number of infected individuals is plotted for 10^2 stochastic runs and the solid curve shows the median evaluated for $5\,10^3$ runs in which the epidemic final size is at least 0.1% of N. The parameters are fixed $R_0 = 2$, $\beta_F = 3\,\text{day}^{-1}$ and $r_\beta = 0.1$. In panel **c** the phase diagram of infection waves is plotted on the (R_0, β_F) plane for three values of $r_\beta = [0, 0.15, 0.3]$. The phase diagram is obtained by integrating numerically Eqs. (3.4)-(3.7). In all panels $N = 10^6$, $\mu = \mu_F = 0.1\,\text{day}^{-1}$. Image adapted from [163] under Creative Commons Attribution License.

global information [163], in which a global information induces adaptive behaviours in the population, even if a node is not in contact with a large fraction of infected individuals. This is the case of public control and containment measures. The adoption of awareness is not represented by the mass-action law, but is replaced by:

$$\beta_F \frac{I(t)}{N} \to \beta_F (1 - e^{-\delta I(t)}), \tag{3.8}$$

with $\delta \in (0, 1]$ that estimate the adaptiveness intensity. Assuming δ small we obtain:

$$\beta_F (1 - e^{-\delta I(t)}) = \beta_F [\delta I(t) + \mathcal{O}(\delta^2)], \tag{3.9}$$

therefore δ^{-1} estimates the characteristic number of infected publicly reported above which the adaptive behaviour spreads rapidly in the population. See Figure 3.3 for a schematic representation of the complete compartmental epidemic model with adaptive behaviours. In the homogeneous mixing approximation, the system is described by:

$$\partial_t S(t) = -\beta S(t) \frac{I(t)}{N} - \beta_F S(t)[1 - e^{-\delta I(t)}] + \mu_F S^F(t) \frac{S(t) + R(t)}{N}, \tag{3.10}$$

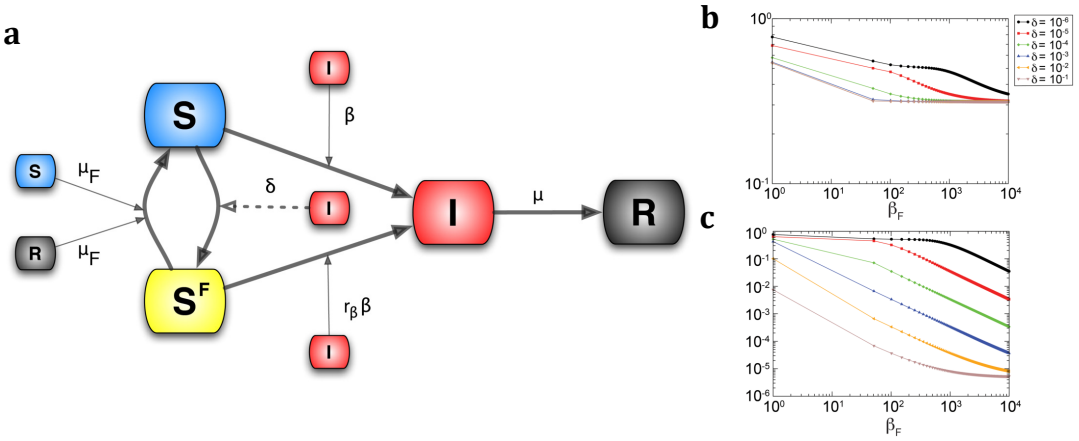

FIGURE 3.3: **Prevalence-based adaptive behaviour with global information.** Panel **a** shows the compartmental epidemic model with prevalence-based adaptive behaviours induced by global information: all transitions are described in the main text. In panels **b-c** the reduction in the epidemic final size R_∞ is plotted as a function of β_F for different δ values. The parameters are fixed $\mu = 0.4\,\text{day}^{-1}$, $R_0 = 2$, $\mu_F = 0.5\,\text{day}^{-1}$ and $N = 10^6$. In panel **b** $r_\beta = 0.6$, so that $R_0 r_\beta > 1$, while in panel **c** $r_\beta = 0.4$, so that $R_0 r_\beta < 1$. The curves are obtained by integrating numerically Eqs. (3.10)-(3.13). Image adapted from [163] under Creative Commons Attribution License.

$$\partial_t S^F(t) = -r_\beta \beta S^F(t)\frac{I(t)}{N} + \beta_F S(t)[1 - e^{-\delta I(t)}] - \mu_F S^F(t)\frac{S(t)+R(t)}{N}, \tag{3.11}$$

$$\partial_t I(t) = -\mu I(t) + \beta S(t)\frac{I(t)}{N} + r_\beta \beta S^F(t)\frac{I(t)}{N}, \tag{3.12}$$

$$\partial_t R(t) = \mu I(t). \tag{3.13}$$

The model is completely analogous to the one with local information in the limits $\beta \gg \beta_F$ and $\beta \ll \beta_F$ for each δ. Moreover, the two models are equivalent for small δ by simply redefining the parameters [163]: in these regimes the behaviours already described are obtained with multiple peaks. In general, this model produces a reduction of the epidemic final size R_∞ that is a function of δ, r_β and β_F: with increasing δ the spread of fear is faster and thus the epidemic size decreases (see Figure 3.3).

Simple adaptation mechanisms induce non-trivial changes to the temporal dynamics of the epidemic and to its overall impact, producing a very rich dynamic even neglecting the network structure within the homogeneous mixing approximation. However, more complex and challenging effects emerge considering the true network structure of interactions.

In the most realistic scenario, the epidemic process is coupled to the *diffusion of awareness*: in this case the nodes are connected at two different level, through the face-to-face interactions and through communication connections (e.g. internet connections, telephone connections) [147, 165]. The awareness spread on the information network, while the pathogen on the face-to-face interactions network. The effectiveness of the adaptive behaviours induced by the awareness depends on the networks overlap: it is very low if the information network and the interaction network differ, since awareness is generated in nodes that are not directly connected epidemiologically; while it is very high if the two networks overlap [165].

3.2.2 Adaptive link rewiring

The role of the network structure is even more crucial when complex adaptive behaviour directly induce changes in the topology and in the dynamics of the network: for example the *rewiring* of links for self-protection or for relational exchange, the destruction of links for the implementation of lockdown or quarantine. In these cases the disease and the network topology coevolve coupled through complex mechanisms of removal and redirection of links which depends on the epidemic: this induces non-trivial effects in the topology, in the epidemic and in the network dynamics [166].

Let us now consider a static network of N nodes on which the SIS epidemic process occurs inducing a simple adaptive behaviour: susceptible nodes can protect themselves by rewiring with probability w their links with infected individuals towards other susceptible nodes, selected randomly [166]. In the absence of rewiring (i.e. $w = 0$) in a homogeneous population (i.e. all nodes in contact with $\langle k \rangle$ nodes), the epidemic threshold is $\lambda_C = \mu / \langle k \rangle$; in the presence of rewiring an infected node loses on average a fraction w of its contacts per unit of time, reducing its degree according to the law:

$$k(t) = \langle k \rangle e^{-wt}, \tag{3.14}$$

where t is the time passed since the infection. Therefore the epidemic threshold is:

$$\lambda_C = \frac{w}{\langle k \rangle [1 - e^{-w/\mu}]}. \tag{3.15}$$

In the limit $w \simeq 0$ the case without adaptive behaviours is recovered; while for $w \gg \mu$ the threshold is $\lambda_C = w / \langle k \rangle$: the threshold is considerably increased by the adaptive behaviour.

Moreover, the adaptive behaviour induces relevant effects on the topology: due to rewiring, the system features two poorly interconnected clusters, one susceptible and one infected, since all the links SI are redirected to form SS. New connections between the two clusters are formed by the recovery of the infected and are then removed by rewiring: this leads to strong temporal fluctuations in the degree of the nodes, indeed if a node is susceptible its degree grows linearly $\partial_t k_S(t) = w l_{SI}(t)$ (where $l_{SI}(t)$ is the number of links SI at time t), while if it is infected its degree decreases exponentially $\partial_t k_I(t) \sim -w k_I(t)$. The two processes produce a dynamic equilibrium with a constant number of links between the two clusters and within the two clusters, generating a widening of the infected and susceptible degree distributions and introducing assortativity, even if the network was initially homogeneous and without degrees correlations [166]. Moreover, the susceptible nodes show a strong increase in the average degree and in the fluctuations, indicating the formation of highly interconnected clusters and of temporally isolated nodes.

The rewiring isolates infected individuals, thus locally weakening the epidemic, but at the same time topologically favours node mixing and the formation of clusters of highly connected susceptible nodes with high degree fluctuations, thus globally favouring the epidemic. Indeed an infected node in the highly connected cluster of susceptibles is able to infect many nodes quickly, furthermore the heterogeneity and the mixing favour the epidemic. To investigate this behaviour we can consider a mean-field approach, considering $X(t)$, the average fraction of nodes in compartment X at time t, and l_{XY}, the average fraction of links XY with $X, Y \in [S, I]$. Assuming the moment closure approximation $l_{XYZ} = l_{XY} l_{YZ} / Y$ with $X, Y, Z \in [S, I]$,

the coevolution of the network and the epidemic is described by the equations:

$$\partial_t I(t) = \lambda l_{SI}(t) - \mu I(t), \tag{3.16}$$

$$\partial_t l_{II}(t) = \lambda l_{SI}(t) \left(\frac{l_{SI}(t)}{S(t)} + 1 \right) - 2\mu l_{II}(t), \tag{3.17}$$

$$\partial_t l_{SS}(t) = (\mu + w) l_{SI}(t) - \frac{2\lambda l_{SI}(t) l_{SS}(t)}{S(t)}. \tag{3.18}$$

In the absence of rewiring there is only one continuous phase transition at the critical point λ_C; activating the rewiring rate the threshold is consistently increased with Eq. (3.15), however a second threshold appears with a saddle-node bifurcation [166]. A bistability region is activated in which both the endemic state and the absorbing state are stable, producing an hysteresis cycle. The dynamics of the system is extremely rich: increasing w the saddle-node bifurcation is replaced by a subcritical Hopf bifurcation, which produces an unstable limit cycle, and then for higher w it is replaced by a supercritical Hopf bifurcation with a stable limit cycle, which produces oscillations in dynamics [166].

Many adaptive behaviours impact on the network topology and can be described through the links rewiring, even if not directly undertaken for self-protection or to reduce the impact of the epidemic. This is the case of the *relational exchange* [156]: during the spreading of an infectious disease individuals with an essential role for society (e.g. teachers, health-care workers) when ill are replaced by susceptible individuals with the same role. This mechanism can be modelled by assuming that an infected node is replaced by a susceptible one: the infected node is isolated while the susceptible one maintains their links and acquires those originally belonging to the replaced individual. Even if the infected individual is isolated, this mechanism favours the epidemic [156]. Indeed, the new susceptible individual is introduced into a potentially dangerous environment, since the infected node could have infected their contacts, and furthermore the replacement determines a contraction in the diameter of the network. Moreover, in heterogeneous populations the nodes with high degree are initially infected and then are immunized, reducing the epidemic potential of the population. However, the relational exchange keeps high the number of susceptible individuals with high degree, favouring the persistence of the pathogen. The relational exchange thus impact on the epidemic accelerating the spreading and increasing the epidemic final size, introducing also non-trivial dynamic behaviours such as discontinuous phase transitions [156].

3.2.3 Adaptiveness in activity-driven networks

We showed the implementation of adaptive behaviours in the homogeneous mixing approach and in static networks, however the most realistic case is that of adaptive temporal networks. In recent years, some adaptive behaviours have been implemented on the activity-driven network, exploiting the flexibility of the AD model [167–171]. The AD model indeed allows to introduce a coupling between the network and the epidemic process also at the adaptive level, allowing to treat the system analytically and numerically despite the complexity of the feedback loop and without assumptions on the time-scales.

Some *immunization strategies* can be implemented on the original AD network (see Section 1.6) [167]. Immunized nodes belong to an immunized compartment R

and the equations for the SIS model in the activity-based mean-field approach are:

$$\begin{aligned} I_a(t+\Delta t) - I_a(t) = -\mu \Delta t I_a(t) + \lambda m (N_a - I_a(t) - R_a) a \Delta t \int da' \frac{I_{a'}(t)}{N} \\ + \lambda m (N_a - I_a(t) - R_a) \int da' \frac{I_{a'}(t)}{N} a' \Delta t, \end{aligned} \tag{3.19}$$

where $I_a(t)$ is the number of infected individuals in class a at time t, R_a is the number of immunized nodes with activity a and N_a is the total number of nodes with activity a, so that $N = \int da' N_{a'}$.

A random strategy (RS) immunizes a fraction p of the population with uniform probability: in this case $R_a = pN_a$. The epidemic threshold therefore becomes [167]:

$$r_C^{RS} = \left.\frac{\lambda}{\mu}\right|_C = \frac{1}{1-p}\frac{1}{m}\frac{1}{\langle a \rangle + \sqrt{\langle a^2 \rangle}} = \frac{1}{1-p} r_C^{AD}. \tag{3.20}$$

The epidemic threshold of the non-adaptive case (Eq. (2.43)) is rescaled by a factor $(1-p)$, i.e. the fraction of nodes still available for infection. Indeed, the random immunization strategy effectively corresponds to rescaling the probability of infection λ with the fraction of available nodes.

Another strategy can be that of a preferential immunization on the nodes with high activity (TS), i.e. all nodes with $a \geq a_c$, thus the fraction of nodes immunized is $p = \int_{a_c}^{\infty} da' \rho(a')$ and $R_a = \theta(a - a_c)$. An explicit form of the threshold is obtained [167]:

$$r_C^{TS} = \left.\frac{\lambda}{\mu}\right|_C = \frac{1}{m}\frac{1}{\langle a \rangle^c + \sqrt{(1-p)\langle a^2 \rangle^c}}, \tag{3.21}$$

where $\langle f(a) \rangle^c = \int_0^{a_c} da \rho(a) f(a)$, i.e. the average on activities in the absence of the immunized nodes. In this case, not only a rescaling of the threshold is obtained, but a drastically different behaviour of the threshold. This immunization strategy is extremely effective, acting on the hubs, but it is based on global information of the network properties which are typically not available in real situations, since the network structure is only partially known [11, 167]. Thus, local immunization strategies have been developed recently, based on the local sampling of the network [167].

The immunization processes not only protect directly immunized individuals, but also can preclude the global propagation of the disease in non-immunized individuals: this is the *heard immunity* effect [11, 167]. It is possible to define the *immunization threshold* p_C as the critical value of p necessary to stop the contagion process: for $p \geq p_C$ the system will be below the threshold, for $p < p_C$ immunization reduces transmission but is not sufficient to block the contagion. Clearly p_C depends on the immunization strategy implemented, on the pattern of contacts, i.e. on the $\rho(a)$, and on the epidemiological properties of the epidemic, i.e. on $R_0 = r/r_C^{AD}$. For the random strategy p_C is obtained by inverting Eq. (3.20):

$$p_C^{RS} = 1 - \frac{1}{m}\frac{1}{\langle a \rangle + \sqrt{\langle a^2 \rangle}}\frac{1}{r} = 1 - \frac{1}{R_0}. \tag{3.22}$$

On the contrary, for the targeted vaccination strategy an explicit form for p_C cannot be obtained, but it can be evaluated numerically imposing $r_C^{TS} - r = 0$, i.e. $r_C^{TS}/r_C^{AD} = R_0$: a targeted strategy allows to block the diffusion by immunizing a very small percentage of the population, acting on the most active nodes that would behave as super-spreaders if they were not immunized [167].

Adaptiveness can be introduced in the AD model allowing infected and susceptible nodes to rescale their activity of a specific factor when infected or in case of risk perception [168]: this is implemented by rescaling the activity a of a node of a factor η_S if susceptible, i.e. $a' = \eta_S a$ with $\eta_S \in [0,1)$, and a factor η_I if infected, i.e. $a' = \eta_I a$ with $\eta_I \in [0,1)$. This is completely equivalent to draw the activity a when a node is susceptible from $\rho(a)$ and rescale the activity in the infected state for all nodes by a factor η_I/η_S, indeed the reduction in susceptible activity is independent of the epidemics and thus is always active, replacing the baseline of the activity a. The epidemic threshold can be obtained analytically with an activity-based mean-field approach and is [168]:

$$r_C = \frac{\lambda}{\mu}\bigg|_C = \frac{1}{m}\frac{2}{(\eta_S+\eta_I)\langle a\rangle + \sqrt{(\eta_S-\eta_I)^2\langle a\rangle^2 + 4\eta_S\eta_I\langle a^2\rangle}}. \tag{3.23}$$

The threshold again depends on the moments of the distribution $\rho(a)$ and on the rescaling η_S and η_I. If $\eta_S = \eta_I = 1$ the threshold of the non-adaptive case of Eq. (2.43) is recovered, while for $\eta_I \ll \eta_S$ we get $r_C = 1/m\eta_S\langle a\rangle$. In the case of a strong reduction in the activity of the infected nodes, the threshold depends only on the activity of the susceptible nodes and on $\langle a\rangle$, since only the activations of the susceptible ones produce contagion in this regime and infected nodes can only passively receive links. In this regime the fluctuations in activity no longer matter. The epidemic threshold is strongly increased in case of a strong reduction of activity in infected nodes, especially in heterogeneous populations with broad $\rho(a)$ [168].

The self-protective behaviour of healthy people can be modelled by assuming a reduction in social activity as a function of global prevalence [168]:

$$\eta_S(t) = \begin{cases} \eta_S^0(1 - I(t)/\overline{I}) & \text{if } I(t) \le \overline{I} \\ 0 & \text{if } I(t) > \overline{I} \end{cases} \tag{3.24}$$

where $I(t) = \int da' I_{a'}(t)$ is the total number of infected individuals at time t, $\overline{I}$ regulates the intensity of the adaptive behaviour and η_S^0 regulates the baseline reduction when $I(t) = 0$. Analogously the activity reduction in susceptibles can be tuned by the global epidemic prevalence growth rate $\Delta_I(t) = I(t) - I(t - \Delta t)$:

$$\eta_S(t) = \begin{cases} \eta_S^0 & \text{if } \Delta_I(t) \le 0 \\ \eta_S^0(1 - \Delta_I(t)/\overline{\Delta}) & \text{if } 0 < \Delta_I(t) < \overline{\Delta} \\ 0 & \text{if } \Delta_I(t) \ge \overline{\Delta} \end{cases} \tag{3.25}$$

where $\Delta_I(t)$ regulates the intensity of the adaptive behaviour. In both cases, numerical simulations show an increase in the epidemic threshold and a reduction in epidemic prevalence [168], with a more pronounced effect when the behaviour is induced by prevalence than by the growth rate. In general, a reduction in the social activity of infected or susceptible nodes has a strong impact on the network dynamics and on the epidemic, weakening its spread.

Other models of adaptive behaviours have been implemented on the AD network [171], for example considering an alert status in the compartmental model [169] or a prevalence-based local information which trigger protective behaviours [170]. All these examples show once again the flexibility of the AD model, which allow to introduce the coupling of the network with the epidemic process also at the adaptive level despite the complexity of the feedback loop.

Chapter 4

A general formalism for adaptive activity-driven networks

In this Chapter we describe the results of Ref. [14]: we propose a general formalism for *adaptive activity-driven temporal networks* which can model several adaptive behaviours observed during epidemics. Through this formalism we implement two quarantine mechanisms, the *active* and the *inactive quarantine*, inspired by real case studies observed during the early stages of the COVID-19 pandemic.

4.1 Epidemics on adaptive AD networks

Public interventions and adaptive behaviours described in Chapter 3 act directly on potentially contagious social activity, reducing (e.g. protective measures) or increasing it (e.g. disease-party). The modification in social activity and the effect on the epidemic spreading strongly depend on the specific implementation of the adaptive behaviours.

Many adaptive mechanisms can be modelled in the activity-driven network with attractiveness (see Section 1.6.1 and Section 2.3.1), by introducing an adaptive coupling between the network evolution and the epidemic spreading [14]. In the activity-driven network with attractiveness (ADA) [71, 72], the behaviour of individuals is completely encoded in their activity, which set the number of interactions actively created, and in their attractivenesses, which set the number of interactions passively received. The ADA network is well-suited for simply modelling a broad spectrum of adaptive behaviours, since any self-induced adaptive behaviour or public containment policy can be modelled through a change in the nodes activity and attractiveness [172, 173]. For example, infected individuals can partially or totally reduce their activity [168], due to the emergence of symptoms or due to publicly imposed restrictions; moreover infected individuals can undergo an attractiveness reduction as a consequence of self-protective behaviours of the rest of the population.

We consider an epidemic, described by a general compartmental epidemic model with compartments $X = \{1, 2, ..., \kappa\}$, spreading on the ADA network [14]. In the network without adaptive behaviours, each node is assigned with two parameters, the activity a and the attractiveness b, extracted from a joint probability distribution $\rho(a, b)$. A general adaptive behaviour can be implemented assuming that the activity a_X and the attractiveness b_X of a node depend on the dynamic state of the node X: thus, the change in the dynamic state of an individual (e.g. a change in the health status) determines a change in the activity and attractiveness of the node, affecting the social behaviour. In this case, each node is assigned with 2κ parameters: κ activity and κ attractiveness parameters, where κ is the number of compartments of

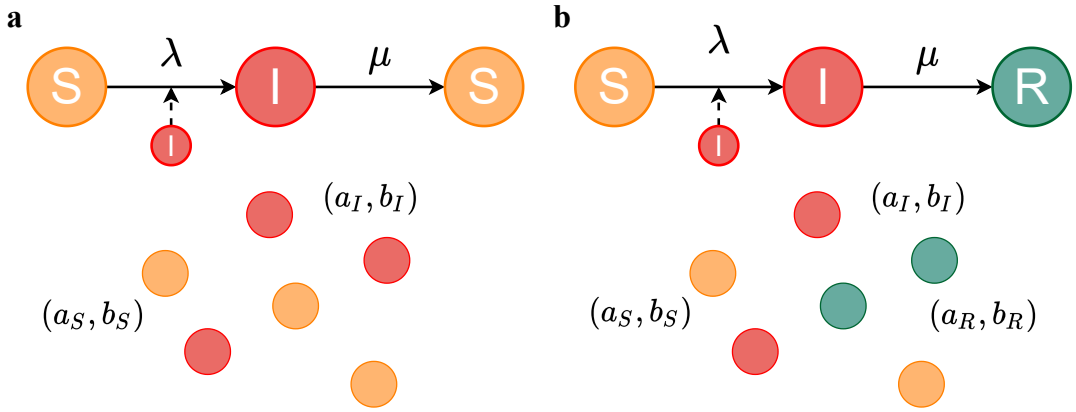

FIGURE 4.1: **Schematic representation of the adaptive activity-driven network.** In panel **a** and panel **b** we represent schematically the adaptive activity-driven model, respectively for the SIS and SIR epidemic models. The network is composed of $N = 6$ nodes: each of them is coloured according to its health status and is assigned with activity and attractiveness.

the epidemic model. These parameters are extracted from a general joint probability distribution $\rho(a_1, b_1, a_2, b_2, ..., a_\kappa, b_\kappa)$: this distribution encodes all the correlations between activity and attractiveness in the same compartment (a_X, b_X) and all the cross-correlations between the behaviours of a node in different compartments. See Figure 4.1 for a schematic representation of the adaptive model for the SIS and SIR epidemic models.

4.1.1 The model: active vs inactive implementation

We consider here the SIS epidemic model, with λ probability of infection per effective link and μ recovery rate. In the proposed adaptive activity-driven network each node is assigned with four parameters: the activity and attractiveness in the susceptible (a_S, b_S) and in the infected state (a_I, b_I) (see Figure 4.1). These four parameters are drawn from the joint distribution $\rho(a_S, a_I, b_S, b_I)$. Hereafter, we define $\overline{f}(t) = \int da_S da_I db_S db_I \rho(a_S, a_I, b_S, b_I) f_{a_S, a_I, b_S, b_I}(t)$.

The network is composed of N nodes initially disconnected and evolves analogously to the ADA model. Each node i is characterized by an independent Poissonian activation process: the activation rate is a_X^i, where X is the compartment to which the node belongs. When a node is active generates m links with m randomly-selected nodes (we fix $m = 1$ for simplicity): the probability of contacting a node depends on its attractiveness b_X, in particular $p_{b_X} = b_X/\alpha$ where $X = S, I$ and α is the normalization factor. All interactions are instantaneous, thus the links are removed and the procedure is iterated.

In Section 2.3.1 we show that the epidemic is strongly coupled to the dynamics of the ADA network, especially to the average activity and attractiveness of the nodes and their correlations. In this adaptive model the overall network dynamics is also strongly coupled to the epidemic, since the nodes activity and attractiveness depend on their health status and therefore on the spread of the epidemic. For example, the average activity $\langle a(t) \rangle = \sum_i^N a_X^i / N$ and the average attractiveness $\langle b(t) \rangle = \sum_i^N b_X^i / N$ evolve over time, because of the change in the activity and attractiveness induced by infections and recoveries (i.e. transitions). The two dynamics coevolve over time, since the change in activity and attractiveness of a node impact both on the interaction dynamics of the node itself and on the overall dynamics of the network, i.e. on the interaction dynamics of the other nodes.

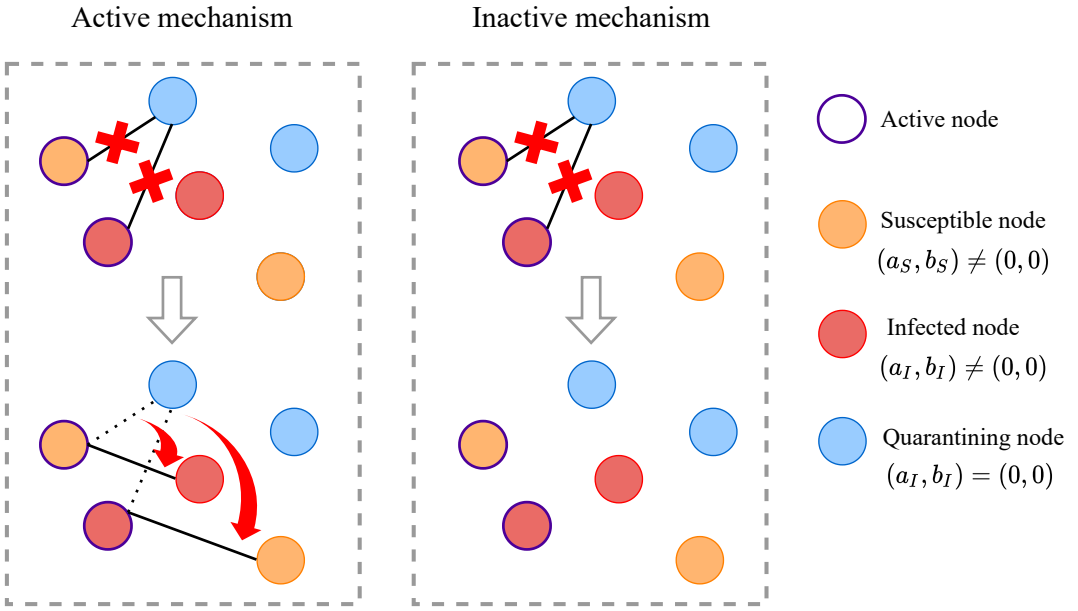

FIGURE 4.2: **Schematic representation of the active and inactive quarantine.** We represent schematically the active and inactive quarantine, as a paradigmatic example of the active and inactive implementations of adaptive behaviours. We consider a network of $N = 6$ nodes, in which there are two active nodes that generate two links with a quarantined node $(a_I, b_I) = (0,0)$: in the active case, the links are redirected to other non-quarantining nodes $(a, b) \neq (0,0)$ which can be susceptible or infected; in the inactive case the links are simply removed, thus the active nodes have no effective links.

The *change in activity* induces a higher or lower activation rate for the affected node: this impacts on the average activity of the population. All the other nodes are affected in the same way, changing the number of links received by a factor proportional to their attractiveness. However, it does not change the probability for the other nodes to be contacted $p_{b_X} = b_X/\alpha$.

The *change in attractiveness* induces a higher or lower attraction of active links for the affected node: this impacts on the average attractiveness of the population. The population need to compensate this effect, adapting the probability for the other nodes to receive links, in order to counteract the increase or decrease in the probability for the affected node to attract links, eventually redirecting or adjusting the population activity. Thus, it can also impact on the probability that the other nodes are contacted $p_{b_X} = b_X/\alpha$.

If the attractiveness is reduced, part of the population activity initially directed to the node is no longer attracted by it. The population can compensate this change in two ways:

- ***Active implementation,*** assuming that an active node connects securely to another node. The population compensate the change in the attractiveness of the node, readdressing the activity originally attracted by the affected node towards the other nodes, proportionally to their attractiveness. This corresponds to an effective rewiring of the links originally directed to the node (see Figure 4.2) and it is formally implemented by setting the normalization factor α as the average attractiveness at time t:

$$\alpha(t) = \langle b(t) \rangle, \tag{4.1}$$

so that the probability for an active node to contact another node is 1. The normalization factor evolves over time due to the temporal evolution of the average attractiveness $\langle b(t)\rangle$, induced by the epidemic spreading and by the adaptive behaviours. The probability of contacting a node $p_{b_X}(t) = b_X/\langle b(t)\rangle$ also evolves over time t due to the evolution of $\langle b(t)\rangle$. This implementation is defined *active*, as the population compensates the reduction in attractiveness by rewiring the links, thus preserving the population activity level: indeed, the average activity is not changed since active nodes always create links.

- ***Inactive implementation,*** assuming that an active node may also not connect to any node due to the reduction in the average population attractiveness. The population does not compensate the change in the attractiveness of the affected node, but provides a non-zero probability that an active node does not produce a link. The activity originally attracted by the affected node produces ineffective and inactive links (see Figure 4.2) and this is formally implemented by setting the normalization factor α as the average attractiveness with all susceptible nodes:

$$\alpha = \overline{b_S}, \tag{4.2}$$

The normalization factor is constant, therefore the probability of contacting a node $p_{b_X} = b_X/\overline{b_S}$ is constant over time t and is not affected by the adaptive behaviour of the other nodes. Moreover, the probability for an active node to not form a link is:

$$Q = \frac{\overline{b_S} - \langle b(t)\rangle}{\overline{b_S}}. \tag{4.3}$$

This implementation is defined *inactive*, as the population does not compensate the reduction in attractiveness: this produces a reduction and deterioration in the population activity since part of the activations result in inactive and ineffective links. Thus, not only the node changing attractiveness suffer a reduction in social activity, but also the other nodes as a consequence of this mechanism.

The two approaches are profoundly different, since the active one is based on a dynamic rewiring of the links, while inactive one is not: this mechanism can produce highly non-trivial effects both on the topology and on the epidemic dynamics (see Section 3.2.2) [156, 166]. In Figure 4.2 we schematically represent the active and inactive implementations, describing the quarantine as a paradigmatic example.

4.1.2 Epidemic threshold and the SIS epidemic prevalence

The SIS epidemic dynamics can be described by means of an activity-attractiveness-based mean-field approach, dividing the population into classes of nodes with the same quadruple of parameters (a_S, a_I, b_S, b_I) and considering them statistically equivalent. In this approach, the epidemic is described by the probability $P_{a_S,a_I,b_S,b_I}(t)$ that a node in the class (a_S, a_I, b_S, b_I) is infected at time t. Thus, the average activity and attractiveness at time t are:

$$\begin{aligned}\langle a(t)\rangle &= \int \prod_{X=S,I} da_X db_X \rho(a_S, a_I, b_S, b_I) \left\{a_S[1 - P_{a_S,a_I,b_S,b_I}(t)] + a_I P_{a_S,a_I,b_S,b_I}(t)\right\} \\ &= \overline{a_S} + \overline{a_I P}(t) - \overline{a_S P}(t),\end{aligned} \tag{4.4}$$

$$\begin{aligned}\langle b(t)\rangle &= \int \prod_{X=S,I} da_X db_X \rho(a_S, a_I, b_S, b_I) \left\{ b_S[1 - P_{a_S,a_I,b_S,b_I}(t)] + b_I P_{a_S,a_I,b_S,b_I}(t) \right\} \\ &= \overline{b_S} + \overline{b_I P}(t) - \overline{b_S P}(t).\end{aligned} \tag{4.5}$$

The probability $P_{a_S,a_I,b_S,b_I}(t)$ evolves according to the following equation, which takes into account the network dynamics, the epidemic spreading and the adaptive behaviours:

$$\begin{aligned}\partial_t P_{a_S,a_I,b_S,b_I}(t) = &- \mu P_{a_S,a_I,b_S,b_I}(t) \\ &+ \lambda(1 - P_{a_S,a_I,b_S,b_I}(t)) a_S \int \prod_{X=S,I} da'_X db'_X \rho(a'_S, a'_I, b'_S, b'_I) \frac{b'_I}{\alpha} P_{a'_S,a'_I,b'_S,b'_I}(t) \\ &+ \lambda(1 - P_{a_S,a_I,b_S,b_I}(t)) \frac{b_S}{\alpha} \int \prod_{X=S,I} da'_X db'_X \rho(a'_S, a'_I, b'_S, b'_I) a'_I P_{a'_S,a'_I,b'_S,b'_I}(t).\end{aligned} \tag{4.6}$$

The first term on the right-hand side is the recovery term; the second term corresponds to the infection process in which a susceptible node of class (a_S, a_I, b_S, b_I) is activated creating a link with an infected node, who attracts the link and can belong to any class (i.e. the term is averaged on the class (a'_S, a'_I, b'_S, b'_I) of the infected node); the third term corresponds to the infection process in which an infected node of any class is activated and create a link with a susceptible node in class (a_S, a_I, b_S, b_I) who attracts the link. Thus in the notation reported above:

$$\partial_t P_{a_S,a_I,b_S,b_I}(t) = -\mu P_{a_S,a_I,b_S,b_I}(t) + \lambda(1 - P_{a_S,a_I,b_S,b_I}(t)) \frac{a_S \overline{b_I P}(t) + b_S \overline{a_I P}(t)}{\alpha}. \tag{4.7}$$

This equation holds for both the active and the inactive implementations and is valid for arbitrary distribution $\rho(a_S, a_I, b_S, b_I)$, i.e. for arbitrary adaptive behaviour.

Let us now consider the active implementation $\alpha = \langle b(t)\rangle = \overline{b_S} + \overline{b_I P}(t) - \overline{b_S P}(t)$, the Eq. (4.7) becomes:

$$\partial_t P_{a_S,a_I,b_S,b_I}(t) = -\mu P_{a_S,a_I,b_S,b_I}(t) + \lambda(1 - P_{a_S,a_I,b_S,b_I}(t)) \frac{a_S \overline{b_I P}(t) + b_S \overline{a_I P}(t)}{\overline{b_S} + \overline{b_I P}(t) - \overline{b_S P}(t)}. \tag{4.8}$$

The evolution of the average probability that a node is infected $\overline{P}(t)$ can be obtained by multiplying both members of Eq. (4.8) for $\rho(a_S, a_I, b_S, b_I)$ and integrating on classes (a_S, a_I, b_S, b_I):

$$\partial_t \overline{P}(t) = -\mu \overline{P}(t) + \lambda \frac{[\overline{a_S} - \overline{a_S P}(t)]\overline{b_I P}(t) + [\overline{b_S} - \overline{b_S P}(t)]\overline{a_I P}(t)}{\overline{b_S} + \overline{b_I P}(t) - \overline{b_S P}(t)}. \tag{4.9}$$

Similarly we obtain the temporal evolution of $\overline{a_I P}(t)$ and of $\overline{b_I P}(t)$, by multiplying both sides of Eq. (4.8) for $a_I \rho(a_S, a_I, b_S, b_I)$ and for $b_I \rho(a_S, a_I, b_S, b_I)$ respectively and then integrating on the classes (a_S, a_I, b_S, b_I):

$$\partial_t \overline{a_I P}(t) = -\mu \overline{a_I P}(t) + \lambda \frac{[\overline{a_I a_S} - \overline{a_I a_S P}(t)]\overline{b_I P}(t) + [\overline{a_I b_S} - \overline{a_I b_S P}(t)]\overline{a_I P}(t)}{\overline{b_S} + \overline{b_I P}(t) - \overline{b_S P}(t)}, \tag{4.10}$$

$$\partial_t \overline{b_I P}(t) = -\mu \overline{b_I P}(t) + \lambda \frac{\left[\overline{b_I a_S} - \overline{b_I a_S P}(t)\right] \overline{b_I P}(t) + \left[\overline{b_I b_S} - \overline{b_I b_S P}(t)\right] \overline{a_I P}(t)}{\overline{b_S} + \overline{b_I P}(t) - \overline{b_S P}(t)}. \tag{4.11}$$

Thus, Eqs. (4.9)-(4.11) constitute a complete set of three coupled non-linear differential equations that admits the absorbing state $(\overline{P}(t), \overline{a_I P}(t), \overline{b_I P}(t)) = (0, 0, 0)$ as a solution: this state corresponds to a fully susceptible population. We can obtain the epidemic threshold by analyzing the stability of this absorbing state; we linearize the Eqs. (4.9)-(4.11) around the absorbing state obtaining:

$$\partial_t \overline{P}(t) = -\mu \overline{P}(t) + \frac{\lambda}{\overline{b_S}} \left(\overline{a_S}\, \overline{b_I P}(t) + \overline{b_S}\, \overline{a_I P}(t) \right), \tag{4.12}$$

$$\partial_t \overline{a_I P}(t) = -\mu \overline{a_I P}(t) + \frac{\lambda}{\overline{b_S}} \left(\overline{a_I a_S}\, \overline{b_I P}(t) + \overline{a_I b_S}\, \overline{a_I P}(t) \right), \tag{4.13}$$

$$\partial_t \overline{b_I P}(t) = -\mu \overline{b_I P}(t) + \frac{\lambda}{\overline{b_S}} \left(\overline{b_I a_S}\, \overline{b_I P}(t) + \overline{b_I b_S}\, \overline{a_I P}(t) \right), \tag{4.14}$$

which is a set of three coupled linear differential equations.

We proceed in the same way for the inactive implementation $\alpha = \overline{b_S}$. The equation for the temporal evolution of $P_{a_S,a_I,b_S,b_I}(t)$ is:

$$\partial_t P_{a_S,a_I,b_S,b_I}(t) = -\mu P_{a_S,a_I,b_S,b_I}(t) + \lambda(1 - P_{a_S,a_I,b_S,b_I}(t)) \frac{a_S \overline{b_I P}(t) + b_S \overline{a_I P}(t)}{\overline{b_S}}. \tag{4.15}$$

Therefore the equations for $\overline{P}(t)$, $\overline{a_I P}(t)$ and $\overline{b_I P}(t)$ become:

$$\partial_t \overline{P}(t) = -\mu \overline{P}(t) + \frac{\lambda}{\overline{b_S}} \left[(\overline{a_S} - \overline{a_S P}(t)) \overline{b_I P}(t) + (\overline{b_S} - \overline{b_S P}(t)) \overline{a_I P}(t) \right], \tag{4.16}$$

$$\partial_t \overline{a_I P}(t) = -\mu \overline{a_I P}(t) + \frac{\lambda}{\overline{b_S}} \left[(\overline{a_I a_S} - \overline{a_I a_S P}(t)) \overline{b_I P}(t) + (\overline{a_I b_S} - \overline{a_I b_S P}(t)) \overline{a_I P}(t) \right], \tag{4.17}$$

$$\partial_t \overline{b_I P}(t) = -\mu \overline{b_I P}(t) + \frac{\lambda}{\overline{b_S}} \left[\left(\overline{b_I a_S} - \overline{b_I a_S P}(t) \right) \overline{b_I P}(t) + \left(\overline{b_I b_S} - \overline{b_I b_S P}(t) \right) \overline{a_I P}(t) \right]. \tag{4.18}$$

Thus, Eqs. (4.16)-(4.18) constitute a complete set of three coupled non-linear differential equations that admit the absorbing state $(\overline{P}(t), \overline{a_I P}(t), \overline{b_I P}(t)) = (0, 0, 0)$ as a solution. We linearize them around the absorbing state and we get:

$$\partial_t \overline{P}(t) = -\mu \overline{P}(t) + \frac{\lambda}{\overline{b_S}} \left(\overline{a_S}\, \overline{b_I P}(t) + \overline{b_S}\, \overline{a_I P}(t) \right), \tag{4.19}$$

$$\partial_t \overline{a_I P}(t) = -\mu \overline{a_I P}(t) + \frac{\lambda}{\overline{b_S}} \left(\overline{a_I a_S}\, \overline{b_I P}(t) + \overline{a_I b_S}\, \overline{a_I P}(t) \right), \tag{4.20}$$

$$\partial_t \overline{b_I P}(t) = -\mu \overline{b_I P}(t) + \frac{\lambda}{\overline{b_S}} \left(\overline{b_I a_S}\, \overline{b_I P}(t) + \overline{b_I b_S}\, \overline{a_I P}(t) \right). \tag{4.21}$$

The active and inactive implementation of adaptive behaviours produce the same set of linearized equations for epidemic evolution (compare the Eqs. (4.12)-(4.14) and Eqs. (4.19)-(4.21)). Indeed, the parameter α expanded around the critical point $r = \lambda/\mu \sim r_C$, i.e. for $P_{a_S,a_I,b_S,b_I}(t) \simeq 0$, is the same for the two approaches since $\langle b(t) \rangle \sim \overline{b_S}$, thus the epidemic dynamics in the active and inactive implementation show the same behaviour in the linearized regime. The two implementations admit

the same Jacobian matrix:

$$J = \begin{bmatrix} -\mu & \lambda & \lambda\frac{\overline{a_S}}{\overline{b_S}} \\ 0 & -\mu + \lambda\frac{\overline{a_I b_S}}{\overline{b_S}} & \lambda\frac{\overline{a_I a_S}}{\overline{b_S}} \\ 0 & \lambda\frac{\overline{b_I b_S}}{\overline{b_S}} & -\mu + \lambda\frac{\overline{a_S b_I}}{\overline{b_S}} \end{bmatrix} \tag{4.22}$$

The eigenvalues of J are:

$$\xi_1 = -\mu, \ , \ \xi_{2,3} = \frac{1}{2\overline{b_S}}\left[-2\mu\overline{b_S} + \lambda(\overline{a_S b_I} + \overline{a_I b_S}) \pm \lambda\sqrt{(\overline{a_S b_I} - \overline{a_I b_S})^2 + 4\overline{a_S a_I}\,\overline{b_S b_I}}\right]. \tag{4.23}$$

The conditions for the stability of the absorbing state are obtained by imposing $\xi_{max} < 0$. Therefore, the epidemic threshold is:

$$r_C = \frac{\lambda}{\mu}\bigg|_C = \frac{2\overline{b_S}}{\overline{a_S b_I} + \overline{a_I b_S} + \sqrt{(\overline{a_S b_I} - \overline{a_I b_S})^2 + 4\overline{a_S a_I}\,\overline{b_S b_I}}}. \tag{4.24}$$

The epidemic threshold is the same for both the active and the inactive implementation of the adaptive behaviours and is exact, indeed the model is exactly mean-field since we do not consider memory effects and the local correlations are destroyed at each time-step through link reshuffling. Moreover, the threshold is valid for arbitrary distribution $\rho(a_S, a_I, b_S, b_I)$, i.e. for arbitrary adaptive behaviour.

The epidemic threshold depends on all the cross-correlations between activity and attractiveness in the susceptible and infected state: this suggests that a crucial role in the spread of the epidemic is played by the way nodes behave when infected, considering how they behave when susceptible, thus on behavioural correlations.

Positive behavioural correlations reduce the epidemic threshold, i.e. the spread of the pathogen is favoured by the presence of nodes that keep their activity and/or attractiveness high when they are infected, acting as temporal hubs for connections and thus as super-spreaders for the epidemic. Indeed, very active/attractive susceptible nodes have a high probability of being infected: if they are very active/attractive also when infected they spread the infection through the network very easily (super-spreaders). Furthermore, these nodes are characterized by continuous waves of reinfection and recovery, actively driving the epidemic.

The joint distribution $\rho(a_S, a_I, b_S, b_I)$ plays a key role in the model, since it defines the overall dynamics of the network, its topology and the specific adaptive behaviour implemented. Moreover, $\rho(a_S, a_I, b_S, b_I)$ encodes all the cross-correlations between the variables (a_S, a_I, b_S, b_I), which shape the epidemic spreading as pointed out by the epidemic threshold (Eq. (4.24)). The correlations can be made explicit in the distribution $\rho(a_S, a_I, b_S, b_I) = \rho_S(a_S, b_S)\rho_{I|S}(a_I, b_I|a_S, b_S)$, where $\rho_S(a_S, b_S)$ is the probability for a node to have (a_S, b_S) and where $\rho_{I|S}(a_I, b_I|a_S, b_S)$ is the conditional probability for a node with (a_S, b_S) to have (a_I, b_I). The $\rho_S(a_S, b_S)$ has already been extensively discussed in Section 1.6.1 and Section 2.3.1 showing significant positive correlations between activity and attractiveness in real systems, as well as strong heterogeneity in both variables. The conditional distribution $\rho_{I|S}(a_I, b_I|a_S, b_S)$ fixes the adaptive behaviour and all the behavioural correlations.

A large set of adaptive behaviours can be modelled through the joint distribution $\rho(a_S, a_I, b_S, b_I)$, both mild (such as sick-leave and mild distancing) and strong interventions (such as quarantine and lockdown). For example:

- *Non-adaptive case with attractiveness (NAdwA)* [13, 72]

$\rho(a_S, a_I, b_S, b_I) = \rho_S(a_S, b_S)\delta(a_I - a_S)\delta(b_I - b_S)$
In this case no adaptive behaviours are implemented, i.e. $a_I = a_S$ and $b_I = b_S$ for all nodes ($\delta(x)$ is the Dirac delta function). Thus, Eq. (4.24) is reduced to the epidemic threshold for the activity-driven network with attractiveness $r_C^{NAdwA} = \overline{b_S}/(\overline{a_S b_S} + \sqrt{\overline{a_S^2} \cdot \overline{b_S^2}})$ (see Eq. (2.53)). If we assume a linear correlation between b_S and a_S, i.e. $b_S = ca_S$ as observed in real systems [72, 76] with c arbitrary constant:

$$r_C^{NAdwA} = \frac{\overline{a_S}}{2\overline{a_S^2}}. \tag{4.25}$$

While if we assume $\rho_S(a_S, b_S) = \rho_S(a_S)\delta(b_S - 1)$, i.e. $b_S = 1$ for all nodes, Eq. (4.24) reduces to the epidemic threshold of the AD network $r_C^{AD} = (\overline{a_S} + \sqrt{\overline{a_S^2}})^{-1}$ (see Eq. (2.43)).

- *Social or physical distancing* [140, 172–174]
  $\rho(a_S, a_I, b_S, b_I) = \rho_S(a_S, b_S)[f\delta(a_I - \eta a_S)\delta(b_I - \xi b_S) + (1 - f)\delta(a_I - a_S)\delta(b_I - b_S)]$
  This behaviour requires an infected node to reduce its social activity $a_I = \eta a_S$, with $\eta \in [0, 1)$, and its attractiveness $b_I = \xi b_S$, with $\xi \in [0, 1)$. This reduction is due to distancing measures, which produces a reduction in the number of potentially contagious contacts, or to self-initiated practices in the population (e.g. sick-leave) for the appearance of symptoms and self-protection. The parameters η and ξ define the intensity of the distancing and the parameter f the level of adhesion in the population. For example, for $f = 1$, $\eta = \eta_I/\eta_S$, $\xi = 1$ and $b_S = 1$ the model of Ref. [168] is recovered as a specific case, obtaining the threshold of Eq. (3.23).

- *Quarantine* [140, 174, 175]
  $\rho(a_S, a_I, b_S, b_I) = \rho_S(a_S, b_S)[\delta \cdot \delta(a_I)\delta(b_I) + (1 - \delta)\delta(a_I - a_S)\delta(b_I - b_S)]$
  This behaviour can be self-initiated by the population or imposed by public interventions, and requires an infected node to be completely isolated $a_I = 0$ and $b_I = 0$. The parameter δ defines the level of adherence in the population.

- *Disease-party* [150–155]
  $\rho(a_S, a_I, b_S, b_I) = \rho_S(a_S, b_S)[f\delta(a_I - \eta a_S)\delta(b_I - \xi b_S) + (1 - f)\delta(a_I - a_S)\delta(b_I - b_S)]$
  This behaviour is self-initiated by the population and requires an infected node to increase its activity $a_I = \eta a_S$, with $\eta \in (1, \infty)$, and attractiveness $b_I = \xi b_S$, with $\xi \in (1, \infty)$, by participating in events such as disease-party. In such events susceptible individuals voluntarily expose themselves to infection, increasing the attractiveness of infected nodes, and infected individuals increase their activity to promote infection. The parameter f defines the level of adherence.

The model allows also to implement specific levels of adhesion for the different classes (a_S, b_S) and thus targeted measures on specific classes. Moreover, it can describe many other types of behaviours with different $\rho_{I|S}(a_I, b_I|a_S, b_S)$, such as combined adaptive behaviours: e.g. a population that in part reduces activity and attractiveness during infection and in part organizes disease-parties.

Adaptive behaviours can be implemented in the active or inactive way: the epidemic threshold is the same for the two implementations, however the epidemic prevalence $\overline{P} = \lim_{t\to\infty} \overline{P}(t)$ is different. We define $P^{\infty}_{a_S,a_I,b_S,b_I} = \lim_{t\to\infty} P_{a_S,a_I,b_S,b_I}(t)$ as the stationary asymptotic probability for a node in class (a_S, a_I, b_S, b_I) to be infected, so that $\overline{P} = \int \prod_{X=S,I} da_X db_X \rho(a_S, a_I, b_S, b_I) P^{\infty}_{a_S,a_I,b_S,b_I}$. The asymptotic probability can be obtained for the active case and the inactive case respectively from Eqs.

(4.8) and (4.15), by setting $\partial_t P^{\infty}_{a_S,a_I,b_S,b_I} = 0$. We obtain for the active case:

$$P^{\infty}_{a_S,a_I,b_S,b_I} = \frac{a_S\overline{b_I P} + b_S\overline{a_I P}}{\frac{\mu}{\lambda}(\overline{b_S} + \overline{b_I P} - \overline{b_S P}) + a_S\overline{b_I P} + b_S\overline{a_I P}}, \tag{4.26}$$

and for the inactive case:

$$P^{\infty}_{a_S,a_I,b_S,b_I} = \frac{a_S\overline{b_I P} + b_S\overline{a_I P}}{\frac{\mu}{\lambda}\overline{b_S} + a_S\overline{b_I P} + b_S\overline{a_I P}}. \tag{4.27}$$

The active phase of the epidemic depends on the specific implementation of the behaviour: this suggests that it is not enough to investigate the effects of adaptive mechanisms on the epidemic threshold since different implementations of adaptive behaviours can produce the same threshold but different active phase dynamics.

Please note that $P^{\infty}_{a_S,a_I,b_S,b_I}$ depends only on (a_S, b_S), i.e. on the susceptible behaviour of the nodes: this holds also for $P_{a_S,a_I,b_S,b_I}(t)$ (see Eqs. (4.8) and (4.15)). The probability that a node is infected depends only on its behaviour in the susceptible phase (a_S, b_S): indeed the probability of contagion depends on the susceptible behaviour of the node and on the behaviour of the averaged infected population, while the recovery process does not depend on infected behaviour of the node.

4.1.3 SIR active phase

We consider now the SIR epidemic model: in this case each node is described by six parameters $(a_S, a_I, a_R, b_S, b_I, b_R)$ drawn from the joint distribution $\rho_{SIR}(a_S, a_I, a_R, b_S, b_I, b_R)$, where (a_R, b_R) describe the behaviour of a recovered node (see Figure 4.1). In the activity-attractiveness-based mean-field approach the epidemic is described by the probabilities $P_{a_S,a_I,a_R,b_S,b_I,b_R}(t)$ and $R_{a_S,a_I,a_R,b_S,b_I,b_R}(t)$ that a node in class $(a_S, a_I, a_R, b_S, b_I, b_R)$ is respectively infected or recovered at time t. The average activity and attractiveness at time t are:

$$\begin{aligned}\langle a(t)\rangle &= \int \prod_{X=S,I,R} da_X db_X \rho_{SIR} \{a_S[1 - P(t) - R(t)] + a_I P(t) + a_R R(t)\} \\ &= \overline{a_S} + \overline{a_I P}(t) + \overline{a_R R}(t) - \overline{a_S P}(t) - \overline{a_S R}(t),\end{aligned} \tag{4.28}$$

$$\begin{aligned}\langle b(t)\rangle &= \int \prod_{X=S,I,R} da_X db_X \rho_{SIR} \{b_S[1 - P(t) - R(t)] + b_I P(t) + b_R R(t)\} \\ &= \overline{b_S} + \overline{b_I P}(t) + \overline{b_R R}(t) - \overline{b_S P}(t) - \overline{b_S R}(t),\end{aligned} \tag{4.29}$$

where for simplicity we do not indicate the dependence on $(a_S, a_I, a_R, b_S, b_I, b_R)$ in the integrals and we define $\overline{f}(t) = \int \prod_{X=S,I,R} da_X db_X \rho_{SIR} f_{a_S,a_I,a_R,b_S,b_I,b_R}(t)$. Moreover, also in this case it is possible to distinguish an active and an inactive implementation of adaptive behaviours, by respectively considering $\alpha = \langle b(t)\rangle = \overline{b_S} + \overline{b_I P}(t) + \overline{b_R R}(t) - \overline{b_S P}(t) - \overline{b_S R}(t)$ and $\alpha = \overline{b_S}$, as normalization factor for the probability $p_X = b_X/\alpha$ that a link is attracted by a node with attractiveness b_X.

Since the model is completely mean-field, with Markovian dynamics (i.e. there is no memory), the epidemic threshold of the SIR model and that of the SIS model are the same, regardless of (a_R, b_R) (see Chapter 2) [126, 128–130]. On the contrary, the epidemic active phase is different for the two model, since the SIR model lacks a stationary endemic state. In particular, it is not possible to investigate the SIR active phase similarly to the SIS model, but it is necessary to perform numerical simulations to obtain insights in the epidemic dynamics. In particular, we are interested

in the epidemic final size $R_\infty = \lim_{t\to\infty} \overline{R}(t)$ and in the temporal dynamics of the epidemic $\overline{P}(t)$.

The recovered (a_R, b_R) behaviour does not affect the epidemic threshold, but modifies the network topology, the network dynamics and the active phase of the epidemic. The activations of the recovered nodes do not generate contagious links, thus do not influence the epidemic dynamics, but their attractiveness modifies the epidemic dynamics by intervening on the formation of contagious links. Indeed, if the recovered nodes attract links the probability of potentially contagious links is reduced, since they attract part of the activity generating non-contagious links, which otherwise would be potentially contagious.

The dynamics of the network and of the epidemic can be numerically simulated by means of a Gillespie-like algorithm [85, 176]. We consider a network of N nodes and each node is initially assigned with six parameters $(a_S, a_I, a_R, b_S, b_I, b_R)$ extracted from the joint distribution $\rho_{SIR}(a_S, a_I, a_R, b_S, b_I, b_R)$. Initially the network evolve in the absorbing state (i.e. all nodes susceptible) in which the pathogen does not spread:

1. At time $t = 0$ each node i is assigned with its activation time extracted from the distribution $\Psi_{a_S^i}(t_i) = a_S^i e^{-a_S^i t_i}$;

2. The time is set at the minimum activation time $t = t_i$: the node i with the minimum activation time t_i is activated and generates m links with m nodes randomly selected with probability proportional to their attractiveness b_S^j;

3. The new activation time $t_i + \tau$ of node i is obtained by drawing the inter-event time τ from the inter-event times distribution $\Psi_{a_S^i}(\tau) = a_S^i e^{-a_S^i \tau}$;

4. All the links are destroyed and the process is iterated from point 2 up to the relaxation time t_0, in which the dynamics of the network is relaxed to equilibrium (i.e. no more aging effects are present).

At this point the epidemic dynamic is implemented:

1. At time $t = t_0$ each node is assigned with an activation time t_i, resulting from the relaxation dynamics, and the system is then initialized in a configuration of susceptible, infected and recovered.

2. The minimum activation time t_i is considered. Nodes infected at time t heal at time t_i with probability $\left[1 - e^{-\mu(t_i - t)}\right]$ and change their activity and attractiveness $(a_I, b_I) \to (a_R, b_R)$. The time is then set at the minimum activation time $t = t_i$ and the node i with the minimum activation time t_i is activated;

3. For the active implementation of the adaptive behaviour, the active node i generates exactly m links with m randomly selected nodes, with probability proportional to their attractiveness b_j.

   For the inactive implementation of the adaptive behaviour, each of the m links activated by node i is inactive with probability $Q = (\overline{b_S} - \langle b(t)\rangle)/\overline{b_S}$. The remaining links are created with randomly selected nodes, with probability proportional to their attractiveness b_j.

4. If the nodes involved in an active link are one susceptible and one infected, an infection occurs with probability λ and in this case the infected node changes its behaviour $(a_S, b_S) \to (a_I, b_I)$;

5. The new activation time $t_i + \tau$ of node i is obtained by drawing the inter-event time τ from the inter-event times distribution $\Psi_{a_k^i}(\tau) = a_k^i e^{-a_k^i \tau}$, where $k = S, I, R$ denotes the dynamic status of node i at time t_i. All links are destroyed and the process is iterated from step 2 until the system reaches the configuration without infected individuals.

4.2 Active and inactive quarantine

During the early stages of the COVID-19 pandemic, extraordinary and unprecedented containment measures were implemented aiming to contain the spread of SARS-CoV-2 [20, 177–181]. These measures initially included severe mobility restrictions and then extended lockdowns, in order to massively reduce the social activity of individuals, avoiding potentially contagious contacts and stopping community-wide spreading. It is crucial to determine the effects and the relevance of these massive isolation and quarantine measures implemented, also through simplified models that allow to include analytically the relevant aspects of the dynamics.

Recent real case studies show that the restrictions introduced with *quarantine* can be implemented in an *active* way, in which interactions with quarantining nodes are effectively rewired towards non-quarantining ones [145, 182] (e.g. in the early phases of COVID-19 in Italy during the first *"red zones"* or with patients admission to hospitals), and in an *inactive* way, in which contacts towards quarantining nodes are inactive and ineffective [20, 145, 183] (e.g. during the strict COVID-19 lockdowns and strict restrictions to the mobility). Our model allows naturally to distinguish between active and inactive quarantine (see Section 4.1.1 and Figure 4.2).

4.2.1 Effects on the epidemic threshold and the SIS epidemic prevalence

We consider the SIS epidemic model on the proposed adaptive activity-driven network, in the presence of *quarantine*: a fraction δ of the nodes when infected perform quarantine, setting their activity and attractiveness to zero $(a_I, b_I) = (0, 0)$, while the remaining nodes behave as if they were susceptible $(a_I, b_I) = (a_S, b_S)$. The parameter δ takes into account that some nodes are unaware of the infection (e.g. asymptomatic) or do not follow public prescriptions. This behaviour is described by the joint distribution $\rho(a_S, a_I, b_S, b_I) = \rho_S(a_S)\delta(b_S - ca_S)[\delta \cdot \delta(a_I)\delta(b_I) + (1-\delta)\delta(a_I - a_S)\delta(b_I - b_S)]$, assuming a linear correlation $b_S = ca_S$, with c constant value.

Both in the presence of active and inactive quarantine, the epidemic threshold is:

$$r_C^{quarantine} = \frac{\lambda}{\mu}\bigg|_C = \frac{1}{1-\delta}\frac{\overline{a_S}}{2\overline{a_S^2}} = \frac{r_C^{NAdwA}}{1-\delta}. \tag{4.30}$$

obtained by Eq. (4.24) replacing the specific distribution $\rho(a_S, a_I, b_S, b_I)$. The epidemic threshold is increased by the quarantine, compared to the non-adaptive case r_C^{NAdwA}, by a factor $(1-\delta)^{-1}$ which is extremely relevant for $\delta \sim 1$.

Similarly, substituting the specific $\rho(a_S, a_I, b_S, b_I)$ in Eqs. (4.26) and (4.27) it is possible to obtain the stationary asymptotic probability $P^{\infty}_{a_S,a_I,b_S,b_I}(t)$ that a node in class (a_S, a_I, b_S, b_I) is infected at time t. In the active case we obtain:

$$P^{\infty}_{a_S,a_I,b_S,b_I} = \frac{2a_S\overline{a_S P}}{\frac{\mu}{\lambda}\left(\frac{\overline{a_S} - \overline{a_S P}}{1-\delta} + \overline{a_S P}\right) + 2a_S\overline{a_S P}}, \tag{4.31}$$

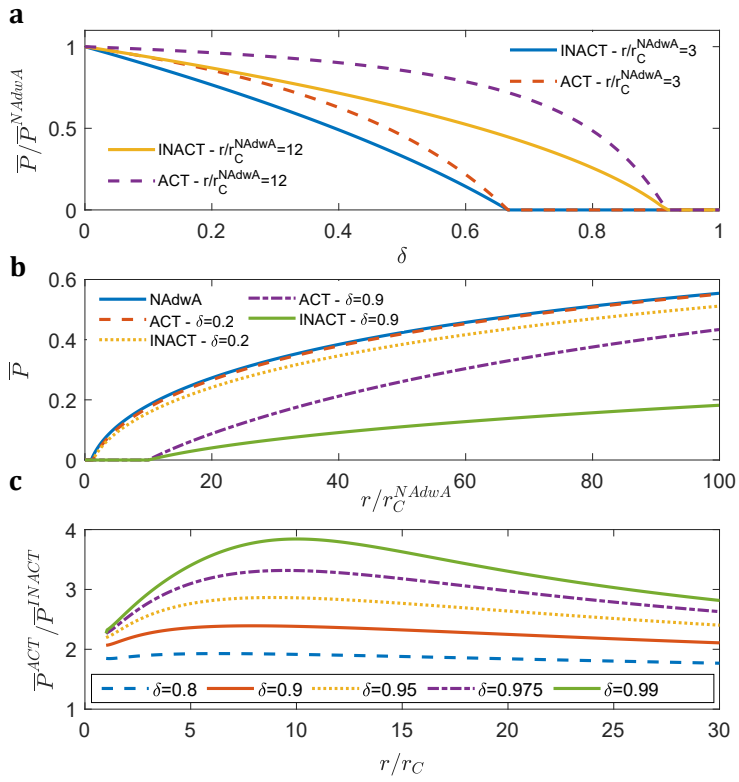

FIGURE 4.3: **Effects of quarantine on the SIS epidemic prevalence.** In panel **a** the ratio $\overline{P}/\overline{P}^{NAdwA}$ between epidemic prevalence in the presence of quarantine and in the non-adaptive case (NAdwA), is plotted as a function of δ for both the active and the inactive case, with fixed $r/r_C^{NAdwA} = [3, 12]$. In panel **b** we plotted the epidemic prevalence $\overline{P}$ as a function of the control parameter r/r_C^{NAdwA}, in the non-adaptive case (NAdwA) and in the presence of quarantine (both in the active and inactive case), fixing $\delta = [0.2, 0.9]$. In panel **c** the ratio $\overline{P}^{ACT}/\overline{P}^{INACT}$, between epidemic prevalence for active and inactive quarantine, is plotted as a function of r/r_C (where r_C is the epidemic threshold in the adaptive case) for different values of δ. In all panels $\rho_S(a_S) \sim a_S^{-(\nu+1)}$, $\nu = 0.5$ and $a \in [10^{-3}, 1]$. Reproduced from [14].

while in the inactive case it is obtained;

$$P^{\infty}_{a_S,a_I,b_S,b_I} = \frac{2a_S\overline{a_S P}}{\frac{\mu}{\lambda}\frac{\overline{a_S}}{1-\delta} + 2a_S\overline{a_S P}}. \tag{4.32}$$

Eqs. (4.31) and (4.32) can be solved self-consistently after fixing the $\rho_S(a_S)$, thus obtaining the epidemic prevalence $\overline{P}$ by averaging $P^{\infty}_{a_S,a_I,b_S,b_I}$ on the activity-attractiveness classes. Many real systems of human interactions feature a heterogeneous distribution of activity (and attractiveness), typically power-law $\rho(a_S) \sim a_S^{-(\nu+1)}$ with exponent $\nu \sim 0.3 - 1.5$ (see Section 1.6 and Section 1.6.1) [13]: hereafter we consider $\rho_S(a_S) \sim a_S^{-(\nu+1)}$, with $\nu = 0.5$ and $a_S \in [a_m, a_M]$, lower and upper cut-off.

Both active and inactive quarantine produce a significant reduction in the epidemic prevalence, i.e. in the endemicity of the epidemic, weakening the epidemic and its transmission. This is shown in Figure 4.3 **a**, where we plot the ratio between epidemic prevalence in the presence of quarantine $\overline{P}$ and in the absence of adaptive measures $\overline{P}^{NAdwA}$ (i.e. for $\delta = 0$) as a function of δ and for fixed $r = \lambda/\mu$. The reduction is significant (at least by a factor of 2) for $\delta \gtrsim 0.5$: by increasing δ the epidemic

prevalence is reduced until it vanishes for $\delta \geq \delta_C$, where $\delta_C = 1 - r_C^{NAdwA}/r$ is the critical value of δ above which the system is moved under the threshold for the specific r fixed, i.e. producing $R = 1$ for the specific $R_0 = r/r_C^{NAdwA}$ fixed since r_C^{NAdwA} is fixed by $\rho_S(a_S)$ (see Eq. (4.25)). This is also shown in the phase diagram of Figure 4.3 **b** where the epidemic prevalence $\overline{P}$ (order parameter) is plotted as a function of r/r_C^{NADdwA} (control parameter) for $\delta = 0.2$ and for $\delta = 0.9$: quarantine reduces the epidemic prevalence for δ sufficiently high, while for small δ the differences are quite small.

Figure 4.3 **a**-**b** shows that the epidemic threshold for the active and inactive quarantine is the same, while the epidemic prevalence of the inactive case is much lower than that of the active case, for the same r/r_C^{NAdwA} and δ. To obtain the same effect on epidemic prevalence with active quarantine, for fixed r/r_C^{NADdwA}, it is necessary to significantly increase δ, i.e. the intensity of the measure. This is summarized in Figure 4.3 **c**, where the ratio between epidemic prevalence in the active and inactive case $\overline{P}^{ACT}/\overline{P}^{INACT}$ is plotted as a function of r/r_C: the ratio is always larger than 1, suggesting the higher effectiveness of the inactive approach. Furthermore, the difference between the two approaches is maximized for $r/r_C \sim 5 - 10$ and is increased by incrementing δ. Under realistic conditions of strong quarantine measures, i.e. $\delta \sim 1$, we expect interventions to move the system under or close to the critical point, i.e. $r/r_C \sim 1$: even in that regime the differences are significant, with $\overline{P}^{ACT}$ being about twice $\overline{P}^{INACT}$.

This difference is due to the basic mechanisms of the two types of quarantine (see Figure 4.2). In the inactive quarantine the links directed towards quarantined nodes are ineffective and therefore cannot transmit the contagion; in the active quarantine the effective link rewiring produces potentially contagious links and a cluster of highly connected non-quarantining nodes. Furthermore the rewiring takes place preferentially towards the nodes with high attractiveness, which have a high probability of being infected and a high spreading capacity. Thus, the rewiring mechanism maintain high the activity level of non-quarantining node but also favour the epidemic spreading compared to the inactive case, producing potentially contagious links which are absent in the inactive implementation with an activity reduction.

4.2.2 Effects on the SIR active phase: the role of interventions timing

We now consider the SIR model, assuming that a recovered individual behaves as susceptible $(a_R, b_R) = (a_S, b_S)$, and we implement the quarantine with the joint distribution $\rho_{SIR}(a_S, a_I, a_R, b_S, b_I, b_R) = \rho_S(a_S)\delta(b_S - ca_S)\delta(a_R - a_S)\delta(b_R - b_S)[\delta \cdot \delta(a_I)\delta(b_I) + (1-\delta)\delta(a_I - a_S)\delta(b_I - b_S)]$. As discussed in Section 4.1.3, the epidemic threshold for the SIR epidemic model is the same of the SIS model of Eq. (4.30), while the SIR epidemic active phase can be investigated by means of numerical simulations.

We performed numerical simulations on a network of N nodes, following the algorithm presented in Section 4.1.3: the initial conditions are imposed by infecting the node with highest a_I [184] and the quarantine measures are immediately implemented. We considered $\delta = 0.7 - 1$ in accordance with the extended and massive quarantine measures implemented during the early stages of COVID-19 spreading [20, 177–181]; moreover we assume that $r/r_C \sim 1$, i.e. that the measures implemented are strong enough to move the system near the critical point.

Both active and inactive quarantine significantly reduce the epidemic final size R_∞ compared to the case without interventions: this is shown in Figure 4.4 **a** where R_∞ is plotted as a function of r/r_C. Furthermore, they also impact on the temporal dynamics of the epidemic: in Figure 4.4 **b** we show the temporal evolution of the

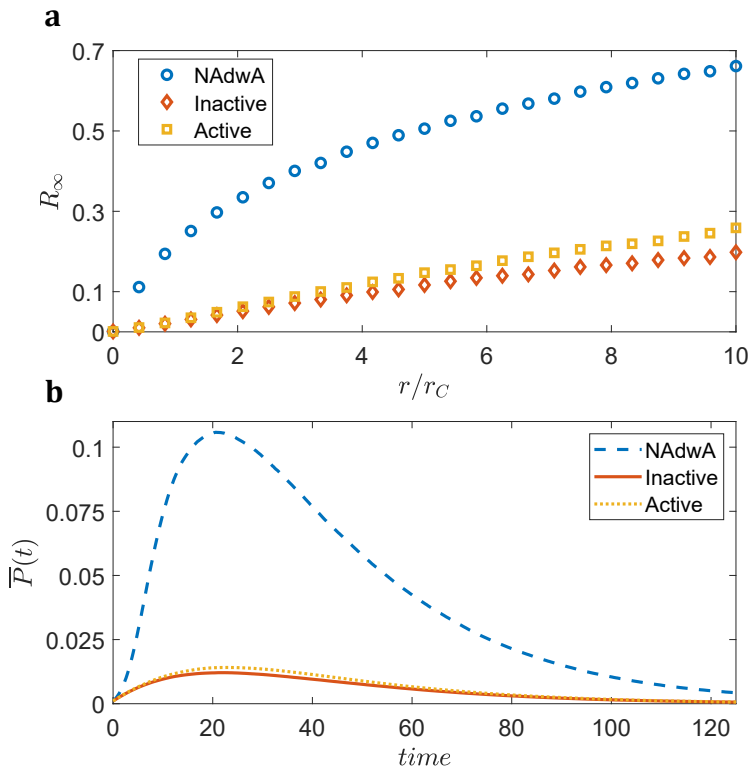

FIGURE 4.4: **Effects of quarantine on the SIR epidemic final size and temporal dynamics.** In panel **a** the epidemic final size R_∞ for the non-adaptive case (NAdwA) and for both the active and inactive quarantine is plotted as a function of r/r_C (where r_C is the epidemic threshold in the adaptive case). In panel **b** we plotted the temporal dynamics of the average probability $\overline{P}(t)$ for a node to be infected for the non-adaptive case (NAdwA) and in the presence of active and inactive quarantine, by fixing $r/r_C = 1.4$. In all panels $\delta = 0.9$, $N = 10^3$, $\rho_S(a_S) \sim a_S^{-(\nu+1)}$, $\nu = 0.5$ and $a \in [10^{-3}, 1]$; moreover, each point or curve is obtained by averaging over several realizations of the temporal dynamics and of the disorder so that the error on R_∞ is lower than 1%. Reproduced from [14].

average probability for a node to be infected $\overline{P}(t)$ for fixed r/r_C and δ. The infection curve is considerably flattened by the quarantine: the infection peak is considerably reduced and slightly anticipated, compared to the non-adaptive case, moreover the duration of the epidemic, i.e. the width of the peak, is also reduced. This suggests that the implemented quarantine is a strong control measures since the curve decay is anticipated: the quarantine reduces the propagation of the pathogen by immediately blocking the spread of the epidemic.

Also in the SIR model the inactive quarantine is more effective than the active one in limiting the effects of the epidemic. This is shown in Figure 4.4: the active quarantine produce an epidemic final size and an infection peak about 10%-20% larger than the inactive ones, in the $r/r_C \sim 1$ significant regime. However the differences are smaller when compared with the SIS model. Indeed, in the SIS model the recovered nodes are again susceptible and the rewiring favours the formation of potentially contagious SI links between non-quarantining nodes; in the SIR model the recovered nodes are immunized, thus the rewiring redirects links also towards them but these links are not contagious. The danger of the rewiring is mitigated by the attractiveness of recovered nodes, making the two implementations more similar.

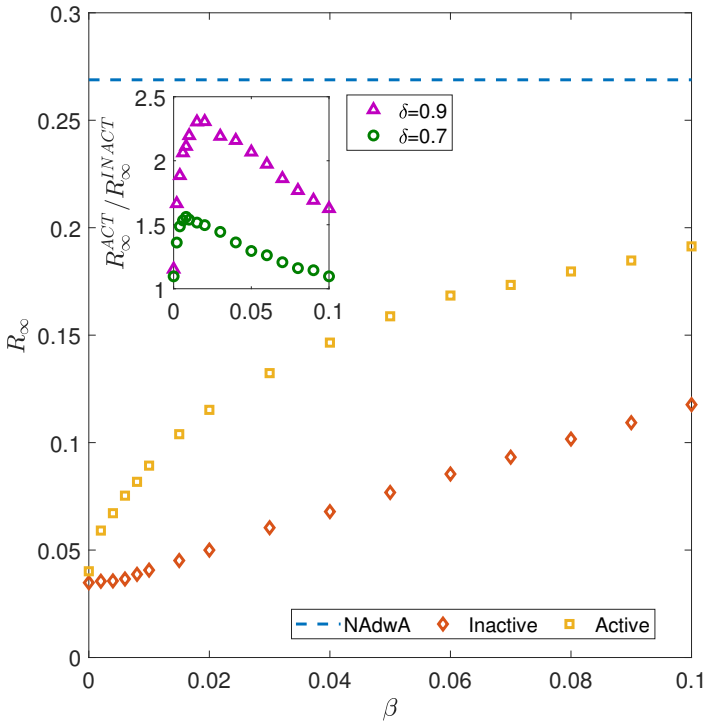

FIGURE 4.5: **Effects of timing in quarantine measures on the SIR epidemic final size.** In panel **a** we plot the epidemic final size R_∞ as a function of the fraction β of nodes been infected before the implementation of the quarantine, both in the active and inactive case for fixed $\delta = 0.9$. The dashed line indicates the value of R_∞ for the non-adaptive case (NAdwA). In the inset the ratio $R_\infty^{ACT}/R_\infty^{INACT}$ between the epidemic final size in the case of active and inactive quarantine is plotted as a function of β for different values of δ. Both in the main and in the inset $r/r_C = 1.4$ (where r_C is the epidemic threshold in the adaptive case), $N = 10^3$, $\rho_S(a_S) \sim a_S^{-(\nu+1)}$, $\nu = 0.5$ and $a \in [10^{-3}, 1]$; moreover, each point or curve is obtained by averaging over several realizations of the temporal dynamics and of the disorder so that the error on R_∞ is lower than 1%. Reproduced from [14].

However, containment measures are often implemented only after a fraction β of the population has been infected, due to delays in detection of the epidemic and due to specific threshold effects that activate the epidemic control [145, 181, 185, 186]: thus it is crucial to understand the role of interventions timing. This is relevant for the SIR epidemic model, whose dynamics strongly depends on the initial conditions, unlike the SIS model. We consider numerical simulations in which the system initially evolves in the non-adaptive configuration until a fraction β of the population has been infected, then the quarantine measures are applied and are kept active until the end of the epidemic.

The results of the simulations show the importance of a timely adoption of measures in the early stages of the outbreak. We show in Figure 4.5 that for both active and inactive quarantine the epidemic final size R_∞ grows strongly with β: this suggests that a delay in the intervention allows the pathogen to infect a significantly higher number of individuals. Furthermore, the delay also has a strong impact on the temporal dynamics of the epidemic as shown in Figure 4.6: increasing the delay β both quarantine implementations become less effective in flattening the epidemic curve, indeed the infection peak $\overline{P}_{max}$ is higher and also the duration of the epidemic is increased, with potential problems for the health system since the incidence is higher both at long at short times (see Figure 4.6 **a**-**b** and Figure 4.4 **b**).

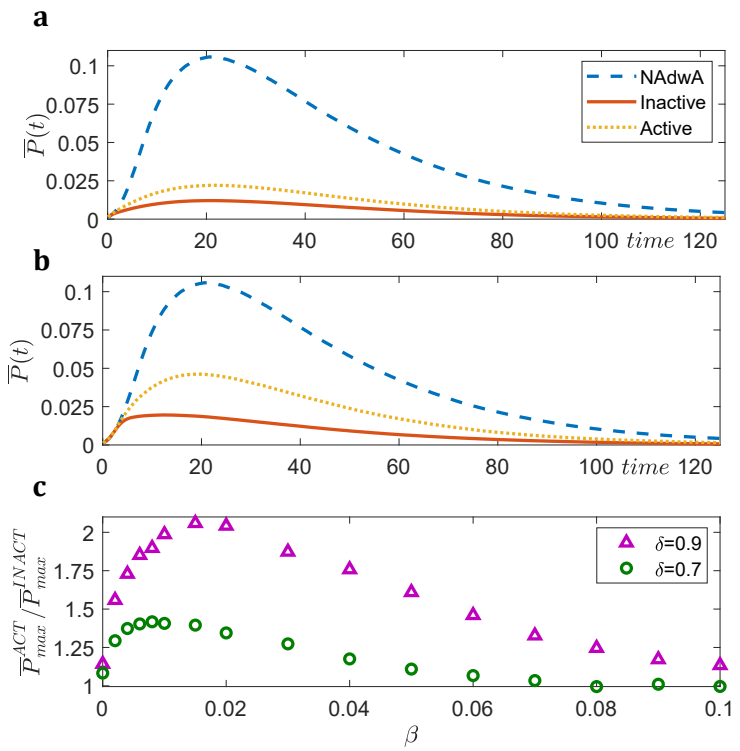

FIGURE 4.6: **Effects of timing in quarantine measures on the SIR temporal dynamics.** In panel **a** and **b** the temporal evolution of the average probability $\overline{P}(t)$ for a node to be infected is plotted, for the non-adaptive case (NAdwA) and for active and inactive quarantine, by fixing $\delta = 0.9$ and $\beta = 0.0025$ in panel **a** and $\beta = 0.02$ in panel **b**. In panel **c** we plot the ratio $\overline{P}^{ACT}_{max}/\overline{P}^{INACT}_{max}$ between the height of the infection peak in the active and inactive quarantine as a function of the fraction β of individuals been infected before the quarantine measures were implemented, for different δ. In all panels $r/r_C = 1.4$ (where r_C is the epidemic threshold in the adaptive case), $N = 10^3$, $\rho_S(a_S) \sim a_S^{-(\nu+1)}$, $\nu = 0.5$ and $a \in [10^{-3}, 1]$; moreover, each point or curve is obtained by averaging over several realizations of the temporal dynamics and of the disorder so that the error on R_∞ is lower than 1%. Reproduced from [14].

In the presence of a delay β in the adoption of quarantine, the differences between the active and inactive quarantine are considerably amplified: in the inactive case $R^{INACT}_\infty(\beta) \sim R^{INACT}_\infty(\beta = 0) + \beta$ grows with β approximately linearly, while in the active case R^{ACT}_∞ grows much faster with β widening the differences with the inactive quarantine. This is shown in the inset of Figure 4.5 where the ratio $R^{ACT}_\infty/R^{INACT}_\infty$ is plotted as a function of β for fixed r/r_C: the difference is about 10% if the quarantine is immediately active $\beta = 0$, while it grows considerably up to $R^{ACT}_\infty/R^{INACT}_\infty \sim 2.5$ when the measures are activated after 2% of the population has been infected. Similarly, the differences on the temporal dynamics are amplified with β: if the quarantine measures are applied immediately the infection peak in the active case is approximately 10% higher than the inactive one, while if measures are adopted after 0.25%-4% of the population has been infected, the peak height in the active case is twice that of the inactive quarantine. This is shown in Figure 4.6 **c** where the ratio $\overline{P}^{ACT}_{max}/\overline{P}^{INACT}_{max}$ between the height of the infection peak in the active and inactive case is plotted as a function of β for r/r_C and δ fixed.

In the presence of delays the measures are implemented when many infected individuals are already present in the population: the inactive quarantine is therefore much more effective than the active one, since the dynamic rewiring has an increased

probability of producing contagious links, thus amplifying the differences between the two implementations. The differences, however, feature a non-monotonous trend with the delay β, as shown in the inset of Figure 4.5 and in Figure 4.6 **c**: indeed for very high β the measures are implemented very late, when the system is already at the peak of infection of the non-adaptive case (or close to it), therefore both quarantine strategies are very ineffective since the epidemic has already reached the descending phase.

These results suggest that the timing in the implementation of control measures is crucial for the good success of the containment [185, 186]: if the quarantine is implemented immediately a reduction of 75%-85% of the infection peak and of the epidemic final size can be achieved (depending on δ). Any delay in adoption significantly reduces the effectiveness of both strategies, but also amplifies the differences, reducing the effectiveness of the active strategy more markedly than the inactive one. If the control measures are not immediately implemented, it is necessary to adopt a more stringent inactive quarantine to produce significant effects on the epidemic spread, thus also affecting the activity of the rest of the population and in particular of susceptible and non-quarantining nodes. If the measures are implemented immediately, the differences are small between the two strategies, so it is also possible to obtain effective containment also through active quarantine, which guarantees susceptible and non-quarantining nodes to maintain their level of activity. This is crucial when a cost-benefit analysis is performed before the implementation of any control strategy.

We developed a general model of adaptive activity-driven network coupled to an epidemic, keeping track of the true dynamics of the two processes and modelling a wide spectrum of adaptive behaviours [14]. We show the crucial role of adaptive behaviours and their implementation (active vs. inactive) on the epidemic spreading, through a full characterization of the spreading process. In particular, our model points out the key role of the correlations between the susceptible and infected behaviour and the crucial role of super-spreaders in the spread of the epidemic. Moreover, in the framework of the control measures implemented in the early-stages of the COVID-19 pandemic [20, 145, 177–183], we model active and inactive quarantine through the proposed model, showing that the inactive quarantine is much more effective than the active one in reducing the impact of the epidemic, due to the dynamic rewiring mechanism. The differences are amplified by delays in interventions adoption, showing the key role of interventions timing.

Chapter 5

Manual and digital contact tracing

In this Chapter we describe the results of Ref. [28]: we present *contact tracing* (CT) as a control measure and, within the adaptive activity-driven framework, we implement the *manual tracing* (interview-based) and the *digital tracing* (app-based) protocols. We compare their effectiveness in reducing the impact of an epidemic tailored to describe SARS-CoV-2, in the presence of heterogeneity in the individuals behaviour, i.e. of *superspreaders*. We implement a *hybrid tracing* protocol, suggesting directions for the integration of the two tracing mechanisms.

5.1 Contact tracing (CT)

The COVID-19 pandemic had an unprecedented impact on everyday life globally. Controlling and containing the spread of SARS-CoV-2 become a constant goal to safeguard public health, keeping low the hospital occupancy, avoiding costs in terms of direct and indirect deaths, long-term health problems and the socio-economic consequences of sustained transmission of the pathogen [18, 190]. In the early stages of the epidemic massive measures were undertaken in many states, based on strong limitations to mobility, the closure of not strictly necessary activities and generalized lockdowns [20, 174, 177–181]. These measures, as discussed in Chapters 3-4, were extremely effective in stopping the transmission of SARS-CoV-2 by easing hospital pressure and the number of correlated deaths [15, 181, 191] but at the cost of strong socio-economic repercussions, making these measures difficult to be replicated in the same intensity [17, 18, 192]. With the improvement of the epidemiological situation, the restrictive measures have been progressively relaxed through exit strategies based on new non-pharmaceutical control tools that allow to keep the spread of SARS-CoV-2 under control and the population active [16, 143, 174, 193, 194]. These exit strategies are based on the integration of measures on the individual and environmental level (such as the use of protective equipment, e.g. face masks, reinforced hygiene and physical distancing) and active surveillance to break the chains of infection. The active surveillance is based on the periodic testing of individuals at risk, the isolation of infected individuals (symptomatic or identified with testing), the tracing of the contacts of infected individuals (index cases), their testing and isolation. The contact tracing plays an essential role in the control of COVID-19 due to the high fraction of presymptomatic and asymptomatic transmissions observed from the early stages of the pandemic [20, 24, 187, 195–197].

Contact tracing, unlike generalized restrictions such as lockdown, act locally in a targeted way. The tracing is activated starting from an infected individual, identified through a diagnostic test: the infected individual becomes index case and all their potentially contagious contacts are identified (traced), tested and isolated or quarantined [21, 188, 198–202]. This procedure allows to identify individuals infected by

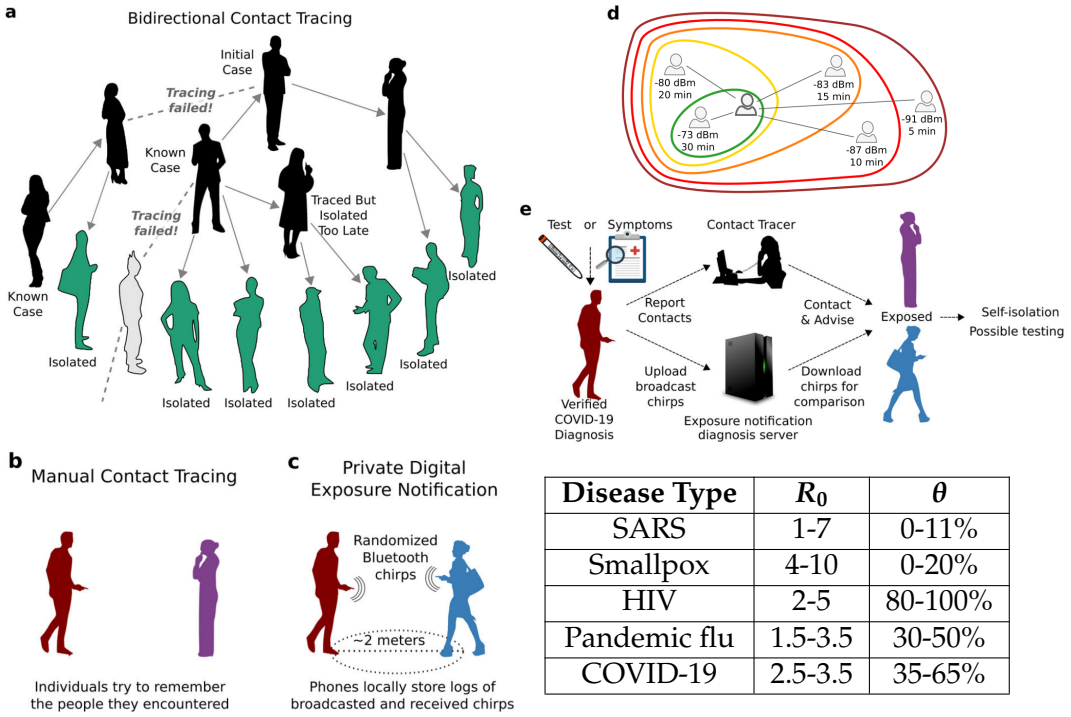

Disease Type	R_0	θ
SARS	1-7	0-11%
Smallpox	4-10	0-20%
HIV	2-5	80-100%
Pandemic flu	1.5-3.5	30-50%
COVID-19	2.5-3.5	35-65%

FIGURE 5.1 & TABLE 5.1: **Contact tracing (CT).** In panel **a** a schematic representation of contact tracing is shown. Panels **b-c** schematically show the basic mechanisms of manual and digital CT. In app-based CT a score parameter classifies the risk for contacts according to the contact duration and distance, measured in terms of Bluetooth signal intensity reduction (see panel **d**). Panel **e** shows the complete tracing procedure, up to notification. In the table we report the estimated ranges for R_0 and θ of some infectious diseases [21, 99, 187]. Panels **a**,**b**,**c** and **e** are adapted from [188], while panel **d** is adapted from [189], both under CC BY 4.0 license.

the index case (forward CT - see Chapter 6) or the source of infection for the index case (backward CT - see Chapter 6) [188, 202], even if presymptomatic or asymptomatic. The transmission chains are broken, reducing the spread of the epidemic, without excessively deteriorating the activity of the population.

The contact tracing effectiveness depend on many technical aspects of the CT implementation [198, 199]: *the tracing protocol,* that is the specific mechanism for reconstructing the contacts (e.g. traditional manual tracing (interview-based) or digital tracing (app-based)); *the definition of epidemiologically relevant contacts*, which depends on the type of infectious disease considered and is based on the proximity, on the duration and frequency of a contact; *the tracing capacity,* which depends on the probability to activate CT for the index case, the capacity to trace all the potentially contagious contacts and the probability for the contacts to adhere to tracing and isolation; *the timing in tracing and isolation.*

Moreover, the efficacy of contact tracing depends on the specific epidemiological properties of the infectious disease [21], encoded in two parameters: the fraction of presymptomatic or asymptomatic transmissions θ; the inherent transmissibility of the pathogen, measured with the basic reproduction number R_0. The parameter θ depends only on the infectious disease and on the timing of the infectious peak compared to the onset of symptoms. Homogeneous mixing models show that for infectious diseases with $\theta < 1/R_0$ it is enough to isolate symptomatic individuals

to obtain control of the epidemic, while if $\theta > 1/R_0$ the contact tracing must necessarily be implemented to achieve epidemic containment [21]. Furthermore, for very high values of θ or R_0 even the contact tracing combined with the isolation of the symptomatic is not sufficient to contain the outbreak. This suggests that θ and R_0 must be considered when estimating the risk posed by an emerging disease: infectious diseases with moderate (θ, R_0) are easily controlled with CT, while those with high (θ, R_0) are hardly. For example, as shown in Table 5.1, SARS and Smallpox are effectively controllable with CT; on the contrary, pandemic influenza and HIV are not controllable only with these techniques: in this case it is necessary to combine these measures with additional control measures, such as physical distancing, the use of protective devices or restrictions on social activity. These additional measures reduce R_0, thus moving the system in the range of parameters (θ, R_0) in which the CT is sufficient to contain the epidemic [21].

5.1.1 CT models

The contact tracing is an adaptive mechanism of the population that can be implemented through the adaptive temporal networks described in Chapter 3: the tracing can be seen as a superinfection process that follows the paths of primary infection and removes infected individuals from the interaction dynamics. It is a process of exploration and sampling of contacts activated in the past and is dynamically activated by the epidemic, thus CT deeply couples the dynamics of the network and the epidemic dynamics. Moreover, the tracing occurs on time scales comparable with those of the epidemic dynamics and the interactions dynamics, indeed it is dynamically activated by infections and takes place precisely along the history of contacts: it is not possible to neglect the coupling and their temporal dimension through a timescales separation approximation. This introduces highly non-trivial and challenging difficulties as three dynamic processes are active and deeply coupled.

Many models for contact tracing have been proposed [198]. Some models implement CT in *individual (or agent) based models*, by considering explicitly a static (empirical or synthetic) network of contacts and implementing CT numerically through stochastic simulations. To obtain general insights on the tracing process in an analytical way, *deterministic mean-field models* have been developed, based on mean-field approaches which allow to obtain a deep understanding of the tracing mechanism on static networks: for example, unveiling the role of clustering and targeted CT strategy [203, 204]. Finally, in order to quantitatively estimate the impact of CT in real conditions, *phenomenological approaches* have been proposed, in which the effect of CT is simply introduced at the macroscopic scale through phenomenological terms into the epidemic dynamic equations.

These models, with different levels of approximations, underline the crucial role of the network of interactions and of the basic CT mechanisms: however very few CT models really take into account the coupling between the three dynamics, the temporal dimension and the detailed CT mechanisms.

5.1.2 Traditional CT

Traditionally, the contact tracing has been performed in its *manual implementation (interview-based CT)*. The tracing is performed by trained healthcare personnel, the contact tracers, through interviews of infected individuals: index cases are asked to provide a list of contacts they had in a specific time window. Contacts are classified as epidemiologically relevant according to a specific definition depending on

proximity, duration and frequency of the contact. The tracers collect the information, then contact individuals who may have been infected, prepare a test for them, and finally proceed with the isolation of the infected (see Figure 5.1). This requires an impressive infrastructure with personnel, tools and resources, with a significant economic cost.

COVID-19 pandemic shows that the adherence to the tracing is fundamental [205]: in November 2020 in England the tracers were unable to reach 1/8 of the positive cases and of the cases reached 18% did not provide information on close contacts, in the United States this fraction increased to over 50%. Furthermore, some of the contacts listed may not be reachable by the tracer or may not comply with the requirements. In total, it is estimated that in the UK tracing reached on average the 50% of close contacts during 2020 [205].

In the presence of a low incidence and prevalence, manual tracing is implemented relatively easily, without long delays or resources problems; on the other hand, tracing becomes almost impossible to apply for high incidence and prevalence, since the number of index cases and related contacts to be traced grows introducing delays and the impossibility of tracing all relevant contacts (scalability) [22, 198, 206]. Therefore, manual tracing is effective and applicable in low diffusion regimes: in the early stages of an epidemic or concurrently with the relaxation of highly restrictive measures (e.g. the lockdown) that moved the system into an epidemic regressive phase. Otherwise, it can be implemented effectively in combination with other containment measures which reduce the activity of the population, thus reducing the average number of contacts per individual [205]. This limitation in manual CT applicability is called *global limited scalability*.

Another crucial aspect in the effectiveness of manual tracing is the timing in the tracing activation, in the identification and notification of the contacts and in their isolation, since delays in the various phases of the protocol could make it ineffective [22, 24, 26, 198, 207]. This could be dramatically problematic for a disease such as COVID-19 with a high fraction of asymptomatic and presymptomatic transmissions [22, 206]: the World Health Organization defines a tracing protocol effective for COVID-19 if it is able to trace the 80% of close contacts within 3 days of the positive index case [205].

5.1.3 CT reinforcement: the digital CT

The traditional CT mechanism has been applied effectively in the past to contain various infectious diseases [206, 208–210]. An impressive and effective tracing system was developed to contain the 2002-2004 SARS epidemic [206, 210]; similarly, tracing was implemented for the containment of MERS in the 2012 and 2015 outbreaks [198]. However, recently several proposals have been put forward to reinforce tracing, overcoming the main problems of traditional CT.

The traditional tracing, from a network point of view, corresponds to trace only the first-nearest neighbours of the index case, however the approach can be extended with: the *recursive tracing*, in which infected neighbours of the index case become new index cases by activating the tracing on their contacts [205, 211, 212]; the *higher-order tracing*, in which the tracing does not stop only at first-nearest neighbours but also extends to the k-nearest neighbours [205]. These extensions are useful for pathogens with a high spreading capacity and when the index cases are identified late with respect to the infection, however they require the tracing of an enormous number of contacts for each index case, with respect to the traditional tracing, strongly limiting the applicability of the approaches. For example, in Vietnam a

recursive tracing up to the third order has been implemented for index cases identified late during the COVID-19 pandemic, obtaining a significant improvement in the tracing effectiveness: the average number of individuals traced for index case has been increased from 15 to about 200, with respect to the first-order approach [205].

In response to COVID-19 pandemic, health authorities implemented CT with different procedures and protocols, attempting to enhance and strengthen the traditional manual tracing through alternative protocols, based on digital tools (e.g. WiFi data, mobile phones data) [159, 205, 213]. For example, South Korea authorities use credit-card data, cell phones and closed-circuit cameras to trace the movements of infected individuals and identify their contacts, thanks to a system implemented during the 2015 MERS epidemic [205]; in Vietnam, data deriving from posts published on Facebook and Instagram are used to validate the list of contacts and movements reported by index cases [205].

In many countries a *digital CT (app-based CT)* protocol has been developed, based on the use of smartphones to trace automatically contacts: this is a new approach being first proposed in a semi-automatic protocol during the 2014-2016 Ebola outbreak [198]. This procedure is based on the use of a tracing application with which smartphones are able to keep trace of contacts with other devices endowed with the app, through the proximity sensors of smartphones [23, 159, 213–215] (e.g. Immuni in Italy [216], SwissCovid app in Switzerland [217], NHS COVID-19 app in UK [218], Corona-Warn-App in Germany [219]). This app broadcasts rotating pseudorandom "chirps" and records those emitted by nearby devices, via Bluetooth technology (see Figure 5.1): only epidemiologically significant contacts are recorded and notified, by assigning to each contact a score parameter. This parameter is obtained in a complex way considering the contact time, the frequency of the contact, the distance between the individuals involved in the contact (measured in terms of Bluetooth signal intensity reduction) and also the epidemiological property of the disease (see Figure 5.1). The index case loads the broadcast "chirps" through the app in server for exposure notifications: all the users download automatically and periodically the "chirps" for comparison of the recorded ones and in case of concurrence are notified (see Figure 5.1).

The digital CT is able to overcome some of the limitations of manual tracing [22, 23, 198, 206]: reducing the delays in identifying and reporting exposure via an automatic mechanism [24]; increasing the probability of tracing unknown contacts (e.g. sporadic contact on public transport); avoiding the limited scalability of manual tracing, through technological solutions that allow to obtain a arbitrarily scalable system [215].

Many works evaluated the impact of digital tracing and its performance, also in relation to manual tracing [24, 189, 207, 220–224]. A quantitative comparison of the two approaches shows that a 3-days delay in manual tracing prohibits the ability to control the spread of COVID-19, suggesting that only digital tracing can overcome this by reducing the delay [24]. However, this comparison is made only on the level of timing in tracing and isolation, without an in-depth comparison at the level of the real implementation of the two protocols.

Other works, raise doubts about the assumptions underlying digital tracing and its effectiveness, showing the main limitations of digital CT [23, 25–27]. Some works have attempted to evaluate the impact of digital CT through epidemiological data-driven models, on real networks of interactions [189, 224]: all have shown a crucial role of the adoption level f of the tracing app in the population, observing that any value of f helps in mitigating the epidemic but significant results are obtained only

for $f \sim 60\%$ [24, 26, 27, 201, 225]. These values are in contrast with the app adoption in most states, where in the most optimistic case $f \sim 30\%$ also due to mistrust linked to privacy [27, 226–228]. Moreover, f has strong upper limits determined by the penetration in the population of smartphones (that is about 64%-70% [25, 221, 225]) and by the penetration of smartphones with the technology needed for the tracing app functionality [229]. Moreover, surveys and population analysis indicate that, individuals adopting the app are those with more cautious behaviour and fewer contacts, i.e. individuals less at risk [230, 231]: this further reduces the effectiveness of digital CT, since the most dangerous individuals driving the epidemic, i.e. superspreaders with a high number of interactions, are invisible to CT.

Some drawbacks of digital CT are linked directly to its technical implementation[23, 25]: privacy issues strongly limit the flexibility of the model [214, 215], for example prohibiting recursive tracing or higher-order tracing; the Bluetooth technology is unreliable, especially for COVID-19 airborne transmission in which proximity is not the only indicator of risk; some systems require the infected user to request a code from health authorities to activate the notification system, this produces delays that can reduce the speed up of digital CT [205, 220].

Results on the use of digital CT show that it speeds up the exposure notification and the isolation of traced contacts by an average of 1-2 days compared to manual tracing (e.g. SwissCovid app and NHS COVID-19 app) [23, 205, 217, 218, 232]. Moreover, digital tracing in the UK had significant results [232], albeit with strong repercussions on the functionality of the population: indeed, the digital CT induced the so-called *"pingdemics"*, i.e. an epidemic of exposure notifications, which led to more than one million people in quarantine. This significantly deteriorate the population functionality: to remedy this, the quarantine period has been reduced in the UK and also the parameter for the definition of close contacts in the NHS COVID-19 app have been redefined [233–235]. From a technical point of view the digital CT do not present global limited scalability, however in a real implementation analogous effects emerge (e.g. "pingdemics").

In this framework, in the next Sections we propose a model to implement manual and digital contact tracing on the adaptive activity-driven network proposed in Chapter 4, determining their effectiveness in reducing the impact of an epidemic for the SARS-CoV-2 spreading [28]. Our work takes a different approach than previous works, overcoming some of their limitations: it takes into account the dynamics of the network, the epidemic dynamics and the tracing process and their coupling, considering their true time scales; moreover, it compares the different tracing protocols taking into account their specific properties and differences; it allows for a robust analytical analysis of the effect of the manual and digital CT protocol.

5.2 Epidemic model with asymptomatic infections on AD network

We consider an epidemic model describing the main clinical phases of SARS-CoV-2 [16, 179, 236], which is applicable to any infectious disease presenting asymptomatic and presymptomatic transmission [195–197]. The epidemic model is composed of five compartments: S susceptible, A infected asymptomatic, P infected presymptomatic, I infected symptomatic, and R recovered (see Figure 5.2) Susceptible individuals can be infected with probability λ when involved in a contact with an infected node (either A, P and I). An infected node has probability δ of following a

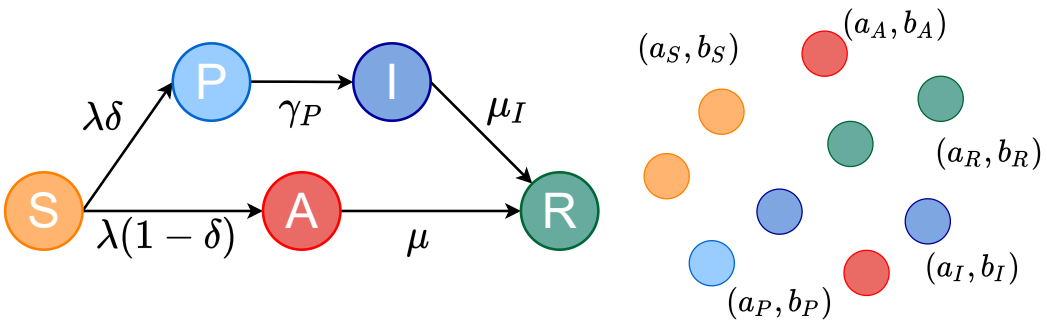

FIGURE 5.2: **Epidemic model without contact tracing.** We schematically represent the compartmental epidemic model without contact tracing and the corresponding adaptive activity-driven network, with different (a_X, b_X) depending on the health status of the node.

symptomatic route, becoming presymptomatic after infection $S \xrightarrow{\lambda\delta} P$, and a probability $(1-\delta)$ of following the asymptomatic route becoming infected asymptomatic $S \xrightarrow{\lambda(1-\delta)} A$. A presymptomatic individual spontaneously develops symptoms with rate γ_P becoming symptomatic: with a Poissonian process $P \xrightarrow{\gamma_P} I$ where $\gamma_P = 1/\tau_P$ and τ_P is the average duration of the presymptomatic phase. Asymptomatic and symptomatic nodes recover spontaneously respectively with rate $\mu = 1/\tau$ and $\mu_I = \mu\gamma_P/(\gamma_P - \mu)$, so that the average period of contagiousness is τ for both symptomatic and asymptomatic ones. The model neglects hospitalizations and deaths, which do not modify the dynamics of infection and do not modify the results on the effectiveness of the CT.

This epidemic model is implemented on the adaptive activity-driven network proposed in Chapter 4, thus taking into account both the heterogeneity in the behaviour of individuals and the temporal dynamics of the network [14]. The network is composed of N nodes and each node is assigned with five couples of parameters (a_X, b_X) with $X = \{S, A, P, I, R\}$ which define the activity and attractiveness of the node when it is in the compartment X. Each node features a Poissonian activation dynamics with activation rate a_X, i.e. the activity; b_X instead defines the probability that the node receives a link from an active node $p_X \propto b_X$. At the beginning all the nodes are disconnected and when a node is activated generates m links with m nodes selected randomly with probability proportional to their attractiveness b_X (hereafter we fix $m = 1$ with no loss of generality). Then all the links are destroyed and the procedure is repeated.

We assume that (a_S, b_S) are drawn from the distribution $\rho(a_S, b_S)$, which allow to model heterogeneity in the agent behaviour (see Chapters 1-2): hereafter we will consider $\rho(a_S, b_S) = \rho_S(a_S)\delta(b_S - a_S)$, i.e. assuming a linear correlation between activity and attractiveness as observed empirically [72, 76], with arbitrary $\rho_S(a_S)$. Adaptive behaviour is implemented assuming that symptomatic individuals are immediately isolated $(a_I, b_I) = (0, 0)$ as soon as they develop symptoms, while presymptomatic, asymptomatic and recovered individuals, in the absence of tracing or other measures, behave exactly as when susceptible $(a_P, b_P) = (a_A, b_A) = (a_R, b_R) = (a_S, b_S)$. We implement this behaviour in the active mode $p_X = b_X / \langle b(t) \rangle$ (see Chapter 4), i.e. assuming that the adaptive behaviour of a node does not affect the activity of the nodes that are not isolated: this is reasonable since we are considering the case in which measures are implemented to control the epidemic without disrupting societal activity and functionality [14].

The control parameter of the epidemic model is the effective infection rate $r =$

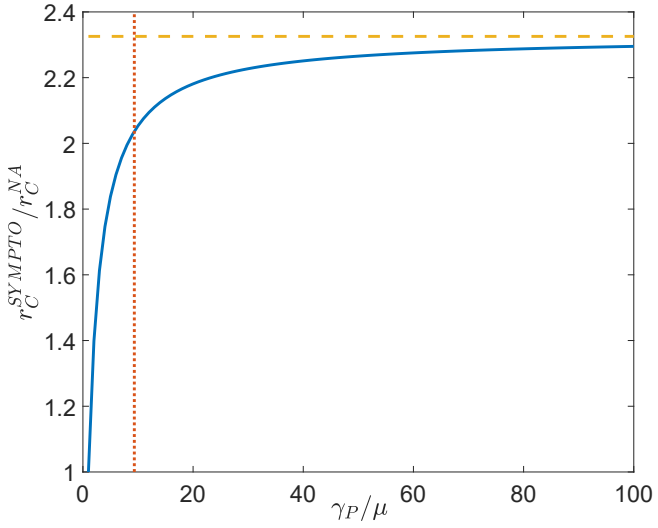

FIGURE 5.3: **Effect of isolation of symptomatic individuals.** We plot, as a function of γ_P/μ, the ratio r_C^{SYMPTO}/r_C^{NA} between the epidemic threshold when symptomatic nodes are isolated and the threshold in the non-adaptive case. The dashed orange horizontal line corresponds to the value of r_C^{SYMPTO}/r_C^{NA} for instantaneous symptoms development $\gamma_P/\mu \to \infty$; the dotted red vertical line corresponds to the value of γ_P/μ tailored to describe SARS-CoV-2, i.e. $\tau_P = 1/\gamma_P = 1.5$ days and $\tau = 1/\mu = 14$ days. The curves are obtained by fixing $(1-\delta) = 0.43$ and $\rho(a_S, b_S) = \rho_S(a_S)\delta(b_S - a_S)$ and hold for arbitrary $\rho_S(a_S)$ [28].

λ/μ whose critical value r_C is the epidemic threshold and is one of the descriptors of the measures effectiveness. The epidemic threshold, in the absence of tracing and with the isolation of symptomatic nodes, can be obtained analytically through an *activity-attractiveness-based mean-field approach* (see Appendix A for the detailed derivation), which is exact since all local correlations are destroyed by the link reshuffling thanks to the Markov dynamics. In the non-adaptive case (NA), i.e. if we assume that also symptomatic individuals are not isolated $(a_I, b_I) = (a_S, b_S)$, we obtain:

$$r_C^{NA} = \frac{\overline{a_S}}{2\overline{a_S^2}}, \tag{5.1}$$

for $\rho(a_S, b_S) = \rho_S(a_S)\delta(b_S - a_S)$, with arbitrary $\rho_S(a_S)$, and this threshold is that of Eq. (4.25) [14, 72].

If we consider the isolation of symptomatic individuals $(a_I, b_I) = (0, 0)$, the threshold is:

$$r_C^{SYMPTO} = r_C^{NA} \frac{\frac{\gamma_P}{\mu}}{\delta + (1-\delta)\frac{\gamma_P}{\mu}}, \tag{5.2}$$

and these results hold for $\rho(a_S, b_S) = \rho_S(a_S)\delta(b_S - a_S)$, with arbitrary $\rho_S(a_S)$.

In Figure 5.3 we plotted the increase in the epidemic threshold produced by the isolation of symptomatic nodes r_C^{SYMPTO}/r_C^{NA}, varying the duration of the presymptomatic phase γ_P/μ and for δ fixed. In the case of an instantaneous development of symptoms $\gamma_P/\mu \to \infty$, i.e. in the absence of the presymptomatic phase $\tau_P/\tau \to 0$, the threshold is increased by a factor $(1-\delta)^{-1}$; while for lower values of γ_P/μ the increase is reduced until it is cancelled out by $\gamma_P/\mu = 1$ since in that case nodes behave like asymptomatics. This represents the baseline on which to evaluate the effect of additional contact tracing to isolate even asymptomatic individuals.

The model presented is extremely general as it describes an arbitrary epidemic

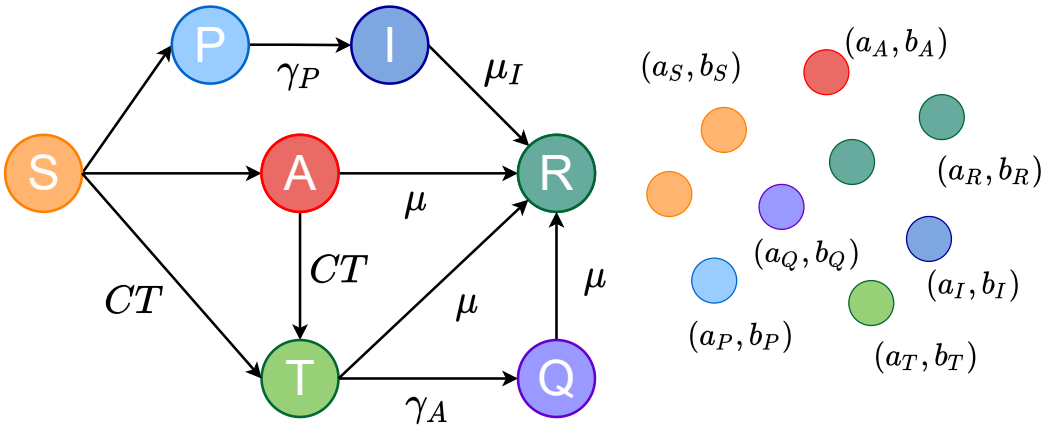

FIGURE 5.4: **Epidemic model with contact tracing.** We schematically represent the compartmental epidemic model with contact tracing and the corresponding adaptive activity-driven network, with different (a_X, b_X) depending on the status of the node. The rates for infection and tracing events are not indicated, since they are complex but are fully described in the main text and in Appendix A. This model holds both for manual CT, applied to all nodes, and for digital CT, applied only to nodes endowed with the tracing app, while nodes without the app follow the compartmental epidemic model of Figure 5.2.

with asymptomatic, presymptomatic and symptomatic phases: in this thesis we focus mainly on the case of the COVID-19 epidemic, however it is sufficient to modify the epidemiological parameters to describe other infectious diseases. In particular, we fix the parameters to describe SARS-CoV-2: the fraction of individuals who develop symptoms $\delta = 0.57$ [187], the average time of the presymptomatic phase $\tau_P = 1.5$ days [16, 197, 237] and the average time of contagiousness $\tau = 14$ days, which is the average recovery time [179, 238]. The whole general approach, as we will see in the next Sections, is performed for arbitrary values and therefore is valid for a general epidemic with asymptomatic and presymptomatic transmissions.

In the next Sections we introduce manual and digital CT into the model, through an adaptive coupling of the network to the epidemic.

5.3 Manual contact tracing on AD network

We introduce in our model the traditional manual tracing (interview-based), described in Section 5.1.2, by assuming that it is activated as soon as a presymptomatic individual develops symptoms $P \to I$. Manual tracing is performed over a time window T_{CT} and each of the nodes contacted in that window is traced with recall probability $\varepsilon(a_S)$, where a_S is the index case activity. Then a traced node is tested and, if asymptomatic A, is isolated $(a, b) = (0, 0)$: we assume a delay between the isolation of the index case and the isolation of their asymptomatic contacts τ_C. See Figures 5.4 and 5.5 for a schematic representation of the manual CT.

The tracing is implemented by introducing two further compartments into the compartmental model: T traced asymptomatic and Q isolated asymptomatic. Asymptomatic individuals A become traced asymptomatics T with probability $\varepsilon(a_s)$ as soon as they engage a contact with an individual who will then activate CT. A traced node T is still infectious, behaving as susceptible $(a_T, b_T) = (a_S, b_S)$, and with a rate $\gamma_A = 1/\tau_A$ it is isolated $T \xrightarrow{\gamma_A} Q$; isolated asymptomatic nodes Q are no longer infectious $(a_Q, b_Q) = (0, 0)$. Taking into account delays in manual CT, τ_C, and the need

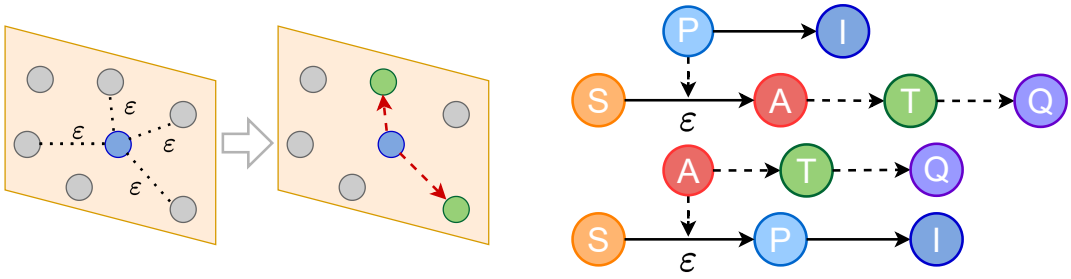

FIGURE 5.5: **Manual CT.** We schematically represent the manual tracing protocol. A symptomatic individual (blue) activates CT: each contact engaged in the time window T_{CT} (dashed links) is traced with probability ε and effectively traced asymptomatic nodes become traced asymptomatic (green). We show the two main processes on which CT can be applied: asymptomatic individuals can be traced if infected by a presymptomatic node, or if they infect a node who will then develop symptoms.

for the presymptomatic node to develop symptoms to activate tracing, τ_P, we have $\tau_A = \tau_C + \tau_P$. See Figure 5.4 for the complete epidemic compartmental model in the presence of manual CT, which hold for all the nodes. In Appendix A we report all the contact-induced (e.g. infection and tracing) and spontaneous (e.g. recovery) transitions.

The key parameters of manual tracing are therefore the delay in isolation τ_C, the time window T_{CT} on which the tracing is performed and the recall probability $\varepsilon(a_S)$.

The delay τ_C can be large because of delays in the technical procedures of manual CT, such as the collection of the contact diary and reaching the contacts.

We fix the same time-window T_{CT} for both manual and digital CT, assuming that it is long enough to implement both backward tracing and forward tracing [188, 202, 237] (see Chapter 6 for more details), i.e. asymptomatic nodes can be traced if they are the primary source of infection of the index case or if they are infected by the index case during the presymptomatic phase (see Figure 5.5). For example, we will fix $T_{CT} = \tau = 14$ days for the COVID-19 epidemic [237].

The recall probability $\varepsilon(a_S)$ takes into account several factors: the limited memory/knowledge of the index case of some contacts (e.g. occasional meetings in a supermarket or restaurant), the voluntary decision not to provide all the contacts engaged, the non-adherence of some of its contacts to the tracing and the limited resources allocated for CT (see Figure 5.5). We considered the most general case where the recall probability $\varepsilon(a_S)$ depends on the activity of the index case activating the CT. This allows to model the *local limited scalability* of the traditional manual tracing system: individuals with low social activity are involved in a small number of interactions and a fraction ε^* of their contacts can be easily traced, since a small number of individuals can be easily remembered and reachable by the tracers; on the contrary, individuals with high social activity are involved in a large number of interactions and therefore, the same fraction ε^* would require the tracing of a very large number of contacts. Due to limitations on memory/knowledge and tracing capacity (i.e. limited resources allocated), only a finite number of contacts can be traced for these nodes [237, 239, 240]. We model the local limited scalability property of manual CT by assuming that for each index case the manual CT is able to trace at most a number k_c of contacts:

$$\varepsilon(a_S) = \begin{cases} \varepsilon^*, & \text{if } a_S \leq a^* \\ \varepsilon^* \frac{a^*}{a_S} = \frac{k_c}{2T_{CT}a_S}, & \text{if } a_S > a^* \end{cases} \tag{5.3}$$

where $a^* = k_c/2T_{CT}\varepsilon^*$. Manual CT reaches a fraction ε^* of the links generated in the

time window T_{CT} until the number of traced individuals reaches k_c, i.e. for nodes with $a_S \leq a^*$; then the fraction $\varepsilon(a_S)$ decays with the activity a_S to keep fixed the number of traced nodes at the maximum k_c [237, 239, 240].

In addition to the local limited scalability of the index case, modelled through Eq. (5.3), a global limited scalability is active in manual CT, as discussed in Section 5.1. In this thesis we focus mainly on the effects of CT on the epidemic threshold, i.e. for low prevalence, and in conditions of low incidence, e.g. to control the epidemic before a widespread diffusion, after the relaxation of very restrictive measures or at the beginning of an epidemic. This allows us to neglect the global limited scalability effects.

The epidemic model corresponds to a SIR model where infected individuals are distinguished on the basis of the presence of symptoms, the tracing and isolation status, identifying different states during the period of contagiousness (see Figure 5.4). Furthermore, the model is exactly mean-field given that the dynamics is Markovian and there are no local correlations, which are continually destroyed by the reshuffling of the links: this allows us to state that the SIS and SIR model have the same epidemic threshold [126, 128–130]. The analytical calculation of epidemic threshold is performed with reference to the SIS model without loss of generality (see Appendix A).

The epidemic dynamics can be described through an *activity-attractiveness-based mean-field approach*: we divide the population into classes of nodes with the same (a_S, b_S) and we consider them statistically equivalent. In this framework, we initially assign to each node the status of symptomatic (with probability δ) or asymptomatic (with probability $(1-\delta)$), instead of at the time of infection: this choice is completely equivalent to the model described and allows us to write the mean field equations in a simpler way. At the mean-field level, the epidemic dynamics is described by the probabilities: $P_{a_S,b_S}(t)$, $I_{a_S,b_S}(t)$ and $1 - P_{a_S,b_S}(t) - I_{a_S,b_S}(t)$ for a node of class (a_S, b_S), that will develop symptoms (if infected), to be respectively presymptomatic, infected symptomatic or susceptible, at time t; $A_{a_S,b_S}(t)$, $T_{a_S,b_S}(t)$, $Q_{a_S,b_S}(t)$ and $1 - A_{a_S,b_S}(t) - T_{a_S,b_S}(t) - Q_{a_S,b_S}(t)$ for node of class (a_S, b_S), that will not develop symptoms (if infected), to be respectively infected asymptomatic, traced asymptomatic, isolated asymptomatic or susceptible, at time t.

In this approach the average attractiveness is:

$$\langle b(t) \rangle = \overline{b_S} - (1-\delta)\overline{b_S Q}(t) - \delta \overline{b_S I}(t), \tag{5.4}$$

where we define $\overline{g} = \int da_S db_S \rho(a_S, b_S) g_{a_S,b_S}$. We assume to be in the thermodynamic limit and we consider the case of a general joint distribution $\rho(a_S, b_S)$, so this is the most general case in which the recall probability $\varepsilon(a_S, b_S)$ depends on the class (a_S, b_S), but later we will consider $\varepsilon(a_S)$.

The probabilities that define the epidemic dynamics evolve according to the following equations:

$$\begin{aligned} \partial_t P_{a_S,b_S}(t) = -\gamma_P P_{a_S,b_S}(t) + \lambda a_S (1 - I_{a_S,b_S}(t) - P_{a_S,b_S}(t)) \frac{B(t)}{\langle b(t) \rangle} \\ + \lambda b_S (1 - I_{a_S,b_S}(t) - P_{a_S,b_S}(t)) \frac{C(t)}{\langle b(t) \rangle}, \end{aligned} \tag{5.5}$$

with $B(t) = \delta \overline{b_S P}(t) + (1-\delta)[\overline{b_S T}(t) + \overline{b_S A}(t)]$ and $C(t) = \delta \overline{a_S P}(t) + (1-\delta)[\overline{a_S T}(t) + \overline{a_S A}(t)]$. The first term on the right-hand side is due to the spontaneous symptoms

development; the second and third terms are the contagion terms in which a susceptible node of class (a_S, b_S) is infected through contact with a presymptomatic individual or with an asymptomatic non-isolated infected individual of any class (a'_S, b'_S) (i.e. the term is averaged on the class of the involved infected node), respectively in the case in which the link is activated by the susceptible or the infected node.

$$\partial_t I_{a_S,b_S}(t) = -\mu_I I_{a_S,b_S}(t) + \gamma_P P_{a_S,b_S}(t), \tag{5.6}$$

where the first term on the right-hand side is due to the spontaneous recovery process and the second to the spontaneous symptoms development.

$$\begin{aligned}
\partial_t A_{a_S,b_S}(t) = &- \mu A_{a_S,b_S}(t) \\
&+ \lambda a_S(1 - A_{a_S,b_S}(t) - T_{a_S,b_S}(t) - Q_{a_S,b_S}(t))\frac{B(t) - \delta\overline{\varepsilon b_S P}(t)}{\langle b(t)\rangle} \\
&+ \lambda b_S(1 - A_{a_S,b_S}(t) - T_{a_S,b_S}(t) - Q_{a_S,b_S}(t))\frac{C(t) - \delta\overline{\varepsilon a_S P}(t)}{\langle b(t)\rangle} \\
&- \lambda a_S \delta A_{a_S,b_S}(t)\frac{\overline{\varepsilon b_S} - \overline{\varepsilon b_S I}(t) - \overline{\varepsilon b_S P}(t)}{\langle b(t)\rangle} \\
&- \lambda b_S \delta A_{a_S,b_S}(t)\frac{\overline{\varepsilon a_S} - \overline{\varepsilon a_S I}(t) - \overline{\varepsilon a_S P}(t)}{\langle b(t)\rangle},
\end{aligned} \tag{5.7}$$

where the first term on the right-hand side is due to the spontaneous recovery process; the second and third terms are the contagion terms in which a susceptible node of class (a_S, b_S) is infected through a contact with an infected individual respectively when the link is activated by the susceptible or the infected node. These terms take into account that the infection may be due to an asymptomatic non-isolated infected individual or to a presymptomatic individual, if the corresponding link has not been traced, i.e. with probability $(1 - \varepsilon(a'_S, b'_S))$ where (a'_S, b'_S) are the activity and attractiveness of the presymptomatic node who activate the CT. Both terms of contagion are mediated on the activity and attractiveness of the infected node involved. The fourth and fifth terms correspond to the contribution of the CT of asymptomatic infected individuals who are the source of infection for a symptomatic node that will later activate CT: in this case an asymptomatic node of class (a_S, b_S) is traced with probability $\varepsilon(a'_S, b'_S)$ which depends on the activity and attractiveness of the susceptible node (a'_S, b'_S) infected in the event. The two terms correspond respectively to the case in which the link is activated by the infected node or by the susceptible node and are both averaged on the class (a'_S, b'_S) of the susceptible node.

$$\begin{aligned}
\partial_t T_{a_S,b_S}(t) = &- (\mu + \gamma_A) T_{a_S,b_S}(t) \\
&+ \lambda b_S(1 - A_{a_S,b_S}(t) - T_{a_S,b_S}(t) - Q_{a_S,b_S}(t))\frac{\delta\overline{\varepsilon a_S P}(t)}{\langle b(t)\rangle} \\
&+ \lambda a_S(1 - A_{a_S,b_S}(t) - T_{a_S,b_S}(t) - Q_{a_S,b_S}(t))\frac{\delta\overline{\varepsilon b_S P}(t)}{\langle b(t)\rangle} \\
&+ \lambda b_S \delta A_{a_S,b_S}(t)\frac{\overline{\varepsilon a_S} - \overline{\varepsilon a_S I}(t) - \overline{\varepsilon a_S P}(t)}{\langle b(t)\rangle} \\
&+ \lambda a_S \delta A_{a_S,b_S}(t)\frac{\overline{\varepsilon b_S} - \overline{\varepsilon b_S I}(t) - \overline{\varepsilon b_S P}(t)}{\langle b(t)\rangle},
\end{aligned} \tag{5.8}$$

where the first term on the right-hand side is due to the spontaneous recovery process and the isolation process after tracing; the second and third terms instead are the contagion terms in which a susceptible node of class (a_S, b_S) is infected through a contact with a presymptomatic infected individual and the corresponding link has been traced effectively, with probability $\varepsilon(a'_S, b'_S)$ where (a'_S, b'_S) are the activity and attractiveness of the presymptomatic node. The two terms correspond respectively to the case in which the link is activated by the susceptible or the infected node and both are averaged on the activity and attractiveness of the infected node involved. The fourth and fifth terms correspond to the contribution of the CT of asymptomatic infected individuals who are the source of infection for a symptomatic node that will later activate CT: in this case an asymptomatic node of class (a_S, b_S) is traced with probability $\varepsilon(a'_S, b'_S)$ which depends on the activity and attractiveness of the susceptible node (a'_S, b'_S) infected in the event. The two terms correspond respectively to the case in which the link is activated by the infected node or by the susceptible node and are both averaged on the class (a'_S, b'_S) of the susceptible node.

$$\partial_t Q_{a_S,b_S}(t) = -\mu Q_{a_S,b_S}(t) + \gamma_A T_{a_S,b_S}(t), \tag{5.9}$$

where the first term on the right-hand side is due to spontaneous recovery while the second term to the isolation of traced asymptomatic nodes.

These equations constitute a set of five coupled non-linear differential equations for each class (a_S, b_S) and it is not closed nor complete due to the presence of the averaged probabilities. Moreover, the averaged probabilities $\overline{P}(t)$, $\overline{I}(t)$, $\overline{A}(t)$, $\overline{T}(t)$ and $\overline{Q}(t)$, which represent the average probability for a node to belong to these compartments, are much more interesting variables compared to the single probability for each class (a_S, b_S). Thus, by averaging on the classes (a_S, b_S) it is possible to obtain a system of nine coupled non-linear differential equations that is closed and complete: this set of equations admits as a solution the absorbing state, that is the configuration with all nodes susceptible. The epidemic threshold can thus be obtained with a linear stability analysis around the absorbing state: see Appendix A for the details of the computation of the system of equations and for the linear stability analysis. The epidemic threshold can be obtained from the following relation:

$$\begin{aligned} 8r^3\delta^2(1-\delta)\frac{\overline{\varepsilon a_S^2}\,\overline{\varepsilon a_S}}{\overline{a_S}}\overline{\frac{a_S^3}{1+2r\delta a_S\frac{\varepsilon a_S}{a_S}}}\frac{\gamma_A}{\mu} - 4r^2\delta(1-\delta)\left[\overline{\varepsilon a_S^2}\,\overline{a_S^2} + \frac{\gamma_P}{\mu}\overline{\varepsilon a_S}\,\overline{\frac{a_S^3}{1+2r\delta a_S\frac{\varepsilon a_S}{a_S}}}\right]\frac{\gamma_A}{\mu} \\ + 2r\overline{a_S^2}\,\overline{a_S}\left(\frac{\gamma_A}{\mu}+1\right)\left(\delta+\frac{\gamma_P}{\mu}(1-\delta)\right) \\ - \overline{a_S}^2\frac{\gamma_P}{\mu}\left(\frac{\gamma_A}{\mu}+1\right) = 0, \end{aligned} \tag{5.10}$$

which hold for $\rho(a_S, b_S) = \rho_S(a_S)\delta(b_S - a_S)$, with generic $\rho_S(a_S)$ and thus the recall probability becomes $\varepsilon(a_S)$.

Eq. (5.10) represents a closed and exact relation for the analytical estimation of the epidemic threshold. Furthermore, the relation is strongly general since it holds for a generic epidemic with symptomatic and asymptomatic infections, i.e. for arbitrary δ, τ_P and τ, which occurs on an AD network with arbitrary $\rho_S(a_S)$, assuming $\rho(a_S, b_S) = \rho_S(a_S)\delta(a_S - b_S)$, with symptomatic isolation and manual CT, with arbitrary delay τ_C and arbitrary recall probability $\varepsilon(a_S)$.

The epidemic threshold depends in a complex way on all the parameters of the epidemic model (see Eq. (5.10)): in particular, it depends on the correlations between the recall probability $\varepsilon(a_S)$ and the activity a_S and also on high-order moments of the distribution $\rho(a_S)$. This suggests that the epidemic threshold strongly depends

on the heterogeneity of $\rho_S(a_S)$, on its shape and on how the recall probability is distributed in the heterogeneous population, as we will see in Sections 5.6 and 5.7.

The epidemic threshold r_C can be obtained by solving Eq. (5.10) numerically in r in the general case with delays, heterogeneity and limited scalability. However, in some limit cases it is possible to solve Eq. (5.10) analytically and obtain an explicit form of the epidemic threshold.

The *non-adaptive case (NA)*, in which all infected nodes behave as susceptible, can be obtained by fixing $\varepsilon(a_S) = 0 \,\forall\, a_S$, i.e. no tracing of the asymptomatic, and $\gamma_P/\mu = 1$, i.e. the presymptomatic phase coincide with the period of contagiousness and thus no isolation occurs. Substituting this in Eq. (5.10) is obtained:

$$2r\overline{a_S^2}\overline{a_S} - \overline{a_S}^2 = 0, \tag{5.11}$$

which admits as a solution:

$$r_C^{NA} = \frac{\overline{a_S}}{2\overline{a_S^2}}. \tag{5.12}$$

This threshold is that of Eq. (5.1) and is valid for arbitrary $\rho_S(a_S)$; moreover it reproduces the result obtained in Chapters 2 and 4 for the ADA model without adaptivity (see Eq. (2.53) and Eq. (4.25)).

The case in which *only the symptomatics* are isolated can be obtained by fixing $\varepsilon(a_S) = 0 \,\forall\, a_S$. Substituting this in Eq. (5.10) is obtained:

$$2r\overline{a_S^2}\overline{a_S}\left(\delta + (1-\delta)\frac{\gamma_P}{\mu}\right) - \overline{a_S}^2\frac{\gamma_P}{\mu} = 0, \tag{5.13}$$

which admits as a solution:

$$r_C^{SYMPTO} = r_C^{NA}\frac{\frac{\gamma_P}{\mu}}{\delta + (1-\delta)\frac{\gamma_P}{\mu}}. \tag{5.14}$$

This threshold is that of Eq. (5.2) and is valid for arbitrary $\rho_A(a_S)$.

Finally, the epidemic threshold can be obtained explicitly also assuming a *homogeneous population* $\rho_S(a_S) = \delta(a_S - a)$ in the absence of delays $\tau_C = 0$ in manual CT, i.e. $\gamma_A = \gamma_P$. Substituting this in Eq. (5.10) we get a quadratic equation in r:

$$4a^2\delta^2\varepsilon r^2 + 2a\left(\delta + \frac{\gamma_P}{\mu}(1-\delta-\delta\varepsilon)\right)r - \frac{\gamma_P}{\mu} = 0, \tag{5.15}$$

which admits as a solution for the epidemic threshold:

$$r_C^{MANUAL} = \frac{2\frac{\gamma_P}{\mu}r_C^{NA}}{\delta + (1-\delta-\varepsilon\delta)\frac{\gamma_P}{\mu} + \sqrt{(\delta + (1-\delta-\varepsilon\delta)\frac{\gamma_P}{\mu})^2 + 4\delta^2\varepsilon\frac{\gamma_P}{\mu}}}. \tag{5.16}$$

In this case the epidemic threshold explicitly shows a non-trivial dependence on the parameters of the model and in particular on the recall probability ε.

5.4 Digital contact tracing on AD network

We introduce in our model the digital tracing (app-based), described in Section 5.1.3, by assuming that each node with activity a_S has a probability $f(a_S)$ of downloading the tracing app before the outbreak begins. As soon as presymptomatic individuals

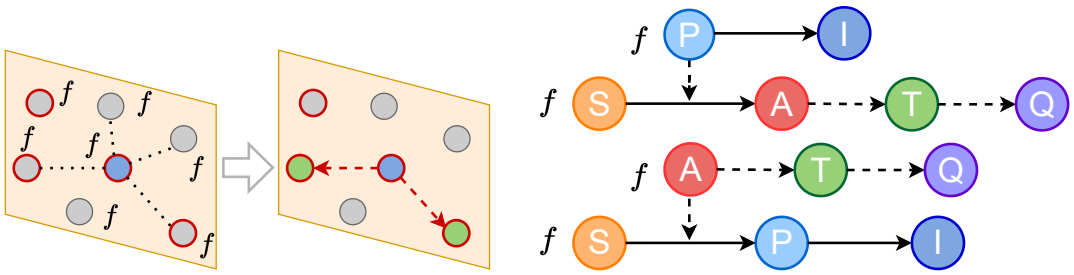

FIGURE 5.6: **Digital CT.** We schematically represent the digital tracing protocol: all nodes are endowed with the app with probability f (red edge). Asymptomatic individuals (blue) activate CT only if they downloaded the app: every contact engaged in the time window T_{CT} (dashed links) with other nodes with the app is traced, while the other links are not. Effectively traced asymptomatic nodes become traced asymptomatic (green). We show the two main processes on which CT can be applied: asymptomatic individuals can be traced if infected by a presymptomatic node or if they infect a node who will then develop symptoms, only if both downloaded the app.

develop symptoms $P \to I$ the digital CT is activated only if they downloaded the app, otherwise the tracing is not activated. When digital CT is activated, all and only the contacts engaged with nodes endowed with the app are traced with probability 1, while the other contacts are not traced. Then a traced node is tested and, if asymptomatic A, is isolated $(a, b) = (0, 0)$: we assume that in the digital case there are no delays in tracing and isolation, therefore the time elapsed between the isolation of the index case and its asymptomatic contacts is 0. This is an approximation that favours digital tracing, given that technical delays are always present in the notifications, in the isolation and adherence to quarantine. However, in this way we can interpret the delay in manual CT τ_C as the relative delay of the manual CT with respect to the digital CT: results in the UK and Switzerland estimated an acceleration in the digital CT of about 1-2 days compared to the manual one [205]. See Figures 5.4 and 5.6 for a schematic representation of the digital CT.

The tracing is implemented also in this case by introducing two further compartments into the compartment model: T traced asymptomatic and Q isolated asymptomatic. Asymptomatic individuals A become traced asymptomatics T as soon as they make a contact with an individual who will then activate CT. A traced node T is still infectious, behaving as susceptible $(a_T, b_T) = (a_S, b_S)$, and with a rate $\gamma_A = 1/\tau_A$ it is isolated $T \xrightarrow{\gamma_A} Q$; isolated asymptomatic nodes Q are no longer infectious $(a_Q, b_Q) = (0, 0)$. Taking into account the need for the presymptomatic node to develop symptoms to activate tracing we have $\tau_A = \tau_P$, i.e. $\gamma_A = \gamma_P$.

The key parameters of digital tracing are the time-window T_{CT} on which the CT is performed and the probability $f(a_S)$ that a node has adopted the app. The time window T_{CT} is set equal in the manual and digital case $T_{CT} = \tau$, as discussed in Section 5.3.

We consider the most general condition in which f depends on the activity of a node a_S, thus the level of penetration of the app in the population is $\overline{f} = \int da_S \rho_S(a_S) f(a_S)$. This allows to model different distributions of the app in a heterogeneous population, i.e. correlations between f and a_S, which can emerge spontaneously, as observed empirically [230, 231], or can be implemented app adoption strategies (see Section 5.9.3).

In the presence of digital CT the population is divided into two subpopulations, one of nodes endowed with the app and one of those without the app (see Figure 5.6), whose epidemic clinical stages are described through different compartmental

epidemic models: nodes with the app follow the compartmental epidemic model shown in Figure 5.4; nodes without the app follow the compartmental epidemic model of Figure 5.2. Thus, in this case it is necessary to distinguish the compartments for the two populations, indicating with X the compartments for individuals without an app and indicating with X^α (with the superscript $^\alpha$) compartments for individuals with the app. In the presence of a purely digital CT, tracing can only take place on events involving two nodes with the app (within the same subpopulation), while in all other cases (contacts between nodes in the subpopulation without the app or contacts between two different subpopulations) it cannot be activated. In Appendix A we report all the contact-induced (e.g. infection and tracing) and spontaneous (e.g. recovery) transitions.

Similarly to the manual CT, the model is exactly mean-field and the analytical calculation of epidemic threshold can be performed with reference to the SIS model without loss of generality (see Appendix A). We describe the epidemic dynamics through the same *activity-attractiveness-based mean-field approach* described for the manual CT in Section 5.3.

At the mean-field level, the epidemic dynamics is described by the probabilities (one for each compartment in the two different subpopulations): $P_{a_S,b_S}(t)$, $I_{a_S,b_S}(t)$, $1 - P_{a_S,b_S}(t) - I_{a_S,b_S}(t)$ for a node of class (a_S, b_S) without the app, that will develop symptoms (if infected), to be respectively presymptomatic, infected symptomatic or susceptible at time t; $A_{a_S,b_S}(t)$, $1 - A_{a_S,b_S}(t)$ for a node of class (a_S, b_S) without the app, that will not develop symptoms (if infected), to be respectively infected asymptomatic or susceptible at time t; $P^\alpha_{a_S,b_S}(t)$, $I^\alpha_{a_S,b_S}(t)$, $1 - P^\alpha_{a_S,b_S}(t) - I^\alpha_{a_S,b_S}(t)$ for a node of class (a_S, b_S) with the app, that will develop symptoms (if infected), to be respectively presymptomatic, infected symptomatic or susceptible at time t; $A^\alpha_{a_S,b_S}(t)$, $T^\alpha_{a_S,b_S}(t)$, $Q^\alpha_{a_S,b_S}(t)$, $1 - A^\alpha_{a_S,b_S}(t) - T^\alpha_{a_S,b_S}(t) - Q^\alpha_{a_S,b_S}(t)$ for a node of class (a_S, b_S) with the app, that will not develop symptoms (if infected), to be respectively infected asymptomatic, traced asymptomatic, isolated asymptomatic or susceptible at time t.

In the mean-field approach, the average attractiveness is:

$$\langle b(t)\rangle = \overline{b_S} - (1-\delta)\overline{f b_S Q^\alpha}(t) - \delta(\overline{f b_S I^\alpha}(t) + \overline{(1-f) b_S I}(t)), \tag{5.17}$$

where we define $\overline{g} = \int da_S db_S \rho(a_S, b_S) g_{a_S,b_S}$.

We assume to be in the thermodynamic limit and we consider the case of a general joint distribution $\rho(a_S, b_S)$, so this is the most general case in which the probability of app adoption $f(a_S, b_S)$ depends on the class (a_S, b_S), but later we will consider $f(a_S)$.

The probabilities that define the epidemic dynamics evolve according to the following equations:

$$\begin{aligned}\partial_t P_{a_S,b_S}(t) = &-\gamma_P P_{a_S,b_S}(t) + \lambda a_S (1 - I_{a_S,b_S}(t) - P_{a_S,b_S}(t)) \frac{F(t)}{\langle b(t)\rangle} \\ &+ \lambda b_S (1 - I_{a_S,b_S}(t) - P_{a_S,b_S}(t)) \frac{G(t)}{\langle b(t)\rangle},\end{aligned} \tag{5.18}$$

$$\begin{aligned}\partial_t P^\alpha_{a_S,b_S}(t) = &-\gamma_P P^\alpha_{a_S,b_S}(t) + \lambda a_S (1 - I^\alpha_{a_S,b_S}(t) - P^\alpha_{a_S,b_S}(t)) \frac{F(t)}{\langle b(t)\rangle} \\ &+ \lambda b_S (1 - I^\alpha_{a_S,b_S}(t) - P^\alpha_{a_S,b_S}(t)) \frac{G(t)}{\langle b(t)\rangle},\end{aligned} \tag{5.19}$$

with $F(t) = \delta(\overline{f b_S P^\alpha}(t) + \overline{(1-f) b_S P}(t)) + (1-\delta)(\overline{f b_S T^\alpha}(t) + \overline{f b_S A^\alpha}(t) + \overline{(1-f) b_S A}(t))$

and $G(t) = \delta(\overline{fa_S P^\alpha}(t) + \overline{(1-f)a_S P}(t)) + (1-\delta)(\overline{fa_S T^\alpha}(t) + \overline{fa_S A^\alpha}(t) + \overline{(1-f)a_S A}(t))$. For both the subpopulations, the first term on the right-hand side is due to the spontaneous symptoms development; the second and third terms are the contagion terms in which a susceptible node of class (a_S, b_S) is infected through a contact with a presymptomatic or with an asymptomatic non-isolated infected of any class (a'_S, b'_S) (i.e. the term is averaged on the class of the involved infected node) and belonging to any subpopulation. The two terms correspond respectively to the case in which the link is activated by the susceptible node or by the infected node.

$$\partial_t I_{a_S,b_S}(t) = -\mu_I I_{a_S,b_S}(t) + \gamma_P P_{a_S,b_S}(t), \tag{5.20}$$
$$\partial_t I^\alpha_{a_S,b_S}(t) = -\mu_I I^\alpha_{a_S,b_S}(t) + \gamma_P P^\alpha_{a_S,b_S}(t), \tag{5.21}$$

for both subpopulations, the first term on the right-hand side is due to the spontaneous recovery process and the second to the spontaneous symptoms development process.

$$\begin{aligned}\partial_t A_{a_S,b_S}(t) = -\mu A_{a_S,b_S}(t) + \lambda a_S(1 - A_{a_S,b_S}(t))\frac{F(t)}{\langle b(t)\rangle} \\ + \lambda b_S(1 - A_{a_S,b_S}(t))\frac{G(t)}{\langle b(t)\rangle},\end{aligned} \tag{5.22}$$

where the first term on the right-hand side is due to the spontaneous recovery; the second and third terms are the contagion terms in which a susceptible node of class (a_S, b_S) is infected through a contact with a presymptomatic individual or with an asymptomatic non-isolated infected individual of any class (a'_S, b'_S) (i.e. the term is averaged on the class of the involved infected node) and belonging to any subpopulation. The two terms correspond respectively to the case in which the link is activated by the susceptible node or by the infected node. In this case, there are no tracing terms since the equations describe an asymptomatic without the app.

$$\begin{aligned}\partial_t A^\alpha_{a_S,b_S}(t) = & -\mu A^\alpha_{a_S,b_S}(t) \\ & + \lambda a_S(1 - A^\alpha_{a_S,b_S}(t) - T^\alpha_{a_S,b_S}(t) - Q^\alpha_{a_S,b_S}(t))\frac{F(t) - \delta\overline{fb_S P^\alpha}(t)}{\langle b(t)\rangle} \\ & + \lambda b_S(1 - A^\alpha_{a_S,b_S}(t) - T^\alpha_{a_S,b_S}(t) - Q^\alpha_{a_S,b_S}(t))\frac{G(t) - \delta\overline{fa_S P^\alpha}(t)}{\langle b(t)\rangle} \\ & - \lambda\delta a_S A^\alpha_{a_S,b_S}(t)\frac{\overline{fb_S} - \overline{fb_S P^\alpha}(t) - \overline{fb_S I^\alpha}(t)}{\langle b(t)\rangle} \\ & - \lambda\delta b_S A^\alpha_{a_S,b_S}(t)\frac{\overline{fa_S} - \overline{fa_S P^\alpha}(t) - \overline{fa_S I^\alpha}(t)}{\langle b(t)\rangle},\end{aligned} \tag{5.23}$$

where the first term on the right-hand side is due to the spontaneous recovery process; the second and third term are the contagion terms in which a susceptible node of class (a_S, b_S) is infected through a contact with an infected individual respectively in the case in which the link is activated by the susceptible node or by the infected node. These terms take into account that the contagion may be due to an asymptomatic non-isolated infected individual belonging to both subpopulations or to a presymptomatic individual without the app. Both terms of contagion are mediated on the activity and attractiveness of the infected node involved. The fourth and fifth

term correspond to the contribution of the tracing of infected asymptomatic individuals with the app and of class (a_S, b_S) who have infected a susceptible node with the app who will then develop symptoms. The two terms correspond respectively to the case in which the link is activated by the infected node or by the susceptible node and are both mediated on the activity and attractiveness (a'_S, b'_S) of the susceptible.

$$\begin{aligned}\partial_t T^{\alpha}_{a_S,b_S}(t) = & -(\mu+\gamma_P)T^{\alpha}_{a_S,b_S}(t) \\ & + \lambda a_S(1-A^{\alpha}_{a_S,b_S}(t)-T^{\alpha}_{a_S,b_S}(t)-Q^{\alpha}_{a_S,b_S}(t))\frac{\delta\overline{fb_SP^{\alpha}}(t)}{\langle b(t)\rangle} \\ & + \lambda b_S(1-A^{\alpha}_{a_S,b_S}(t)-T^{\alpha}_{a_S,b_S}(t)-Q^{\alpha}_{a_S,b_S}(t))\frac{\delta\overline{fa_SP^{\alpha}}(t)}{\langle b(t)\rangle} \\ & + \lambda\delta a_S A^{\alpha}_{a_S,b_S}(t)\frac{\overline{fb_S}-\overline{fb_SP^{\alpha}}(t)-\overline{fb_SI^{\alpha}}(t)}{\langle b(t)\rangle} \\ & + \lambda\delta b_S A^{\alpha}_{a_S,b_S}(t)\frac{\overline{fa_S}-\overline{fa_SP^{\alpha}}(t)-\overline{fa_SI^{\alpha}}(t)}{\langle b(t)\rangle},\end{aligned} \tag{5.24}$$

where the first term on the right-hand side is due to the spontaneous recovery process and isolation by tracing; the second and third terms are the contagion terms in which a susceptible node of class (a_S, b_S) with the app is infected through a contact with a presymptomatic infected individual with app and is traced. The two terms correspond respectively to the case in which the link is activated by the susceptible node or by the infected node and both are averaged on the activity and attractiveness of the infected node involved. The fourth and fifth terms correspond to the contribution of the tracing of asymptomatic infected individuals with the app and of class (a_S, b_S) who have infected a susceptible node with the app who will then develop symptoms. The two terms correspond respectively to the case in which the link is activated by the infected node or by the susceptible node and are both mediated on the activity and attractiveness (a'_S, b'_S) of the susceptible node.

$$\partial_t Q^{\alpha}_{a_S,b_S}(t) = -\mu Q^{\alpha}_{a_S,b_S}(t) + \gamma_P T^{\alpha}_{a_S,b_S}(t), \tag{5.25}$$

where the first term on the right-hand side is due to spontaneous recovery while the second term to the isolation of traced asymptomatic nodes.

These equations constitute a set of eight coupled non-linear differential equations for each class (a_S, b_S), which are not closed nor complete due to the presence of the averaged probabilities. Moreover, the averaged probabilities $\overline{P}(t)$, $\overline{I}(t)$, $\overline{A}(t)$, $\overline{P^{\alpha}}(t)$, $\overline{I^{\alpha}}(t)$, $\overline{A^{\alpha}}(t)$, $\overline{T^{\alpha}}(t)$ and $\overline{Q^{\alpha}}(t)$, which represent the average probability for a node to belong to these compartments, are much more interesting variables compared to the single probability for each class (a_S, b_S). Thus, by averaging on the classes (a_S, b_S) it is possible to obtain a system of fourteen coupled non-linear differential equations that is closed and complete: this set of equations admits as a solution the absorbing state, that is the configuration with all nodes susceptible. The epidemic threshold can thus be obtained with a linear stability analysis around the absorbing state: see Appendix A for the details of the computation of the system of equations and for the linear stability analysis. The epidemic threshold can be obtained from the following

relation:

$$8r^3\delta^2(1-\delta)\frac{\overline{fa_S^2}\,\overline{fa_S}}{\overline{a_S}}\frac{\overline{fa_S^3}}{1+2r\delta a_S\frac{\overline{fa_S}}{\overline{a_S}}}\frac{\gamma_P}{\mu}-4r^2\delta(1-\delta)\left[\overline{fa_S^2}^2+\frac{\gamma_P}{\mu}\overline{fa_S}\frac{\overline{fa_S^3}}{1+2r\delta a_S\frac{\overline{fa_S}}{\overline{a_S}}}\right]\frac{\gamma_P}{\mu}$$
$$+2r\overline{a_S^2}\overline{a_S}\left(\frac{\gamma_P}{\mu}+1\right)\left(\delta+\frac{\gamma_P}{\mu}(1-\delta)\right)$$
$$-\overline{a_S}^2\frac{\gamma_P}{\mu}\left(\frac{\gamma_P}{\mu}+1\right)=0, \tag{5.26}$$

which hold for $\rho(a_S,b_S)=\rho_S(a_S)\delta(b_S-a_S)$, with generic $\rho_S(a_S)$ and thus the recall probability becomes $\varepsilon(a_S)$.

Eq. (5.26) represents a closed and exact relation for the analytical estimation of the epidemic threshold. Furthermore, the relation is strongly general since it holds for a generic epidemic with symptomatic and asymptomatic infections, i.e. for arbitrary δ, τ_P and τ, which occurs on an AD network with arbitrary $\rho_S(a_S)$, assuming $\rho(a_S,b_S)=\rho_S(a_S)\delta(a_S-b_S)$, with symptomatic isolation and manual CT, with arbitrary distribution of the app in the population $f(a_S)$ and with arbitrary penetration of the app $\overline{f}$.

The epidemic threshold depends in a complex way on all the parameters of the epidemic model (see Eq. (5.26)): in particular, it depends on the correlations between the probability of adoption of the app $f(a_S)$ and the activity a_S and also depends on high-order moments of the distribution $\rho_S(a_S)$. This suggests that the epidemic threshold strongly depends on the heterogeneity of $\rho_S(a_S)$, on its shape and on how the app is distributed in the population, as we will see in Sections 5.6 and 5.9.3.

The epidemic threshold r_C can be obtained by solving Eq. (5.26) numerically in r in the general case with heterogeneity and specific distribution of the app in the population. However, in some limit cases it is possible to solve Eq. (5.26) analytically and obtain an explicit form of the epidemic threshold.

The *non-adaptive case (NA)*, in which all infected nodes behave as susceptible, can be obtained by fixing $f(a_S)=0\,\forall\,a_S$ and $\gamma_P/\mu=1$. Substituting this in Eq. (5.26) is obtained:

$$r_C^{NA}=\frac{\overline{a_S}}{2\overline{a_S^2}}. \tag{5.27}$$

This threshold is that of Eq. (5.1) (as in the manual case) and is valid for arbitrary $\rho_S(a_S)$; moreover it reproduces the result obtained in Chapters 2 and 4 for the ADA model without adaptivity (see Eq. (2.53) and Eq. (4.25)).

The case in which *only the symptomatics* are isolated can be obtained by fixing $f(a_S)=0\,\forall\,a_S$. Substituting this in Eq. (5.26) is obtained:

$$r_C^{SYMPTO}=r_C^{NA}\frac{\frac{\gamma_P}{\mu}}{\delta+(1-\delta)\frac{\gamma_P}{\mu}}. \tag{5.28}$$

This threshold is that of Eq. (5.2) (as in the manual case) and is valid for arbitrary $\rho_S(a_S)$.

Finally, the epidemic threshold can be obtained explicitly also assuming a *homogeneous population* $\rho_S(a_S)=\delta(a_S-a)$. Substituting this in Eq. (5.26) we get a quadratic equation in r:

$$4a^2\delta f\left(\delta+\frac{\gamma_P}{\mu}(1-\delta)(1-f)\right)r^2+2a\left(\delta+\frac{\gamma_P}{\mu}(1-\delta-\delta f)\right)r-\frac{\gamma_P}{\mu}=0, \tag{5.29}$$

which admits as a solution for the epidemic threshold:

$$r_C^{APP} = \frac{2\frac{\gamma_P}{\mu} r_C^{NA}}{\delta + (1-\delta-f\delta)\frac{\gamma_P}{\mu} + \sqrt{(\delta + (1-\delta-f\delta)\frac{\gamma_P}{\mu})^2 + 4\delta f \frac{\gamma_P}{\mu}(\delta + \frac{\gamma_P}{\mu}(1-f)(1-\delta))}}. \tag{5.30}$$

In this case, the epidemic threshold explicitly shows a non-trivial dependence on the model parameters and in particular on the level of adoption of the app in the population f.

5.5 Stochastic vs prearranged contacts sampling

Hereafter, we compare the effectiveness of manual and digital CT in reducing the impact of the epidemic, obtaining fundamental insights into the detailed mechanisms of the two protocols and their intrinsic differences. We fix $\bar{\varepsilon} = f^2$, assuming a uniform $f(a_S) = f \; \forall a_S$: under this condition manual and digital CT have the same probability of tracing a single contact, i.e. they reconstruct the same number of contacts. This allows to compare the two protocols and obtain their relative effectiveness under the same tracing conditions, thus comparing their basic mechanisms. However, it should be noted that typically in real conditions $f^2 < \bar{\varepsilon}$, indeed $f^2 \approx 0.01 - 0.1$ in many states [27, 205, 227, 228], while $\bar{\varepsilon} \approx 0.3 - 0.5$ since typically the 30%-50% of the contacts is easily traceable as it occurs at home, at school or at work [172, 205]. These considerations allow to compare the two protocols in a more realistic scenario, even if we consider the same conditions of tracing a link to compare them in principle.

At first, we compare the two tracing protocols in case of a population with homogeneous activity and attractiveness, i.e. $\rho(a_S, b_S) = \delta(a_S - a)\delta(b_S - a)$, and in the absence of delays in manual tracing, i.e. $\tau_C = 0$: thus both f and ε are constant. In this case, we have an explicit form of the epidemic threshold for both manual and digital CT (see Eqs. (5.16) and (5.30)).

In Figure 5.7 we compare the increase in the epidemic threshold r_C/r_C^{NA} produced by the two tracing protocols as a function of $\varepsilon = f^2$. Both protocols increase significantly the epidemic threshold and produce the same increase, i.e. the same epidemic threshold r_C, for $\varepsilon = f^2 = 0$ and for $\varepsilon = f^2 = 1$: in the former case, the tracing is not applied and only symptomatic individuals are isolated, thus the epidemic threshold is r_C^{SYMPTO} of Eq. (5.2); in the latter case, all contacts are traced in both protocols and therefore the threshold is the same, since all asymptomatic are traced with no delay in both processes. For intermediate values of $\varepsilon = f^2$ the manual tracing is surprisingly always more effective than the digital one, since the increase produced in the epidemic threshold is always higher than that of the app-based mechanism (see the inset of Figure 5.7).

We are considering the simplest case of a homogeneous population without delays, therefore the difference observed between the performance of the two protocols is completely due to an intrinsic difference in the two types of tracing, i.e. an intrinsic difference in contacts sampling and exploration.

Digital CT divides the population into two subpopulations, one that downloaded the app and one that did not, generating a sub-network: all the links created within this sub-network are traceable, while all the links outside it or involving a single node of the sub-network cannot be traced. The digital CT does not take place on the complete population but is localized on a prearranged subpopulation. Digital CT

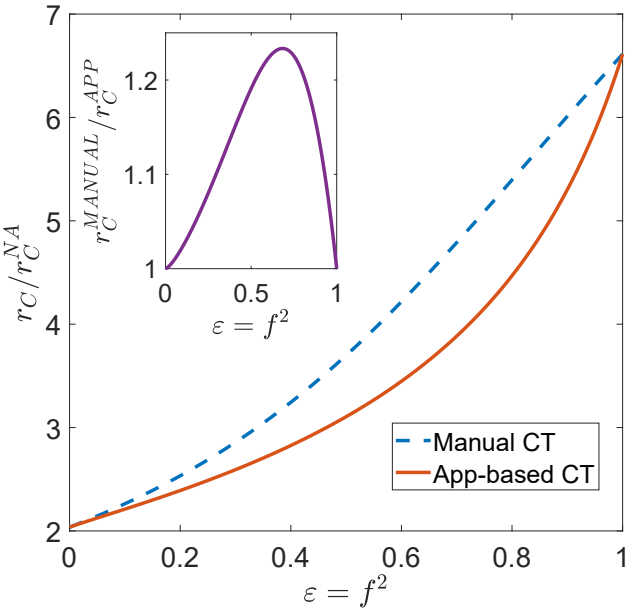

FIGURE 5.7: **Effects of manual and digital CT in homogeneous population.** We plot, as a function of $\varepsilon = f^2$, the ratio r_C/r_C^{NA} between the epidemic threshold in the presence of CT and symptomatic isolation and the threshold of the non-adaptive case. The inset shows the ratio r_C^{MANUAL}/r_C^{APP} between the epidemic threshold in the presence of manual CT and that in the presence of digital CT, as a function of $\varepsilon = f^2$. We consider $\rho(a_S, b_S) = \delta(a_S - a)\delta(b_S - b)$, $(1-\delta) = 0.43$, $\tau_P = 1.5$ days, $\tau = 14$ days and $\tau_C = 0$ [28].

corresponds to a *quenched* configuration: traceable nodes are pre-allocated and belong deterministically to a quenched prearranged fraction of nodes that have downloaded the app. See Figure 5.8 for a schematic representation of the digital sampling.

The manual CT performs a stochastic sampling of the contacts and the network of traceable nodes coincides with the entire population. Indeed, the manual approach can potentially reach the entire population since anyone who has come into contact with a symptomatic index case can be traced through the random exploration of the contacts. Manual CT corresponds to an *annealed* configuration: the traced nodes are dynamically generated by the epidemic, which producing symptomatics activates tracing potentially on the entire population of the node contacts. See Figure 5.8 for a schematic representation of the manual sampling.

The two protocols present an intrinsic difference in the nature of the contacts sampling and exploration, i.e. quenched vs annealed or prearranged vs stochastic sampling. This inherent difference favours manual over digital CT in reducing the impact of the epidemic, since manual CT is able to reach a wider set of nodes compared to digital CT, even in the hypothesis of equal probability of tracing a link $\varepsilon = f^2$. This is clearly shown analyzing the differences of the two protocols in tracing multiple infection processes: in Figure 5.8 we show the simplest example.

If an asymptomatic node A infects a node through symptomatic infection, the infector will be traced with probability ε in the manual CT and f^2 in the digital CT: thus the node is traced with the same probability for $\varepsilon = f^2$. However, if the same node infects two susceptible nodes with symptomatic infections, the infector will be traced if at least one of the two links has been traced: in the manual CT it is traced with probability $p_M = 1 - (1-\varepsilon)^2$, while in the digital CT it is traced with probability $p_D = f(1-(1-f)^2)$. For $\varepsilon = f^2$, the probability of tracing the

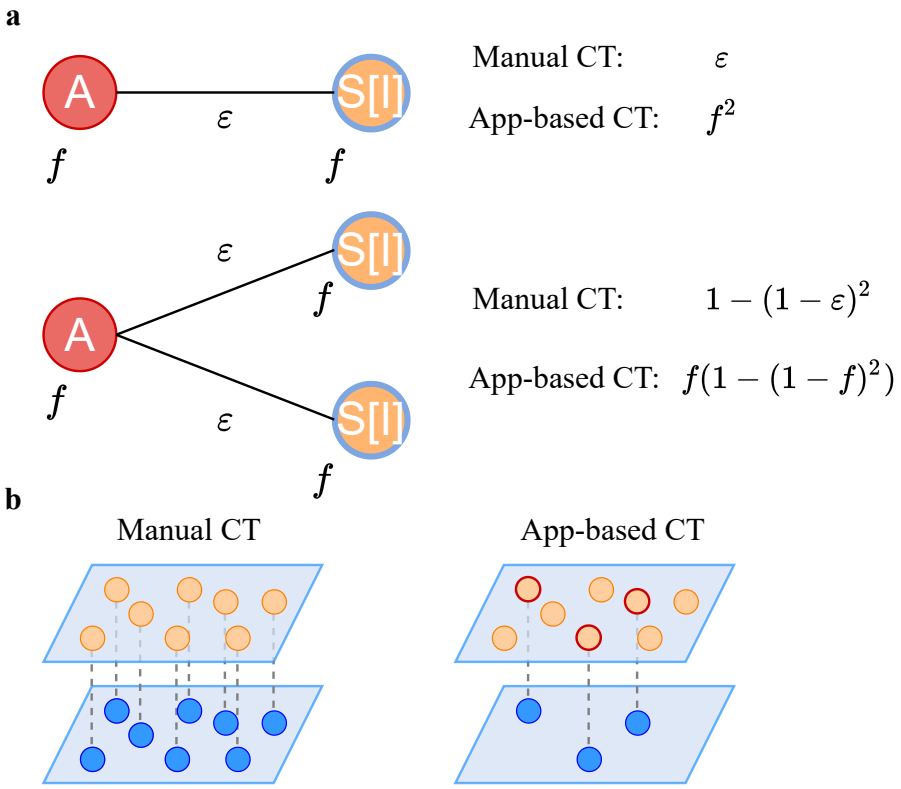

FIGURE 5.8: **Prearranged vs stochastic sampling in CT (i.e. quenched vs annealed).** In panel **a** we show schematically a simple example of tracing multiple infection processes, which clarify the inherent difference in contact sampling between manual and digital CT (see the main text for the detailed description) [28]. In panel **b** we show the intrinsic difference between manual and digital CT in tracing the population (orange nodes): for the manual procedure, the whole population is potentially reachable (blue nodes); for the digital procedure, only a preallocated sub-network is reachable (blue nodes), corresponding to the nodes who downloaded the app (red edge).

asymptomatic node with the manual CT is $p_M = 2f^2 - f^4$, while in the digital CT it is $p_D = 2f^2 - f^3$: p_M is always higher or equal to p_D. This simple example shows that considering a many-body process with multiple infections, the probability of tracing an asymptomatic node is always higher in the manual CT than in the digital CT, even assuming the same probability of tracing a link $\varepsilon = f^2$: this is due to the intrinsic difference of the two protocols in the sampling of contacts.

This result is obtained shifting the point of view from a single two-body infection process to a two-link infection process involving three nodes: the reasoning is similar when considering multiple higher-order infection processes involving a larger number of nodes. In such conditions this effect is further amplified up to the complete sequence of interactions in the network, favouring the manual protocol over the digital one and producing the better performance of the manual CT observed in Figure 5.7 in which the complete network is considered.

This first comparison highlights the intrinsic difference in the nature of contacts sampling performed by the two tracing protocols, which favours manual CT over digital CT and is crucial for understanding the fundamental mechanisms of CT. Starting from this baseline, we investigate the effects of realistic conditions such as a heterogeneous population, delays in manual tracing and limited scalability, to understand their role in realistic implementation of CT.

5.6 Effects of heterogeneity in agents behaviour

Many real systems present strong heterogeneity in the agents behaviour, due to a different propensity of individuals to undertake social interactions: this can be modelled into our model by considering a realistic power-law distribution of activity and a positive correlation between activity and attractiveness, as observed in many empirical cases [13, 14, 72, 76]:

$$\rho(a_S, b_S) = \rho_S(a_S)\delta(b_S - a_S) \sim a_S^{-(\nu+1)}\delta(b_S - a_S), \tag{5.31}$$

with $a \in [a_m, a_M]$, $a_M = \eta a_m$, with $\nu \in [0.5, 2]$ coherent with those obtained empirically. In this case, the population is characterized by the presence of hubs with high activity and attractiveness. Hereafter, unless otherwise specified, we set $\eta = 10^3$ and a_m is fixed so that $\overline{a_S} = 6.7$ days^{-1}, reproducing the average number of daily contacts per individual observed in real populations through surveys [172, 241].

The distribution $\rho_S(a_S)$ of Eq. (5.31) is maximally broad for $\nu = 1$, indeed the ratio $\overline{a_S^2}/\overline{a_S}^2$ is maximized for $\nu = 1$, as shown in Figure 5.9**a**, and it estimates the heterogeneity of $\rho_S(a_S)$. Indeed, for $\nu \to \infty$ the distribution approximates a maximally homogeneous Dirac delta function $\rho_S(a_S) \to \delta(a_S - \overline{a_S})$; for $\nu \to 0$ the distribution is counterintuitively more homogeneous than at $\nu = 1$ due to cut-off effects and to the constraints imposed on the distribution. Figure 5.9**b** shows the distribution $P(k)$ of the number of contacts k performed by an individual in the time window T_{CT} in our network model, for the described parameters: the obtained distribution is compatible with those obtained from empirical dataset and surveys, both for the average number of contacts and for the overall shape of the distribution.

We determine the pure effect of heterogeneity on the relative effectiveness of the two tracing protocols, by setting $\rho(a_S, b_S)$ as in Eq. (5.31), by considering the manual CT without delays $\tau_C = 0$ and without limited scalability $\varepsilon(a_S) = \varepsilon \, \forall a_S$ and considering $f(a_S) = f \, \forall a_S$. The epidemic threshold r_C is obtained numerically starting from the Eqs. (5.10) and (5.26).

In Figure 5.10**a**-**b** we show the increase in the epidemic threshold r_C/r_C^{NA} produced by the two CT protocols with respect to the non-adaptive case, as a function of the exponent ν of the distribution $\rho_S(a_S)$ of Eq. (5.31), by fixing $\varepsilon = f^2 = 0.1$ (i.e. $f \approx 0.316$) and $\varepsilon = f^2 = 0.6$ (i.e. $f \approx 0.775$). Both tracing protocols maximize their effectiveness in heterogeneous populations for $\nu \sim 1 - 1.5$: indeed, in heterogeneous populations the epidemic is driven by hubs, who behave like superspreaders, and the CT significantly reduce the impact of the epidemic by tracing and isolating some of them. The maximum efficacy does not occur exactly at $\nu = 1$, where the distribution $\rho_S(a_S)$ is maximally heterogeneous (see Figure 5.9**a**), but it shifts to different values of $\nu \sim 1$: indeed the epidemic threshold for both CT protocols depends both on the fluctuations of a_S, i.e. $\overline{a_S^2}/\overline{a_S}^2$, and on higher-order moments such as $\overline{a_S^3}$ (see Eqs. (5.10) and (5.26)), as well as on the epidemiological parameters.

Figure 5.10**a**-**c** shows clearly that manual CT produces a significantly higher increase in the epidemic threshold than the digital CT, even assuming $\varepsilon = f^2$. Moreover these differences are maximized for $\nu \sim 1 - 1.5$, i.e. they are wider in the heterogeneous case with respect to the homogeneous case, as shown by comparing the homogeneous case of Figure 5.7 and the heterogeneous case of Figure 5.10**c**. Thus, heterogeneity in agent behaviour strongly amplify the intrinsic differences between the two tracing procedure, enhancing the stochastic effects of contact sampling and exploration and extending the advantage of manual CT over digital CT.

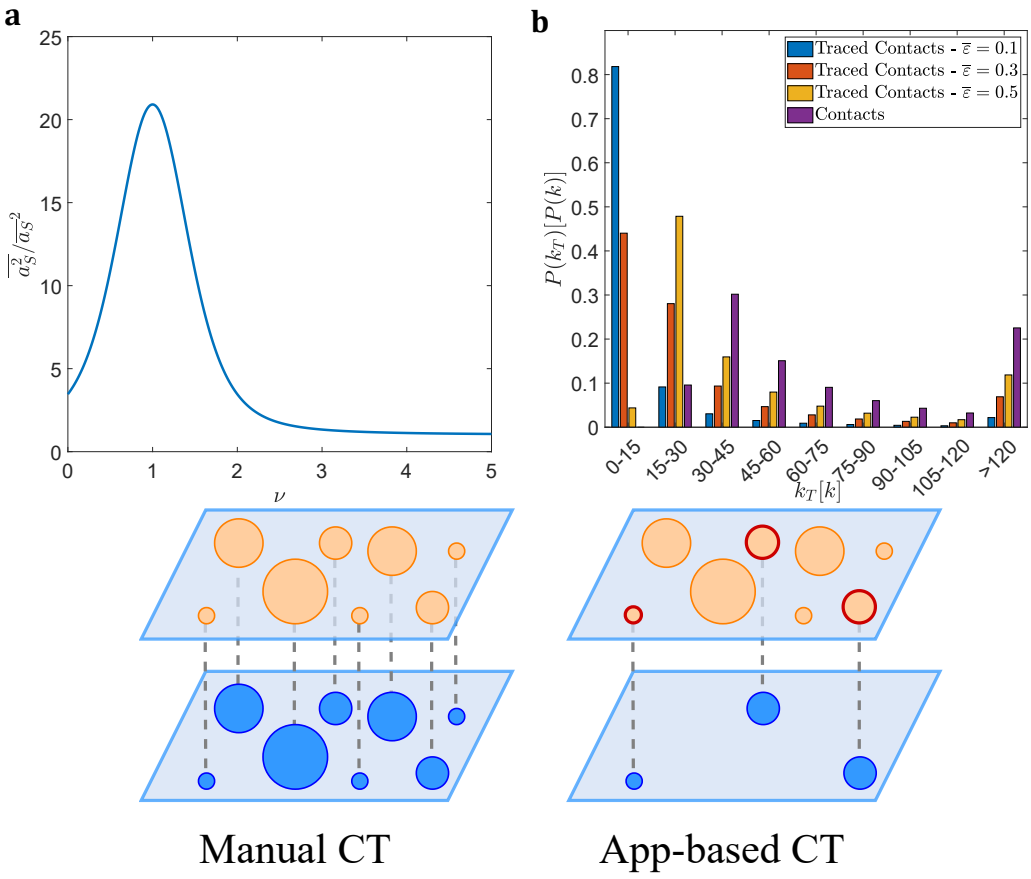

FIGURE 5.9: **Heterogeneous activity distribution.** Panel **a** shows the ratio $\overline{a_S^2}/\overline{a_S}^2$ as a function of the exponent ν for the distribution $\rho_S(a_S) \sim a_S^{-(\nu+1)}$, with $a_S \in [a_m, a_M]$, $\eta = a_M/a_m = 10^3$ [28]. In panel **b** we plot the distribution $P(k)$ of the contacts performed by an individual in a time window T_{CT} and the distribution $P(k_T)$ of the contacts traced with manual CT for an index case on the window T_{CT}, in the presence of the limited scalability described by $\varepsilon(a_S)$ as in Eq. (5.3) for $k_c = 130$, and for different values of $\bar{\varepsilon}$ (see legend). All distributions are obtained for the considered AD network model with $\rho(a_S, b_S) \sim a_S^{-(\nu+1)}\delta(b_S - a_S)$, fixing $\nu = 1$, $a_S \in [a_m, a_M]$, $\eta = a_M/a_m = 10^3$, $\overline{a_S} = 6.7$ days^{-1} and $T_{CT} = 14$ days [28]. In the lower panel we show schematically the difference between manual and digital CT in a heterogeneous population (orange nodes - their size is proportional to their activity): in manual CT all nodes are traceable (blue nodes), including the hubs; in digital CT only the nodes with the app (red edge) are traceable (blue nodes). The hubs without the app are completely invisible to digital CT.

This effect is due to the superior ability of manual CT to sample and trace hubs, i.e. nodes with high activity, compared to the digital CT. In a heterogeneous population the epidemic is driven and sustained by nodes with high activity/attractiveness (i.e. superspreaders). In the presence of digital CT, hubs without the app are invisible to the tracing and cannot be traced (see Figure 5.9): thus, they continue to be involved in interactions, producing contagion and sustaining the epidemic. On the contrary, manual CT is very effective in identifying hubs due to their high number of contacts and thanks to the stochastic nature of the sampling of contacts (see Figure 5.9): indeed, the hubs appear with high probability in the contact list of many index cases, due to their high number of contacts, and the stochastic annealed exploration

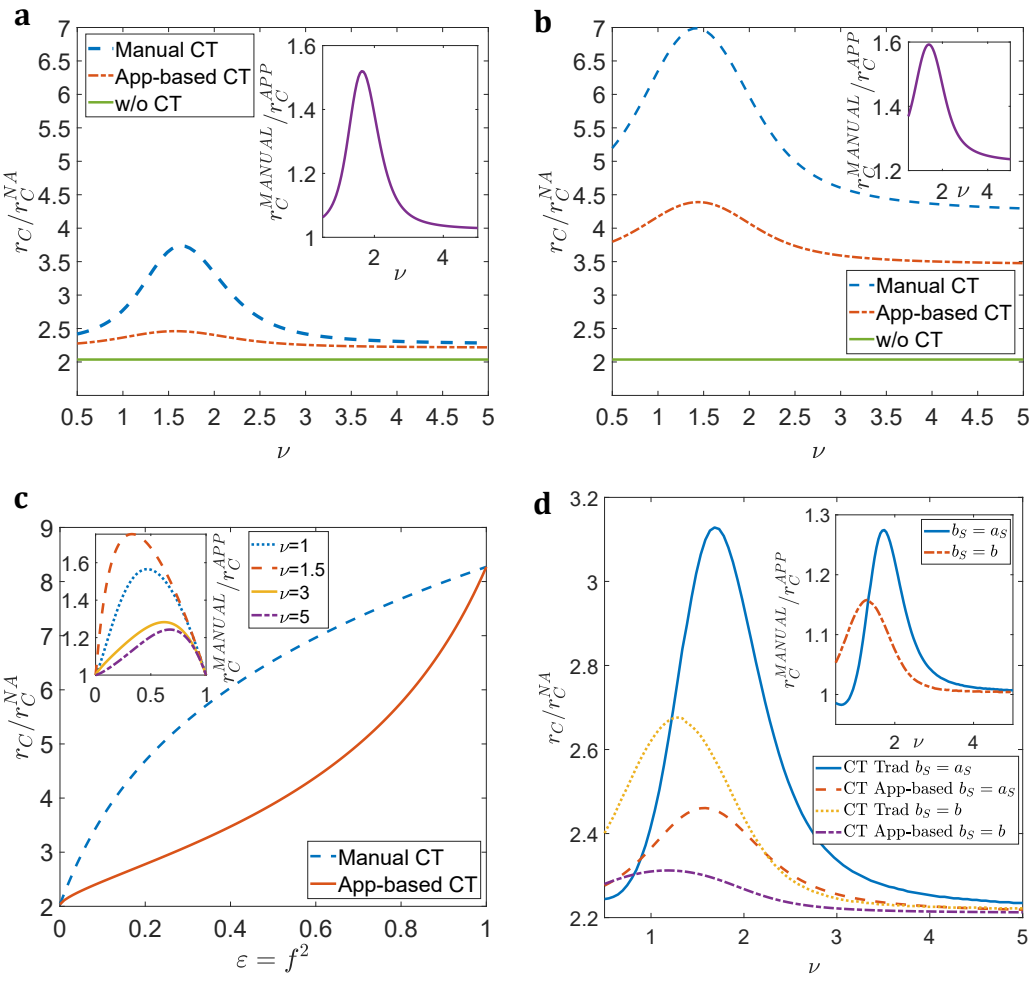

FIGURE 5.10: **Effects of heterogeneity on CT.** In panels **a-b** we plot, as a function of the exponent ν, the ratio r_C/r_C^{NA} between the epidemic threshold in the presence of CT and the threshold of the non-adaptive case. The inset shows, as a function of ν, the ratio r_C^{MANUAL}/r_C^{APP} between the threshold in the presence of manual CT and that in the presence of digital CT. In panel **a** $\varepsilon = f^2 = 0.1$ ($f \approx 0.316$), while in the panel **b** $\varepsilon = f^2 = 0.6$ ($f \approx 0.775$). In panel **c** the ratio r_C/r_C^{NA} is plotted as a function of $\varepsilon = f^2$ for both the tracing protocols and for $\nu = 1.5$. In the inset the ratio r_C^{MANUAL}/r_C^{APP} is plotted as a function of $\varepsilon = f^2$ for several exponents ν. In panels **a-c** we consider $\rho(a_S, b_S)$ as in Eq. (5.31), with $a_S \in [a_m, a_M = 10^3 a_m]$, $\overline{a_S} = 6.7$ days^{-1}, $(1-\delta) = 0.43$, $\tau_P = 1.5$ days, $\tau = T_{CT} = 14$ days, $\tau_C = 0$ and $\varepsilon(a_S) = \varepsilon \, \forall a_S$. Panel **d** is the same of panel **a** but different distributions $\rho(a_S, b_S)$ are considered (see legend), manual CT is characterized by a delay of $\tau_C = 3$ days and by limited scalability with $\varepsilon(a_S)$ as in Eq. (5.3) for $k_c = 130$ [28].

is able to reach them easily.

The results obtained are also robust by modifying the functional form of $\rho(a_S, b_S)$: in Figure 5.10**d** we compare the increase in the epidemic threshold produced by the two CT procedures for two distributions $\rho(a_S, b_S)$: the one of Eq. (5.31) and $\rho(a_S, b_S) \sim a_S^{-(\nu+1)} \delta(b_S - b)$, i.e. the same distribution but the attractiveness is the same $b_S = b$ for all nodes. In the latter case, the differences between manual and digital CT are reduced compared to the former case, as shown in the inset of Figure 5.10**d**. However, manual CT is still more effective for heterogeneous populations, under moderate τ_C and $\bar{\varepsilon} = f^2$ conditions, even in the presence of delays and limited scalability (see Section 5.7). The reduction in the differences between the two

CT protocols is due to the removal of the correlations between activity and attractiveness: indeed, this reduces the heterogeneity of the population by introducing a term of homogeneity, further confirming the effect of heterogeneity.

5.7 Effects of limited scalability and delays in manual CT

As we point out in Section 5.1.3, in real conditions there are some limitations to the effectiveness of manual CT, which could be overcome by digital CT, such as the presence of delays and limited scalability. We introduce into our model a relative delay in isolation in manual CT with respect to digital CT of about $\tau_C = 3$ days, consistent with estimated speed-up is isolation observed through the digital CT in UK and Switzerland [24, 205].

We also introduce local limited scalability in manual CT with $\varepsilon(a_S)$ as in Eq. (5.3). We consider $\rho(a_S, b_S)$ heterogeneous as in Eq. (5.31) with $\nu = 1$ and, in accordance with realistic estimates for the maximum number of contacts manually traced for very active individuals, we fix $k_c = 130$ [237, 240, 242]: this allows our model to reproduce several distributions and statistics in the number of contacts manually traced [172, 237, 243]. Indeed, as shown in Figure 5.9**b**, the distribution $P(k_T)$ of the number of contacts traced by an index case on the time window T_{CT} by manual CT reproduces the distributions observed empirically, both for its shape and its momenta [237, 243]. For example, the average number of contacts traced for each index case is approximately $10 - 60$ (depending on $\bar{\varepsilon} \approx 0.1 - 0.5$), consistent with the data reported on the effects of manual CT for COVID-19 and on the estimates of resources allocated for tracing when no other restrictions are implemented [237, 240, 242]. Indeed, in the presence of other measures, such as social distancing or lockdowns, the average number of daily contacts would be lower and thus also the number of traced contacts per index case. Analogous distributions, consistent with those observed empirically, are obtained for different parameters of k_c or for different ν.

The epidemic threshold r_C is obtained numerically, solving Eqs. (5.10) and (5.26): in Figure 5.11**a**-**b** we compare the increase in the epidemic threshold produced by the two protocols by setting $\bar{\varepsilon} = f^2$, where $\bar{\varepsilon} = \int da_S \rho_S(a_S)\varepsilon(a_S)$, as the exponent ν of the distribution $\rho_S(a_S)$ varies. Regardless of $\bar{\varepsilon}$, the effectiveness of manual CT is reduced by delays and limited scalability. For small $\bar{\varepsilon} = f^2 = 0.1$ (which however correspond to a high adoption of the app $f \approx 0.316$) and realistic delay $\tau_C = 3$ days, the limited scalability and delays make digital CT more effective than the manual CT only in homogeneous populations, i.e. for $\nu \to \infty$ or for $\nu \to 0$, while in heterogeneous populations manual CT is still more efficient (see Figure 5.11**a**). Thus, for moderates $\bar{\varepsilon} = f^2$ and τ_C, the inherent differences in contact sampling amplified by heterogeneity still favour manual over digital CT, also considering limited scalability and delays. On the contrary, for high delays τ_C and for high values $\bar{\varepsilon} = f^2$, digital CT becomes more effective than manual CT even in heterogeneous populations (see Figure 5.11**b**).

The advantages of manual CT induced by the sampling properties and by heterogeneity are quite robust in realistic conditions to delays and limited scalability. Indeed, in realistic heterogeneous populations digital CT produces effects comparable to manual CT only for high levels $\bar{\varepsilon} = f^2$, i.e. for irrealistic high app adoption level such as $f \approx 0.775$, and for considerable delays in manual CT. This is illustrated in Figure 5.11**c**, where the increase in the epidemic threshold for manual and digital CT is plotted as a function of $\bar{\varepsilon} = f^2$ for several τ_C values and for a heterogeneous

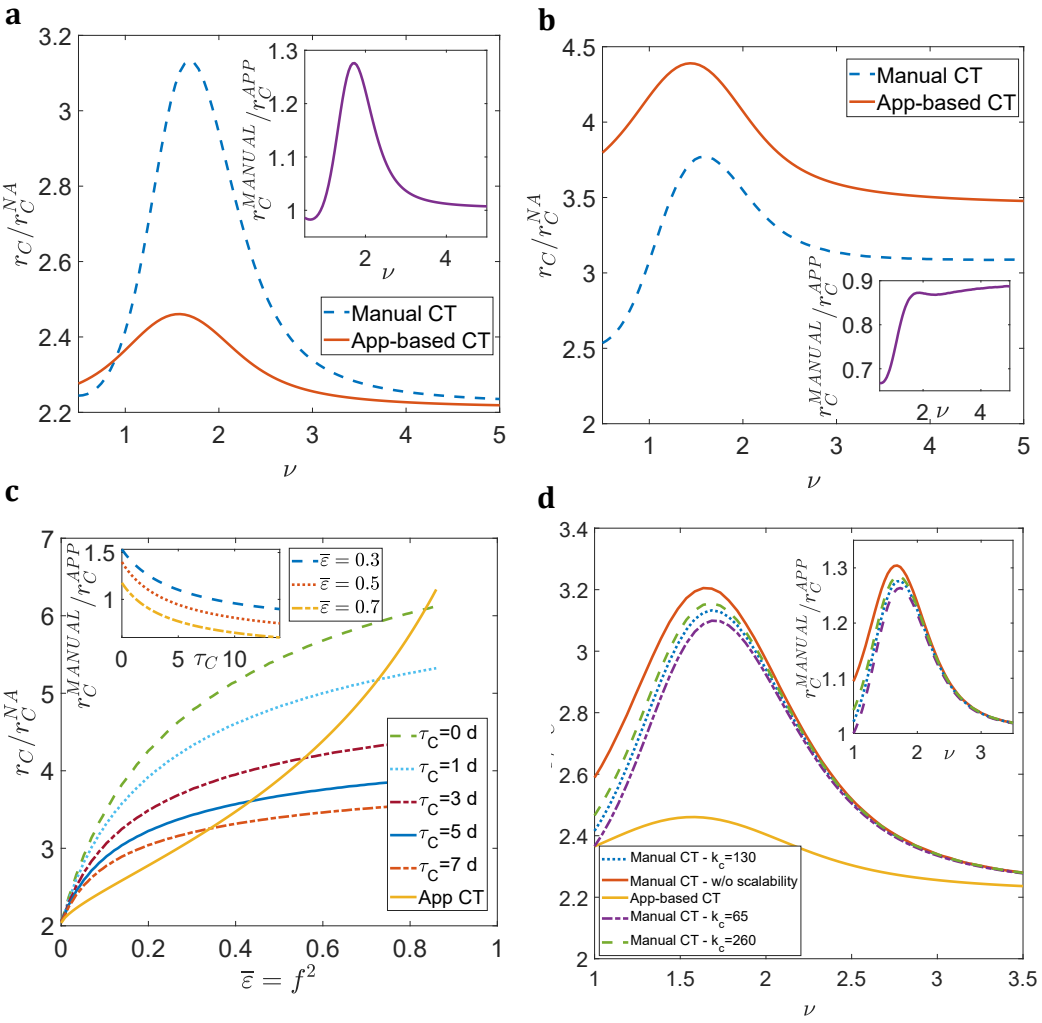

FIGURE 5.11: **Effects of tracing delay and limited scalability in manual contact tracing.** In panels **a**-**b** we plot, as a function of the exponent ν, the ratio r_C/r_C^{NA} between the epidemic threshold in the presence of CT and the threshold of the non-adaptive case. The insets show, as a function of ν, the ratio r_C^{MANUAL}/r_C^{APP} between the threshold in the presence of manual CT and that in the presence of digital CT. In panel **a** $\overline{\varepsilon} = f^2 = 0.1$ ($f \approx 0.316$) and $\tau_C = 3$ days; in panel **b** $\overline{\varepsilon} = f^2 = 0.6$ ($f \approx 0.775$) and $\tau_C = 5$ days. In panel **c** we plot the ratio r_C/r_C^{NA} as a function of $\overline{\varepsilon} = f^2$ for both tracing protocols, by fixing $\nu = 1.5$. In the inset the ratio r_C^{MANUAL}/r_C^{APP} is plotted as a function of τ_C for several $\overline{\varepsilon}$ values. Panel **d** is the same of panel **a** but different values of k_c are considered, also considering the case without limited scalability, i.e. $k_c \to \infty$ (see legend). In all panels we consider $\rho(a_S, b_S)$ of Eq. (5.31) with $a_S \in [a_m, a_M = 10^3 a_m]$, $\overline{a_S} = 6.7$ days^{-1}, $(1-\delta) = 0.43$, $\tau_P = 1.5$ days, $\tau = T_{CT} = 14$ days and limited scalability $\varepsilon(a_S)$ as in Eq. (5.3), moreover in panels **a**-**c** $k_c = 130$ [28].

population: high values of $\overline{\varepsilon} = f^2$ and τ_C are required for digital tracing to perform better than manual tracing in a heterogeneous population. Moreover, considering realistic $f^2 \approx 0.01 - 0.1$ values and $\overline{\varepsilon} \approx 0.3 - 0.5$ values, manual CT is still strongly more effective than the digital one in heterogeneous populations, even considering delays and local limited scalability.

The results obtained holds also by considering different k_c values. A higher value of k_c reduces the effects of limited scalability by bringing the results closer to the scalable case; while a lower value of k_c increases the effect of limited scalability, reducing the differences between the two procedures of CT. However, a change of k_c in a realistic range has minimal effects on the results, especially for heterogeneous

populations (see Figure 5.11**d**).

5.8 Effects of CT on the epidemic active phase

So far we focused on the effects of tracing on the epidemic threshold: we now consider also the active phase of the epidemic, in order to understand comprehensively the overall effect of the CT protocols on the epidemic and also their cost in term of the activity level of the population, i.e. on the population functionality, which is a crucial aspect ad discussed in Sections 5.1.2 and 5.1.3.

We performed numerical simulations of the epidemic process on the adaptive activity-driven network to investigate the active phase: the simulations are implemented using a continuous-time Gillespie-like algorithm [176], described in detail in Appendix B.

The results of the numerical simulation are averaged over different realizations of the temporal dynamics and of the disorder, so that the error on the height of the infection peak is less than 6%. In all simulations the initial conditions are imposed by infecting the node with the highest activity a_S [184] and the tracing is immediately implemented from the beginning of the epidemic.

In Figure 5.12 we show the temporal dynamics of the epidemic, plotting the temporal evolution of the fraction of infected individuals $Inf(t)$ and of the fraction of recovered nodes $R(t)$, by considering several values of $\bar{\varepsilon} = f^2$, of τ_C and of r/r_C^{NA}, and by taking into account local limited scalability in manual CT. Furthermore, in the insets of Figure 5.12 we report the temporal evolution of the average activity $\langle a(t) \rangle$ of the population and of the fraction of nodes in isolation $Iso(t)$: these variables allow to understand the cost of the CT protocols in terms of the activity level of the population, i.e. on the population functionality.

In Figure 5.12**a** we consider $\bar{\varepsilon} = f^2 = 0.1$, $\tau_C = 3$ days and $r/r_C^{NA} = 3.1$, i.e. $r \sim r_C$ in the presence of CT (see Figure 5.11). The infection peak with manual CT is lower than the digital one, it is slightly anticipated and the overall duration of the epidemic is reduced (peak width). This temporal dynamic produces an epidemic final size that in the manual CT is about half of that obtained by applying digital CT. Both the manual and digital CT produce a reduction in the average activity, which presents a minimum that slightly anticipates the peak in the number of isolated nodes: indeed the first nodes to get infected and to be isolated are those with high activity, thus their isolation produce a reduction of the activity in the early stages of the epidemic. The average activity, even at the minimum, still remains very high equal to about 98% of the pre-epidemic period for both the CT protocols. These results confirms that both manual and digital CT are very effective in limiting the impact of the epidemic on the population without disrupting societal activity and functionality of the population. Furthermore, the infection peak is lower for the manual CT, since this procedure produce a lower fraction of infected individuals.

These differences between manual and digital CT are again due to the heterogeneity of the population and to the intrinsic difference in contact sampling: manual CT is very effective in tracing high-activity nodes (see Section 5.6) and therefore isolates them at the beginning of the epidemic, drastically reducing the spread of the epidemic and partially the activity of the population by isolating only a few very active nodes. This produce a reduced peak of infection, a reduced peak of isolation and a reduction in activity. Digital CT, on the other hand, is not effective in tracing high-activity nodes (see Section 5.6), therefore the epidemic spreads more, sustained by the superspreaders, producing a higher infection peak and consequently a higher

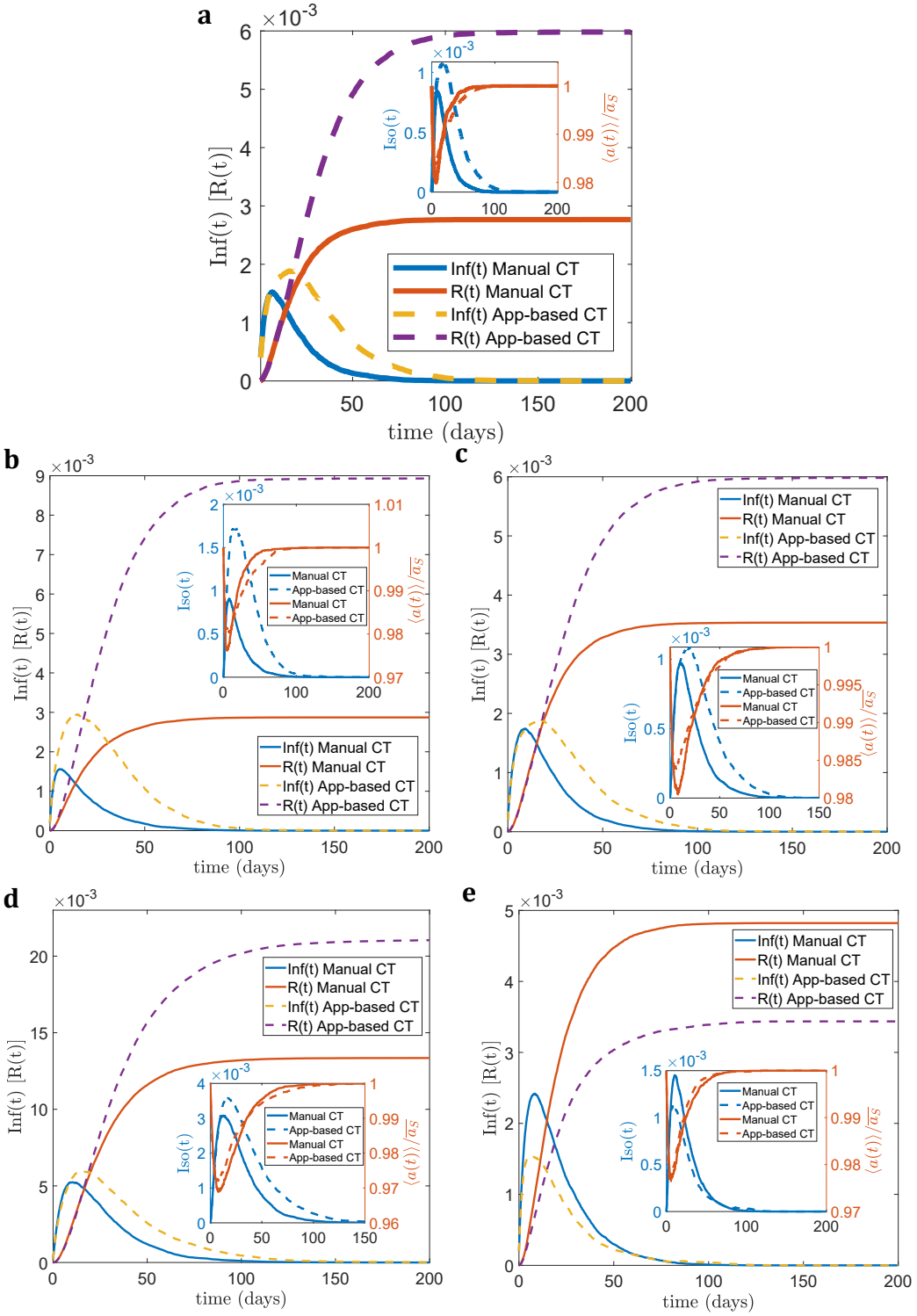

FIGURE 5.12: **Effects of CT on the epidemic active phase.** In all panels we plot the temporal evolution of the fraction of infected nodes $Inf(t)$ and the fraction of recovered nodes $R(t)$, for manual and digital CT. The insets represent the temporal evolution of the fraction of isolated nodes $Iso(t)$ and of the average activity $\langle a(t)\rangle$ normalized with $\overline{a_S}$. The curves are obtained through numerical simulations and are mediated on different realizations of the temporal dynamics and disorder. The errors, evaluated through the standard deviation, are smaller or comparable with the curves thickness. In all panels $\rho(a_S, b_S)$ is fixed as in Eq. (5.31) with $a_S \in [a_m, a_M = 10^3 a_m]$, $\nu = 1.5$, $\overline{a_S} = 6.7$ days^{-1}, $N = 5\,10^3$, $(1-\delta) = 0.43$, $\tau_P = 1.5$ days, $\tau = T_{CT} = 14$ days and $\varepsilon(a_S)$ as in Eq. (5.3) with $k_c = 130$. In panel **a** $\bar{\varepsilon} = f^2 = 0.1$, $\tau_C = 3$ days, $r/r_C^{NA} = 3.1$; in panel **b** $\bar{\varepsilon} = f^2 = 0.1$, $\tau_C = 0$ days, $r/r_C^{NA} = 4$; in panel **c** $\bar{\varepsilon} = f^2 = 0.1$, $\tau_C = 5$ days, $r/r_C^{NA} = 3.1$; in panel **d** $\bar{\varepsilon} = f^2 = 0.1$, $\tau_C = 5$ days, $r/r_C^{NA} = 7$; in panel **e** $\bar{\varepsilon} = f^2 = 0.6$, $\tau_C = 5$ days, $r/r_C^{NA} = 4.5$ [28].

isolation peak. The reduction in activity, however, is similar to the manual CT: in the manual procedure are isolate less nodes but with a higher activity, while in the digital approach are isolated more nodes but with a lower activity.

The differences in the active phase between the two protocols are reduced by increasing the delay in manual tracing τ_C: indeed the differences are maximized for $\tau_C = 0$, as shown in Figure 5.12**b** to be compared with Figure 5.12**a**. However, manual CT remains more effective for small $\bar{\varepsilon} = f^2$ even with considerable delays τ_C, as show in Figure 5.12**c**. If the system is deeply in the active phase $r \gg r_C$, the differences between the two protocols are reduced due to the high infectivity of the system, but manual CT remains more advantageous (see Figure 5.12**d**). Digital CT becomes more effective than manual tracing only in unrealistic conditions of high app adoption $\bar{\varepsilon} = f^2$ and severe delays τ_C: in this case the infection peak in the presence of the digital protocol is lower, narrower and anticipated, producing a lower epidemic final size compared to the manual CT (see Figure 5.12**e**).

These results show that the results obtained focusing on the epidemic threshold hold also for the epidemic active phase: the manual CT is more effective than the digital CT, for realistic parameter values, in reducing the impact of the epidemic. These effects are obtained by isolating a smaller number of individual and without interrupting the population activity: this is a crucial property of all containment measures aimed at ensuring the functionality of the population.

5.9 Hybrid contact tracing on AD network

We compare the purely manual CT and the purely digital CT in reducing the impact of an epidemic, characterizing their specific properties: however, typically digital CT and manual CT are complementary tools integrated in hybrid protocols. Indeed, digital CT was proposed alongside the traditional manual CT, with the aim of enhancing tracing and overcoming the main critical issues of manual tracing (see Section 5.1.3).

We now integrate the two procedures into a *hybrid protocol* to determine their relative contribution in reducing the impact of the epidemic when combined. This allows to obtain crucial insights for the optimization of the tracing strategies, through a careful integration of the two protocols and allocation of tracing resources.

In the hybrid protocol, each node with activity a_S downloads the app with probability $f(a_S)$. When presymptomatic nodes develop symptoms $P \to I$ they activate CT on the contacts engaged in the previous time window T_{CT}. If the index case downloaded the app, activates both manual and digital CT: all their contacts with the app are traced digitally and, if found in state A, they are isolated without delay; while the other contacts are traced manually with probability $\varepsilon(a_S)$ and, if found in state A, they are isolated with a delay τ_C. If the index case did not download the app, only the manual CT is activated and all contacts, whether they have the app or not, are traced manually with probability $\varepsilon(a_S)$ and isolated with delay τ_C, if found to be infected asymptomatic A. The hybrid protocol is schematically shown in Figure 5.13.

The compartmental epidemic model is analogous to that of digital tracing and the detailed spontaneous and contact-induced transitions are analogous to those of digital CT (see Appendix A). The population is divided into two subpopulations, one with the app and one without the app, therefore the epidemic compartments are distinguished for the two populations, as in the digital tracing (see Section 5.4), indicating with X the compartments for individuals without the app and indicating

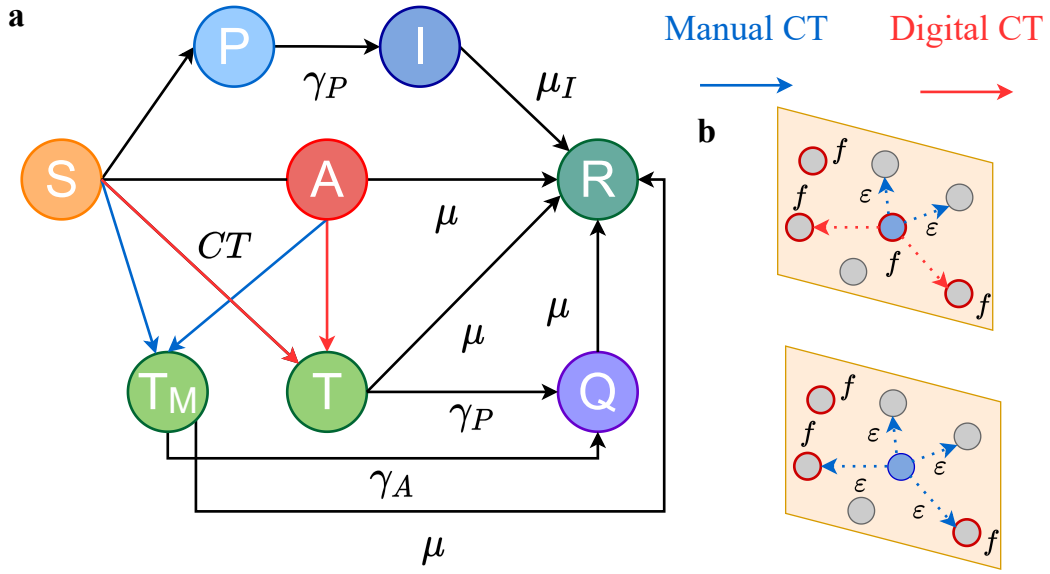

FIGURE 5.13: **Epidemic model with hybrid CT.** In panel **a** we schematically represent the compartmental epidemic model with hybrid CT for a node endowed with the tracing app, who can be traced both manually (red arrows) or digitally (blue arrows). Nodes without the app follow the compartmental epidemic model of Figure 5.4 since they can only be traced manually. The infection and tracing rates are not indicated, since they are complex but are described in detail in the main text and in Appendix A. In panel **b** we schematically show the main tracing mechanisms of the hybrid protocol activated by a symptomatic individual (blue node): an index case who downloaded the app (with probability f - red edge) digitally traces (red arrows) all the contacts engaged with nodes with the app and manually traces (blue arrows) contacts engaged with nodes without the app with probability ε; an index case who did not download the app traces all the contacts manually (blue arrows) with probability ε.

with SX^{α} (with the superscript $^{\alpha}$) compartments for individuals with the app. However, in the hybrid protocol an individual who downloaded the app can be traced either with the manual protocol, with an isolation delay τ_C, or with the digital protocol, without isolation delay. On the contrary, a node without the app can only be traced manually with isolation delay τ_C. It is necessary to introduce an additional compartment T_M^{α} for nodes with app traced manually: their transition to the compartment of the isolated asymptomatic $T_M^{\alpha} \to Q^{\alpha}$ occurs with rate $\gamma_A = 1/(\tau_P + \tau_C)$, while the transition $T^{\alpha} \to Q^{\alpha}$ occurs with rate $\gamma_P = 1/\tau_P$, where T^{α} indicates now the compartment of asymptomatic with the app traced digitally. Thus, nodes with the app follow the compartmental epidemic model in Figure 5.13, while nodes without the app follow the compartmental epidemic model of Figure 5.4.

The population is divided into two subpopulations, however, unlike the pure digital tracing, hybrid CT can trace links between the two different subpopulations and within each subpopulation. Indeed, the links in the subpopulation with the app are traced digitally, while the links between the different subpopulations and in the app-free subpopulation are traced manually. This aspect enhances both manual and digital CT: all links invisible to the pure digital CT due to the quenched nature of the protocol are now traceable manually; compared to the pure manual case some links can be traced faster and without limited scalability. Integrating the two protocols the advantages of the two approaches are combined, i.e. the advantage of the stochastic sampling of the manual CT, especially in heterogeneous populations, and the advantage of digital CT in the rapidity of the tracing and in the scalability.

Similarly to the purely manual and digital CT, the model is exactly mean-field and the analytical calculation of epidemic threshold can be performed with reference to the SIS model without loss of generality (see Appendix A). We describe the epidemic dynamics through the same *activity-attractiveness-based mean-field approach* described for the manual CT in Section 5.3.

At the mean-field level, the epidemic dynamics are described by the probabilities defined in Section 5.4 for the digital protocol, with these additional/redefined probabilities: $T^{\alpha}_{a_S,b_S}(t)$, $T^{\alpha}_{a_S,b_S|M}(t)$, $1-A^{\alpha}_{a_S,b_S}(t)-T^{\alpha}_{a_S,b_S}(t)-T^{\alpha}_{a_S,b_S|M}(t)-Q^{\alpha}_{a_S,b_S}(t)$ for a node of class (a_S,b_S) with the app, that will not develop symptoms (if infected), to be respectively asymptomatic traced digitally, asymptomatic traced manually or susceptible at time t; $T_{a_S,b_S}(t)$, $Q_{a_S,b_S}(t)$, $1-A_{a_S,b_S}(t)-T_{a_S,b_S}(t)-Q_{a_S,b_S}(t)$ for a node of class (a_S,b_S) without the app, that will not develop symptoms (if infected), to be respectively traced asymptomatic, isolated asymptomatic or susceptible at time t.

In the mean-field approach, the average attractiveness is:

$$\langle b(t)\rangle = \overline{b_S} - (1-\delta)(\overline{fb_S Q^{\alpha}}(t) + \overline{(1-f)b_S Q}(t)) - \delta(\overline{fb_S I^{\alpha}}(t) + \overline{(1-f)b_S I}(t)), \tag{5.32}$$

where we define $\overline{g} = \int da_S db_S \rho(a_S,b_S) g_{a_S,b_S}$. We assume to be in the thermodynamic limit and we consider the case of $\rho(a_S,b_S) = \rho_S(a_S)\delta(b_S-a_S)$, so in this case the probability of adoption of the app $f(a_S)$ and the recall probability $\varepsilon(a_S)$ depend on the activity class a_S of the node.

The probabilities that define the epidemic dynamics evolve according to the following equations, which are obtained analogously to the equations for the manual and digital CT separately:

$$\partial_t P_{a_S}(t) = -\gamma_P P_{a_S}(t) + 2\lambda(1-P_{a_S}(t)-I_{a_S}(t))\frac{a_S}{\langle b(t)\rangle}Z(t) \tag{5.33}$$

$$\partial_t I_{a_S}(t) = -\mu_I I_{a_S}(t) + \gamma_P P_{a_S}(t) \tag{5.34}$$

$$\partial_t P^{\alpha}_{a_S}(t) = -\gamma_P P^{\alpha}_{a_S}(t) + 2\lambda(1-P^{\alpha}_{a_S}(t)-I^{\alpha}_{a_S}(t))\frac{a_S}{\langle b(t)\rangle}Z(t) \tag{5.35}$$

$$\partial_t I^{\alpha}_{a_S}(t) = -\mu_I I^{\alpha}_{a_S}(t) + \gamma_P P^{\alpha}_{a_S}(t) \tag{5.36}$$

$$\begin{aligned}\partial_t A_{a_S}(t) = &-\mu A_{a_S}(t)\\ &+2\lambda(1-A_{a_S}(t)-T_{a_S}(t)-Q_{a_S}(t))\frac{a_S}{\langle b(t)\rangle}W(t)\\ &-2\lambda\delta A_{a_S}(t)\frac{a_S}{\langle b(t)\rangle}(\overline{a_S\varepsilon f}-\overline{a_S\varepsilon f P^{\alpha}}(t)-\overline{a_S\varepsilon f I^{\alpha}}(t))\\ &-2\lambda\delta A_{a_S}(t)\frac{a_S}{\langle b(t)\rangle}(\overline{a_S\varepsilon(1-f)}-\overline{a_S\varepsilon(1-f)P}(t)-\overline{a_S\varepsilon(1-f)I}(t))]\end{aligned} \tag{5.37}$$

$$\begin{aligned}\partial_t T_{a_S}(t) = &-(\mu+\gamma_A)T_{a_S}(t)\\ &+2\lambda\delta\frac{a_S}{\langle b(t)\rangle}(1-A_{a_S}(t)-T_{a_S}(t)-Q_{a_S}(t))[\overline{a_S\varepsilon f P^{\alpha}}(t)+\overline{a_S\varepsilon(1-f)P}(t)]\\ &+2\lambda\delta A_{a_S}(t)\frac{a_S}{\langle b(t)\rangle}(\overline{a_S\varepsilon f}-\overline{a_S\varepsilon f P^{\alpha}}(t)-\overline{a_S\varepsilon f I^{\alpha}}(t))\\ &+2\lambda\delta A_{a_S}(t)\frac{a_S}{\langle b(t)\rangle}(\overline{a_S\varepsilon(1-f)}-\overline{a_S\varepsilon(1-f)P}(t)-\overline{a_S\varepsilon(1-f)I}(t))]\end{aligned} \tag{5.38}$$

$$\partial_t Q_{a_S}(t) = -\mu Q_{a_S}(t) + \gamma_A T_{a_S}(t) \tag{5.39}$$

$$\begin{aligned}
\partial_t A^{\alpha}_{a_S}(t) = & -\mu A^{\alpha}_{a_S}(t) \\
& + 2\lambda(1 - A^{\alpha}_{a_S}(t) - T^{\alpha}_{a_S}(t) - T^{\alpha}_{a_S|M}(t) - Q^{\alpha}_{a_S}(t))\frac{a_S}{\langle b(t)\rangle}T(t) \\
& - 2\lambda\delta A^{\alpha}_{a_S}(t)\frac{a_S}{\langle b(t)\rangle}(\overline{a_S f} - \overline{a_S f P^{\alpha}}(t) - \overline{a_S f I^{\alpha}}(t)) \\
& - 2\lambda\delta A^{\alpha}_{a_S}(t)\frac{a_S}{\langle b(t)\rangle}(\overline{a_S\varepsilon(1-f)} - \overline{a_S\varepsilon(1-f)P}(t) - \overline{a_S\varepsilon(1-f)I}(t))
\end{aligned} \tag{5.40}$$

$$\begin{aligned}
\partial_t T^{\alpha}_{a_S}(t) = & -(\mu + \gamma_P)T^{\alpha}_{a_S}(t) \\
& + 2\lambda\delta\frac{a_S}{\langle b(t)\rangle}(1 - A^{\alpha}_{a_S}(t) - T^{\alpha}_{a_S}(t) - T^{\alpha}_{a_S|M}(t) - Q^{\alpha}_{a_S}(t))\overline{a_S f P^{\alpha}}(t) \\
& + 2\lambda\delta A^{\alpha}_{a_S}(t)\frac{a_S}{\langle b(t)\rangle}[\overline{a_S f} - \overline{a_S f P^{\alpha}}(t) - \overline{a_S f I^{\alpha}}(t)]
\end{aligned} \tag{5.41}$$

$$\begin{aligned}
\partial_t T^{\alpha}_{a_S|M}(t) = & -(\mu + \gamma_A)T^{\alpha}_{a_S|M}(t) \\
& + 2\lambda\delta\frac{a_S}{\langle b(t)\rangle}(1 - A^{\alpha}_{a_S}(t) - T^{\alpha}_{a_S}(t) - T^{\alpha}_{a_S|M}(t) - Q^{\alpha}_{a_S}(t))\overline{a_S\varepsilon(1-f)P}(t) \\
& + 2\lambda\delta A^{\alpha}_{a_S}(t)\frac{a_S}{\langle b(t)\rangle}[\overline{a_S\varepsilon(1-f)} - \overline{a_S\varepsilon(1-f)P}(t) - \overline{a_S\varepsilon(1-f)I}(t)]
\end{aligned} \tag{5.42}$$

$$\partial_t Q^{\alpha}_{a_S}(t) = -\mu Q^{\alpha}_{a_S}(t) + \gamma_P T^{\alpha}_{a_S}(t) + \gamma_A T^{\alpha}_{a_S|M}(t) \tag{5.43}$$

where

$$\begin{aligned}
Z(t) = & \delta(\overline{a_S f P^{\alpha}}(t) + \overline{a_S(1-f)P}(t)) \\
& + (1-\delta)(\overline{a_S f A^{\alpha}}(t) + \overline{a_S f T^{\alpha}}(t) + \overline{a_S f T^{\alpha}_M}(t) + \overline{a_S(1-f)T}(t) + \overline{a_S(1-f)A}(t))
\end{aligned} \tag{5.44}$$

$$\begin{aligned}
T(t) = & \delta\overline{a_S(1-\varepsilon)(1-f)P}(t) \\
& + (1-\delta)(\overline{a_S f A^{\alpha}}(t) + \overline{a_S f T^{\alpha}}(t) + \overline{a_S f T^{\alpha}_M}(t) + \overline{a_S(1-f)T}(t) + \overline{a_S(1-f)A}(t))
\end{aligned} \tag{5.45}$$

$$\begin{aligned}
W(t) = & \delta(\overline{a_S(1-\varepsilon)f P^{\alpha}}(t) + \overline{a_S(1-\varepsilon)(1-f)P}(t)) \\
& + (1-\delta)(\overline{a_S f A^{\alpha}}(t) + \overline{a_S f T^{\alpha}}(t) + \overline{a_S f T^{\alpha}_M}(t) + \overline{a_S(1-f)T}(t) + \overline{a_S(1-f)A}(t))
\end{aligned} \tag{5.46}$$

These equations constitute a set of eleven coupled non-linear differential equations for each class a_S, which are not closed nor complete due to the presence of the averaged probabilities. Moreover, the averaged probabilities are much more interesting variables compared to the single probability for each class a_S. Thus, by averaging on the activity we obtain a system of twenty-two coupled non-linear differential equations that is closed and complete: this set of equations admits as a solution the absorbing state, that is the configuration with all nodes susceptible. The epidemic threshold can thus be obtained with a linear stability analysis around the absorbing state: see Appendix A for the details of the computation of the system of equations and for the linear stability analysis.

In this case it is not possible to obtain a closed relation for the epidemic threshold, which can only be obtained by imposing numerically the stability of the absorbing state, i.e. by imposing all eigenvalues of the Jacobian matrix of the system to be negative (see Appendix A). We obtain numerically the epidemic threshold for the hybrid protocol for arbitrary distribution of the activity $\rho_S(a_S)$, for arbitrary distribution of the app in the population $f(a_S)$ and for arbitrary recall probability $\varepsilon(a_S)$.

The terms in the matrix J that determines the epidemic threshold suggest that r_C depends strongly on the heterogeneity and on the high-order moments of the distribution $\rho_S(a_S)$; furthermore it depends on the correlations $\varepsilon(a_S)$ and $f(a_S)$, but also on the cross-correlations between f and ε, i.e. on the correlations between the probability for a node to remember their contact and to download the tracing app.

Some limit cases can be considered: by setting $\varepsilon(a_S) = 0 \, \forall \, a_S$ we obtain the same conditions of Eq. (5.26) for the epidemic threshold, i.e. the purely digital CT; by setting $f(a_S) = 0 \, \forall \, a_S$ we obtain the same conditions of Eq. (5.10) for the epidemic threshold, i.e. the purely manual CT.

5.9.1 Effects of hybrid CT

In Figure 5.14**a** we plot the increase $r_C^{APP+MANUAL}/r_C^{NA}$ in the epidemic threshold produced by the hybrid CT protocol with respect to the non-adaptive case for a fixed realistic $\bar{\varepsilon}$ and varying f^2, by assuming $f(a_S) = f \, \forall a_S$, for realistic heterogeneous populations. This allows to estimate the contribution of digital CT in the hybrid protocol for different level of app adoption f, since the manual CT contribution is fixed with $\bar{\varepsilon}$. In general, even a small probability f allows to increase the epidemic threshold compared to the case in which only manual CT is applied, as observed in the inset of Figure 5.14**a**. Since digital CT can reach otherwise untraced nodes and speed up tracing in some cases, even for low levels of app adoption a small mitigation effect is present [189]. However, the digital contribution grows relatively slowly with f^2: the contribution of digital CT is significant only for high f, i.e. an unrealistic level of app adoption, considering the penetration of smartphones in the population [25, 221, 225] and the current levels of app adoption (see Section 5.1.3) [27, 227, 228].

In Figure 5.14**b** we plot the increase in the epidemic threshold produced by manual CT in the hybrid protocol for fixed realistic f app adoption level, estimating its contribution to the mitigation of the epidemic as $\bar{\varepsilon}$ varies. A small $\bar{\varepsilon}$ is sufficient to obtain a strong increase in the epidemic threshold, compared to the case in which only digital tracing was applied. Panels **a** and **b** of Figure 5.14 show that manual and digital CT have very different effects even if integrated into a hybrid protocol: manual CT increases the threshold rapidly, in realistic conditions of digital tracing $f \sim 0.2$, producing an increase of about 80% with only $\bar{\varepsilon} \gtrsim 0.3$; digital CT, in realistic conditions of manual tracing $\bar{\varepsilon} \gtrsim 0.3$, produces a significant increase of at least 50% only for $f \gtrsim 0.6 - 0.75$. These values are consistent with those obtained in other works [24, 26, 27, 201, 225].

This different contribution of the two tracings to the hybrid protocol is further shown in Figure 5.14**c** where the increase in the epidemic threshold produced by the hybrid protocol $r_C^{MANUAL+APP}/r_C^{NA}$ is represented as a function of f^2 and $\bar{\varepsilon}$ via a heat-map. These differences are due to the intrinsic differences of the two protocols. Digital CT, as we discussed in Section 5.6, is not effective in tracing superspreaders, while manual CT is very effective in doing so: thus by activating the manual CT together with the digital one, a small $\bar{\varepsilon}$ is enough to effectively trace the superspreaders otherwise not traced digitally, strongly impacting the mitigation of the epidemic. Then the increment saturates due to the limited scalability and delays that characterize manual CT. By activating digital tracing together with manual tracing, the superspreaders are already traced by the manual method and digital CT need a high f to have a sufficiently large subpopulation with the app to involve many hubs and many nodes, in order to speed up tracing and enhance its effectiveness.

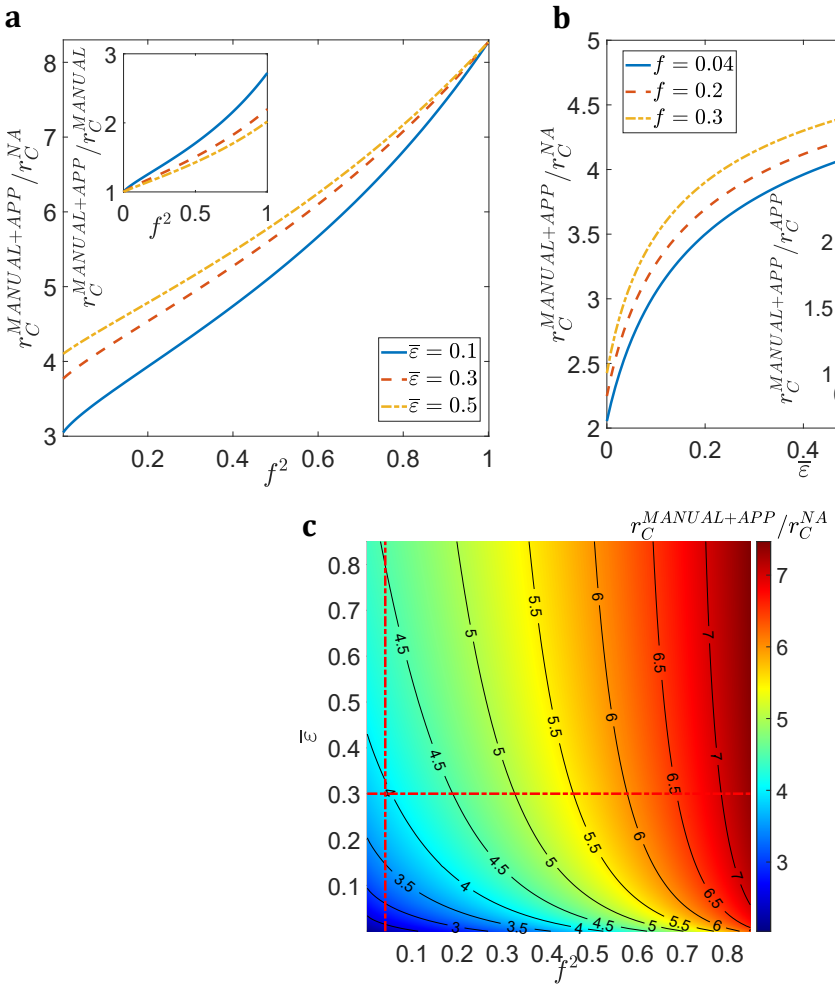

FIGURE 5.14: **Effects of hybrid CT protocol.** In panel **a** we plot, as a function of f^2, the ratio $r_C^{MANUAL+APP}/r_C^{NA}$ between the epidemic threshold in the presence of the hybrid protocol and the threshold of the non-adaptive case, by fixing realistic values of $\overline{\varepsilon}$ (see legend). In the inset the ratio $r_C^{MANUAL+APP}/r_C^{MANUAL}$, between the threshold when the hybrid protocol is implemented and when only the manual CT is considered, is plotted as a function of f^2. In panel **b** the ratio $r_C^{MANUAL+APP}/r_C^{NA}$ is plotted as a function of $\overline{\varepsilon}$, by fixing realistic values of f^2 (see legend). In the inset the ratio $r_C^{MANUAL+APP}/r_C^{APP}$, between the threshold when the hybrid protocol is implemented and when only the digital CT is considered, is plotted as a function of $\overline{\varepsilon}$. In panel **c** we plot the ratio $r_C^{MANUAL+APP}/r_C^{NA}$ as a function of $\overline{\varepsilon}$ and f^2 through a heat-map. The red bash-dotted lines correspond to $\overline{\varepsilon} = 0.3$ and $f = 0.2$, i.e. the red dashed curves in panels **a**-**b**. In all panels we consider $\rho(a_S, b_S)$ as Eq. (5.31) with $a_S \in [a_m, a_M = 10^3 a_m]$, $\nu = 1.5$, $\overline{a_S} = 6.7$ days^{-1}, $(1-\delta) = 0.43$, $\tau_P = 1.5$ days, $\tau = T_{CT} = 14$ days, $\tau_C = 3$ days and limited scalability $\varepsilon(a_S)$ as in Eq. (5.3) with $k_c = 130$ [28].

Integrating the two tracing protocols is always an effective strategy, as the two protocols enhance each other with their mutual advantages. However, the analysis carried out also show a key role played by manual tracing in any hybrid realistic protocol, since it produces a dominant and significantly higher contribution than the digital one in realistically heterogeneous populations and for a realistic parametrization of the model. In particular, careful integration strategies and resources allocation policies need to be implemented in order to optimize the integration and the outcome of CT.

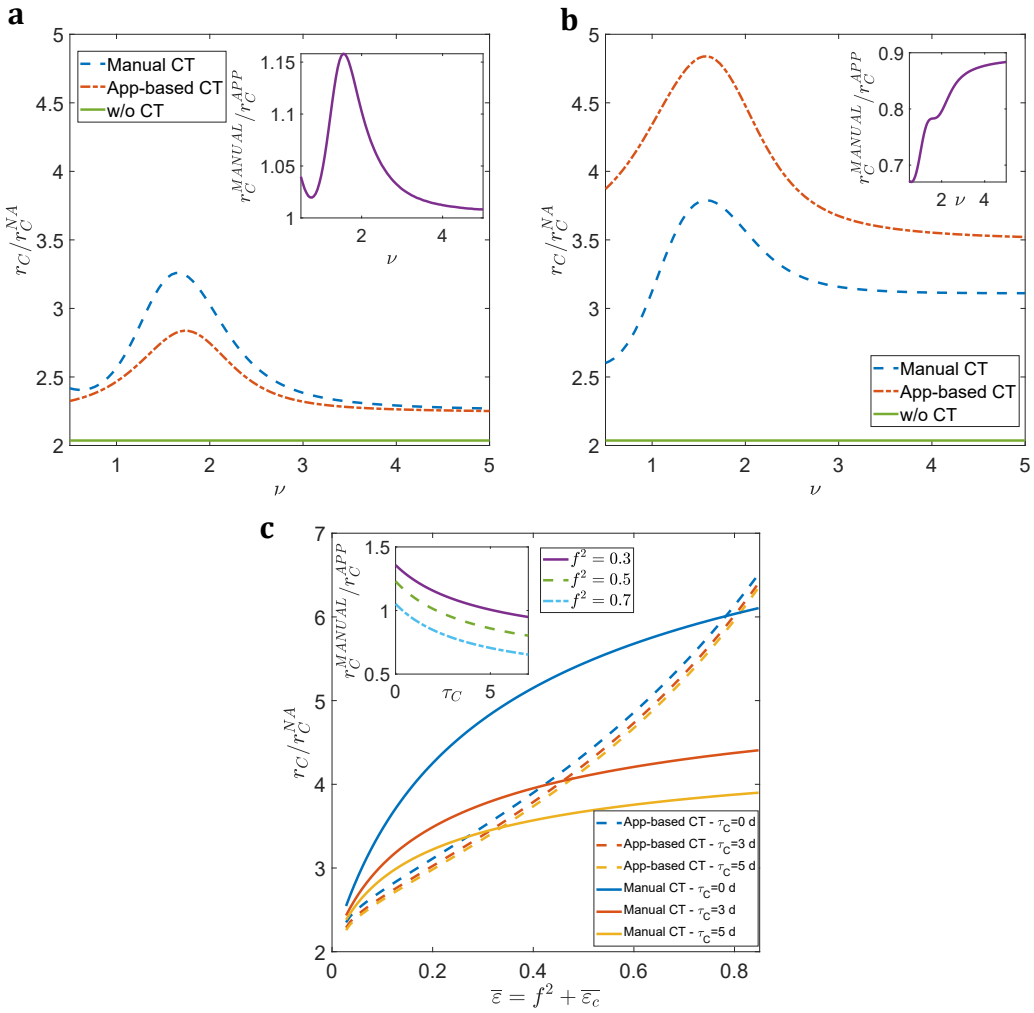

FIGURE 5.15: **Effects of deterministic household CT.** In panels **a**-**b** we plot, as a function of the exponent ν, the ratio r_C/r_C^{NA} between the epidemic threshold in the presence of tracing and the threshold in the non-adaptive case, considering both CT protocols augmented by the additional deterministic household CT. In the inset we plot, as a function of ν, the ratio r_C^{MANUAL}/r_C^{APP} between the epidemic threshold in the presence of augmented manual CT and the threshold of augmented digital CT. In panel **a** we fix $\tau_C = 3$ days and $f^2 = 0.1$; in panel **b** we fix $\tau_C = 5$ days and $f^2 = 0.6$. In panel **c** the ratio r_C/r_C^{NA} is plotted as a function of $\overline{\varepsilon} = f^2 + \overline{\varepsilon_h}$ for both augmented CT protocols, setting $\nu = 1.5$ and for different values of τ_C. In the inset the ratio r_C^{MANUAL}/r_C^{APP} is plotted as a function of τ_C for several values of f^2. In all panels we consider $s = 3$ as the size of household, $\varepsilon_h^* = 1$, i.e. $\overline{\varepsilon_h} = 0.028$, $\rho(a_S, b_S)$ as in Eq. (5.31) with $a_S \in [a_m, a_M = 10^3 a_m]$, $\overline{a_S} = 6.7$ days^{-1}, $(1-\delta) = 0.43$, $\tau_P = 1.5$ days, $\tau = T_{CT} = 14$ days and $\varepsilon(a_S)$ as in Eq. (5.3) with $k_c = 130$ [28].

5.9.2 Deterministic household CT

The hybrid CT presented in Section 5.9 allows to model specific realistic behaviours observed in the implementation of contact tracing in structured populations. For example, when individuals develop symptoms, their household is always traced: this can be modelled in our framework assuming that a number of contacts, corresponding to the household, is always traced [244]. This augment both protocols with a deterministic household tracing term, modelled with a part of the contacts always traced, since in our model the network has no structure or memory.

Augmented digital tracing is modelled using the hybrid tracing formalism: the

digital CT is augmented by assuming an additional manual component of tracing activated by the index case, which traces at least s contacts equal to the size of the household (on average $s = 3$ in several populations [245]). If the index case has less than s contacts in the tracing window, all the contact will be traced: this corresponds to fixing a recall probability $\varepsilon_h(a_S)$ defined as in Eq. (5.3) but with $k_c = s$ and $\varepsilon_h^* = 1$. The probability of tracing a contact in augmented digital CT is $\overline{\varepsilon_h} + f^2$, where $\overline{\varepsilon_h} = \int da_S \rho_S(a_S)\varepsilon_h(a_S)$. Manual CT is implemented considering both delays and limited scalability.

The augmented manual tracing is performed with the formalism of the manual tracing, with delay τ_C and limited scalability $\varepsilon(a_S)$ of Eq. (5.3), only assuming that $\bar{\varepsilon} = f^2 + \overline{\varepsilon_h}$ so that the probability of tracing a link is the same as compared to the augmented digital CT. In this case, even for the augmented manual CT at least the household tracing is performed thanks to the term $\overline{\varepsilon_h}$, indeed for $f^2 = 0$ we have $\bar{\varepsilon} = \overline{\varepsilon_h}$ and therefore both augmented protocols trace a minimum fraction of contacts.

In Figure 5.15 we show that the results produced in Section 5.7 are robust with respect to the addition of the deterministic tracing of the households, which augment the tracing protocols. For low values of f^2, i.e. of $\bar{\varepsilon} = f^2 + \overline{\varepsilon_h}$, augmented manual CT is more advantageous than augmented digital CT in heterogeneous populations: the digital protocol becomes more effective in heterogeneous populations only for high level of app adoption or unrealistic long delays of manual CT (see Figure 5.15).

5.9.3 Correlations in CT app adoption

In the previous Sections we always considered the tracing app uniformly distributed over the population: however we have shown the role of superspreaders in the epidemic and of the correlations $f(a_S)$ in shaping the epidemic threshold. Moreover, economic, social and personal factors are known to favour or disadvantage the download of the app. Thus, it is useful to determine the contribution of digital CT in the presence of an uneven distribution of the application.

Economic and psychological factors may have opposite forces in correlating or uncorrelating f with the activity of the nodes a_S: on the one hand, very active people for economic reasons may decide not to download the app to avoid isolation, while on the other hand, the most active people such as young people are those with more modern smartphones that allow the use of the app [229]. Personal data of the tracing app users are not available for privacy reasons [214, 215] although they could shed light on the real shape of the $f(a_S)$ distribution: however, evidences emerged, mainly through surveys during the COVID-19 pandemic, suggesting that those who downloaded the tracing apps for COVID-19 are very cautious and inactive people, i.e. f and a_S are anti-correlated [230, 231].

To estimate the effect of app distribution in the population $f(a_S)$, we considered the hybrid tracing protocol on a heterogeneous population, investigating the effect of digital tracing by considering different $f(a_S)$ and varying the overall level of adoption $\overline{f} = \int da_S \rho_S(a_S) f(a_S)$. In order to obtain information on the effects of correlations $f(a_S)$ we consider three limit cases, which are hardly realistic but provide useful insight in the understanding of the role of $f(a_S)$:

- **the uncorrelated case**: $f(a_S) = \overline{f} \,\forall\, a_S$, i.e. the app is uniformly distributed over the population;
- **the positively correlated case**: $f(a_S) = \theta(a_S - a_0^p)$, with $\theta(x)$ Heaviside step function, i.e. the app is downloaded from all nodes with activity higher than a_0^p;

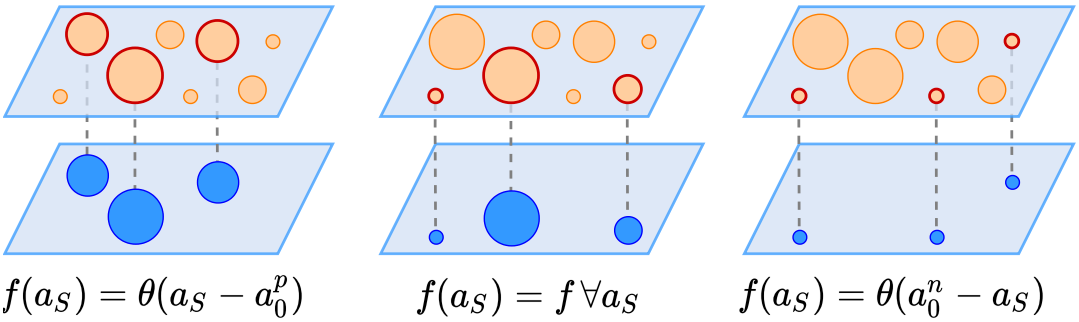

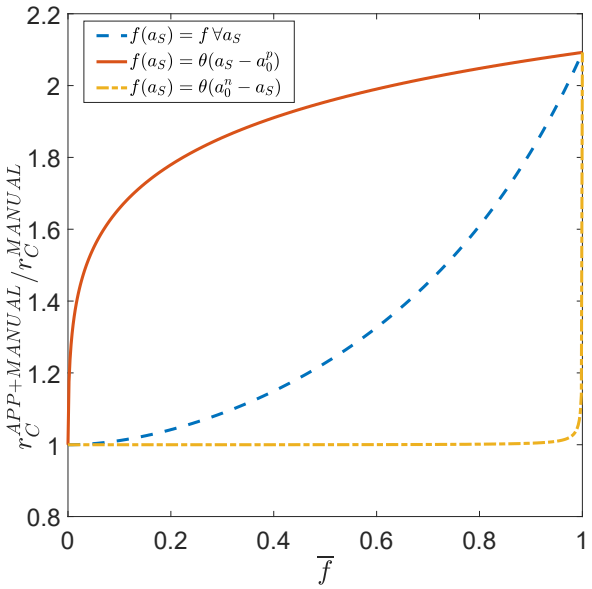

FIGURE 5.16: **Effects of correlations between app adoption and activity.** In the upper panel we schematically represent the three app adoption strategies: the uniform one $f(a_S) = \overline{f}\,\forall a_S$, the one targeted on high-activity nodes $f(a_S) = \theta(a_S - a_0^p)$ and the one targeted on low-activity nodes $f(a_S) = \theta(a_0^n - a_S)$. In the population (orange nodes) nodes size is proportional to their activity and only individuals with the app (red edge) are digitally traceable (blue nodes). In the lower panel we plot, as a function of $\overline{f}$, the ratio $r_C^{APP+MANUAL}/r_C^{MANUAL}$, between the epidemic threshold for the hybrid protocol and the threshold when only the manual CT is applied, for the three app adoption distributions. We consider $\bar{\varepsilon} = 0.4$, $\rho(a_S, b_S)$ as in Eq. (5.31) with $a_S \in [a_m, a_M = 10^3 a_m]$, $\nu = 1.5$, $\overline{a_S} = 6.7$ days^{-1}, $(1-\delta) = 0.43$, $\tau_P = 1.5$ days, $\tau = T_{CT} = 14$ days, $\tau_C = 3$ days and $\varepsilon(a_S)$ as in Eq. (5.3) with $k_c = 130$ [28].

- **the negatively correlated case**: $f(a_S) = \theta(a_0^n - a_S)$, with $\theta(x)$ Heaviside step function, i.e. the app is downloaded from all nodes with activity lower than a_0^n.

We compare the effects of hybrid CT for the three conditions in the app distribution, by fixing a_0^p and a_0^n so that the overall level of adoption of the app in the population is $\overline{f}$ the same.

Figure 5.16 shows that the correlations in the tracing app adoption are crucial for determining the contribution of digital tracing in the hybrid protocol: if the app is downloaded from all hubs (positive correlations) a minimum level of adoption is sufficient $\overline{f} \sim 0$ to achieve a significant increase in the epidemic threshold; on

the contrary, if the app is downloaded from all nodes with lower activity (negative correlations), an almost complete adoption of the app is required $\overline{f} \sim 1$ to obtain a significant increase in the epidemic threshold, much higher than that required for an uniform app distribution.

This result is due to the key role played by superspreaders: if the adoption of the app is targeted on large-activity nodes, all the hubs are traceable and a small $\overline{f} \sim 0$ is sufficient to easily block the diffusion by quickly tracing all the hubs; on the contrary, if the adoption is targeted on low-activity nodes, the hubs do not download the app and sustain the epidemic, thus the digital tracing of poorly active node has no effect. This again shows the crucial role of superspreaders.

These findings further reinforce our findings on the dominant and crucial role of manual tracing: indeed, several evidences emerged recently on negative correlations between app adoption and activity, which further advantage manual over digital CT. Moreover, these results provide hints for optimizing the integration of manual and digital CT in hybrid protocols: for example, a targeted adoption of the app on more active population classes would be extremely beneficial.

The model presented indicates that manual tracing, despite its limitations, is effective in reducing the impact of an epidemic, especially in heterogeneous populations, compared to its digital version. This is due to an intrinsic difference in the nature of the contact sampling and exploration that manual tracing perform in an annealed configuration, as opposed to digital tracing which is in a quenched and prearranged configuration. This is a crucial point, since it emphasizes that digital tracing is not only a faster and more economic version of manual tracing, but they are inherently different protocols. These fundamental differences, amplified by heterogeneities, can be mitigated by some technical limitations of manual CT, but they are nevertheless insurmountable differences.

Manual tracing must play a central role in every epidemic control policy and every hybrid tracing protocol. Effective tracing policies must be based on an accurate integration of the two mechanisms, based on cost analysis, resource allocation and optimization of their effectiveness. Our results and insights in the fundamental properties of manual and digital CT could help in designing optimized tracing strategies.

Finally, due to the complexity of epidemic spreading and epidemic control, especially in reference to their actual implementation, we neglected some realistic elements that could impact equally on both traces, such as non-complete isolation, or could favour manual CT, such as delays in digital CT, the existence of additional sources of heterogeneity such as in the viral load [238], in the recovery time [246] and in the temporal interactions dynamics [85].

Chapter 6

Contact tracing and the control of epidemics in gatherings

In this Chapter we describe the results of Ref. [20, 32]: we discuss the higher-order nature of social interactions, showing its crucial role in the spread of epidemics, due to the generation of *superspreading events (SSEs)*. We also show the role of SSEs for COVID-19 spreading [20]. We implement contact tracing on *simplicial activity-driven networks* [32], investigating its effect for an epidemic tailored to describe SARS-CoV-2 transmission. We characterize the basic mechanism of contact tracing on gatherings, suggesting optimal tracing strategies. Finally, we show the relevance of our results on a real dataset of gatherings collected in a University.

6.1 Simplicial nature of social interactions

In recent years, the architecture of social dynamics has been mainly modelled with networks of pairwise interactions. This approach, as discussed in Chapters 1-2, allowed to unveil the fundamental mechanisms of social dynamics and their effect on the epidemic spreading. However, these two-body interactions represent only a small part of social contacts, since in real settings social interactions are organized into larger groups, whose size depends on the environment in which they were created and on the associated social activity (e.g. meetings at work, meetings with friends, casual encounters on public transport, attendance at school or university), featuring heterogeneity in groups size (see Figure 1.11) [89, 92].

A description of the real contact patterns must take into account both the temporal and the simplicial dimension of social interactions [89, 92]. Thus higher-order structures need to be considered as building blocks of the social structure: more advanced and complex mathematical tools have been introduced to describe higher-order interactions, such as hypergraphs and simplicial complexes (see Figure 6.1) [29, 30, 91, 247].

Simplicial complexes have been introduced in detail in Section 1.6.4 (see Figure 1.9 and Figure 6.1), as collections of simplices $K = \{\sigma_1, \sigma_2, \ldots, \sigma_k\}$ including all the σ_i subfaces of each dimension $\forall i = 1, \ldots, k$. They overcome many of the limitations of considering only pairwise interactions, for example by describing effectively social groups in which reasonably a group interaction implies also all the underlying pairwise interactions.

Hypergraphs represent the most general mathematical framework for describing higher-order interactions (see Figure 6.1): an hypergraph is defined by a pair $(\mathcal{V}, \mathcal{H})$ where $\mathcal{V}$ is a set of nodes and $\mathcal{H}$ is a set of hyperlinks, where a hyperlink is a non-empty subset of $\mathcal{V}$ specifying which nodes participate to an interaction. For example, note that a hypergraph can include a 3-body interaction $[a, b, c]$ without any

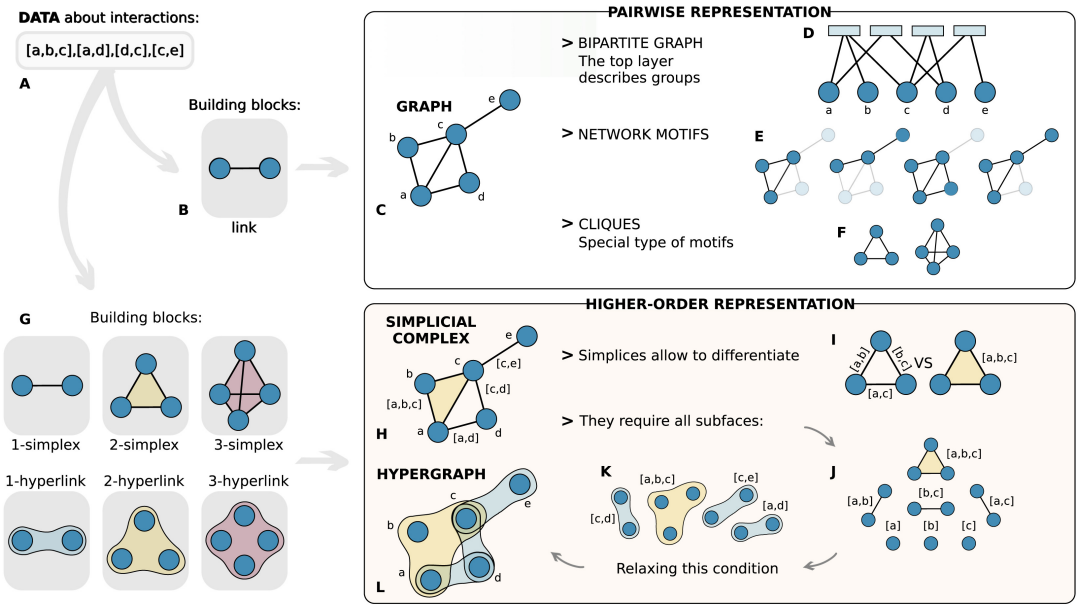

FIGURE 6.1: **Representations of higher-order interactions.** A set of interactions (panel **A**) can be represented using only pairwise interactions (panel **B**): by means of a graph (panel **C**); through a bipartite graph in which one layer corresponds to the interactions and one to the nodes (panel **D**); through a network of motifs (panel **E**), e.g. cliques representing the densest subgraphs (panel **F**). The same set of interactions (panel **A**) can be represented using higher-order structures (panel **G**), in the form of hyperedges and simplices: through simplicial complexes (panel **H**), which require the presence of all possible sub-simplices (panel **J**) and make it possible to distinguish higher-order interactions or combinations of low-order interactions (panel **I**); through hypergraphs (panel **L**) which are a more flexible representation than simplicial complexes (panel **K**). Image from [29] under CC BY 4.0 license.

constraints on the existence of the two-body interactions $[a, b]$, $[a, c]$ and $[b, c]$, unlike a simplicial complex. This mathematical structure is extremely flexible, but at the cost of higher complexity, for example it can be very complicated to extend concepts of graph theory to them [29].

Higher-order structures exhibit structural properties that strongly differ from the simple pairwise representation [29, 247]; moreover the simplicial nature of interactions profoundly impacts epidemic processes occurring on such structures (see Section 2.3.4). In the presence of higher-order interactions, new contagion mechanisms are active beside the standard simple contagion, such as simplicial and complex contagions (see Figure 2.11), which produce a rich and complex epidemic dynamics [30].

Even considering simple contagion alone, an epidemic on a system with higher-order interactions is characterized by an extremely different dynamic compared to the spread on a network of pairwise interactions [29, 87]. The formation of large social groups implies the formation of a number of connections that grows quadratically with the size of the group: this can be highly dangerous for the generation of explosive superspreading events (SSEs). Understanding these types of events is critical for characterizing the spread of an epidemic.

6.1.1 Superspreading events (SSEs)

A key role in the epidemic spreading is played by *superspreading events (SSEs)*, that are events in which a large number of infections occurs at the same time, compared

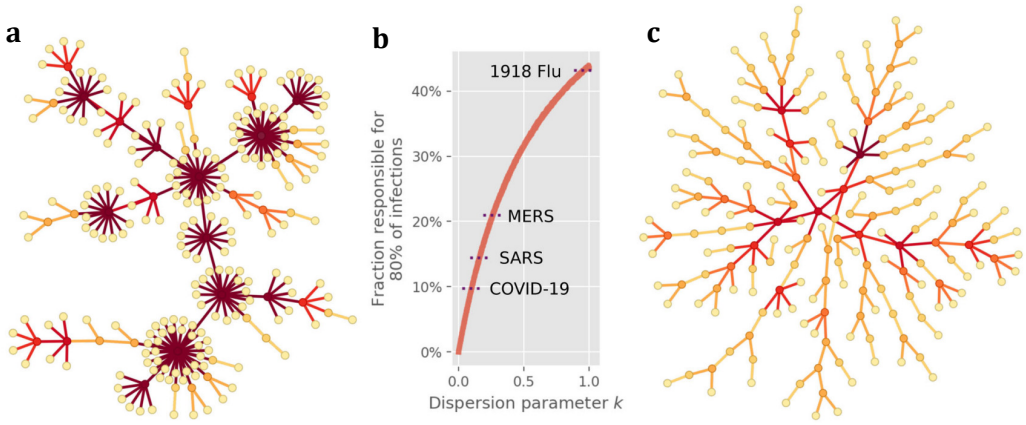

FIGURE 6.2: **Superspreading events (SSEs).** Panel **a** shows an infection network characterized by SSEs, which appear as hubs (coloured dark red), while most of the nodes feature small degree being events with few infections. The network is obtained with $k = 0.1$ dispersion parameter, i.e. 80% of infections are caused by 10% of the population. k provides a measure of the intensity of the SSEs (see panel **b**): low k corresponds to strong SSEs (e.g. COVID-19, MERS, SARS), while higher k represents diseases more homogeneous (e.g. 1918 pandemic flu). In panel **c** an infection network is shown without SSEs. Image from [248] under CC BY 4.0 license.

to the usual events. Hence, they represent a constant fuel for the epidemic, sustaining and driving the transmission. Their presence may be due to specific pathogen transmission mechanisms, e.g. specific transmission mechanisms in different environments, such as closed and poorly ventilated environments for pathogens characterized by airborne transmission, and to the interaction dynamics, e.g. large gatherings [31]. Indeed, in the latter case an infected node experiences a significant increase in the susceptible population reachable compared to the usual average. See Figure 6.2 for a schematic representation of infection networks with and without SSEs.

Epidemics characterized by SSEs feature an overdispersion in the transmissibility: few cases are responsible for the majority of infections (Pareto rule or 80/20 rule), while most of the infected individuals do not generate secondary infections, producing outbreak extinctions (see Figure 6.2) [31, 249, 250]. Indeed, most of the infections are determined by SSEs events, i.e. by a limited number of explosive events. Thus, the early epidemic phases are characterized by a higher randomness and stochasticity, with rare and explosive increases in the number of new secondary infections reported in the first few generations [31, 249]. After the initial stages the growth becomes exponential, since the number of infected individuals is high enough to continuously produce SSEs, which act as the fuel for the epidemic and for the outbreaks.

6.1.2 SSEs in COVID-19 pandemic

Superspreading events have been identified during the COVID-19 pandemic, even in the early stages of the pandemic, suggesting that the transmission of SARS-CoV-2 is mainly driven by SSEs [31, 249]. During the early stages of the COVID-19 pandemic, I spent a research period at the EPIcx lab of the Pierre Louis Institute of Epidemiology and Public Health (INSERM, Sorbonne Université - Paris). We dealt with the early data on the spread of COVID-19 in China and outside China, developing risk assessments of the pathogen importation.

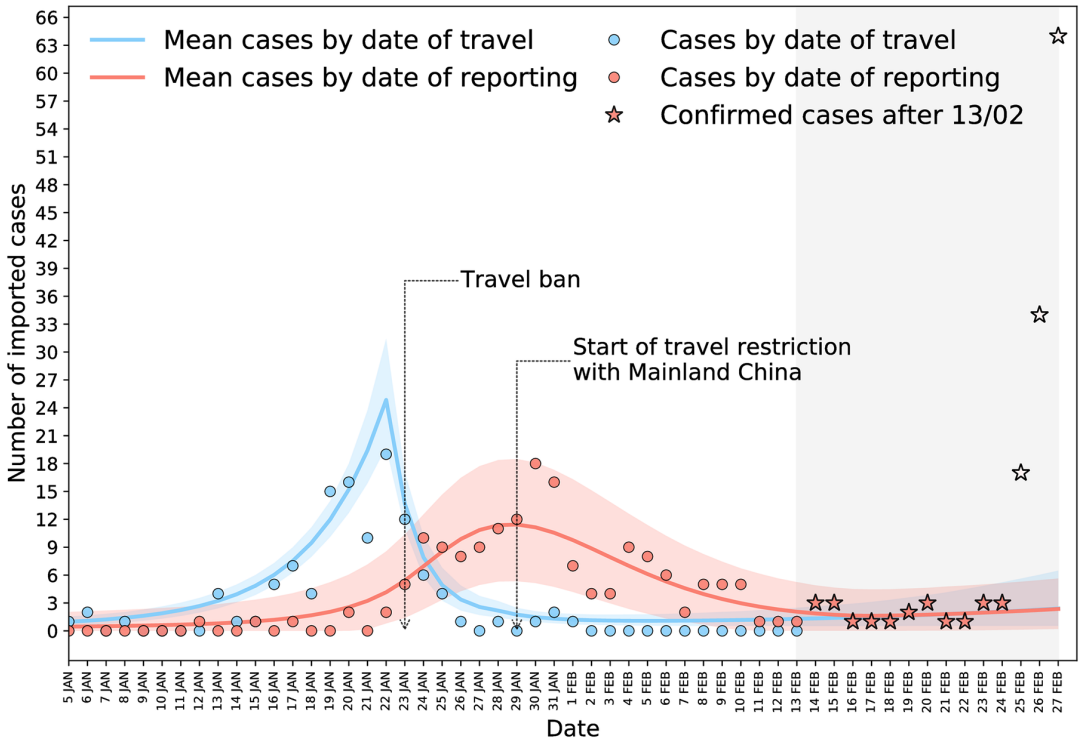

FIGURE 6.3: **Imported cases of COVID-19 by date of travel and of reporting.** We plot the number of confirmed international cases of COVID-19 imported outside China by date of travel and by date of reporting, between 03rd January 2020 and 13th February 2020. Coloured stars correspond to the model predictions, while void stars correspond to importations from Iran and Italy, originated in late February 2020 and not captured by the model because of its assumptions. We also indicate the timing of the interventions implemented by China to contain the spreading. Image from [20] under CC BY 4.0 license.

We collected and recorded all the available information for the first 288 confirmed COVID-19 cases outside China from 03rd January 2020 to 13th February 2020, through institutional sources (e.g. local Ministry of Health), health authorities and the media [20, 251]. We traced each of the 288 cases in detail, identifying whether they were successfully identified and isolated after the travel from China, whether they resulted in onward transmission or whether they originated from local transmission. We built a model for the temporal dynamics of the number of confirmed cases outside China, accounting for the control measures implemented in China [107], for the early stages of COVID-19 spread when China was the only epicentre of the epidemic and in the other states extensive local transmission had not been identified. The model, whose results are shown in Figure 6.3, shows the strong effectiveness of the drastic measures imposed by China, i.e. travel bans and containment measures, and estimates that only the 36% of imported cases were detected, i.e 6 out of 10 imported cases went undetected. This underdetection fuelled local community transmission in many states, leading in the late February 2020 to a sustained transmission in many states around the world (e.g. Italy, Iran).

The detailed tracing of the first clusters of COVID-19 infection allowed to obtain important information on the basic mechanisms of transmission, in particular on superspreading events. Despite in that period the testing capacity was low and the actual number of infections was underestimated, we identified numerous SSEs. One of the most well-known superspreading events, also reported by media [252], was the case of GB03 (according to our database [251]): an asymptomatic Briton who

infected at least 11 people at a ski resort in the Alps (cluster cFR02). The index case GB03 was infected during a conference at the Grand Hyatt Singapore (cluster cSG02), in which at least 8 infections occurred. We identified other SSEs: the contagion of at least 16 people in the cluster cDE01 in Germany with index case DE0; the contagion of at least 10 people in the cluster cSG01 in Singapore at the Yong Thai Hang shop.

All these events show the role of SSEs, occurring mainly in social environments, in the early stages of the pandemic, which shaped the stochastic dynamics observed in the number of imported confirmed cases (see Figure 6.3).

In the following phases the evidences of the role of SSEs in COVID-19 transmission were consolidated [31, 249, 253–257]. A huge number of SSEs have been observed and documented worldwide [258, 259], whose details have been collected in several databases [253, 260, 261]: these events are predominantly related to social activities (e.g. religious events, restaurants, sporting events, conferences) and almost always involve large social groups, i.e. large gatherings. They also occur mostly indoors, in crowded and poorly ventilated environments, due to the transmission mechanisms of SARS-CoV-2 [253, 260, 261].

The SARS-CoV-2 transmission dynamics is mainly driven and sustained by superspreading events: indeed about 60-75% of new infected individuals do not produce secondary infections, while about 10-20% of them produce 80% of secondary infections, propelled by SSEs (see Figure 6.2) [249, 250].

The presence of superspreading events cannot be overlooked due to their central role in transmission dynamics. This is crucial for the development of control and containment measure.

6.1.3 Control of epidemics in gatherings

On the one hand SSEs are threatening, but on the other hand they can be exploited to improve the effectiveness of response measures with the same resources implemented, since optimized targeted measures on SSEs are more effective than population-wide ones [31, 249, 257].

The control of outbreaks and their suppression can be obtained by reducing the size and frequency of SSEs: trimming the heavy tails of large secondary infections by blocking the SSEs would make the transmission chains collapse more frequently leading to the extinction of the outbreaks [31]. This goal can be pursued with different control and containment measures [31, 249] due to the different possible sources of SSEs. The first targeted measures for limiting SSEs consisted in the closure of non-essential social activities in which the risk of SSEs was higher (e.g. gyms, restaurants) with strong economic, social and psychological costs. Thus, an alternative strategy was that of controlling SSEs by implementing limitations to the maximum size of allowed gatherings: in many states gatherings beyond a certain size s_M were prohibited, with s_M ranging in $4 - 1000$ according to the epidemiological situation [19, 262]: also limiting the gatherings size proved to be an effective measure for limiting SSEs [19, 248, 254, 262, 263].

These interventions are incompatible with a fully active population: hence, alternative measures should be developed to limit SSEs and at the same time keep the population active, without activity disruption. One of the main measures for controlling SSEs is intensive contact tracing, which identifies individuals who participated in a superspreading event and remove them from the chains of infection: for example, CT allowed to identify the largest cluster of infection in South Korea at the Shincheonji Church in which more than 5000 cases were produced [31].

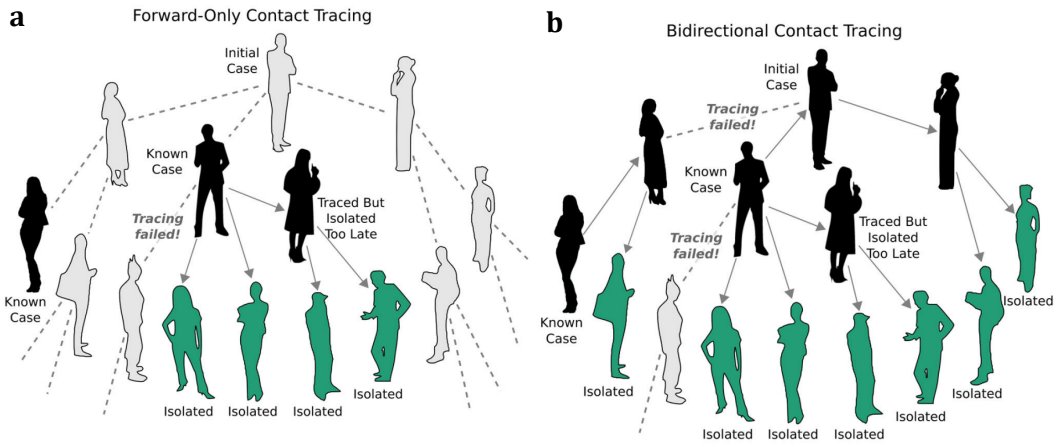

FIGURE 6.4: **Forward and backward CT.** In panel **a** a schematic representation of forward CT is shown: starting from known cases (black), only people exposed to them and potentially infected by them (forward) are notified and isolated (green). In panel **b** a schematic representation of bidirectional CT, i.e. forward and backward CT combined, is shown: starting from known cases (black), people exposed to them (forward) and also potential infectors (backward) are notified and isolated (green). Image from [188] under CC BY 4.0 license.

The effectiveness of CT significantly increases if CT not only searches to whom the diseases spread (from the index case) but also searches the infector of the index case [188, 202, 249, 264]. Indeed, when considering pairwise interactions, two CT mechanisms can be identified (see Figure 6.4): *forward CT*, which searches for individuals infected by the index case who activate the CT: thus this tracing progresses forward in time; *backward CT*, which searches for the primary source of infection of the index case who activate the CT: thus this tracing progresses backward in time. For the real implementation, the two mechanisms differ in the time window on which the CT is activated, since backward CT requires to consider wider time windows in order to be activated. The backward CT is therefore more expensive and labour-intensive, requiring to trace a higher number of people for each index case [249].

In the presence of SSEs backward CT is extremely effective. Each newly infected individual has a high probability of being infected in a SSEs and of transmitting the infection to few people, due to overdispersion: therefore the forward CT can trace only a small number of individuals, while the backward CT is able to identify and trace SSEs (see Figure 6.4) [188, 202, 264]. Bidirectional tracing, which combines forward and backward CT, has been successfully implemented in Japan [249, 265–267]. Conversely, the European countries mainly implement forward CT, due to the high cost of implementing backward CT [249, 268, 269].

All these results on the efficacy of the CT were obtained considering branching processes and static networks, i.e. only for pairwise interactions. However, a crucial role in the generation of SSEs is played by large gatherings, whose modelling requires considering higher-order interactions. To determine the overall effectiveness of CT, its basic mechanisms and its effect on SSEs, it is necessary to take into account the simplicial nature of social interactions.

The effectiveness and basic mechanisms of CT on gatherings and groups have not been fully assessed so far: in the next Sections we introduce an epidemic model on a simplicial temporal activity-driven network, with the implementation of CT on groups and gatherings [32].

6.2 Epidemics on simplicial AD network

We consider an epidemic model describing the main clinical phases of SARS-CoV-2 [16, 179, 236], which is applicable to any infectious disease presenting asymptomatic and presymptomatic transmission as observed for COVID-19 [106, 195–197, 270, 271]. The epidemic model is composed of five compartments: S susceptible, A infected asymptomatic, P infected presymptomatic, I infected symptomatic, and R recovered (see Figure 6.5). Susceptible individuals can be infected with probability λ when involved in a contact with an infected node (either A, P and I). An infected node has probability δ of following a symptomatic route, becoming presymptomatic after infection $S \xrightarrow{\lambda\delta} P$, and a probability $(1-\delta)$ of following the asymptomatic route becoming infected asymptomatic $S \xrightarrow{\lambda(1-\delta)} A$. A presymptomatic individual spontaneously develops symptoms with rate γ_P becoming symptomatic: with a Poissonian process $P \xrightarrow{\gamma_P} I$ where $\gamma_P = 1/\tau_P$ and τ_P is the average duration of the presymptomatic phase. Asymptomatic and symptomatic nodes recover spontaneously respectively with rate $\mu = 1/\tau$ and $\mu_I = \mu\gamma_P/(\gamma_P - \mu)$, so that the average period of contagiousness is τ for both symptomatic and asymptomatic ones. The model neglects hospitalizations and deaths, which do not modify the dynamics of infection and do not modify the results on the effectiveness of the CT.

The epidemic model is implemented on an equivalent formulation of the simplicial activity-driven model (SAD) introduced in Section 1.6.4. The building blocks of the model are simplices which describe social groups [87]: the individuals in the population are represented by nodes and interact with each other by participating in active simplices of different sizes. The network of interactions evolves over time through a Poissonian activation dynamics of simplices with activation rate a, i.e. the activity of simplices. The activation of a simplex of size s corresponds to an instantaneous event (see Section 1.6.4), thus the links are destroyed and the process is then iterated without memory of past interactions. The size of an active simplex s is extracted from the distribution $\Psi(s)$, which model the heterogeneity in the gatherings size [87, 89, 92]. See Figure 6.5 for a schematic representation of the simplicial network evolution.

The nodes participating in an active simplex are randomly selected in the population, with probability $p_j \propto b_j$ proportional to their attractiveness b_j [14, 28, 72]. We assume that initially each node is assigned an attractiveness b_S in the susceptible state, extracted from the distribution $\rho_S(b_S)$. As discussed in Chapter 4, adaptive behaviours can be modelled by a change in the attractiveness of a node: thus, we assume that the attractiveness b_X of a node changes with the dynamic state of the node $X = \{S, P, I, A, R\}$ (see Figure 6.5). Susceptible S, presymptomatic P, asymptomatic A and recovered R individuals participate in simplices with the same probability, i.e. they do not change attractiveness $b_S = b_A = b_P = b_R$; while symptomatics I are immediately isolated $b_I = 0$ upon the symptoms development and do not participate in active simplices [241]. Notice that P presymptomatic individuals can also represent individuals with mild symptoms still participating in simplices, at least for some time before isolation. These adaptive behaviours are implemented in active formulation (see Chapter 4), with the aim of guaranteeing the functionality and activity of the population [14].

Hereafter, we consider the homogeneous case $\rho_S(b_S) = \delta(b_S - b)$ in which all nodes participate with the same probability in active simplices (when they are not isolated), i.e. $b_S = b_A = b_P = b_R = b$: this allows to develop a completely analytical

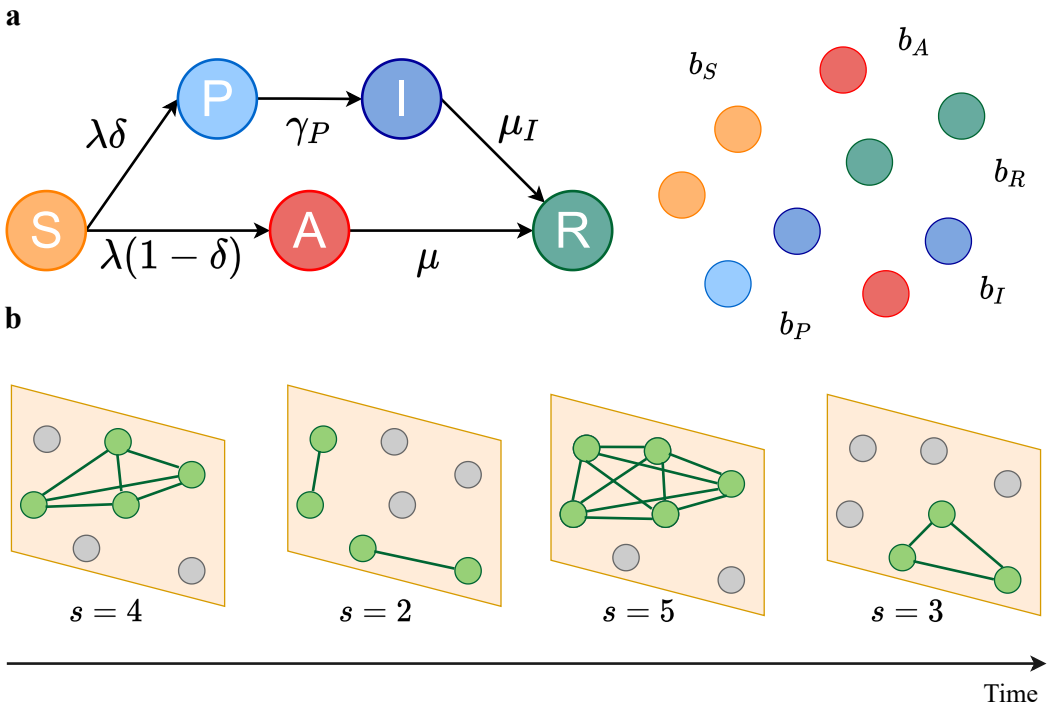

FIGURE 6.5: **Epidemic model without contact tracing and network evolution.** In panel **a** we schematically represent the compartmental epidemic model without contact tracing and the corresponding adaptive activity-driven network, with different attractiveness b_X depending on the health status of the node X. In panel **b** a schematic representation of the temporal evolution of the simplicial activity-driven network is shown: simplices of different size s activate over time and involve randomly selected (green) nodes in instantaneous interactions, creating a fully connected cluster.

description of the epidemic dynamics, even in the presence of CT. See Chapter 5 for details on the effects of heterogeneity in agents behaviour [28].

The control parameter of the epidemic model is the infection probability λ and the epidemic threshold is λ_C, i.e. the critical value of λ above which the epidemic produce extensive outbreaks, reaching a finite fraction of the entire population.

The epidemic threshold can be obtained analytically through a *mean-field approach* (see Appendix C for the detailed derivation), which is exact since all local correlations are destroyed by the random selection of participants in the simplices without memory (Markovian dynamics). In the non-adaptive case (NA), i.e. if we assume that also symptomatic individuals are not isolated $b_I = b_S$, we obtain:

$$\lambda_C^{NA} = \frac{\mu}{a\langle s(s-1)\rangle} = \frac{\mu}{\overline{n}}, \tag{6.1}$$

where $\langle f(s)\rangle = \int ds \Psi(s) f(s)$ and $\overline{n} = a\langle s(s-1)\rangle$ is the average number of contacts engaged by an individual per unit of time. This threshold is that of Eq. (2.72), since the epidemic model is the SIR model in which the infected are distinguished in P, A and I but with no differences in their behaviour or infectiousness.

If we consider the isolation of symptomatic individuals $b_I = 0$, the threshold is (see Appendix C for the detailed derivation):

$$\lambda_C^{sympto} = \lambda_C^{NA} \frac{\frac{\gamma_P}{\mu}}{\delta + \frac{\gamma_P}{\mu}(1-\delta)}. \tag{6.2}$$

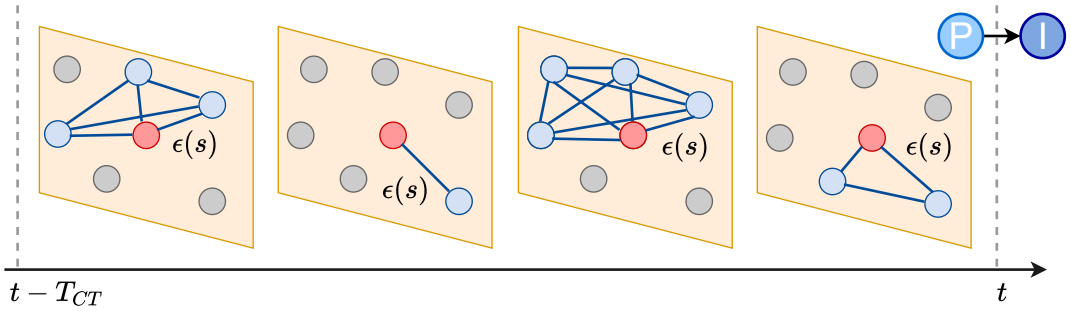

FIGURE 6.6: **Contact tracing on simplices.** We schematically represent the contact tracing on simplices: a presymptomatic individual (red node) develops symptoms at time t and activates CT on all the simplices in which participated over the time window T_{CT}.

These results represent the baseline on which we will evaluate the effect of the tracing of gatherings.

6.3 Contact tracing on simplices

On the proposed model we introduce the contact tracing in its manual formulation, to trace and isolate asymptomatic infected individuals. The CT is activated by a presymptomatic individual who develops symptoms and is isolated $P \to I$: each of the simplices in which the index case participated in the time window T_{CT} is traced as a whole with recall probability $\epsilon(s)$ regardless of the actual number of presymptomatic nodes in it. All nodes that participated in a traced simplex are tested and, if found in the asymptomatic infected state A, are isolated: see Figure 6.6 for a schematic representation of the tracing procedure. The CT is directly implemented on simplices, which are traced as a whole, thus implementing a tracing on gatherings.

This is a realistic implementation of the tracing of gatherings: generally health authorities trace an event with a certain probability $\epsilon(s)$ if it contained at least one node which then became symptomatic. For example school class are very easy to be traced even with just one symptomatic, while gatherings on public transport are almost impossible to be traced even in presence of many presymptomatic in the gathering. This allows to model specific policies and tracing strategies on gatherings and events implemented by authorities. Moreover, this approach realistically assumes that the entire event or gathering is identified as a cluster of infection and is traced as potentially contagious, as a whole group [249, 252, 259, 272].

The probability $\epsilon(s)$ takes into account several factors: first of all, the recall probability, i.e. the fact that the index case can report only a part of the gatherings in which participated, for limited memory but also for the decision of not reporting all the simplices. Furthermore, $\epsilon(s)$ takes into account that some of the gatherings are very easy to be traced (e.g. school classes or work meetings), while others are almost impossible to be reconstructed (e.g. gatherings on public transport, restaurants or shops). Finally, note that we consider the general case of $\epsilon(s)$ dependent on the simplex size: this allows to model realistic conditions of correlations between the probability of tracing a simplex and its size, or specific tracing strategies on gatherings guided by their size (e.g. targeted).

The tracing is implemented by introducing two further compartments into the compartmental model: A_T traced asymptomatic and A_Q isolated asymptomatic.

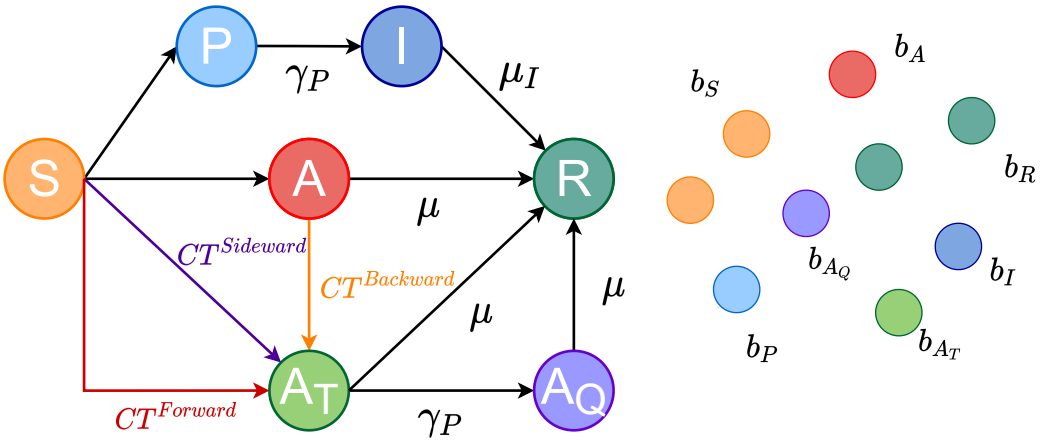

FIGURE 6.7: **Epidemic model with contact tracing.** We schematically represent the enlarged compartmental epidemic model with contact tracing on gatherings, explicitly differentiating its forward, backward and sideward implementations: the transition rates for the infection and for the tracing are discussed in detail in Appendix C. Moreover, we show the corresponding adaptive activity-driven network, with different attractiveness b_X depending on the dynamic status of the node X.

Asymptomatic individuals A become traced asymptomatics A_T as soon as they participate in a simplex with a presymptomatic individual who will then activate CT and trace the simplex (with probability $\epsilon(s)$). A traced node A_T is still infectious, behaving as susceptible $b_{A_T} = b_S$ and participating in new simplices, and with a rate γ_A is isolated $A_T \xrightarrow{\gamma_A} A_Q$; isolated asymptomatic nodes A_Q are no longer infectious $b_{A_Q} = 0$, since they do not participate in simplices (see Figure 6.7 for the complete epidemic compartmental model with CT). We assume that the tracing is faster than the epidemic evolutions, hence it can be considered instantaneous: thus, the transition $A_T \to A_Q$ occurs with rate $\gamma_A = \gamma_P = 1/\tau_P$, i.e. the same rate of symptoms onset, taking into account the need for the index case to develop symptoms to activate CT. See Chapter 5 for details on the effects of delay in CT [28].

The epidemic model corresponds to a SIR model where infected individuals are distinguished on the basis of the presence of symptoms, the tracing and isolation status, identifying different states during the period of contagiousness (see Figure 6.7). Furthermore, the model is exactly mean-field given that the dynamics is Markovian and there are no local correlations, which are continuously destroyed by the random selections of participants for active simplices: this allows to state that the SIS and SIR model have the same epidemic threshold [126, 128–130]. Hence, the analytical calculation of epidemic threshold is performed for the SIS model (see Appendix C).

The epidemic dynamics can be described through a *mean-field approach*, since all nodes participate equally in active simplices, featuring the same attractiveness b, and since the model is exactly mean-field. The epidemic dynamics is described by the probabilities $X(t)$ that a node belongs to the compartment X at time t, with $X = \{S, P, I, A, A_T, A_Q\}$. In this approach the average attractiveness is $\langle b(t) \rangle = b[S(t) + P(t) + A(t) + A_T(t)]$, we assume to be in the thermodynamic limit and we consider arbitrary $\epsilon(s)$ and $\Psi(s)$.

The evolution equations for the probabilities $X(t)$ can be obtained by considering the simplices temporal evolution, the epidemic spreading and the adaptive coupling between the two dynamics due to symptomatic isolation and CT. In Appendix C we report in details all the contact-induced (e.g. infection and tracing) and spontaneous (e.g. recovery) transitions.

The probability $P(t)$ that a node is infected presymptomatic evolves accordingly to the equation (see Appendix C for the detailed derivation):

$$\partial_t P(t) = -\gamma_P P(t) + a\frac{S(t)}{S(t)+Y(t)}\delta\left\langle s\left[1-\left(1-\lambda\frac{Y(t)}{S(t)+Y(t)}\right)^{s-1}\right]\right\rangle, \tag{6.3}$$

where $Y(t) = P(t) + A(t) + A_T(t)$. The first term on the right-hand side takes into account the spontaneous development of symptoms, while the second term describes symptomatic infections within active simplices.

The temporal evolution of the probability $I(t)$ that a node is infected symptomatic is governed by the equation:

$$\partial_t I(t) = -\mu_I I(t) + \gamma_P P(t), \tag{6.4}$$

where the first and second terms on the right-hand side are respectively due to spontaneous recovery and spontaneous symptoms development.

The probability $A(t)$ that a node is infected asymptomatic evolves accordingly to the equation (see Appendix C for the detailed derivation):

$$\partial_t A(t) = -\mu A(t) + a\frac{S(t)}{S(t)+Y(t)}(1-\delta)\left\langle s\left[1-\left(1-\lambda\frac{Y(t)}{S(t)+Y(t)}\right)^{s-1}\right]\right\rangle - C(t), \tag{6.5}$$

where $Y(t) = P(t) + A(t) + A_T(t)$. The first term on the right-hand side takes into account spontaneous recovery, the second term describes asymptomatic infections within active simplices and the third term $C(t)$ is the CT term.

The evolution equation for the probability $A_T(t)$ that a node is traced asymptomatic is:

$$\partial_t A_T(t) = -(\mu+\gamma_P)A_T(t) + C(t) \tag{6.6}$$

where the first term on the right-hand side is due to the spontaneous recovery and to the isolation of traced asymptomatic, the second term $C(t)$ is the CT term.

Finally, the temporal evolution of the probability $A_Q(t)$ that a node is isolated asymptomatic is:

$$\partial_t A_Q(t) = -\mu A_Q(t) + \gamma_P A_T(t), \tag{6.7}$$

where the first term on right-hand side is due to spontaneous recovery while the second term accounts for isolation of traced asymptomatic nodes.

The set of equations describing the epidemic can be completed by obtaining the tracing term $C(t)$, which closes the equations for the probabilities $A(t)$ and $A_T(t)$. When contact tracing is implemented on gatherings three basic tracing mechanisms are activated: forward CT, backward CT and sideward CT. Therefore, the tracing term $C(t)$ in the mean-field equations is the sum of three contributions:

$$C(t) = C^{Forward}(t) + C^{Backward}(t) + C^{Sideward}(t). \tag{6.8}$$

Forward and backward CT have been briefly described in Section 6.1.3, highlighting their differences and effects in model with pairwise interactions; the sideward CT is a mechanism emerging from the implementation of the tracing on gatherings, which exploits the higher-order structure of the interactions and we first identify in simplices, dubbing it sideward CT for its basic lateral mechanism (see Section 6.3.3). Each of the three CT mechanisms contributes to the epidemic equations differently, depending on their properties and basic functioning.

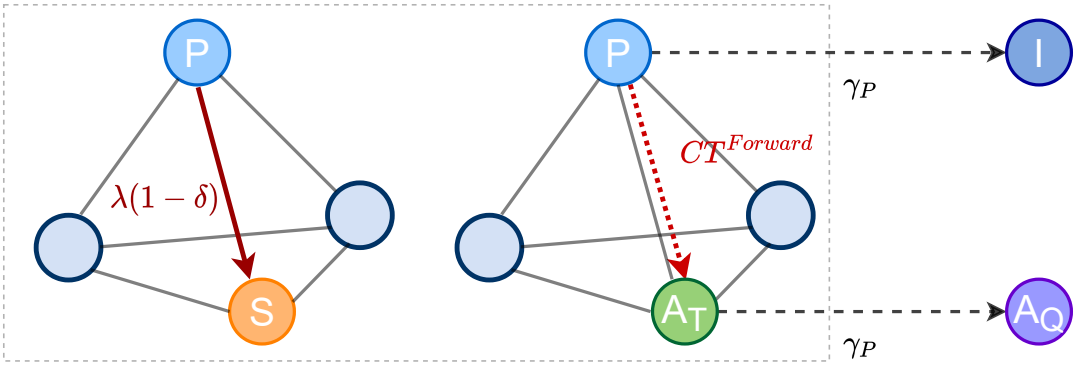

FIGURE 6.8: **Forward CT on simplices.** We schematically represent the forward CT on simplices: the detailed description of the CT mechanism is reported in the main text and in Appendix C.

6.3.1 Forward CT

The forward CT is a tracing mechanism that searches individuals infected by the index case before detection, thus it occurs following the infection links forwards in time. In particular, forward CT looks for asymptomatic individuals infected by a presymptomatic individual, who activates CT upon symptoms development.

This mechanism is activated if in a simplex there are at least one presymptomatic node and one susceptible node, who is infected by the presymptomatic with an asymptomatic infection. If the presymptomatic node effectively traces the simplex (probability $\epsilon(s)$), the susceptible node is traced at the time of the infection event, i.e. directly becomes traced asymptomatic $S \to A_T$, and will then be isolated $A_T \to A_Q$ when the presymptomatic develops symptoms. In Figure 6.8 a schematic representation of forward CT is shown.

Forward tracing takes place along the infection link that generates the infected asymptomatic and in the same direction of the pathogen transmission: thus it is dubbed as forward CT (see Figure 6.8).

The forward CT term in the mean-field equations is (see Appendix C for the detailed derivation):

$$C^{Forward}(t) = a\frac{S(t)}{S(t)+Y(t)}(1-\delta)\left\langle \epsilon(s)s\left[1-\left(1-\lambda\frac{P(t)}{S(t)+Y(t)}\right)^{s-1}\right]\right\rangle, \quad (6.9)$$

where we recall that $Y(t) = P(t) + A(t) + A_T(t)$. This term accounts for the activation a of a simplex, the probability $sS(t)/(S(t)+Y(t))$ that a susceptible node participates in a simplex of size s and the probability $\left[1-(1-\lambda P(t)/[S(t)+Y(t)])^{s-1}\right]$ that among the remaining $(s-1)$ nodes at least one of them is presymptomatic and infects the susceptible one with an asymptomatic infection $(1-\delta)$. Finally $\epsilon(s)$ is the probability that the simplex is traced and the term is averaged over the size s of the active simplex.

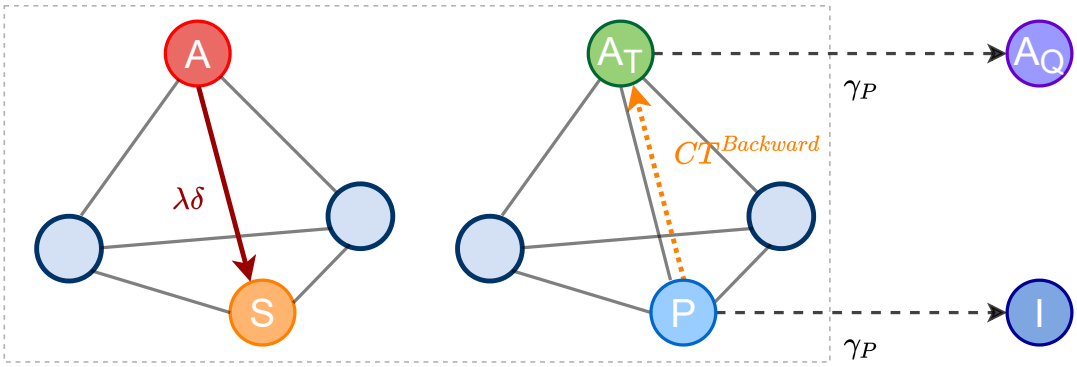

FIGURE 6.9: **Backward CT on simplices.** We schematically represent the backward CT on simplices: the detailed description of the CT mechanism is reported in the main text and in Appendix C.

6.3.2 Backward CT

The backward CT is a tracing mechanism that searches for the primary source of infection of the index case, thus it occurs following the transmission chain backwards in time. In particular, backward CT looks for asymptomatic individuals who infected a susceptible through symptomatic infection, producing a presymptomatic that activates CT upon symptoms development.

This mechanism is activated if in a simplex there are an asymptomatic node and at least one susceptible node, who is infected by the asymptomatic node with symptomatic infection. If the new presymptomatic node effectively traces the simplex (probability $\epsilon(s)$), the asymptomatic node is traced at the time of the infection event, i.e. becomes traced asymptomatic $A \to A_T$, and will then be isolated $A_T \to A_Q$ when the presymptomatic develops symptoms. The asymptomatic nodes traced with backward CT are already infected when entering in the active simplex, thus before tracing they have potentially already infected other nodes, at least in the traced simplex. In Figure 6.9 a schematic representation of backward CT is shown.

Backward tracing takes place along the infection link that generates the index case but in the opposite direction of the pathogen transmission: thus it is dubbed backward CT, following the infection process backwards in time (see Figure 6.9).

The backward CT term in the mean-field equations is (see Appendix C for the detailed derivation):

$$C^{Backward}(t) = a\frac{A(t)}{S(t)+Y(t)}\left\langle \epsilon(s)s\left[1-\left(1-\lambda\delta\frac{S(t)}{S(t)+Y(t)}\right)^{s-1}\right]\right\rangle, \qquad (6.10)$$

where we recall that $Y(t) = P(t) + A(t) + A_T(t)$. This term accounts for the activation a of a simplex, the probability $sA(t)/(S(t)+Y(t))$ that an asymptomatic node participates in a simplex of size s and the probability $\left[1-(1-\lambda\delta S(t)/[S(t)+Y(t)])^{s-1}\right]$ that among the remaining $(s-1)$ nodes at least one of them is susceptible and infected by the asymptomatic node with a symptomatic infection. Finally $\epsilon(s)$ is the probability that the simplex is traced and the term is averaged over the size s of the active simplex.

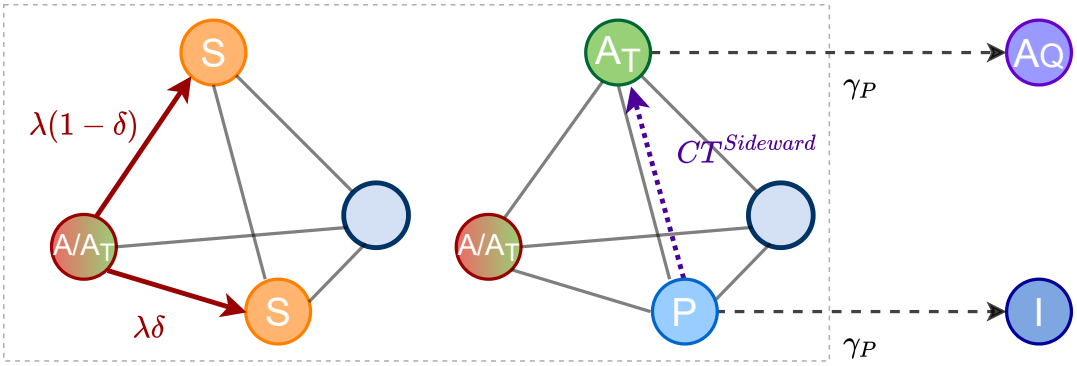

FIGURE 6.10: **Sideward CT on simplices.** We schematically represent the sideward CT on simplices: the detailed description of the CT mechanism is reported in the main text and in Appendix C. Sideward CT can be activated both if the infector is infected asymptomatic A or traced asymptomatic A_T. In the former case, the backward CT is also activated in the same simplex by the new presymptomatic $S \to P$, as shown in Figure 6.9: for simplicity we do not indicate this tracing.

6.3.3 Sideward CT

The sideward CT is a tracing mechanism that indirectly traces individuals who participated in a gathering together with the index case, who activates the CT, even if they were not directly infected by nor they have directly transmitted the infection to the index case. It is a qualitatively different tracing mechanism compared to the forward and backward CT, which instead trace links in which the nodes involved are directly linked by an infection event. In particular, the sideward CT searches for asymptomatic individuals infected by other asymptomatics, exploiting the presence in the simplex of a third presymptomatic node, who activates CT.

This mechanism is activated if in a simplex there are at least one asymptomatic node (or traced asymptomatic), a susceptible node that is infected by the asymptomatic (or traced asymptomatic) node with an asymptomatic infection and at least one susceptible node that is infected by the asymptomatic node (or traced asymptomatic) with a symptomatic infection. If the new presymptomatic node effectively traces the simplex (probability $\epsilon(s)$), the new asymptomatic node is traced, with sideward CT, at the time of the infection event, i.e. directly becomes traced asymptomatic $S \to A_T$, and will then be isolated $A_T \to A_Q$ when the presymptomatic develops symptoms. In Figure 6.10 a schematic representation of forward CT is shown. Note that the backward CT is also activated on the source of infection of the presymptomatic, i.e. on the asymptomatic node that entered the simplex infected.

Sideward tracing occurs laterally and indirectly, since it takes place along a link that does not transmit the infection: indeed, the tracing occurs along the contact between the new presymptomatic index case $S \to P$ and the new asymptomatic node $S \to A_T$, while the infections occurred along the contacts connecting the asymptomatic (or traced asymptomatic) individual and the two susceptibles. Thus, we dub this mechanism as sideward CT (see Figure 6.10).

The sideward CT requires the presence of a gathering of size $s \geq 3$: this necessary condition and the lateral nature of sideward CT highlight that this mechanism is peculiar of CT on gatherings, exploiting the simplicial structure of the interactions. In model with pairwise interactions sideward CT cannot be activated.

	Forward CT	Backward CT	Sideward CT
Involved Nodes	P $S \to A_T$	A $S \to P$	A/A_T $S \to A_T$ $S \to P$
Traced Nodes	$S \xrightarrow{P} A_T$	$A \to A_T$	$S \xrightarrow{A/A_T} A_T$
Conditions	Tracing following **forwards** infection link. Existing $\forall s$	Tracing following **backwards** infection link. Existing $\forall s$	**Lateral** tracing following a link different from infection links. Existing for $s \geq 3$

TABLE 6.1: **Summary of the basic mechanisms of CT on simplices.** We summarize the main features of forward, backward and sideward CT, distinguishing the nodes involved in the process, the traced nodes and the conditions for the specific CT mechanisms to occur.

The sideward CT term in the mean-field equations is (see Appendix C for the detailed derivation):

$$C^{Sideward}(t) = a\frac{S(t)}{S(t)+Y(t)}(1-\delta)\Bigg\langle \epsilon(s)s\left[1-\left(1-\lambda\frac{A(t)+A_T(t)}{S(t)+Y(t)}\right)^{s-1}\right] \times \left[1-\left(1-\lambda\delta\frac{S(t)}{S(t)+Y(t)}\right)^{s-2}\right]\Bigg\rangle \tag{6.11}$$

where we recall that $Y(t) = P(t) + A(t) + A_T(t)$. This term accounts for the activation a of a simplex, the probability $sS(t)/(S(t)+Y(t))$ that a susceptible node participates in a simplex of size s, the probability $\left[1-(1-\lambda[A(t)+A_T(t)]/[S(t)+Y(t)])^{s-1}\right]$ that among the remaining $(s-1)$ nodes at least one of them is infected asymptomatic (or traced asymptomatic) and infects the susceptible node with an asymptomatic infection $(1-\delta)$, the probability $\left[1-(1-\lambda\delta S(t)/[S(t)+Y(t)])^{s-2}\right]$ that at least one of the remaining $(s-2)$ nodes is susceptible and is infected in the simplex with a symptomatic infection. Finally $\epsilon(s)$ is the probability that the simplex is traced and the term is averaged over the size s of the activate simplex.

6.3.4 Complete CT on gatherings

When the contact tracing is implemented on gatherings, over a sufficiently large time window T_{CT}, all three tracing mechanisms are active. These mechanisms solve all the possible tracing processes: symptomatic individuals are immediately isolated with the appearance of symptoms; asymptomatic individuals are traced and isolated at their infection with forward CT, if infected by a presymptomatic node, and with sideward CT, if infected by an asymptomatic node (or traced asymptomatic); asymptomatic individuals who escape forward and sideward CT are traced with backward CT when they infect an individual with symptomatic infection. The three tracing mechanisms are qualitatively different: a comparison between the tracing mechanisms is shown in Table 6.1 and comparing Figures 6.8-6.10.

The tracing processes described consider the necessary and sufficient conditions, i.e. the minimum conditions, for the CT mechanisms to be activated: they describe

the first-order mechanisms in the density of infected individuals, requiring the presence of one infected individual for the activation of CT. For example, the sideward CT could be activated even if the two infections are generated by two distinct infected individuals or if a presymptomatic individual is present initially in the simplex, without the need for a symptomatic infection: however these are second-order terms, requiring the presence of at least two infected nodes initially in the simplex. We only consider first-order terms, since we focus on the epidemic threshold and all the higher-order terms do not survive the linearization procedure for the calculation of the threshold. Moreover, as discussed in Chapter 5, contact tracing is applicable only in low incidence regimes, i.e. when the system is near the critical point [249]: thus, in realistic regimes for CT implementation it is a good approximation to consider only the first-order mechanisms for CT activation.

The CT terms obtained for the different tracing mechanisms allow to obtain the complete CT term $C(t)$ in Eqs. (6.5) and (6.6) for the evolution of $A(t)$ and $A_T(t)$, closing the set of Eqs. (6.3)-(6.7) (see Appendix C):

$$\partial_t P(t) = -\gamma_P P(t) + a\frac{S(t)}{S(t)+Y(t)}\delta\left\langle s\left[1-\left(1-\lambda\frac{Y(t)}{S(t)+Y(t)}\right)^{s-1}\right]\right\rangle \tag{6.12}$$

$$\partial_t I(t) = -\mu_I I(t) + \gamma_P P(t) \tag{6.13}$$

$$\begin{aligned}\partial_t A(t) = -\mu A(t) + a\frac{S(t)}{S(t)+Y(t)}(1-\delta)\left\langle s\left[1-\left(1-\lambda\frac{Y(t)}{S(t)+Y(t)}\right)^{s-1}\right]\right\rangle \\ - C^{Forward}(t) - C^{Backward}(t) - C^{Sideward}(t)\end{aligned} \tag{6.14}$$

$$\partial_t A_T(t) = -(\mu+\gamma_P)A_T(t) + C^{Forward}(t) + C^{Backward}(t) + C^{Sideward}(t) \tag{6.15}$$

$$\partial_t A_Q(t) = -\mu A_Q(t) + \gamma_P A_T(t) \tag{6.16}$$

with:

$$C^{Forward}(t) = a\frac{S(t)}{S(t)+Y(t)}(1-\delta)\left\langle \epsilon(s)s\left[1-\left(1-\lambda\frac{P(t)}{S(t)+Y(t)}\right)^{s-1}\right]\right\rangle \tag{6.17}$$

$$C^{Backward}(t) = a\frac{A(t)}{S(t)+Y(t)}\left\langle \epsilon(s)s\left[1-\left(1-\lambda\delta\frac{S(t)}{S(t)+Y(t)}\right)^{s-1}\right]\right\rangle \tag{6.18}$$

$$\begin{aligned}C^{Sideward}(t) = a\frac{S(t)}{S(t)+Y(t)}(1-\delta)\Bigg\langle \epsilon(s)s\left[1-\left(1-\lambda\frac{A(t)+A_T(t)}{S(t)+Y(t)}\right)^{s-1}\right] \\ \times\left[1-\left(1-\lambda\delta\frac{S(t)}{S(t)+Y(t)}\right)^{s-2}\right]\Bigg\rangle\end{aligned} \tag{6.19}$$

where $S(t) = 1 - P(t) - I(t) - A(t) - A_T(t) - A_Q(t)$, $Y(t) = P(t) + A(t) + A_T(t)$.

The CT terms feature a non-trivial dependence on the probability of infection λ: this complicates the calculation of the epidemic threshold and requires to consider λ as the control parameter, since in this case μ is not simply a scaling factor of λ and the stability conditions do not depend solely on λ/μ (see Section 6.7.1). The critical behaviour of the system is defined by the epidemic threshold λ_C, i.e. the critical value of λ, above which the system reaches a finite fraction of the population through extensive outbreaks.

Eqs. (6.12)-(6.16) admit the absorbing state, in which all individuals are susceptible, as a stationary state: thus, the epidemic threshold can be obtained by imposing

the stability of the absorbing state, through a linear stability analysis. We linearize Eqs. (6.12)-(6.16) around the absorbing state, obtaining a closed and complete set of five linear coupled differential equations:

$$\partial_t P(t) = -\gamma_P P(t) + \lambda\delta a\langle s(s-1)\rangle[P(t) + A(t) + A_T(t)] \tag{6.20}$$

$$\partial_t I(t) = -\mu_I I(t) + \gamma_P P(t) \tag{6.21}$$

$$\partial_t A(t) = -\mu A(t) + \lambda(1-\delta)a\langle s(s-1)\rangle[P(t) + A(t) + A_T(t)] - C^{Forward}(t) - C^{Backward}(t) - C^{Sideward}(t) \tag{6.22}$$

$$\partial_t A_T(t) = -(\mu + \gamma_P)A_T(t) + C^{Forward}(t) + C^{Backward}(t) + C^{Sideward}(t) \tag{6.23}$$

$$\partial_t A_Q(t) = -\mu A_Q(t) + \gamma_P A_T(t) \tag{6.24}$$

with the linearized CT terms:

$$C^{Forward}(t) = \lambda(1-\delta)a\langle\epsilon(s)s(s-1)\rangle P(t) \tag{6.25}$$

$$C^{Backward}(t) = a\left\langle\epsilon(s)s\left[1-(1-\lambda\delta)^{s-1}\right]\right\rangle A(t) \tag{6.26}$$

$$C^{Sideward}(t) = \lambda(1-\delta)a\left\langle\epsilon(s)s(s-1)\left[1-(1-\lambda\delta)^{s-2}\right]\right\rangle[A(t) + A_T(t)] \tag{6.27}$$

This approach allows to obtain the epidemic threshold for an arbitrary epidemic with asymptomatic and presymptomatic infection (arbitrary epidemiological parameters) in the presence of CT on gatherings, for arbitrary distribution of the simplex size $\Psi(s)$ and for arbitrary recall probability $\epsilon(s)$.

In the general case it is not possible to obtain a closed relation for the epidemic threshold λ_C, which can only be obtained by imposing numerically the stability of the absorbing state (see Appendix C). However, in some limit cases it is possible to solve analytically the stability conditions and obtain an explicit analytic form for λ_C.

The *non-adaptive case (NA)*, in which all infected nodes behave as susceptible, can be obtained by fixing $\epsilon(s) = 0\,\forall\, s$, i.e. no tracing of the asymptomatics, and $\gamma_P/\mu = 1$, i.e. the presymptomatic phase coincide with the period of contagiousness and thus no isolation occurs. Considering this scenario, the condition for the epidemic threshold becomes:

$$-\mu + \lambda a\langle s(s-1)\rangle = 0, \tag{6.28}$$

which admits as a solution:

$$\lambda_C^{NA} = \frac{\mu}{a\langle s(s-1)\rangle} = \frac{\mu}{\overline{n}}. \tag{6.29}$$

This threshold is that of Eq. (6.1) and is valid for arbitrary $\Psi(s)$ [87].

The case in which *only the symptomatics* are isolated can be obtained by fixing $\epsilon(s) = 0\,\forall\, s$. Considering this scenario, the condition for the epidemic threshold becomes:

$$-\gamma_P\mu + \lambda\overline{n}(\delta\mu + (1-\delta)\gamma_P) = 0, \tag{6.30}$$

which admits as a solution:

$$\lambda_C^{sympto} = \lambda_C^{NA}\frac{\frac{\gamma_P}{\mu}}{\delta + (1-\delta)\frac{\gamma_P}{\mu}}. \tag{6.31}$$

This threshold is that of Eq. (6.2) and is valid for arbitrary $\Psi(s)$.

Finally, the epidemic threshold can be obtained explicitly also assuming a *homogeneous distribution of the simplices size* $\Psi(s) = \delta(s - \bar{s})$, with a constant recall probability $\epsilon(s) = \epsilon$. At first we consider $\bar{s} = 2$, i.e. the formation of only pairwise interactions, obtaining a quadratic equation in λ for the epidemic threshold:

$$\frac{\lambda^2}{\mu^2}\overline{n}^2\delta^2\epsilon + \frac{\lambda}{\mu}\overline{n}\left(\delta + (1-\delta-\delta\epsilon)\frac{\gamma_P}{\mu}\right) - \frac{\gamma_P}{\mu} = 0, \tag{6.32}$$

which admits as a solution:

$$\lambda_C^{\bar{s}=2} = \lambda_C^{NA}\frac{2\frac{\gamma_P}{\mu}}{\delta + (1-\delta-\epsilon\delta)\frac{\gamma_P}{\mu} + \sqrt{(\delta + (1-\delta-\epsilon\delta)\frac{\gamma_P}{\mu})^2 + 4\delta^2\epsilon\frac{\gamma_P}{\mu}}}. \tag{6.33}$$

This threshold reproduces the results obtained in Chapter 5 (see Eq. (5.16)) [28].

On the other side, considering $\bar{s} \to \infty$, i.e. active simplices involve all the population, a linear equation in λ for the epidemic threshold is obtained:

$$\lambda[\delta\mu\overline{n}(\gamma_P + \mu) + \overline{n}\gamma_P(1-\delta)(\mu + \gamma_P(1-\epsilon))] - \gamma_P\mu(\mu + \gamma_P) = 0, \tag{6.34}$$

which admits as a solution:

$$\lambda_C^{\bar{s}\to\infty} = \lambda_C^{NA}\frac{\frac{\gamma_P}{\mu}(\gamma_P + \mu)}{\delta(\gamma_P + \mu) + \gamma_P(1-\delta)(1 + \frac{\gamma_P}{\mu}(1-\epsilon))} \tag{6.35}$$

This threshold allows to obtain the maximum allowed value of the epidemic threshold: indeed, the threshold is maximized for $\bar{s} \to \infty$ and $\epsilon = 1$. In this case, all the simplices are effectively traced $\epsilon = 1$ and all the asymptomatic nodes are traced at their infection $S \to A_T$, with the sideward CT if infected by A or A_T and with the forward CT if infected by P: indeed for $\bar{s} \to \infty$ the probability that a node is traced with sideward CT $\to 1$ while the probability to be traced with backward CT $\to 0$ (see Eqs. (6.11) and (6.10)). The maximum threshold then becomes (replacing $\epsilon = 1$ in Eq. (6.35)):

$$\lambda_C^{max} = \lambda_C^{NA}\frac{\frac{\gamma_P}{\mu}(\gamma_P + \mu)}{\gamma_P + \delta\mu} \tag{6.36}$$

Notice that the epidemic threshold λ_C is always finite (also considering a generic $\Psi(s)$), even if $\epsilon(s) = 1\,\forall s$, due to the presymptomatic phase P in which infections occur and due to the delay between tracing and isolation.

6.4 Effects of CT mechanisms on simplices

In order to estimate the effectiveness of CT on gatherings and to compare the contribution of the three CT mechanisms for different structure of interactions, we consider different size distribution $\Psi(s)$ and we fix the average number of contacts engaged by an individual per unit of time $\overline{n} = a\langle s(s-1)\rangle$, comparing different $\Psi(s)$ but under the same conditions of link formation. Indeed, the average number of contacts performed by an individual is the same, but by changing $\Psi(s)$ these contacts are organized on simplices with a differently distributed size. This allows to determine the pure effect of the distribution $\Psi(s)$, i.e. of the structure of the interactions, without bias due to an increase or a reduction in the number of connections determined by a different shape of $\Psi(s)$. The three CT terms in the mean-field equations

can be rewritten by making explicit the dependence on $\overline{n}$:

$$C^{Forward} = \lambda(1-\delta)\overline{n}\frac{\langle \epsilon(s)s(s-1)\rangle}{\langle s(s-1)\rangle}P(t), \tag{6.37}$$

$$C^{Backward} = \frac{\overline{n}}{\langle s(s-1)\rangle}\left\langle \epsilon(s)s\left[1-(1-\lambda\delta)^{s-1}\right]\right\rangle A(t), \tag{6.38}$$

$$C^{Sideward} = \lambda(1-\delta)\frac{\overline{n}}{\langle s(s-1)\rangle}\left\langle \epsilon(s)s(s-1)\left[1-(1-\lambda\delta)^{s-2}\right]\right\rangle \left[A(t)+A_T(t)\right]. \tag{6.39}$$

The model presented is extremely general describing an arbitrary epidemic with asymptomatic and symptomatic phases. In this thesis we focus mainly on the COVID-19 epidemic, tailoring the model parameters to describe SARS-CoV-2: the fraction of individuals who develop symptoms $\delta = 0.57$ [187], the average time of the presymptomatic phase $\tau_P = 1.5$ days [16, 197, 237] and the average time of contagiousness $\tau = 14$ days, i.e. the average recovery time [179, 238]. We fix the CT time-window T_{CT} assuming that it is long enough to implement all the CT mechanisms, thus we fix $T_{CT} = \tau = 14$ days [188, 202, 237]. Finally, we fix the average number of daily contacts per individual $\overline{n} = 14$ days^{-1}, reproducing the value observed in real populations through surveys [172, 241]. Moreover, we consider a uniform tracing strategy $\epsilon(s) = \epsilon$ with $\epsilon \sim 0.3 - 0.5$, as observed from empirical data on CT [172, 249].

The effect of the overall CT and of the single CT mechanisms is estimated by calculating the increase in the epidemic threshold they produce with respect to the non-adaptive case, i.e. when no measures are implemented (see Appendix C and Chapter 3): initially we calculate the increase produced by the symptomatics isolation, then we determine the increase produced by each single CT mechanism and when all the CT mechanisms are active simultaneously. The gain in λ_C is estimated as a function of the average simplex size $\langle s\rangle$ and for different $\Psi(s)$: $\Psi(s) = \delta(s-\bar{s})$, i.e. all the simplices feature the same size $\bar{s} = \langle s\rangle$ (see Figure 6.11**a**,**b**); $\Psi(s) \sim e^{-\beta s}$ with $s \in [2,\infty)$, i.e. an exponential distribution, varying $\langle s\rangle$ with β (see Figure 6.11**c**,**d**); $\Psi(s) \sim s^{-(\nu+1)}$ with $s \in [s_m, s_M]$, i.e. a power-law distribution as observed in many real systems [89, 92], varying $\langle s\rangle$ with ν (see Figure 6.11**e**,**f**).

Figure 6.11**a**,**c**,**e** shows that the three tracing mechanisms feature different efficacy regimes depending on the structure of the interactions, reflecting the different mechanisms underlying them and their specific functioning.

The effects of the symptomatic isolation and of forward CT are independent of the distribution $\Psi(s)$ and of the average size of the simplices $\langle s\rangle$, indeed both are infection-like terms which do not change with $\Psi(s)$ since $\overline{n}$ is fixed. Due to the symptomatic isolation, a fraction δ of the newly infected nodes is isolated after an average time τ_P from the infection, therefore its contribution depends solely on the average number of contacts $\overline{n}$ performed by an infected individual, independently of how they are structured in simplices $\Psi(s)$ (see Eqs. (6.20)-(6.24)). Similarly, forward CT directly follows the chains of infection forward in time, tracing and isolating the asymptomatic products of infections generated by presymptomatics, thus it depends solely on the average number of contacts $\overline{n}$ performed by a presymptomatic node, independently of how they are structured in simplices $\Psi(s)$ (see Eq. (6.37)).

On the contrary, the effects of backward and sideward CT strongly depend on the distribution $\Psi(s)$ and on the average simplices size $\langle s\rangle$ (see Figure 6.11**a**,**c**,**e**), since they are not simply infection-like terms but are influenced by the structure of interactions.

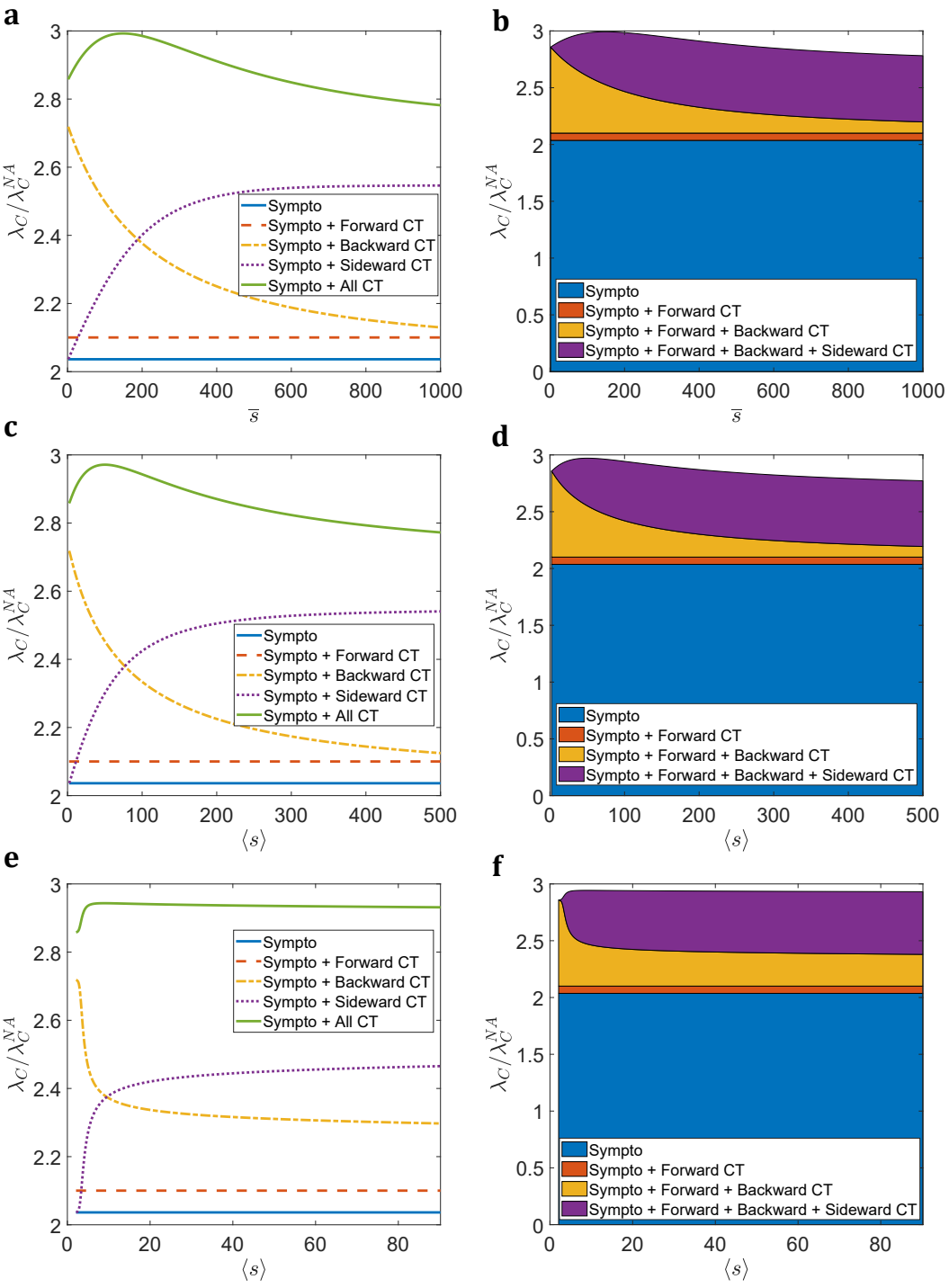

FIGURE 6.11: **Effects of forward, backward and sideward contact tracing.** In panel **a** we plot the ratio λ_C/λ_C^{NA} between the epidemic threshold in the presence of CT and the threshold in the non-adaptive case, as a function of $\overline{s}$ for $\Psi(s) = \delta(s - \overline{s})$: the curves correspond to the activation of a single tracing mechanism, to the simultaneous activation of all the tracing mechanisms and to the activation of only the isolation of the symptomatics (see legend). In panel **b** we plot the ratio λ_C/λ_C^{NA} as a function of $\overline{s}$ under the same conditions as panel **a** and progressively activating all the tracing mechanisms starting from the isolation of the symptomatics. Panels **c-d** are analogous to panels **a-b** but for $\Psi(s) \sim e^{-\beta s}$ with $s \in [2, \infty)$ and $\langle s \rangle$ varies by changing the coefficient β. Panels **e-f** are analogous to panels **a-b** but for $\Psi(s) \sim s^{-(\nu+1)}$ with $s \in [2, 500]$ and $\langle s \rangle$ varies by changing the exponent ν. In all panels $\overline{n} = 14$ days^{-1}, $(1 - \delta) = 0.43$, $\tau_P = 1.5$ days, $\tau = T_{CT} = 14$ days and $\epsilon(s) = \epsilon = 0.3\,\forall s$.

The sideward CT is extremely effective on large gatherings: its effectiveness is minimum for $\langle s \rangle \sim 2$, grows quickly with $\langle s \rangle$ and then saturates to a maximum value. Indeed, for $\langle s \rangle \sim 2$ the sideward CT is not active, since it requires $s \geq 3$ to be activated (see Section 6.3.3). In large simplices, i.e. for large $\langle s \rangle$, the probability of activating the lateral tracing is increased thanks to the wide simplicial structure; sideward CT can trace all the new asymptomatic infections occurring within them: hence, it identifies and isolates a high number of infected nodes, curbing the spread of the epidemic by stopping the explosive effects of SSEs (see Eq. (6.39)).

The backward CT is extremely effective on small gatherings: its effectiveness is maximum for $\langle s \rangle \sim 2$, then decays quickly with $\langle s \rangle$ to a minimum value. Indeed, in large simplices, i.e. for large $\langle s \rangle$, the backward CT traces only the primary source of infection of the index case, while all other numerous infections occurring within it go undetected. In small simplices the backward CT is effective since it easily identifies the sources of infections within pairwise interactions, which could not be blocked otherwise (see Eq. (6.38)).

Non-trivial reinforcement mechanisms emerge when the three types of CT are combined together, because of their deep interplay and their functioning. The increase in the epidemic threshold shows a non-monotonous trend with the average simplices size $\langle s \rangle$, for all the $\Psi(s)$ considered. The effectiveness features a maximum for intermediate $\langle s \rangle$: for nodes all of the same size or with a sharp exponential distribution $\Psi(s)$ the maximum efficacy occurs for $\langle s \rangle$ in the order of 100 nodes, while for broader distributions such as power-law $\Psi(s)$ it is placed at more realistic values $\langle s \rangle \approx 10$. This non-monotonous behaviour emerges from the combination of backward and sideward CT: their opposite behaviour with $\langle s \rangle$ gives rise to the observed non-monotonic behaviour when they are combined.

Finally, we estimate the relative contribution of the three CT mechanisms to the performance of CT on gatherings. In Figure 6.11**b**,**d**,**f**, starting from the symptomatic isolation, we estimate the increase in the threshold produced by the progressive activation of the forward CT, the backward CT and finally the sideward CT, as a function of the average simplex size $\langle s \rangle$ and for several distributions $\Psi(s)$. For $\langle s \rangle \sim 2$ the CT is dominated by the contribution of the backward CT, while increasing $\langle s \rangle$ the contribution of the sideward CT increases significantly dominating the CT. This again confirms the great effectiveness of the sideward CT in tracing large simplices.

6.4.1 The role of the symptomatic fraction

The contribution of the CT mechanisms to the control of the epidemic and the position of the CT maximum efficacy depend on the fraction of symptomatic individuals δ. In the presence of a large fraction of asymptomatics, i.e. small δ, the contribution of forward CT and backward CT is reduced, since symptomatic infections are rare, while sideward CT contribution is increased since it traces asymptomatic infections generated by asymptomatics, which are very frequent. Conversely, for a high fraction of symptomatics δ, an increase in the contribution of forward and backward CT and a reduction in the efficacy of sideward CT are expected.

To investigate the effects of varying the parameter δ, we consider the homogeneous case $\Psi(s) = \delta(s - \bar{s})$ and we compare the case $\bar{s} = 2$, where sideward CT is absent and backward CT dominates, with the case $\bar{s} \to \infty$, where backward CT is absent and dominates the sideward CT (see Eqs. (6.38) and (6.39)). An explicit expression for the epidemic threshold can be obtained for both cases (see Eqs. (6.33)

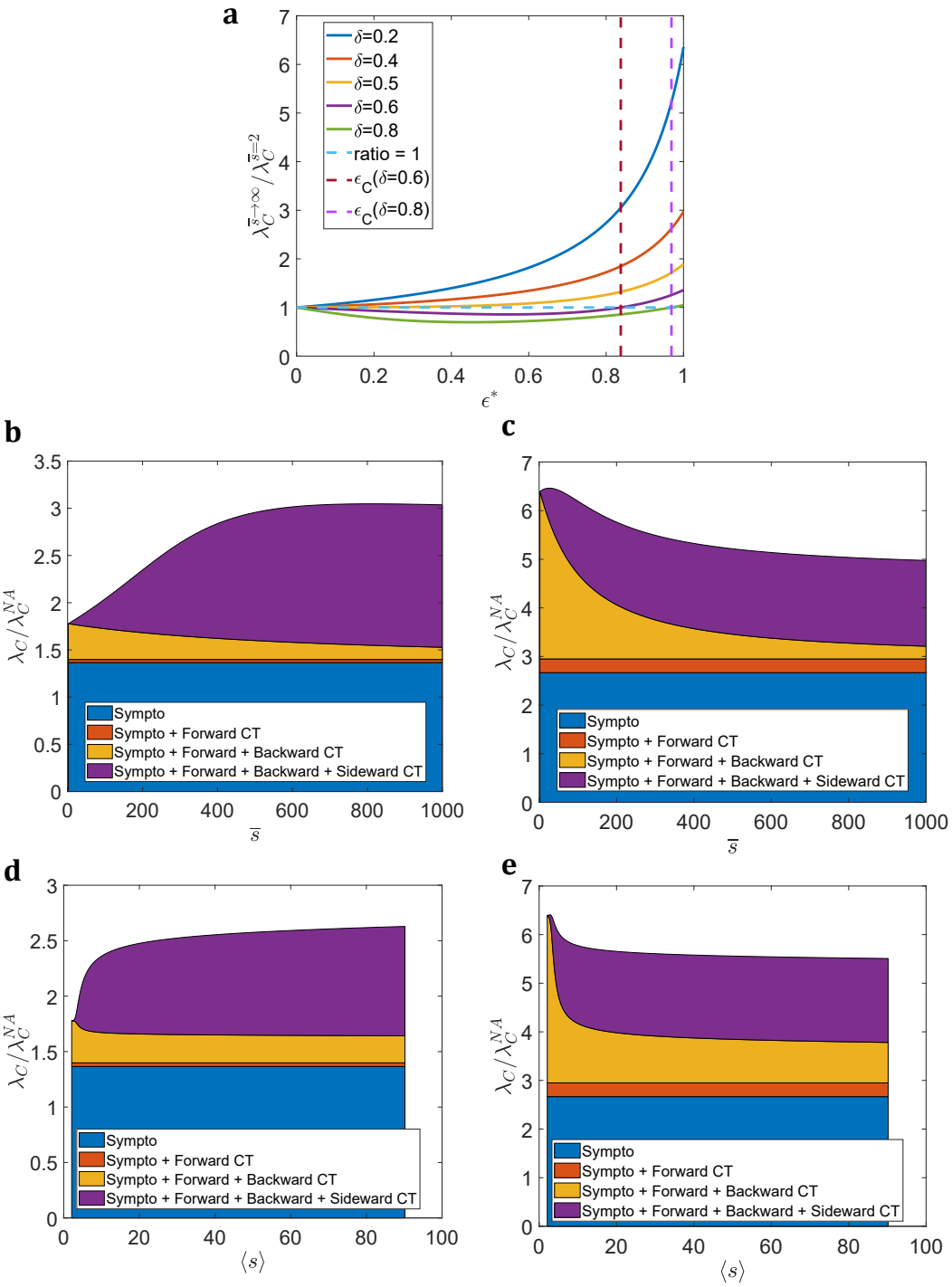

FIGURE 6.12: **The role of the symptomatic fraction.** In panel **a** we plot, as a function of $\epsilon(s) = \epsilon^* \, \forall s$, the ratio $\lambda_C^{\bar{s}\to\infty}/\lambda_C^{\bar{s}=2}$ between the epidemic threshold for $\bar{s} \to \infty$ and the threshold for $\bar{s} = 2$, fixing $\Psi(s) = \delta(s - \bar{s})$. The threshold is obtained in the presence of all the CT mechanisms and for different values of the fraction of symptomatics δ (see legend). The vertical dashed lines identify the value ϵ_C of Eq. (6.42) for the considered $\delta > 1/2$ values. In panels **b**-**c** we plot, as a function of $\bar{s}$, the ratio λ_C/λ_C^{NA} between the epidemic threshold in the presence of CT and the threshold in the non-adaptive case, starting from the symptomatic isolation and progressively activating all the tracing mechanisms. In panel **b** we fix $\delta = 0.3$, while in panel **c** we fix $\delta = 0.7$. Panels **d**-**e** are analogous to panels **b**-**c** but for $\Psi(s) \sim s^{-(\nu+1)}$ with $s \in [2, 500]$ and $\langle s \rangle$ varies by changing the coefficient ν. In all panels $\overline{n} = 14$ days^{-1}, $\tau_P = 1.5$ days, $\tau = T_{CT} = 14$ days and $\epsilon(s) = \epsilon = 0.6 \, \forall s$.

and (6.35)), which allow to directly compare the two regimes. For $\delta < 1/2$:

$$\lambda_C^{\bar{s}=2} < \lambda_C^{\bar{s}\to\infty}. \tag{6.40}$$

Thus, for infectious diseases with a high fraction of asymptomatic (e.g. COVID-19, HIV - see Table 5.1) the sideward CT is more effective than the backward CT, as expected. For $\delta > 1/2$:

$$\begin{cases} \lambda_C^{\bar{s}=2} \geq \lambda_C^{\bar{s}\to\infty} \text{ if } \epsilon \leq \epsilon_C \\ \lambda_C^{\bar{s}=2} < \lambda_C^{\bar{s}\to\infty} \text{ if } \epsilon > \epsilon_C \end{cases} \tag{6.41}$$

where:

$$\epsilon_C = \frac{(\gamma_P + \mu)(1-2\delta)}{(1-2\delta)\gamma_P - \delta\mu}. \tag{6.42}$$

Thus, for infectious diseases with a low fraction of asymptomatic (e.g. SARS, Smallpox - see Table 5.1) the relative efficacy of sideward and backward CT exhibits two different regimes depending on the tracing capacity ϵ. For $\epsilon < \epsilon_C$ the backward CT is more effective than the sideward CT, as expected; for $\epsilon > \epsilon_C$ the sideward CT is more effective than the backward CT, however this effect occurs only for $\epsilon \sim 1$ since ϵ_C grows very rapidly with δ and hence $\epsilon_C \sim 1$.

In Figure 6.12**a** we show this behaviour, plotting the ratio $\lambda_C^{\bar{s}\to\infty}/\lambda_C^{\bar{s}=2}$ as a function of $\epsilon = \epsilon^*$ for several δ values, thus showing the different regimes described. The effect of δ is shown more clearly in Figure 6.12**b**-**e**, where Figure 6.11**b**,**f** is reproduced but for different values of δ: for small δ the most effective mechanism is sideward CT, CT is much more effective on large simplices, i.e. for large $\langle s \rangle$, and the efficacy of symptomatic isolation and forward CT is reduced. For large δ the most effective mechanism is the backward CT, the CT is much more effective in small simplices, i.e. for $\langle s \rangle \sim 2$, and the efficacy of symptomatic isolation and forward CT is increased. On the contrary, for $\delta \sim 1/2$, i.e. close to the critical value between the two regimes, both sideward and backward CT are effective, producing the non-monotonous behaviour of the tracing efficacy observed in Figure 6.11.

6.5 Contact tracing strategies

Many infectious diseases, including COVID-19, are mainly driven by superspreading events (see Sections 6.1.1 and 6.1.2), which easily occur within large gatherings: hence control measures must address them to defuse the explosive effect of SSEs (see Section 6.1.3). This suggests focusing the tracing resources on large groups.

The model we propose allows to implement specific tracing strategies by an appropriate shape of the function $\epsilon(s)$. We consider three extreme strategies (schematically represented in Figure 6.13):

- **the uniform strategy $\epsilon(s) = \epsilon^* \, \forall s$**, where all simplices of any size have the same probability of being traced;
- **the strategy targeted on large simplices $\epsilon(s) = \theta(s - s^*)$**, where $\theta(x)$ is the Heaviside function and all simplices of size $s \geq s^*$ are traced, while all smaller simplices are not traced;
- **the strategy targeted on small simplices $\epsilon(s) = \theta(s^* - s)$**, where $\theta(x)$ is the Heaviside function and all simplices with size $s \leq s^*$ are traced, while all larger simplices are not traced.

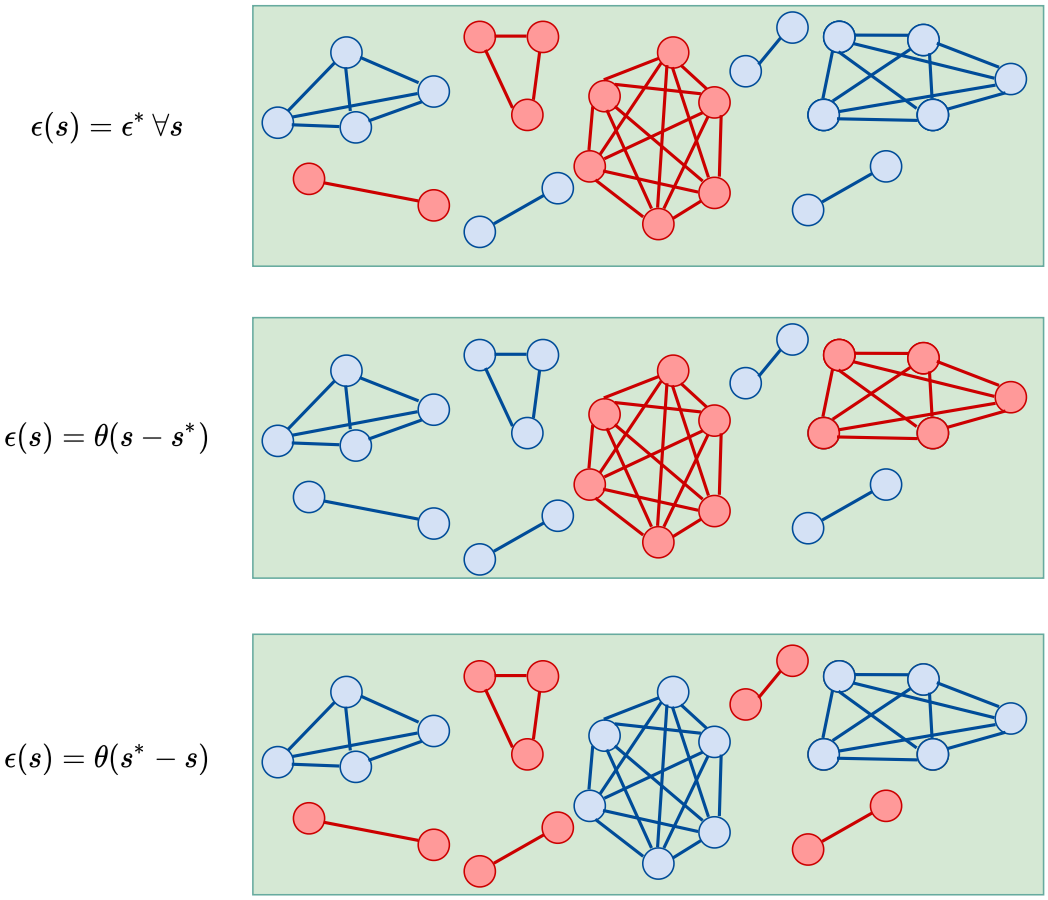

FIGURE 6.13: **Tracing strategies on gatherings.** We schematically represent the three tracing strategies: the uniform strategy $\epsilon(s) = \epsilon^* \; \forall s$; the strategy targeted on large simplices $\epsilon(s) = \theta(s - s^*)$; the strategy targeted on small simplices $\epsilon(s) = \theta(s^* - s)$. The red simplices schematically represent those traced by the corresponding strategy: all the strategies trace 11 nodes, but a different number of links ranging from 7, in the strategy targeted on small simplices, up to 25, in the strategy targeted on large gatherings.

The uniform case corresponds to the absence of a specific tracing policy, since all simplices are traced with the same probability. The tracing targeted on large simplices is a tracing policy requiring to keep track of all participants in events and gatherings larger than a certain threshold s^*, for example by requesting reservations or keeping a list of participants. This policy has been implemented in many states in response to COVID-19 pandemic, during the reopening phase after the extensive lockdowns [249, 273, 274]. The tracing targeted on small simplices in a unrealistic scenario, since it consists in keeping track of only the smallest simplices, concentrating the tracing resources only on binary interactions and completely neglecting large gatherings: we consider this case to further highlight the key role of large gatherings and SSEs, as well as to investigate the effects of negative correlations in $\epsilon(s)$ that could emerge spontaneously in the absence of specific tracing strategies.

We compare the tracing strategies by fixing the resources allocated for tracing, i.e. the average fraction of traced nodes $\epsilon^* = \frac{\langle \epsilon(s)(s-1) \rangle}{\langle s-1 \rangle}$: in the uniform case $\epsilon(s) = \epsilon^* \; \forall s$, while in the two targeted cases we fix ϵ^* by fixing the threshold size s^*.

In Figure 6.14 we show the increase in the epidemic threshold $\lambda_C / \lambda_C^{NA}$ produced by each of the tracing strategies as a function of ϵ^*, for a realistic $\Psi(s) \sim s^{-(\nu+1)}$ with $s \in [s_m, s_M]$ and $\nu = 1.5$ [89, 92]. The three strategies have the same performance

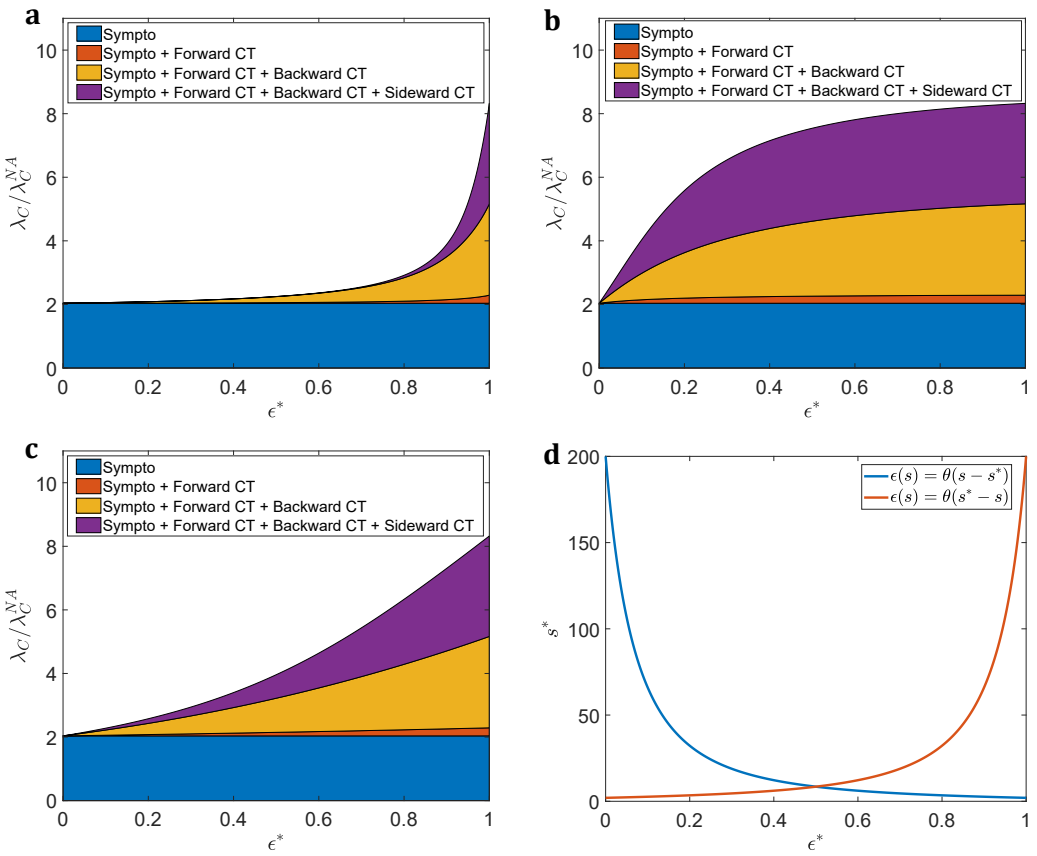

FIGURE 6.14: **The effects of tracing strategies.** In the panel **a** we plot, as a function of $\epsilon^* = \langle \epsilon(s)(s-1)\rangle / \langle s-1\rangle$, the ratio λ_C/λ_C^{NA} between the epidemic threshold in the presence of CT and the threshold of the non-adaptive case, progressively activating the different mechanisms of CT starting from the isolation of the symptomatics. We consider a synthetic distribution $\Psi(s) \sim s^{-(\nu+1)}$ with $s \in [2, 200]$ and $\nu = 1.5$ and the tracing strategy targeted on small simplices. Panel **b** is analogous to panel **a** but considering the targeted strategy on large simplices. Panel **c** is analogous to panel **a** but considering the uniform strategy. In panel **d** we plot s^* as a function of ϵ^* for the targeted strategies (see legend). In all panels $\overline{n} = 14$ days^{-1}, $\tau_P = 1.5$ days, $\tau = T_{CT} = 14$ days and $(1-\delta) = 0.43$.

for $\epsilon^* = 0$, since the CT is not applied, and for $\epsilon^* = 1$, since all the simplices are traced. However, for intermediate ϵ^* their performance is completely different: the strategy targeted on large simplices is the most effective strategy, since a small ϵ^* is sufficient to produce a significant increase in the epidemic threshold; conversely, the strategy targeted on small simplices requires that $\epsilon^* \sim 1$, i.e. to trace almost all nodes, to generate a significant increase in the epidemic threshold; the uniform strategy interpolates between the two targeted strategies. This is due to the role of the SSEs: the three strategies trace the same fraction of nodes ϵ^*, i.e. they have the same cost in tracing resources, but the strategy targeted on large gatherings trace a number of links considerably higher than the other strategies (see Figure 6.13) directly addressing SSEs, since in large simplices the number of interactions is much higher than in small simplices with the same number of nodes involved.

The strategy targeted on small simplices is comparable with that targeted on large gatherings only for $\epsilon^* \sim 1$ since in this condition $s^* \to s_M$ (see Figure 6.14**d**) and also the large gatherings are traced. On the other side, the effectiveness of the strategy targeted on large simplices saturates with ϵ^* since in that case $s^* \to 2$ (see

Figure 6.14**d**) and only small simplices are additionally traced by increasing ϵ^*.

The CT mechanisms play a different role in the various tracing strategies: the effect of the sideward CT is clearly dominant in the strategy targeted on large gatherings, even for $\epsilon^* \sim 0$, while in the strategy targeted on small simplices the backward CT dominates up to $\epsilon^* \sim 1$ where the contribution of the sideward CT increases. In the uniform strategy, on the other hand, there is an intermediate behaviour, with both backward and sideward CTs effectiveness increasing with ϵ^*. This behaviour is clearly due to the effectiveness of sideward CT in tracing large simplices and of backward CT in tracing small gatherings (see Section 6.4), confirming again the crucial role of the sideward CT in tracing gatherings.

6.6 Empirical dataset of gatherings in a University

Now we implement our approach in a real setting, considering data of gatherings within the University of Parma (Italy) and comparing different mitigation and containment measures for the COVID-19 epidemic.

The social interaction dynamics and the formation of gatherings can be reconstructed in detail by various tools (e.g. contact diaries, wearable RFID sensors, apps on smartphones, GPS data in mobile phones) [41–44, 172, 241]. Recently, the WiFi network has been proposed as a tool for reconstructing the social dynamics and thus for contact tracing [26, 275–281]: the users connections to the Access Points (APs) of a WiFi network can provide information on the distance, timing and duration of contacts.

The use of the WiFi connections to the same AP as a proxy for the distance and duration of interactions has some limitations, especially when compared with the precision and detail of other tools such as wearable RFID sensors, since the sensitivity and precision of WiFi approach depends on the APs coverage of the space, i.e. on their number and their location, and on the extension of the area covered by their signal. However, the WiFi approach also has several advantages: it consists in a passive data collection with almost no cost, since data derive automatically from the normal functioning and management of the WiFi infrastructure and not from the direct active implementation of a contact reconstruction system; the approach allows to investigate the social dynamics in large populations and in several settings, since the WiFi networks are already present in many large organizations.

The University of Parma has a unique WiFi network in all its buildings and premises, which consists of 713 wireless APs (see Figure 6.16**a**). The University WiFi network is accessible to all individuals with an institutional account of the University of Parma (i.e. students, professors, researchers and university staff), to guests with a temporary account and to anyone with an account for the EDUROAM network. All wireless APs, user connection requests and user sessions are recorded and managed by the login management system and are collected by the "ICT services" (ICTs) office of the University.

The staff of the ICTs office can extract a tabular file from the login management system on a daily basis, i.e. the log file, containing all the data for user connections to the WiFi network (see Appendix D for a detailed description of the log files). The access to the log files is allowed only to the ICTs office. A procedure has been developed which takes log files as input, completely anonymizes data and computes the aggregate measures of our interest: this procedure is performed directly by the ICTs office in its domain. The complete procedure is described in Appendix D.

We have direct access only to two aggregated and anonymized data: the time series of presences in the University, i.e. the temporal evolution of the total number of connections to the WiFi network, which can estimate the reliability of the measurement and of the data collected; the statistics of the gatherings size in the University, i.e. the number of gatherings of size s observed in the University, which allows to obtain important information on the structure of interactions and the empirical distribution $\Psi(s)$.

6.6.1 Attendance and simplex size distribution from WiFi data

The procedure described in Appendix D is applied to the log files produced by the University login management system over a period of approximately 6 months, from 10th December 2020 to 9th May 2021. During this period, two phases can be distinguished based on the implementation of different levels of restrictions for the COVID-19 pandemic, due to the epidemiological situation in Parma [274]:

- **Closure phase:** this phase covers the period from 10th December 2020 to 21st February 2021 and from 15th March 2021 to 18th April 2021; a total number of 7138 active users has been observed in this phase. All lectures were offered online on video-conferencing platforms, the access to the University was allowed only to authorized personnel (e.g. professors, researchers) and to students for laboratory activities;
- **Partial opening phase:** this phase covers the period from 22nd February 2021 to 14th March 2021 and from 19th April 2021 to 9th May 2021; a total number of 7835 active users has been observed in this phase. First-year lectures were offered in-person (approximately 25% of students enrolled in the degree courses), while the lessons were still offered remotely for all other students. Furthermore, the libraries and study spaces were open, with a reduction in the maximum capacity of the rooms and a compulsory seat reservation.

In Table 6.2 we schematically summarize the main differences in the two periods of restrictions, regarding the University activities [274].

The anonymized and aggregated data on the temporal evolution of presences in the University are useful for showing the reliability of the measure and of the collected data: in Figure 6.15 we show the total number of users connected to the WiFi network over time. The data cover the period from 05th April 2021 to 30th April 2021, thus overlapping both the closure and the partial opening periods: differences can be identified in the attendance level between the two regimes. Moreover, weekly and daily temporal patterns in the attendance can be identified: the presences are minimum during weekends and, among working days, are lower on Mondays and Fridays; during the early hours of the morning the presences increase rapidly, followed by a reduction at lunchtime, a resumption in the afternoon and finally a complete emptying in the evening, with a minimum during night hours (8:00 p.m. - 7:00 a.m.). Notice the low attendance on 05th April 2021 being Easter Monday, which is a holiday in Italy.

Notice that the WiFi data underestimate the total number of presences in the University, since not all individuals connect to the WiFi network. Through a comparison with the seats reservation data in classrooms and study spaces (mandatory for the University regulations [274]) and with data on structured staff presences (e.g. researchers, professors and university staff), based on their personal access badges, we can estimate that the number of people actually present is about double that estimated with WiFi data.

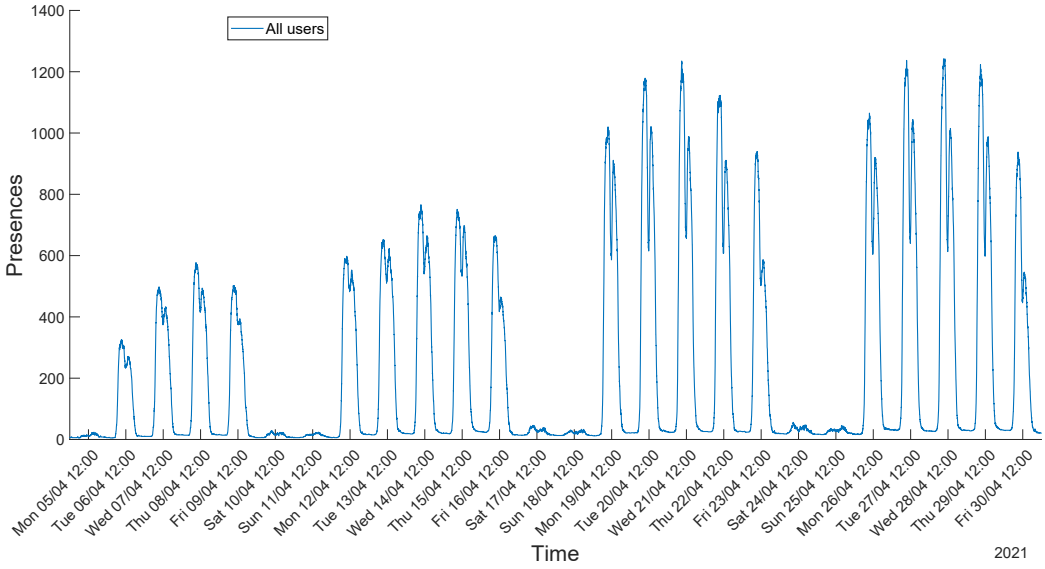

FIGURE 6.15: **Attendance at the University of Parma form WiFi data.** We plot the temporal evolution of the total number of users connected to the WiFi network of the University of Parma from 05th April 2021 to 30th April 2021. The considered period covers both the partial opening phase (from 19th April to 30th April 2021) and closure phase (from 05th April to 18th April 2021).

The anonymized and aggregated WiFi data on connections can provide the gatherings size statistics within the University. We consider a gathering of size s as a group of s users who are simultaneously connected to the same AP for at least $\Delta T = 15$ minutes, by considering epidemiologically relevant gatherings (see Figure 6.16**a** for a schematic representation). Indeed, the indoor transmission of SARS-CoV-2 is mainly due to its airborne nature [275, 282–284] and thus occurs on spatial scales comparable to those covered by the WiFi signal of an AP, making the connection to the same AP a good proxy for a contact. Moreover, we consider clusters with interactions lasting at least 15 minutes, taking into account the average exposure time needed for the transmission of SARS-CoV-2, as considered in the tracing apps and in the traditional tracing [237, 285]. This suggests that, with appropriate privacy-preserving protocols, WiFi data could be used to implement an alternative passive contact tracing for controlling COVID-19 diffusion [279–281].

The procedure described in Appendix D allows to obtain the number of 15-minutes gatherings of size s observed in the University, providing the empirical simplex size distribution $\Psi(s)$. The procedure is implemented on the data by removing holidays, night hours and weekends in order to refer only to working days and working hours, i.e. from 7:00 a.m. to 8:00 p.m..

We distinguish the closure and the partial opening phases, obtaining two distinct distributions $\Psi(s)$ for the two periods which are plotted in Figure 6.16**b**: both are heterogeneous, as observed in other datasets with different data collection methods [89, 92]. However, the two distributions strongly differ: the distribution in the closure period is less heterogeneous, it features an upper cut-off s_M lower than that of the partial opening period and it shows a significantly higher probability of simplices with size $s = 0, 1$, i.e. no one or only one user connected to an AP. This is due to the restrictions in the educational and working activities in the University during the closure phase (see Table 6.2). We consider the same activity a of the APs in the two periods, recording the presence of simplices on fixed time intervals of

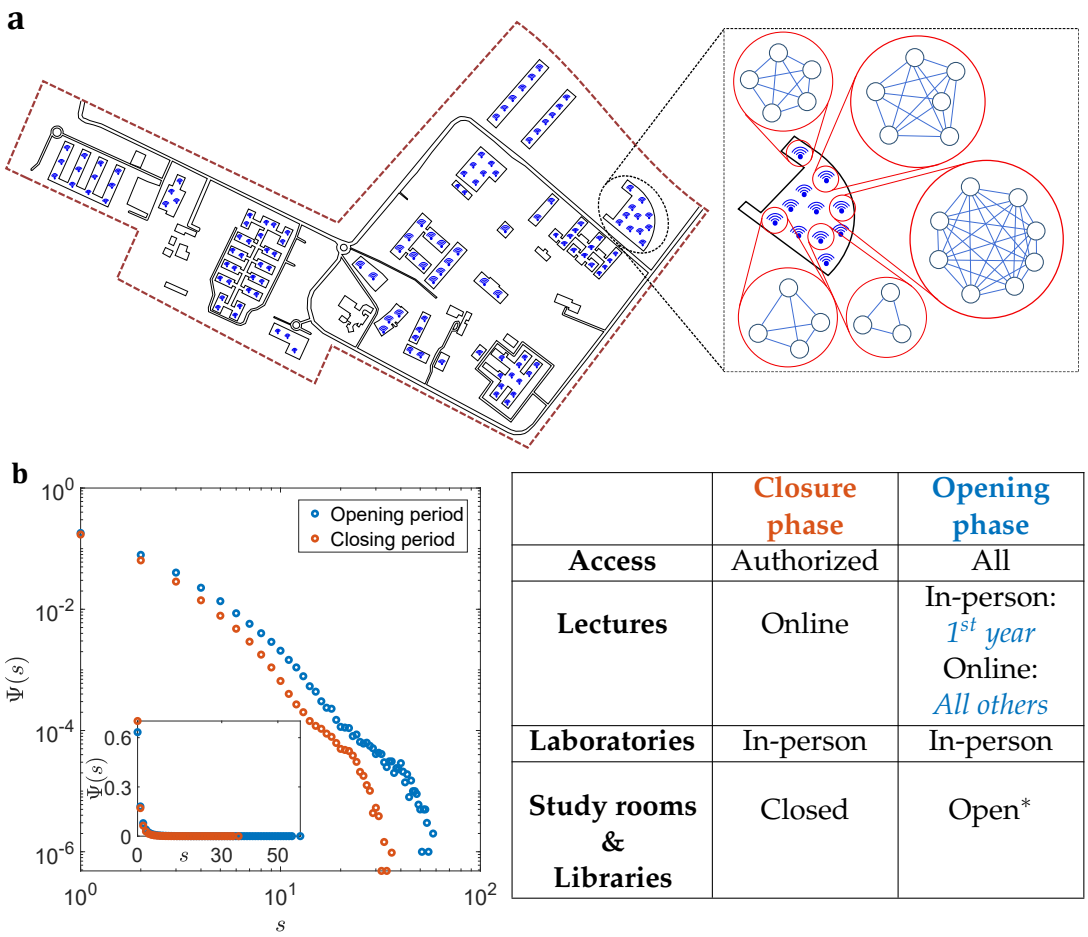

	Closure phase	Opening phase
Access	Authorized	All
Lectures	Online	In-person: *1st year* Online: *All others*
Laboratories	In-person	In-person
Study rooms & Libraries	Closed	Open*

FIGURE 6.16 & TABLE 6.2: **WiFi data for gatherings in the University of Parma.** Panel **a** shows a map of the "Parco Area delle Scienze" Campus of the University of Parma, where all the scientific departments and research institutes are located. The map shows schematically the buildings in which APs of the WiFi network are present and where the gatherings are recorded. In panel **b** we plot the empirical distributions $\Psi(s)$ of the gatherings size recorded through the WiFi data during the partial opening and the closure periods. The main plot is in log-log scale, while the inset is in linear scale. In the Table we briefly summarize the main differences between the closure phase and the partial opening phase. *[* with reduced maximum capacity and mandatory seats reservation].*

15 minutes, and we consider also the activation of simplices of size $s = 0, 1$, which thus encode the effective social activity of the University. This approach allows to describe the data for the two periods with the simplicial activity-driven model described in the previous Sections, with the same activity a for the two periods but different distribution $\Psi(s)$.

6.7 Epidemic control strategies in a University

Starting from the empirical data on gatherings at the University of Parma, we analyze different epidemic control strategies in the framework of the simplicial activity-driven network and the epidemic model presented in the previous Sections.

The closure of teaching and research activities in the University had a strong impact on the interaction dynamics, i.e. on the distribution $\Psi(s)$. Its effect on the epidemic can be estimated by the epidemic threshold: assuming that only the isolation of symptomatic individuals is implemented, the epidemic thresholds in the closure

and partial opening periods can be obtained with Eq. (6.2) by replacing the appropriate empirical distribution $\Psi(s)$. The symptomatic isolation during the partial opening period allows to increase the epidemic threshold by a factor $\lambda_C^{opening}/\lambda_C^{NA} \simeq 2.04$ compared to the non-adaptive case, where we assume that the $\Psi(s)$ is that of the partial opening period. If we consider also the closure of the University, the increment becomes $\lambda_C^{closure}/\lambda_C^{NA} \simeq 5.35$. Thus:

$$\frac{\lambda_C^{closure}}{\lambda_C^{opening}} = \frac{\langle s(s-1)\rangle_{opening}}{\langle s(s-1)\rangle_{closure}} \simeq 2.63, \tag{6.43}$$

The closure deeply affects the epidemic spreading by almost tripling the epidemic threshold compared to the partial opening period.

The University closure was extremely effective for the epidemic control [19, 143, 174], but at a high psychological, social and didactic cost, interrupting most of the didactic, research and working activities [286, 287]. Contact tracing is a good alternative to keep the population active still managing to control the epidemic. We assess whether CT on gatherings can be implemented during the partial opening period to control the epidemic by avoiding closures and their drawbacks.

We consider the system in the partial opening phase and we implement the different CT strategies described in Section 6.5, comparing them by fixing the resources allocated for the tracing, i.e. the average fraction of traced nodes $\epsilon^* = \frac{\langle \epsilon(s)(s-1)\rangle}{\langle s-1\rangle}$. In Figure 6.17**a** we show the increase in the epidemic threshold produced by the different tracing strategies, as a function of ϵ^*: the effects of the different strategies are similar to those observed for a heterogeneous synthetic distribution $\Psi(s)$ in Section 6.5, due to the heterogeneity in the empirical $\Psi(s)$. The strategy targeted on large gatherings is the most effective, defusing SSEs.

In Figure 6.17**a** we compare the impact of closures and of CT during the partial opening period: the tracing strategy targeted on large simplices produces the same results of the closures for $\epsilon^* \gtrsim 0.47$, which corresponds to tracing all simplices with size $s \geq 6$, i.e. the 16.1% of gatherings. Thus, a considerable tracing effort is needed to produce similar result of closure, even targeting the resources on large gatherings. This is due to the differences between the two interventions: the closure directly impacts the structure of the interactions and the distribution $\Psi(s)$, by removing the SSEs; contact tracing does not intervene directly on the structure of the interactions, but identifies and isolates infected individuals after the interactions occurred. The tracing is therefore not able, even if targeted on large simplices, to completely defuse the explosiveness of the SSEs, but can reduce its impact by tracing and isolating the infected generated in them.

The closures were implemented during a phase of sustained community transmission, in order to bring the epidemic into a regressive phase: their intensity was therefore determined by the need of a immediate block of transmission. The University closure produced an increase in the epidemic threshold of $\lambda_C^{closure}/\lambda_C^{NA} \simeq 5.35$, which brings the system deeply into the absorbing phase if we consider a basic reproduction number $R_0 = \lambda/\lambda_C^{NA} \approx 4.5$, e.g. for a variant of SARS-CoV-2 that is highly transmissible and in the presence of additional containment measures (e.g. the use of face masks and physical distancing) [16, 118, 119, 288–293]. CT cannot be used with this aim since it is effective only in low incidence regimes (see Chapter 5), but it is a valid alternative to keep the system close to the critical point, i.e. under control. Figure 6.17**a** shows that targeted tracing on large gatherings keep the system under control for $\epsilon^* \gtrsim 0.27$ by tracing all the gatherings of a size $s \geq 9$, that

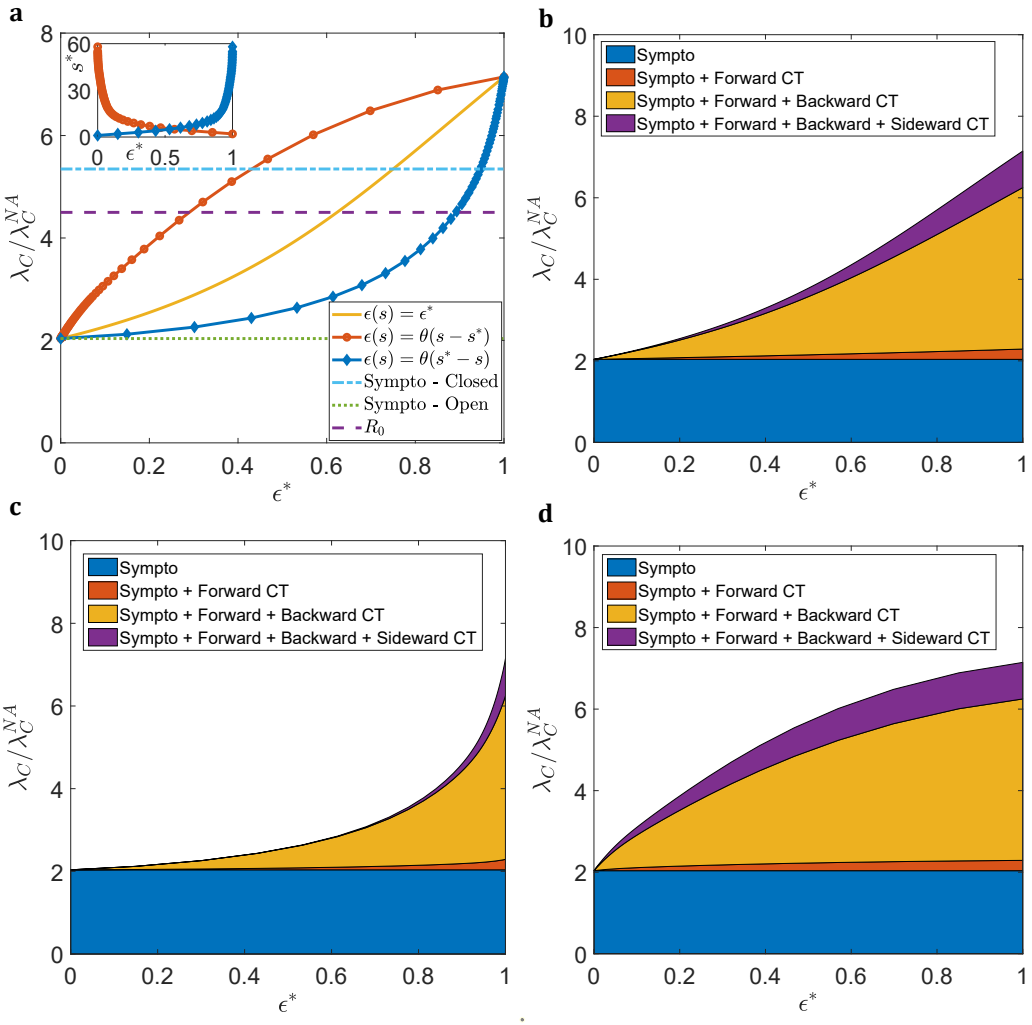

FIGURE 6.17: **Contact tracing on empirical University gatherings data.** In panel **a** we plot, as a function of $\epsilon^* = \langle \epsilon(s)(s-1)\rangle / \langle s-1\rangle$, the ratio λ_C/λ_C^{NA} between the epidemic threshold in the presence of CT and the threshold in the non-adaptive case, by considering the three tracing strategies (see legends). The three horizontal curves correspond to: the increase $\lambda_C^{opening}/\lambda_C^{NA} \simeq 2.04$ produced by the isolation of symptomatics during the partial opening phase (dotted line); the increase $\lambda_C^{closure}/\lambda_C^{NA} \simeq 5.35$ produced by the isolation of symptomatics and by the closure (dot-dashed line); the value of the basic reproduction number $R_0 = \lambda/\lambda_C^{NA} = 4.5$ (dashed line). In the inset we plot the threshold size s^* for the two targeted strategies as a function of ϵ^*. In panel **b** we plot the ratio λ_C/λ_C^{NA} as a function of ϵ^* by progressively activating the CT mechanisms starting from the isolation of the symptomatics. In this case we consider the uniform tracing strategy. Panel **c** is analogous to panel **b** but with the tracing strategy targeted on small simplices. Panel **d** is analogous to panel **b** but with the tracing strategy targeted on large simplices. In all panels we consider the empirical $\Psi(s)$ distribution of the partial opening period, $\overline{n} = 14$ days^{-1}, $\tau_P = 1.5$ days, $\tau = T_{CT} = 14$ days and $(1-\delta) = 0.43$.

corresponds to the 6.2% of the gatherings, which is a reasonably realistic effort.

Our results show that the epidemic can be kept under control in the partial opening period by tracing all gatherings of size $s \geq 9$ occurring within the University. The tracing targeted on large gatherings can be implemented relatively simply in the University, for example making it mandatory to register attendance in university buildings, to reserve seats in classrooms and study spaces [274]. Moreover, the

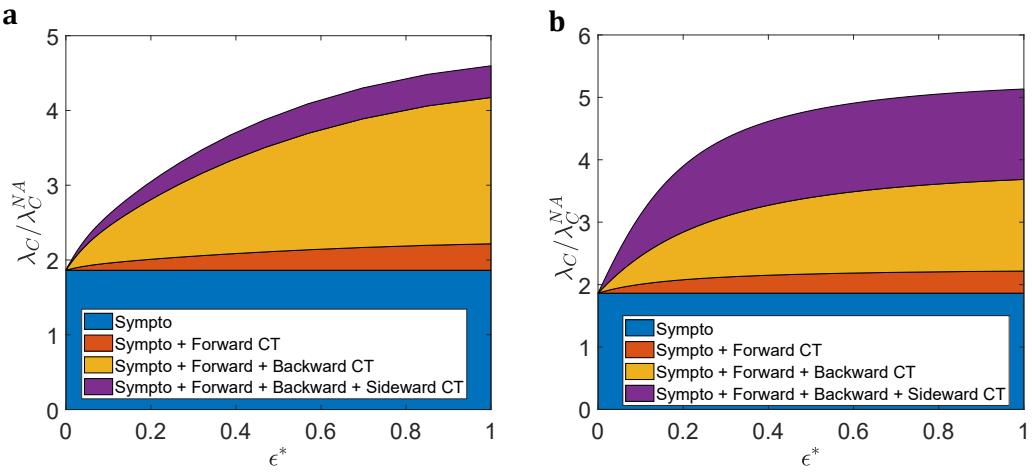

FIGURE 6.18: **The role of the recovery rate.** In panel **a** we plot, as a function of ϵ^*, the ratio λ_C/λ_C^{NA} between the epidemic threshold in the presence of CT and the threshold of the non-adaptive case, progressively activating the different mechanisms of CT starting from the isolation of the symptomatics. We consider the empirical distribution $\Psi(s)$ of the gatherings size during the partial opening phase and we consider a tracing strategy targeted on large simplices. Panel **b** is analogous to panel **a**, but we consider a synthetic distribution $\Psi(s) \sim s^{-(\nu+1)}$ with $s \in [2, 200]$ and $\nu = 1.5$. In all panels $\overline{n} = 14$ days^{-1}, $\tau_P = 1.5$ days, $\tau = T_{CT} = 8$ days and $(1-\delta) = 0.43$.

WiFi data themselves could be exploited directly to implement CT on gatherings, through appropriate privacy-preserving protocols [279–281] (see Section 6.6).

Finally, Figure 6.17**b**-**d** shows that, in the real conditions of the partial opening phase, backward CT plays the dominant role in all the tracing strategies and the sideward CT is crucial in the strategy targeted on large gatherings, by significantly increasing the threshold. The effect of sideward CT, however, is lower compared to that for a synthetic heterogeneous $\Psi(s)$ distribution (Section 6.5): indeed, during the partial opening period many restrictions are still active (see Table 6.2 and Section 6.6.1), which still limit the heterogeneity in $\Psi(s)$, e.g. producing a small upper cut-off $s_M \approx 60$. We expect that in the full opening condition for the University, s_M and heterogeneity in $\Psi(s)$ would be increased, as observed in analogous pre-pandemic data in University Campuses [89, 92], further increasing the effectiveness of the strategy targeted on large simplices and the role of the sideward CT.

6.7.1 The role of the recovery rate

The CT terms feature a non-linear dependence on the probability of infection λ due to the higher-order nature of interactions (see Eqs. (6.37)-(6.39)): hence, the recovery rate μ is not simply a scaling factor of the probability of infection λ and of its critical value λ_C, as typically occurs in epidemics on temporal networks (see Chapter 2). This implies that the conditions for the stability of the absorbing state do not simply depend on the ratio λ/μ: the role of μ need to be investigated.

In Figure 6.18 we reproduce Figures 6.14**b** and Figure 6.17**d**, comparing the contribution of the different CT mechanisms in the presence of a tracing strategy targeted on large simplices, for a different value of μ. The relative contribution of the different CT mechanisms does not change qualitatively with $\tau = 1/\mu$: this is a non-trivial property of the model which confirms the stability of our results. These results are valid both considering the empirical $\Psi(s)$ during the partial opening phase and for a synthetic $\Psi(s) \sim s^{-(\nu+1)}$.

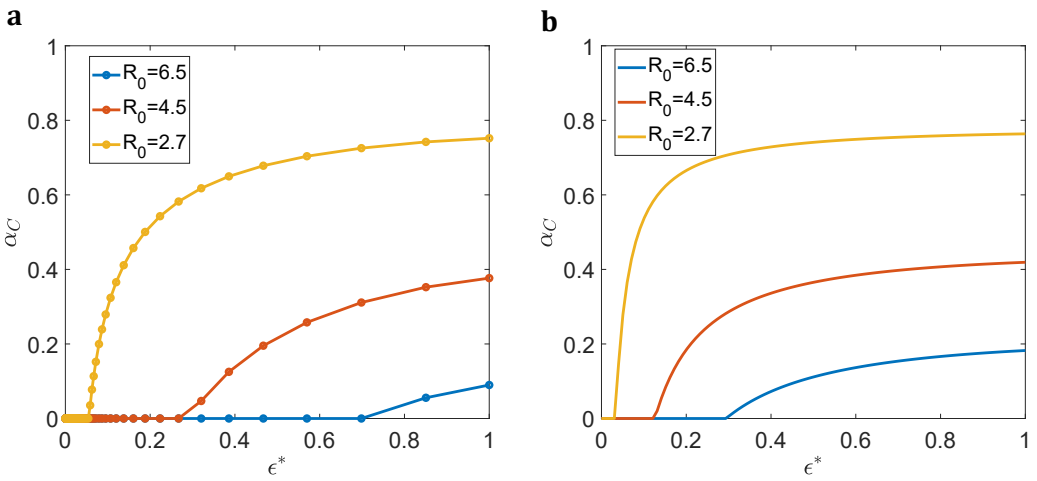

FIGURE 6.19: **Effects of a small fraction of untraced large gatherings.** We consider the tracing strategy targeted on large simplices with a small error $\epsilon(s) = (1-\alpha)\theta(s-s^*)$ with fixed s^*. In the panel **a** we plot the critical value α_C that brings the system above the epidemic threshold, as a function of ϵ^*, i.e. the average fraction of nodes traced when $\alpha = 0$, which fixes s^*. In particular, we plot the curve for different values of $R_0 = \lambda/\lambda_C^{NA}$ and for the empirical distribution $\Psi(s)$ of gatherings size during the partial opening phase. Panel **b** is analogous to panel **a**, but we consider a synthetic distribution $\Psi(s) \sim s^{-(\nu+1)}$ with $s \in [2, 200]$ and $\nu = 1.5$. In all panels $\overline{n} = 14$ days^{-1}, $\tau_P = 1.5$ days, $\tau = T_{CT} = 14$ days and $(1-\delta) = 0.43$.

6.7.2 Effects of small errors in targeted CT strategies

The tracing strategy targeted on large gatherings assumes that all the simplices with $s \geq s^*$ are traced perfectly. However under realistic conditions it is difficult for all major gatherings to be fully traced: in general a fraction α of large simplices cannot be traced for various reasons. Therefore it is important to determine the effect of this small fraction α of untraced large gatherings.

Our model allows to introduce this untraced fraction α by considering the tracing probability $\epsilon(s) = (1-\alpha)\theta(s-s^*)$ and keeping the threshold size s^* fixed, so that the strategy consists in tracing all simplices of size $s \geq s^*$ with a probability $(1-\alpha)$, where $\alpha \in [0,1]$. For $\alpha = 0$ the perfect targeted strategy is recovered and the average fraction of nodes traced is $\epsilon^* = \frac{\langle \epsilon(s)(s-1)\rangle}{\langle s-1\rangle}$; if $\alpha > 0$ in the tracing strategy is not perfect, the average fraction of nodes traced is $\frac{\langle \epsilon(s)(s-1)\rangle}{\langle s-1\rangle} < \epsilon^*$ and the epidemic threshold is reduced; for $\alpha = 1$ no simplex is traced since $\epsilon(s) = 0\,\forall s$ and the epidemic threshold is that of Eq. (6.2), with only symptomatic isolation.

We define the critical fraction of untraced large simplices α_C as the maximum error allowed in tracing large gatherings to keep the epidemic under control with CT, i.e. for $\alpha > \alpha_C$ the system returns in the active phase. α_C depends on $R_0 = \lambda/\lambda_C^{NA}$ and on the traced simplices, i.e. on s^* that fixes the fraction of nodes traced ϵ^* for a perfect tracing $\alpha = 0$. For small ϵ^* the system is in the active phase even for $\alpha = 0$ for the considered R_0: in this case we set $\alpha_C = 0$. For higher values of ϵ^*, the system is in the absorbing phase for $\alpha = 0$, thus $\alpha_C > 0$ is finite. The value of ϵ_C^* that defines the transition between the two regimes depends on the R_0 considered and can be determined starting from Figure 6.17**a** and Figure 6.14**b**.

In Figure 6.19 we plot α_C as a function of ϵ^* for several R_0: as the transmissibility of the pathogen increases, i.e. R_0, a higher ϵ_C^* is required to move the system

into the absorbing state with perfect CT and the critical fraction α_C decreases considerably. Furthermore α_C grows rapidly with the tracing capacity ϵ^*, indicating the stability of our results: if the system is deeply inside the absorbing phase, i.e. if ϵ^* is sufficiently high, for reasonable values of α the system remains under the epidemic threshold. Thus, the effect of a small fraction of untraced large simplices is strong, but not enough to deteriorate the tracing effectiveness in realistic conditions.

We implemented contact tracing on gatherings, showing that due to the simplicial structure of interactions backward and forward CT are augmented with sideward CT, which, by exploiting the higher-order nature of interactions, traces nodes that have not been directly infected by (forward CT) nor they have transmitted the pathogen to the index case (backward CT). We show the crucial role of sideward CT in tracing large gatherings and in reducing the impact of the SSEs, especially in tracing strategies targeted on large simplices.

We implemented our model on an empirical dataset of gatherings within a University Campus, reconstructed from WiFi data. We suggested optimal choices of the typical size of the gatherings to be traced in order to avoid the closure of the University and to manage the control the epidemic. Moreover, we show how these types of passively obtained data constitute a crucial source of information for the tracing of gatherings and could be a new weapon against the spread of epidemics if supported by appropriate privacy-preserving protocols [26, 275–278].

We did not consider vaccinations [294, 295] and others related interventions, such as allowing access to the University only to individuals equipped with a vaccination certificate, e.g. EU Digital COVID Certificate [274, 296, 297], in a full opening regime: however we expect these effects to do not change the overall picture. Moreover, we expect the effect of sideward CT on the active phase to be even more marked, given the non-linear effect due to the presence of more than one infected node within a single gathering. These are promising directions for future works.

Conclusion

In this thesis we dealt with epidemic processes on adaptive temporal networks, presenting some challenging problems in modelling epidemics in the presence of adaptive behaviours and characterizing the basic mechanisms governing epidemic control measures.

In the first part of this work, we reviewed the foundations of the theory of epidemic processes on time-varying adaptive networks. We initially presented the main properties of temporal networks deriving from the temporal dimension, showing its dramatic effects on the structural and temporal properties of the network. Then, we presented the modelling framework of epidemic processes on temporal networks, highlighting how the network evolution deeply influence the epidemic dynamics. We focused on the class of activity-driven networks, which represents an extremely advantageous scheme for introducing specific mechanisms that shape the social dynamics (e.g. memory, burstiness, higher-order interactions) without losing the possibility of treating the model analytically. Finally, we introduced the concept of adaptiveness, that is the second level of coupling between the epidemic dynamics and the interaction dynamics, since the presence of epidemics induces adaptive behaviours in the population that modify the network dynamics (e.g. risk perception, epidemic control and containment measures).

In the second part of this work, we formulated an adaptive variant of the activity-driven network, assuming a generic change in the activity and attractiveness of the nodes depending on their health status. This model allows to directly implement adaptive behaviours observed during the early stages of the COVID-19 pandemic, also with respect to the timing in their implementation. Moreover, by suitably modifying the proposed model, we described several features of contact tracing, by implementing its different protocols and assessing its effect on gatherings, inspired by the crucial role played by tracing in controlling the spread of SARS-CoV-2.

The models and formalisms introduced constitute a significant advance in the modelling of activity-driven networks as a substrate for epidemic processes, introducing the deep adaptive couplings between the social and the epidemic dynamics. By using a simple adaptive mechanism, the model reproduces a large set of behavioural changes, also providing analytical estimates of their impact on the spread of the epidemic. Furthermore, it allows the implementation of complex adaptive behaviours such as the readdressing of social activity, modelled with a rewiring of the links, and the contact tracing, which constitutes a third dynamics of superinfection, that follows infections identifying and isolating exposed contacts. The proposed approach provides a deep understanding of the foundations of the adaptive mechanisms and of the functioning mechanisms of control and containment measures, for example by unveiling the intrinsic differences between manual and digital tracing protocols in contacts sampling (annealed vs quenched). Furthermore, the adopted

modelling framework allows to introduce specific topological and structural properties of the network of interactions and to estimate their effects on control measures and their effectiveness, for example the effect of heterogeneity in the agents behaviour, i.e. the presence of superspreaders, or the presence of groups and gatherings, i.e. the presence of superspreading events.

These results are relevant in the modelling framework of epidemic processes on adaptive temporal networks, but also have relevance in the understanding and implementation of epidemic control policies. The proposed simplified model, amenable of analytic control, allows to clearly estimate the effect of specific measures and their interplay with the social dynamics. For example, the comparison between manual and digital tracing protocols indicated directions for optimizing the integration of the two protocols in hybrid procedures, showing how manual tracing should be crucial and suggesting an app adoption targeted on the most active individuals. Similarly, the implementation of tracing on gatherings shows how tracing strategies targeted on large gatherings are optimal and allow the control of the epidemic without activity disruption. Moreover, it identifies the optimal size of gatherings to be traced to achieve containment in a real University setting, starting from data on gatherings in the University reconstructed from user connections to the WiFi network.

The proposed approach presents some shortcomings: for example, as far as the network evolution is concerned, we do not consider the presence of memory effects in the link formation and we neglect the bursty dynamics of interactions, by assuming a Poissonian activation dynamics of the interactions. However, thanks to the flexibility of activity-driven networks, the model can be straightforwardly extended with the introduction of further mechanisms shaping the evolution of the network, allowing to investigate their coupling with adaptive behaviours. Similarly, other limitations derive from the epidemiological level, for example we do not consider vaccination policies, the presence of heterogeneity in the susceptibility or in the infectious period: we expect that the general picture is not modified by these elements, which however can be introduced in the proposed formalism with suitable modifications.

The approach introduced in this thesis and the proposed modelling framework open promising new directions on different levels, on the one hand for the exploration of adaptive behaviours and control measures starting from first principles, on the other for investigating the complex interplay between the social dynamics and the epidemic dynamics. We believe that this modelling perspective can represent a starting point for the development of simplified models for the study of epidemic processes in temporal networks in the presence of adaptive behaviours, as well as to develop ideas to optimize epidemic control strategies. Promising perspective are in the direction of modelling of multi-step contact tracing, digital contact tracing in gatherings or higher-order contact tracing protocols.

Appendix A

Analytical derivation of the epidemic threshold for CT protocols

In this Appendix we derive the equations for the evolution of an epidemic with presymptomatic and asymptomatic transmission on the activity-driven network with attractiveness, considering the isolation of symptomatic nodes and the implementation of contact tracing protocols on asymptomatic individuals. We derive the mean-field equations for manual, digital and hybrid CT protocols, and we obtain the condition for the stability of the absorbing state, i.e. the epidemic threshold [28]. The detailed epidemic model and the detailed implementation of adaptive behaviours are described in Chapter 5.

A.1 Manual CT

We first focus on manual CT which occurs in two ways: asymptomatic nodes A can be traced when infected by a presymptomatic P or when they are the source of infection of a susceptible node that will develop symptoms (see Figure 5.5). The tracing is effective with probability $\varepsilon(a_S)$, with a_S activity of the index case.

All the possible transitions among the compartments are depicted in Figure 5.4. The infection and CT transitions are:

$$P + S \xrightarrow{\lambda\delta} P + P \qquad A + S \xrightarrow{\lambda\delta\varepsilon} T + P \qquad T + S \xrightarrow{\lambda\delta\varepsilon} T + P \tag{A.1}$$

$$P + S \xrightarrow{\lambda(1-\delta)\varepsilon} P + T \qquad A + S \xrightarrow{\lambda(1-\delta)} A + A \qquad T + S \xrightarrow{\lambda(1-\delta)} T + A \tag{A.2}$$

$$P + S \xrightarrow{\lambda(1-\delta)(1-\varepsilon)} P + A \qquad A + S \xrightarrow{\lambda\delta(1-\varepsilon)} A + P \qquad T + S \xrightarrow{\lambda\delta(1-\varepsilon)} T + P \tag{A.3}$$

In the event $A + S \to T + P$ both individuals change state; in the event $T + S \xrightarrow{\lambda\delta\varepsilon} T + P$ the individual T is traced two times (also from the individual infected while already traced), but this has no consequences.

The spontaneous transitions are:

$$P \xrightarrow{\gamma_P} I \qquad A \xrightarrow{\mu} R \qquad I \xrightarrow{\mu_I} R \tag{A.4}$$

$$T \xrightarrow{\gamma_A} Q \qquad T \xrightarrow{\mu} R \qquad Q \xrightarrow{\mu} R \tag{A.5}$$

We divide the population into classes of nodes with the same activity and attractiveness (a_S, b_S), considering them statistically equivalent: this is the *activity-attractiveness-based mean-field approach*. The approach is exact since the model is exactly mean-field, indeed all local correlations are removed by link reshuffling. Furthermore, the mean-field epidemic threshold of the SIS and SIR model are the same, so we can consider the evolution equations of the SIS model [126, 128–130]. Finally, the proposed model, in which a symptomatic or presymptomatic pathway occurs at the time of infection, is completely equivalent to initially assigning symptomaticity (with probability δ) or asymptomaticity (with probability $(1-\delta)$) to a node: we will deal with the model in this second formulation for simplicity.

As described in Chapter 5, the epidemic is described in the mean-field approach by the following equations for the probabilities that a symptomatic or asymptomatic node belongs to a specific compartment (see Section 5.3 for the full description of each equation):

$$\begin{aligned}
\partial_t P_{a_S,b_S}(t) = &-\gamma_P P_{a_S,b_S}(t) + \lambda a_S(1 - I_{a_S,b_S}(t) - P_{a_S,b_S}(t))\frac{B(t)}{\langle b(t)\rangle} \\
&+ \lambda b_S(1 - I_{a_S,b_S}(t) - P_{a_S,b_S}(t))\frac{C(t)}{\langle b(t)\rangle} \qquad \text{(A.6)}\\
\partial_t I_{a_S,b_S}(t) = &-\mu_I I_{a_S,b_S}(t) + \gamma_P P_{a_S,b_S}(t) \qquad \text{(A.7)}\\
\partial_t A_{a_S,b_S}(t) = &-\mu A_{a_S,b_S}(t) \qquad \text{(A.8)}\\
&+ \lambda a_S(1 - A_{a_S,b_S}(t) - T_{a_S,b_S}(t) - Q_{a_S,b_S}(t))\frac{B(t) - \delta\overline{\varepsilon b_S P}(t)}{\langle b(t)\rangle} \\
&+ \lambda b_S(1 - A_{a_S,b_S}(t) - T_{a_S,b_S}(t) - Q_{a_S,b_S}(t))\frac{C(t) - \delta\overline{\varepsilon a_S P}(t)}{\langle b(t)\rangle} \\
&- \lambda a_S\delta A_{a_S,b_S}(t)\frac{\overline{\varepsilon b_S} - \overline{\varepsilon b_S I}(t) - \overline{\varepsilon b_S P}(t)}{\langle b(t)\rangle} \\
&- \lambda b_S\delta A_{a_S,b_S}(t)\frac{\overline{\varepsilon a_S} - \overline{\varepsilon a_S I}(t) - \overline{\varepsilon a_S P}(t)}{\langle b(t)\rangle} \\
\partial_t T_{a_S,b_S}(t) = &-(\mu + \gamma_A)T_{a_S,b_S}(t) \qquad \text{(A.9)}\\
&+ \lambda b_S(1 - A_{a_S,b_S}(t) - T_{a_S,b_S}(t) - Q_{a_S,b_S}(t))\frac{\delta\overline{\varepsilon a_S P}(t)}{\langle b(t)\rangle} \\
&+ \lambda a_S(1 - A_{a_S,b_S}(t) - T_{a_S,b_S}(t) - Q_{a_S,b_S}(t))\frac{\delta\overline{\varepsilon b_S P}(t)}{\langle b(t)\rangle} \\
&+ \lambda b_S\delta A_{a_S,b_S}(t)\frac{\overline{\varepsilon a_S} - \overline{\varepsilon a_S I}(t) - \overline{\varepsilon a_S P}(t)}{\langle b(t)\rangle} \\
&+ \lambda a_S\delta A_{a_S,b_S}(t)\frac{\overline{\varepsilon b_S} - \overline{\varepsilon b_S I}(t) - \overline{\varepsilon b_S P}(t)}{\langle b(t)\rangle} \\
\partial_t Q_{a_S,b_S}(t) = &-\mu Q_{a_S,b_S}(t) + \gamma_A T_{a_S,b_S}(t) \qquad \text{(A.10)}
\end{aligned}$$

where we define $\overline{g} = \int da_S db_S \rho(a_S, b_S) g_{a_S,b_S}$, $B(t) = \delta\overline{b_S P}(t) + (1-\delta)[\overline{b_S T}(t) + \overline{b_S A}(t)]$, $C(t) = \delta\overline{a_S P}(t) + (1-\delta)[\overline{a_S T}(t) + \overline{a_S A}(t)]$ and the average attractiveness at time t is $\langle b(t)\rangle = \overline{b_S} - (1-\delta)\overline{b_S Q}(t) - \delta\overline{b_S I}(t)$. Moreover, we consider the system in the thermodynamic limit.

Eqs. (A.6)-(A.10) constitute a set of five coupled non-linear differential equations and describes the epidemic in the presence of manual CT. It admits the absorbing state, in which all individuals are susceptible, as a solution: the epidemic threshold

can be obtained by imposing the stability of the absorbing state, through a linear stability analysis.

Hereafter, we consider the realistic case of positive correlations between activity and attractiveness, while we keep the distribution of activities generic, fixing $\rho(a_S, b_S) = \rho_S(a_S)\delta(b_S - a_S)$, with arbitrary $\rho_S(a_S)$.

The variables of interest for the epidemic are the probabilities averaged over activity and attractiveness: $\overline{P}(t)$, $\overline{I}(t)$, $\overline{A}(t)$, $\overline{T}(t)$, $\overline{Q}(t)$. Their temporal dynamics can be obtained by averaging the Eqs. (A.6) - (A.10) on a_S (since we assume $b_S = a_S$). Similarly, the temporal dynamics of $\overline{a_S T}(t)$, $\overline{a_S A}(t)$, $\overline{a_S P}(t)$ and $\overline{\varepsilon a_S P}(t)$ can be obtained by multiplying Eqs. (A.6) - (A.10) for $a_S\rho_S(a_S)$ or $\varepsilon(a_S)a_S\rho_S(a_S)$ and integrating over the activity. Indeed, these equations are necessary to close the system of equations so that it is complete in the averaged variables.

The equations for the averaged probabilities compose a set of nine coupled differential equations (neglecting second order terms):

$$\partial_t \overline{I}(t) = -\mu_I \overline{I}(t) + \gamma_P \overline{P}(t) \tag{A.11}$$

$$\partial_t \overline{P}(t) = -\gamma_P \overline{P}(t) + 2\lambda[\delta \overline{a_S P}(t) + (1-\delta)(\overline{a_S T}(t) + \overline{a_S A}(t))] \tag{A.12}$$

$$\partial_t \overline{Q}(t) = -\mu \overline{Q}(t) + \gamma_A \overline{T}(t) \tag{A.13}$$

$$\partial_t \overline{T}(t) = -(\mu + \gamma_A)\overline{T}(t) + 2\lambda\delta\overline{\varepsilon a_S P}(t) + 2\lambda\delta\overline{a_S A}(t)\frac{\overline{\varepsilon a_S}}{\overline{a_S}} \tag{A.14}$$

$$\begin{aligned}\partial_t \overline{A}(t) = &-\mu\overline{A}(t) + 2\lambda[\delta(\overline{a_S P}(t) - \overline{\varepsilon a_S P}(t)) + (1-\delta)(\overline{a_S T}(t) + \overline{a_S A}(t))] \\ &- 2\lambda\delta\overline{a_S A}(t)\frac{\overline{\varepsilon a_S}}{\overline{a_S}}\end{aligned} \tag{A.15}$$

$$\partial_t \overline{a_S P}(t) = -\gamma_P \overline{a_S P}(t) + 2\lambda\frac{\overline{a_S^2}}{\overline{a_S}}[\delta\overline{a_S P}(t) + (1-\delta)(\overline{a_S T}(t) + \overline{a_S A}(t))] \tag{A.16}$$

$$\partial_t \overline{\varepsilon a_S P}(t) = -\gamma_P \overline{\varepsilon a_S P}(t) + 2\lambda\frac{\overline{\varepsilon a_S^2}}{\overline{a_S}}[\delta\overline{a_S P}(t) + (1-\delta)(\overline{a_S T}(t) + \overline{a_S A}(t))] \tag{A.17}$$

$$\partial_t \overline{a_S T}(t) = -(\mu + \gamma_A)\overline{a_S T}(t) + 2\lambda\delta\frac{\overline{a_S^2}}{\overline{a_S}}\overline{\varepsilon a_S P}(t) + 2\lambda\delta\overline{a_S^2 A}(t)\frac{\overline{\varepsilon a_S}}{\overline{a_S}} \tag{A.18}$$

$$\begin{aligned}\partial_t \overline{a_S A}(t) = &-\mu\overline{a_S A}(t) + 2\lambda\frac{\overline{a_S^2}}{\overline{a_S}}[\delta(\overline{a_S P}(t) - \overline{\varepsilon a_S P}(t)) + (1-\delta)(\overline{a_S T}(t) + \overline{a_S A}(t))] \\ &- 2\lambda\delta\overline{a_S^2 A}(t)\frac{\overline{\varepsilon a_S}}{\overline{a_S}}\end{aligned} \tag{A.19}$$

The linearized set of equations obtained, however, is not closed as it depends on the variable $\overline{a_S^2 A}(t)$. Indeed, in general the linearized equations for the terms $\overline{a_S^n A}(t)$ and $\overline{a_S^n T}(t)$ always involve terms like $\overline{a_S^{n+1} A}(t)$, due to the tracing terms and for each $n \geq 0$. The system would require an infinite set of coupled equations to be closed.

We close the equations by expressing $\overline{a_S^2 A}(t)$ as a function of the other averaged probabilities: by definition $\overline{a_S^2 A}(t) = \int da_S \rho_S(a_S) a_S^2 A_{a_S}(t)$, thus the system can be closed by expressing $A_{a_S}(t)$ as a function of the other average variables. For the calculation of the epidemic threshold we are interested in the steady state and, in particular, in the absorbing state: so we can consider Eq. (A.8) for $A_{a_S,b_S}(t)$ and linearize it around the absorbing state close to the steady state, i.e. for $\partial_t A_{a_S,b_S}(t) \sim 0$

and fixing $\rho(a_S, b_S) = \rho_S(a_S)\delta(a_S - b_S)$:

$$A_{a_S}(t) \simeq \frac{2\lambda a_S[\delta(\overline{a_S P}(t) - \overline{\varepsilon a_S P}(t)) + (1-\delta)(\overline{a_S T}(t) + \overline{a_S A}(t))]}{\mu\overline{a_S} + 2\lambda\delta a_S\overline{\varepsilon a_S}}. \tag{A.20}$$

Substituting Eq. (A.20) in the definition of $\overline{a_S^2 A}(t)$, we obtain $\overline{a_S^2 A}(t)$ as a function of the only nine variables of which we have an equation:

$$\overline{a_S^2 A}(t) \simeq \frac{2r}{\overline{a_S}}[\delta(\overline{a_S P}(t) - \overline{\varepsilon a_S P}(t)) + (1-\delta)(\overline{a_S T}(t) + \overline{a_S A}(t))]K, \tag{A.21}$$

where $r = \lambda/\mu$ and $K = \overline{\frac{a_S^3}{1+2r\delta a_S \frac{\overline{\varepsilon a_S}}{\overline{a_S}}}} = \int da_S \rho_S(a_S) \frac{a_S^3}{1+2r\delta a_S \frac{\overline{\varepsilon a_S}}{\overline{a_S}}}$.

This allows us to obtain the linearized equations for $\overline{a_S T}(t)$ and $\overline{a_S A}(t)$ so that they depend only on the nine variables for which we have an equation:

$$\begin{aligned}
\partial_t \overline{a_S T}(t) = & -(\mu + \gamma_A)\overline{a_S T}(t) + 2\lambda\delta\frac{\overline{a_S^2}}{\overline{a_S}}\overline{\varepsilon a_S P}(t) \qquad (A.22)\\
& + 4\lambda r\frac{\overline{\varepsilon a_S}}{\overline{a_S}^2}\delta K[\delta(\overline{a_S P}(t) - \overline{\varepsilon a_S P}(t)) + (1-\delta)(\overline{a_S T}(t) + \overline{a_S A}(t))]\\
\partial_t \overline{a_S A}(t) = & -\mu\overline{a_S A}(t) \qquad (A.23)\\
& + 2\lambda\frac{\overline{a_S^2}}{\overline{a_S}}[\delta(\overline{a_S P}(t) - \overline{\varepsilon a_S P}(t)) + (1-\delta)(\overline{a_S T}(t) + \overline{a_S A}(t))]\\
& - 4\lambda r\frac{\overline{\varepsilon a_S}}{\overline{a_S}^2}\delta K[\delta(\overline{a_S P}(t) - \overline{\varepsilon a_S P}(t)) + (1-\delta)(\overline{a_S T}(t) + \overline{a_S A}(t))]
\end{aligned}$$

In this way the epidemic is completely described by a closed and complete set of nine linearized equations in nine variables (Eqs. (A.11)-(A.17) and Eqs. (A.22)-(A.23)), which admits the following Jacobian matrix:

$$\begin{aligned}
J = & \begin{bmatrix}
-\mu_I & \gamma_P & 0 & 0 & 0 & 0 & 0 & 0 & 0\\
0 & -\gamma_P & 0 & 0 & 0 & 2\lambda\delta & 0 & 2\lambda(1-\delta) & 2\lambda(1-\delta)\\
0 & 0 & -\mu & \gamma_A & 0 & 0 & 0 & 0 & 0\\
0 & 0 & 0 & -\mu-\gamma_A & 0 & 0 & 2\lambda\delta & 0 & 2\lambda\delta\frac{\overline{\varepsilon a_S}}{\overline{a_S}}\\
0 & 0 & 0 & 0 & -\mu & 2\lambda\delta & -2\lambda\delta & 2\lambda(1-\delta) & 2\lambda(1-\delta) - 2\lambda\delta\frac{\overline{\varepsilon a_S}}{\overline{a_S}}\\
0 & 0 & 0 & 0 & 0 & -\gamma_P + \Delta & 0 & \Gamma & \Gamma\\
0 & 0 & 0 & 0 & 0 & \phi & -\gamma_P & \Phi & \Phi\\
0 & 0 & 0 & 0 & 0 & \theta & \Delta-\theta & -\mu-\gamma_A+\Psi & \Psi\\
0 & 0 & 0 & 0 & 0 & \Delta-\theta & \theta-\Delta & \Gamma-\Psi & -\mu+\Gamma-\Psi
\end{bmatrix}\\
= & \begin{bmatrix} \mathbb{A}(5\text{x}5) & \mathbb{C}(5\text{x}4) \\ \mathbb{O}(4\text{x}5) & \mathbb{B}(4\text{x}4) \end{bmatrix}
\end{aligned} \tag{A.24}$$

where $\Delta = 2\lambda\delta\frac{\overline{a_S^2}}{\overline{a_S}}$, $\Gamma = 2\lambda(1-\delta)\frac{\overline{a_S^2}}{\overline{a_S}}$, $\phi = 2\lambda\delta\frac{\overline{\varepsilon a_S^2}}{\overline{a_S}}$, $\Phi = 2\lambda(1-\delta)\frac{\overline{\varepsilon a_S^2}}{\overline{a_S}}$, $\theta = 4\lambda r\delta^2\frac{\overline{\varepsilon a_S}}{\overline{a_S}^2}K$ and $\Psi = 4\lambda r\delta(1-\delta)\frac{\overline{\varepsilon a_S}}{\overline{a_S}^2}K$.

The absorbing state is stable if all eigenvalues of the Jacobian matrix are negative. Since the matrix is composed of four blocks, we can consider separately the two blocks on the diagonal: for $\mathbb{A}$ the eigenvalues are $\xi_{1,2} = -\mu$, $\xi_3 = -\mu_I$, $\xi_4 = -\gamma_P$, $\xi_5 = -\mu - \gamma_A$, all negative. Thus the epidemic threshold can be obtained by imposing all eigenvalues of the block $\mathbb{B}$, which is a matrix 4x4, to be negative. $\mathbb{B}$ feature a characteristic polynomial of degree 4: we apply the Descartes' rule of signs to

impose all roots to be negative and we obtain the condition for the stability of the absorbing state:

$$8r^3\delta^2(1-\delta)\frac{\overline{\varepsilon a_S^2}\,\overline{\varepsilon a_S}}{\overline{a_S}}\overline{\frac{a_S^3}{1+2r\delta a_S\frac{\varepsilon a_S}{a_S}}}\frac{\gamma_A}{\mu}-4r^2\delta(1-\delta)\left[\overline{\varepsilon a_S^2}\,\overline{a_S^2}+\frac{\gamma_P}{\mu}\overline{\varepsilon a_S}\,\overline{\frac{a_S^3}{1+2r\delta a_S\frac{\varepsilon a_S}{a_S}}}\right]\frac{\gamma_A}{\mu}$$
$$+2r\overline{a_S^2}\,\overline{a_S}\left(\frac{\gamma_A}{\mu}+1\right)\left(\delta+\frac{\gamma_P}{\mu}(1-\delta)\right)$$
$$-\overline{a_S}^2\frac{\gamma_P}{\mu}\left(\frac{\gamma_A}{\mu}+1\right)<0. \tag{A.25}$$

By setting the equality we obtain Eq. (5.10), i.e. a closed relation for the epidemic threshold r_C. Moreover, the epidemic threshold obtained with this mean-field approach is exact and holds for manual CT, with arbitrary delay τ_C (encoded in γ_A), for arbitrary activity distribution $\rho_S(a_S)$ and for arbitrary recall probability $\varepsilon(a_S)$. In general r_C is obtained numerically from Eq. (5.10), however in Section 5.3 we show some limit cases in which the epidemic threshold can be obtained explicitly.

A.2 Digital CT

We now consider the digital CT: each individual is either endowed or not with the app with a probability $f(a_S)$ depending on the activity. Also in this case, asymptomatic individuals A can be traced when infected by a presymptomatic P or when they are the source of infection for a susceptible node that will develop symptoms, but only if both the nodes involved in the contact downloaded the app.

In this case, different compartments are introduced for individuals without the app (S, I, P, etc.) and with the app (denoted with the superscript $^\alpha$: S^α, I^α, P^α, etc.). In this case $T=0$ and $Q=0$, since we are considering purely digital CT, nevertheless here we write also the transitions involving them since they may play a role for hybrid protocols (see Section A.3).

All the possible transitions among the compartments are depicted in Figure 5.4. The infection and CT transitions involving both individuals without the app (in such cases no new traced individuals are generated):

$$P+S\xrightarrow{\lambda\delta}P+P \qquad A+S\xrightarrow{\lambda\delta}A+P \qquad T+S\xrightarrow{\lambda\delta}T+P \tag{A.26}$$

$$P+S\xrightarrow{\lambda(1-\delta)}P+A \qquad A+S\xrightarrow{\lambda(1-\delta)}A+A \qquad T+S\xrightarrow{\lambda(1-\delta)}T+A \tag{A.27}$$

Those involving only one individual with the app (in such cases no new traced individuals are generated):

$$P^\alpha+S\xrightarrow{\lambda\delta}P^\alpha+P \qquad A^\alpha+S\xrightarrow{\lambda\delta}A^\alpha+P \qquad T^\alpha+S\xrightarrow{\lambda\delta}T^\alpha+P \tag{A.28}$$

$$P^\alpha+S\xrightarrow{\lambda(1-\delta)}P^\alpha+A \qquad A^\alpha+S\xrightarrow{\lambda(1-\delta)}A^\alpha+A \qquad T^\alpha+S\xrightarrow{\lambda(1-\delta)}T^\alpha+A \tag{A.29}$$

$$P+S^\alpha\xrightarrow{\lambda\delta}P+P^\alpha \qquad A+S^\alpha\xrightarrow{\lambda\delta}A+P^\alpha \qquad T+S^\alpha\xrightarrow{\lambda\delta}T+P^\alpha \tag{A.30}$$

$$P + S^\alpha \xrightarrow{\lambda(1-\delta)} P + A^\alpha \qquad A + S^\alpha \xrightarrow{\lambda(1-\delta)} A + A^\alpha \qquad T + S^\alpha \xrightarrow{\lambda(1-\delta)} T + A^\alpha \tag{A.31}$$

Those involving both individuals with the app (in such cases new traced individuals can be generated):

$$P^\alpha + S^\alpha \xrightarrow{\lambda\delta} P^\alpha + P^\alpha \qquad A^\alpha + S^\alpha \xrightarrow{\lambda\delta} T^\alpha + P^\alpha \qquad T^\alpha + S^\alpha \xrightarrow{\lambda\delta} T^\alpha + P^\alpha \tag{A.32}$$

$$P^\alpha + S^\alpha \xrightarrow{\lambda(1-\delta)} P^\alpha + T^\alpha \qquad A^\alpha + S^\alpha \xrightarrow{\lambda(1-\delta)} A^\alpha + A^\alpha \qquad T^\alpha + S^\alpha \xrightarrow{\lambda(1-\delta)} T^\alpha + A^\alpha \tag{A.33}$$

We divide the population into classes of nodes with the same activity and attractiveness (a_S, b_S), considering them statistically equivalent: this is the *activity-attractiveness-based mean-field approach*. The approach is exact since the model is exactly mean-field, indeed all local correlations are removed by link reshuffling. Furthermore, the mean-field epidemic threshold of the SIS and SIR model are the same, so we can consider the evolution equations of the SIS model [126, 128–130]. Finally, the proposed model, in which a symptomatic or presymptomatic pathway occurs at the time of infection, is completely equivalent to initially assigning symptomaticity (with probability δ) or asymptomaticity (with probability $(1-\delta)$) to a node: we will deal with the model in this second formulation for simplicity.

As described in Chapter 5, the epidemic is described in the mean-field approach by the following equations for the probabilities that a symptomatic or asymptomatic node belongs to a specific compartment (see Section 5.4 for the full description of each equation):

$$\begin{aligned}
\partial_t P_{a_S,b_S}(t) = &-\gamma_P P_{a_S,b_S}(t) + \lambda a_S(1 - I_{a_S,b_S}(t) - P_{a_S,b_S}(t))\frac{F(t)}{\langle b(t)\rangle} \\
&+ \lambda b_S(1 - I_{a_S,b_S}(t) - P_{a_S,b_S}(t))\frac{G(t)}{\langle b(t)\rangle}
\end{aligned} \tag{A.34}$$

$$\partial_t I_{a_S,b_S}(t) = -\mu_I I_{a_S,b_S}(t) + \gamma_P P_{a_S,b_S}(t) \tag{A.35}$$

$$\begin{aligned}
\partial_t P^\alpha_{a_S,b_S}(t) = &-\gamma_P P^\alpha_{a_S,b_S}(t) + \lambda a_S(1 - I^\alpha_{a_S,b_S}(t) - P^\alpha_{a_S,b_S}(t))\frac{F(t)}{\langle b(t)\rangle} \\
&+ \lambda b_S(1 - I^\alpha_{a_S,b_S}(t) - P^\alpha_{a_S,b_S}(t))\frac{G(t)}{\langle b(t)\rangle}
\end{aligned} \tag{A.36}$$

$$\partial_t I^\alpha_{a_S,b_S}(t) = -\mu_I I^\alpha_{a_S,b_S}(t) + \gamma_P P^\alpha_{a_S,b_S}(t) \tag{A.37}$$

$$\begin{aligned}
\partial_t A^\alpha_{a_S,b_S}(t) = &-\mu A^\alpha_{a_S,b_S}(t) \\
&+ \lambda a_S(1 - A^\alpha_{a_S,b_S}(t) - T^\alpha_{a_S,b_S}(t) - Q^\alpha_{a_S,b_S}(t))\frac{F(t) - \delta\overline{fb_S P^\alpha}(t)}{\langle b(t)\rangle} \\
&+ \lambda b_S(1 - A^\alpha_{a_S,b_S}(t) - T^\alpha_{a_S,b_S}(t) - Q^\alpha_{a_S,b_S}(t))\frac{G(t) - \delta\overline{fa_S P^\alpha(t)}}{\langle b(t)\rangle} \\
&- \lambda\delta a_S A^\alpha_{a_S,b_S}(t)\frac{\overline{fb_S} - \overline{fb_S P^\alpha}(t) - \overline{fb_S I^\alpha}(t)}{\langle b(t)\rangle} \\
&- \lambda\delta b_S A^\alpha_{a_S,b_S}(t)\frac{\overline{fa_S} - \overline{fa_S P^\alpha}(t) - \overline{fa_S I^\alpha}(t)}{\langle b(t)\rangle}
\end{aligned} \tag{A.38}$$

$$\partial_t Q^\alpha_{a_S,b_S}(t) = -\mu Q^\alpha_{a_S,b_S}(t) + \gamma_P T^\alpha_{a_S,b_S}(t) \tag{A.39}$$

$$\begin{aligned}\partial_t T^{\alpha}_{a_S,b_S}(t) = & -(\mu+\gamma_P)T^{\alpha}_{a_S,b_S}(t) \\ & +\lambda a_S(1-A^{\alpha}_{a_S,b_S}(t)-T^{\alpha}_{a_S,b_S}(t)-Q^{\alpha}_{a_S,b_S}(t))\frac{\delta\overline{fb_SP^{\alpha}}(t)}{\langle b(t)\rangle} \\ & +\lambda b_S(1-A^{\alpha}_{a_S,b_S}(t)-T^{\alpha}_{a_S,b_S}(t)-Q^{\alpha}_{a_S,b_S}(t))\frac{\delta\overline{fa_SP^{\alpha}}(t)}{\langle b(t)\rangle} \\ & +\lambda\delta a_S A^{\alpha}_{a_S,b_S}(t)\frac{\overline{fb_S}-\overline{fb_SP^{\alpha}}(t)-\overline{fb_SI^{\alpha}}(t)}{\langle b(t)\rangle} \\ & +\lambda\delta b_S A^{\alpha}_{a_S,b_S}(t)\frac{\overline{fa_S}-\overline{fa_SP^{\alpha}}(t)-\overline{fa_SI^{\alpha}}(t)}{\langle b(t)\rangle}\end{aligned} \tag{A.40}$$

$$\begin{aligned}\partial_t A_{a_S,b_S}(t) = & -\mu A_{a_S,b_S}(t)+\lambda a_S(1-A_{a_S,b_S}(t))\frac{F(t)}{\langle b(t)\rangle} \\ & +\lambda b_S(1-A_{a_S,b_S}(t))\frac{G(t)}{\langle b(t)\rangle}\end{aligned} \tag{A.41}$$

where we define $\overline{g}=\int da_S db_S \rho(a_S,b_S)g_{a_S,b_S}$, $F(t)=\delta(\overline{fb_SP^{\alpha}}(t)+\overline{(1-f)b_SP}(t))+(1-\delta)(\overline{fb_ST^{\alpha}}(t)+\overline{fb_SA^{\alpha}}(t)+\overline{(1-f)b_SA}(t))$, $G(t)=\delta(\overline{fa_SP^{\alpha}}(t)+\overline{(1-f)a_SP}(t))+(1-\delta)(\overline{fa_ST^{\alpha}}(t)+\overline{fa_SA^{\alpha}}(t)+\overline{(1-f)a_SA}(t))$ and the average attractiveness at time t is $\langle b(t)\rangle=\overline{b_S}-(1-\delta)\overline{fb_SQ^{\alpha}}(t)-\delta(\overline{fb_SI^{\alpha}}(t)+\overline{(1-f)b_SI}(t))$. Moreover, we consider the system in the thermodynamic limit.

Eqs. (A.34)-(A.41) constitute a set of eight coupled non-linear differential equations and describes the epidemic in the presence of digital CT. It admits the absorbing state, in which all individuals are susceptible, as a solution: the epidemic threshold can be obtained by imposing the stability of the absorbing state, through a linear stability analysis.

Hereafter, we consider the realistic case of positive correlations between activity and attractiveness, while we keep the distribution of activities generic, fixing $\rho(a_S,b_S)=\rho_S(a_S)\delta(b_S-a_S)$, with arbitrary $\rho_S(a_S)$.

The variables of interest for the epidemic are the probabilities averaged over activity and attractiveness: $\overline{P}(t)$, $\overline{I}(t)$, $\overline{A}(t)$, $\overline{P^{\alpha}}(t)$, $\overline{I^{\alpha}}(t)$, $\overline{A^{\alpha}}(t)$, $\overline{Q^{\alpha}}(t)$, $\overline{T^{\alpha}}(t)$. Their temporal dynamics can be obtained by averaging the Eqs. (A.34) - (A.41) on a_S (since we assume $b_S=a_S$). Similarly, the temporal dynamics of $\overline{fa_SP^{\alpha}}(t)$, $\overline{fa_ST^{\alpha}}(t)$, $\overline{a_SA^{\alpha}}(t)$, $\overline{fa_SA^{\alpha}}(t)$, $\overline{(1-f)a_SP}(t)$, $\overline{(1-f)a_SA}(t)$ can be obtained by multiplying Eqs. (A.34) - (A.41) for $a_S\rho_S(a_S)$, $f(a_S)a_S\rho_S(a_S)$ or $(1-f(a_S))a_S\rho_S(a_S)$ and integrating over the activity. Indeed, these equations are necessary to close the system of equations so that it is complete in the averaged variables.

The equations for the averaged probabilities compose a set of fourteen coupled differential equations (neglecting second order terms):

$$\begin{aligned}\partial_t\overline{P}(t) = & -\gamma_P\overline{P}(t)+2\lambda\delta(\overline{fa_SP^{\alpha}}(t)+\overline{(1-f)a_SP}(t)) \\ & +2\lambda(1-\delta)(\overline{fa_ST^{\alpha}}(t)+\overline{fa_SA^{\alpha}}(t)+\overline{(1-f)a_SA}(t))\end{aligned} \tag{A.42}$$

$$\partial_t\overline{I}(t) = -\mu_I\overline{I}(t)+\gamma_P\overline{P}(t) \tag{A.43}$$

$$\begin{aligned}\partial_t\overline{P^{\alpha}}(t) = & -\gamma_P\overline{P^{\alpha}}(t)+2\lambda\delta(\overline{fa_SP^{\alpha}}(t)+\overline{(1-f)a_SP}(t)) \\ & +2\lambda(1-\delta)(\overline{fa_ST^{\alpha}}(t)+\overline{fa_SA^{\alpha}}(t)+\overline{(1-f)a_SA}(t))\end{aligned} \tag{A.44}$$

$$\partial_t\overline{I^{\alpha}}(t) = -\mu_I\overline{I^{\alpha}}(t)+\gamma_P\overline{P^{\alpha}}(t) \tag{A.45}$$

$$\begin{aligned}\partial_t\overline{A}(t) = & -\mu\overline{A}(t)+2\lambda\delta(\overline{fa_SP^{\alpha}}(t)+\overline{(1-f)a_SP}(t)) \\ & +2\lambda(1-\delta)(\overline{fa_ST^{\alpha}}(t)+\overline{fa_SA^{\alpha}}(t)+\overline{(1-f)a_SA}(t))\end{aligned} \tag{A.46}$$

$$\partial_t \overline{Q^\alpha}(t) = -\mu \overline{Q^\alpha}(t) + \gamma_P \overline{T^\alpha}(t) \tag{A.47}$$

$$\partial_t \overline{T^\alpha}(t) = -(\mu+\gamma_P)\overline{T^\alpha}(t) + 2\lambda\delta\overline{f a_S P^\alpha}(t) + 2\lambda\delta\overline{a_S A^\alpha}(t)\frac{\overline{f a_S}}{\overline{a_S}} \tag{A.48}$$

$$\begin{aligned}\partial_t \overline{A^\alpha}(t) = &-\mu\overline{A^\alpha}(t) + 2\lambda\delta\overline{(1-f)a_S P}(t) \\ &+ 2\lambda(1-\delta)(\overline{f a_S T^\alpha}(t) + \overline{f a_S A^\alpha}(t) + \overline{(1-f)a_S A}(t)) \\ &- 2\lambda\delta\overline{a_S A^\alpha}(t)\frac{\overline{f a_S}}{\overline{a_S}}\end{aligned} \tag{A.49}$$

$$\begin{aligned}\partial_t \overline{f a_S P^\alpha}(t) = &-\gamma_P \overline{f a_S P^\alpha}(t) + 2\lambda\frac{\overline{f a_S^2}}{\overline{a_S}}\delta(\overline{f a_S P^\alpha}(t) + \overline{(1-f)a_S P}(t)) \\ &+ 2\lambda\frac{\overline{f a_S^2}}{\overline{a_S}}(1-\delta)(\overline{f a_S T^\alpha}(t) + \overline{f a_S A^\alpha}(t) + \overline{(1-f)a_S A}(t))\end{aligned} \tag{A.50}$$

$$\begin{aligned}\partial_t \overline{(1-f)a_S P}(t) = &-\gamma_P \overline{(1-f)a_S P}(t) + 2\lambda\frac{\overline{(1-f)a_S^2}}{\overline{a_S}}\delta(\overline{f a_S P^\alpha}(t) + \overline{(1-f)a_S P}(t)) \\ &+ 2\lambda\frac{\overline{(1-f)a_S^2}}{\overline{a_S}}(1-\delta)(\overline{f a_S T^\alpha}(t) + \overline{f a_S A^\alpha}(t) + \overline{(1-f)a_S A}(t))\end{aligned} \tag{A.51}$$

$$\begin{aligned}\partial_t \overline{(1-f)a_S A}(t) = &-\mu\overline{(1-f)a_S A}(t) + 2\lambda\frac{\overline{(1-f)a_S^2}}{\overline{a_S}}\delta(\overline{f a_S P^\alpha}(t) + \overline{(1-f)a_S P}(t)) \\ &+ 2\lambda\frac{\overline{(1-f)a_S^2}}{\overline{a_S}}(1-\delta)(\overline{f a_S T^\alpha}(t) + \overline{f a_S A^\alpha}(t) + \overline{(1-f)a_S A}(t))\end{aligned} \tag{A.52}$$

$$\partial_t \overline{f a_S T^\alpha}(t) = -(\mu+\gamma_P)\overline{f a_S T^\alpha}(t) + 2\lambda\delta\frac{\overline{f a_S^2}}{\overline{a_S}}\overline{f a_S P^\alpha}(t) + 2\lambda\delta\overline{f a_S^2 A^\alpha}(t)\frac{\overline{f a_S}}{\overline{a_S}} \tag{A.53}$$

$$\begin{aligned}\partial_t \overline{a_S A^\alpha}(t) = &-\mu\overline{a_S A^\alpha}(t) + 2\lambda\frac{\overline{a_S^2}}{\overline{a_S}}\delta\overline{(1-f)a_S P}(t) \\ &+ 2\lambda\frac{\overline{a_S^2}}{\overline{a_S}}(1-\delta)(\overline{f a_S T^\alpha}(t) + \overline{f a_S A^\alpha}(t) + \overline{(1-f)a_S A}(t)) \\ &- 2\lambda\delta\overline{a_S^2 A^\alpha}(t)\frac{\overline{f a_S}}{\overline{a_S}}\end{aligned} \tag{A.54}$$

$$\begin{aligned}\partial_t \overline{f a_S A^\alpha}(t) = &-\mu\overline{f a_S A^\alpha}(t) + 2\lambda\frac{\overline{f a_S^2}}{\overline{a_S}}\delta\overline{(1-f)a_S P}(t) \\ &+ 2\lambda\frac{\overline{f a_S^2}}{\overline{a_S}}(1-\delta)(\overline{f a_S T^\alpha}(t) + \overline{f a_S A^\alpha}(t) + \overline{(1-f)a_S A}(t)) \\ &- 2\lambda\delta\overline{f a_S^2 A^\alpha}(t)\frac{\overline{f a_S}}{\overline{a_S}}\end{aligned} \tag{A.55}$$

The linearized set of equations obtained, however, is not closed as it depends on the variables $\overline{f a_S^2 A^\alpha}(t)$ and $\overline{a_S^2 A^\alpha}(t)$. Indeed, in general the linearized equations for the terms $\overline{a_S^n T^\alpha}(t)$ and $\overline{a_S^n A^\alpha}(t)$ always involve terms like $\overline{a_S^{n+1} A^\alpha}(t)$, due to the tracing terms and for each $n \geq 0$. The system would require an infinite set of coupled equations to be closed.

We close the equations by expressing $\overline{fa_S^2 A^\alpha}(t)$ and $\overline{a_S^2 A^\alpha}(t)$ as a function of the other averaged probabilities: by definition $\overline{fa_S^2 A^\alpha}(t) = \int da_S \rho_S(a_S) f(a_S) a_S^2 A^\alpha_{a_S}(t)$ and $\overline{a_S^2 A^\alpha}(t) = \int da_S \rho_S(a_S) a_S^2 A^\alpha_{a_S}(t)$, thus the system can be closed by expressing $A^\alpha_{a_S}(t)$ as a function of the other average variables. For the calculation of the epidemic threshold we are interested in the steady state and, in particular, in the absorbing state: so we can consider Eq. (A.38) for $A^\alpha_{a_S,b_S}(t)$, we linearize it around the absorbing state close to the steady state, i.e. $\partial_t A^\alpha_{a_S,b_S}(t) \sim 0$ by fixing $\rho(a_S, b_S) = \rho_S(a_S)\delta(a_S - b_S)$:

$$A^\alpha_{a_S}(t) \simeq \frac{2\lambda a_S[\delta\overline{(1-f)a_S P}(t) + (1-\delta)(\overline{fa_S T^\alpha}(t) + \overline{fa_S A^\alpha}(t) + \overline{(1-f)a_S A}(t))]}{\mu\overline{a_S} + 2\lambda\delta a_S\overline{fa_S}}. \tag{A.56}$$

Substituting Eq. (A.56) in the definition of $\overline{fa_S^2 A^\alpha}(t)$ and of $\overline{a_S^2 A^\alpha}(t)$, we obtain the two variables as a function of the only fourteen variables of which we have an equation:

$$\overline{fa_S^2 A^\alpha}(t) \simeq \frac{2}{\overline{a_S}} r[\delta\overline{(1-f)a_S P}(t) + (1-\delta)(\overline{fa_S T^\alpha}(t) + \overline{fa_S A^\alpha}(t) + \overline{(1-f)a_S A}(t))]H, \tag{A.57}$$

$$\overline{a_S^2 A^\alpha}(t) \simeq \frac{2}{\overline{a_S}} r[\delta\overline{(1-f)a_S P}(t) + (1-\delta)(\overline{fa_S T^\alpha}(t) + \overline{fa_S A^\alpha}(t) + \overline{(1-f)a_S A}(t))]Z, \tag{A.58}$$

where $H = \overline{\frac{fa_S^3}{1+2r\delta a_S \frac{fa_S}{a_S}}} = \int da_S \rho_S(a_S) \frac{f(a_S)a_S^3}{1+2r\delta a_S \frac{fa_S}{a_S}}$, $Z = \overline{\frac{a_S^3}{1+2r\delta a_S \frac{fa_S}{a_S}}}$.

This allows us to obtain the linearized equations for $\overline{a_S A^\alpha}$, $\overline{fa_S A^\alpha}$ and $\overline{fa_S T^\alpha}$ so that they depend only on the fourteen variables for which we have an equation:

$$\begin{aligned}
\partial_t\overline{a_S A^\alpha}(t) = & -\mu\overline{a_S A^\alpha}(t) \\
& + 2\lambda\frac{\overline{a_S^2}}{\overline{a_S}}[\delta\overline{(1-f)a_S P}(t) + (1-\delta)(\overline{fa_S T^\alpha}(t) + \overline{fa_S A^\alpha}(t) + \overline{(1-f)a_S A}(t))] \\
& - 4\lambda r\delta\frac{\overline{fa_S}}{\overline{a_S}^2}\delta\overline{(1-f)a_S P}(t)Z \\
& - 4\lambda r\delta\frac{\overline{fa_S}}{\overline{a_S}^2}(1-\delta)(\overline{fa_S T^\alpha}(t) + \overline{fa_S A^\alpha}(t) + \overline{(1-f)a_S A}(t))Z
\end{aligned} \tag{A.59}$$

$$\begin{aligned}
\partial_t\overline{fa_S A^\alpha}(t) = & -\mu\overline{fa_S A^\alpha}(t) + 2\lambda\frac{\overline{fa_S^2}}{\overline{a_S}}\delta\overline{(1-f)a_S P}(t) \\
& + 2\lambda\frac{\overline{fa_S^2}}{\overline{a_S}}(1-\delta)(\overline{fa_S T^\alpha}(t) + \overline{fa_S A^\alpha}(t) + \overline{(1-f)a_S A}(t)) \\
& - 4\lambda r\delta\frac{\overline{fa_S}}{\overline{a_S}^2}\delta\overline{(1-f)a_S P}(t)H \\
& - 4\lambda r\delta\frac{\overline{fa_S}}{\overline{a_S}^2}(1-\delta)(\overline{fa_S T^\alpha}(t) + \overline{fa_S A^\alpha}(t) + \overline{(1-f)a_S A}(t))H
\end{aligned} \tag{A.60}$$

$$\begin{aligned}\partial_t \overline{fa_S T^\alpha}(t) = & -(\mu+\gamma_P)\overline{fa_S T^\alpha}(t) + 2\lambda\delta\frac{\overline{fa_S^2}}{\overline{a_S}}\overline{fa_S P^\alpha}(t) \\ & + 4\lambda r\delta\frac{\overline{fa_S}}{\overline{a_S}^2}\delta\overline{(1-f)a_S P}(t)H \\ & + 4\lambda r\delta\frac{\overline{fa_S}}{\overline{a_S}^2}(1-\delta)(\overline{fa_S T^\alpha}(t) + \overline{fa_S A^\alpha}(t) + \overline{(1-f)a_S A}(t))H\end{aligned} \tag{A.61}$$

In this way the epidemic is completely described by a closed and complete set of fourteen linearized equations in fourteen variables (Eqs. (A.42)-(A.52) and Eqs. (A.59)-A.61), which admits the following Jacobian matrix:

$$J = \begin{bmatrix} \mathbb{A}(9\text{x}9) & \mathbb{C}(9\text{x}5) \\ \mathbb{O}(5\text{x}9) & \mathbb{B}(5\text{x}5) \end{bmatrix} \tag{A.62}$$

Where $\mathbb{O}$ is the zero matrix, and:

$$\mathbb{A} = \begin{bmatrix} -\mu_I & \gamma_P & 0 & 0 & 0 & 0 & 0 & 0 & 0 \\ 0 & -\gamma_P & 0 & 0 & 0 & 0 & 0 & 0 & 0 \\ 0 & 0 & -\mu_I & \gamma_P & 0 & 0 & 0 & 0 & 0 \\ 0 & 0 & 0 & -\gamma_P & 0 & 0 & 0 & 0 & 0 \\ 0 & 0 & 0 & 0 & -\mu & 0 & 0 & 0 & 0 \\ 0 & 0 & 0 & 0 & 0 & -\mu & +\gamma_P & 0 & 0 \\ 0 & 0 & 0 & 0 & 0 & 0 & -\mu-\gamma_P & 0 & 2\lambda\delta\frac{\overline{fa_S}}{\overline{a_S}} \\ 0 & 0 & 0 & 0 & 0 & 0 & 0 & -\mu & -2\lambda\delta\frac{\overline{fa_S}}{\overline{a_S}} \\ 0 & 0 & 0 & 0 & 0 & 0 & 0 & 0 & -\mu \end{bmatrix} \tag{A.63}$$

$$\mathbb{C} = \begin{bmatrix} 0 & 0 & 0 & 0 & 0 \\ 2\lambda\delta & 2\lambda\delta & 2\lambda(1-\delta) & 2\lambda(1-\delta) & 2\lambda(1-\delta) \\ 0 & 0 & 0 & 0 & 0 \\ 2\lambda\delta & 2\lambda\delta & 2\lambda(1-\delta) & 2\lambda(1-\delta) & 2\lambda(1-\delta) \\ 2\lambda\delta & 2\lambda\delta & 2\lambda(1-\delta) & 2\lambda(1-\delta) & 2\lambda(1-\delta) \\ 0 & 0 & 0 & 0 & 0 \\ 2\lambda\delta & 0 & 0 & 0 & 0 \\ 0 & 2\lambda\delta & 2\lambda(1-\delta) & 2\lambda(1-\delta) & 2\lambda(1-\delta) \\ 0 & \Delta+\phi-\Phi\frac{Z}{H} & \theta+\Gamma-\Psi\frac{Z}{H} & \theta+\Gamma-\Psi\frac{Z}{H} & \theta+\Gamma-\Psi\frac{Z}{H} \end{bmatrix} \tag{A.64}$$

$$\mathbb{B} = \begin{bmatrix} -\gamma_P+\Delta & \Delta & \Gamma & \Gamma & \Gamma \\ \phi & -\gamma_P+\phi & \theta & \theta & \theta \\ \phi & \phi & -\mu+\theta & \theta & \theta \\ \Delta & \Phi & \Psi & -\mu-\gamma_P+\Psi & \Psi \\ \Delta-\Phi & \Gamma-\Psi & \Gamma-\Psi & -\mu+\Gamma-\Psi & \end{bmatrix} \tag{A.65}$$

where $\Delta = 2\lambda\delta\frac{\overline{fa_S^2}}{\overline{a_S}}$, $\Gamma = 2\lambda(1-\delta)\frac{\overline{fa_S^2}}{\overline{a_S}}$, $\phi = 2\lambda\delta\frac{\overline{(1-f)a_S^2}}{\overline{a_S}}$, $\theta = 2\lambda(1-\delta)\frac{\overline{(1-f)a_S^2}}{\overline{a_S}}$, $\Phi = 4\lambda r\delta^2\frac{\overline{fa_S}}{\overline{a_S}^2}H$ and $\Psi = 4\lambda r\delta(1-\delta)\frac{\overline{fa_S}}{\overline{a_S}^2}H$.

The absorbing state is stable if all eigenvalues of the Jacobian matrix are negative. Since the matrix is composed of four blocks, we can consider separately the two blocks on the diagonal: for $\mathbb{A}$ the eigenvalues are $\xi_{1,2} = -\mu_I$, $\xi_{3,4,5,6} = -\mu$, $\xi_{7,8} = -\gamma_P$, $\xi_9 = -\mu-\gamma_P$, all negative. Thus the epidemic threshold can be obtained by imposing all eigenvalues of the block $\mathbb{B}$, which is a matrix 5x5, to be negative. $\mathbb{B}$

feature a characteristic polynomial of degree 5: we apply the Descartes' rule of signs to impose all roots to be negative and we obtain the condition for the stability of the absorbing state:

$$8r^3\delta^2(1-\delta)\frac{\overline{fa_S^2}\,\overline{fa_S}}{\overline{a_S}}\frac{\overline{fa_S^3}}{1+2r\delta a_S\frac{\overline{fa_S}}{\overline{a_S}}}\frac{\gamma_P}{\mu}-4r^2\delta(1-\delta)\left[\overline{fa_S^2}^2+\frac{\gamma_P}{\mu}\overline{fa_S}\frac{\overline{fa_S^3}}{1+2r\delta a_S\frac{\overline{fa_S}}{\overline{a_S}}}\right]\frac{\gamma_P}{\mu}$$
$$+2r\overline{a_S^2}\,\overline{a_S}\left(\frac{\gamma_P}{\mu}+1\right)\left(\delta+\frac{\gamma_P}{\mu}(1-\delta)\right)$$
$$-\overline{a_S}^2\frac{\gamma_P}{\mu}\left(\frac{\gamma_P}{\mu}+1\right)<0. \tag{A.66}$$

By setting the equality we obtain Eq. (5.26), i.e. a closed relation for the epidemic threshold r_C. Moreover, the epidemic threshold obtained with this mean-field approach is exact and holds for digital CT, for arbitrary activity distribution $\rho_S(a_S)$ and distribution of the app in the population $f(a_S)$. In general r_C is obtained numerically from Eq. (5.26), however in Section 5.4 we show some limit cases in which the epidemic threshold can be obtained explicitly.

A.3 Hybrid CT

We now consider the hybrid CT: each individual is either endowed or not with the app with a probability $f(a_S)$ depending on the activity. Symptomatic nodes with the app activate both digital and manual CT, their contacts with the app are traced digitally while the other contacts are traced manually; symptomatic nodes without the app activate only manual CT on all their contacts.

In this case asymptomatic nodes A can be traced T when infected by a presymptomatic P or when they are source of infection of a susceptible node that will develop symptoms. The contact-induce and spontaneous transitions occurring in the presence of hybrid CT can be deduced by the transitions described in Sections A.1 and A.2 for manual and digital CT: analogously to digital CT, different compartments are introduced for individuals without the app (S, I, P, etc.) and with the app (denoted with the superscript $^\alpha$: S^α, I^α, P^α, etc.). In this case $T \neq 0$ and $Q \neq 0$, since we are considering also manual CT. Moreover, a further compartment is introduced, T_M^α, indicating individuals who downloaded the app traced manually, so that their transition to the Q^α occurs with a rate $\gamma_A = 1/(\tau_P + \tau_C)$.

We divide the population into classes of nodes with the same activity and attractiveness (a_S, b_S), considering them statistically equivalent: this is the *activity-attractiveness-based mean-field approach*. The approach is exact since the model is exactly mean-field, indeed all local correlations are removed by link reshuffling. Furthermore, the mean-field epidemic threshold of the SIS and SIR model are the same, so we can consider the evolution equations of the SIS model [126, 128–130].

Hereafter, we consider the realistic case of positive correlations between activity and attractiveness, while we keep the distribution of activities generic, fixing for $\rho(a_S, b_S) = \rho_S(a_S)\delta(b_S - a_S)$, with arbitrary $\rho_S(a_S)$.

As described in Chapter 5, the epidemic is described in the mean-field approach by the following equations for the probabilities that a symptomatic or asymptomatic

node belongs to a specific compartment (see Section 5.9):

$$\partial_t P_{a_S}(t) = -\gamma_P P_{a_S}(t) + 2\lambda(1 - P_{a_S}(t) - I_{a_S}(t))\frac{a_S}{\langle b(t)\rangle}Z(t) \tag{A.67}$$

$$\partial_t I_{a_S}(t) = -\mu_I I_{a_S}(t) + \gamma_P P_{a_S}(t) \tag{A.68}$$

$$\partial_t P^{\alpha}_{a_S}(t) = -\gamma_P P^{\alpha}_{a_S}(t) + 2\lambda(1 - P^{\alpha}_{a_S}(t) - I^{\alpha}_{a_S}(t))\frac{a_S}{\langle b(t)\rangle}Z(t) \tag{A.69}$$

$$\partial_t I^{\alpha}_{a_S}(t) = -\mu_I I^{\alpha}_{a_S}(t) + \gamma_P P^{\alpha}_{a_S}(t) \tag{A.70}$$

$$\begin{aligned}\partial_t A_{a_S}(t) = & -\mu A_{a_S}(t) \\ & + 2\lambda(1 - A_{a_S}(t) - T_{a_S}(t) - Q_{a_S}(t))\frac{a_S}{\langle b(t)\rangle}W(t) \\ & - 2\lambda\delta A_{a_S}(t)\frac{a_S}{\langle b(t)\rangle}(\overline{a_S\varepsilon f} - \overline{a_S\varepsilon f P^{\alpha}}(t) - \overline{a_S\varepsilon f I^{\alpha}}(t)) \\ & - 2\lambda\delta A_{a_S}(t)\frac{a_S}{\langle b(t)\rangle}(\overline{a_S\varepsilon(1-f)} - \overline{a_S\varepsilon(1-f)P}(t) - \overline{a_S\varepsilon(1-f)I}(t))]\end{aligned} \tag{A.71}$$

$$\begin{aligned}\partial_t T_{a_S}(t) = & -(\mu + \gamma_A)T_{a_S}(t) \\ & + 2\lambda\delta\frac{a_S}{\langle b(t)\rangle}(1 - A_{a_S}(t) - T_{a_S}(t) - Q_{a_S}(t))[\overline{a_S\varepsilon f P^{\alpha}}(t) + \overline{a_S\varepsilon(1-f)P}(t)] \\ & + 2\lambda\delta A_{a_S}(t)\frac{a_S}{\langle b(t)\rangle}(\overline{a_S\varepsilon f} - \overline{a_S\varepsilon f P^{\alpha}}(t) - \overline{a_S\varepsilon f I^{\alpha}}(t)) \\ & + 2\lambda\delta A_{a_S}(t)\frac{a_S}{\langle b(t)\rangle}(\overline{a_S\varepsilon(1-f)} - \overline{a_S\varepsilon(1-f)P}(t) - \overline{a_S\varepsilon(1-f)I}(t))]\end{aligned} \tag{A.72}$$

$$\partial_t Q_{a_S}(t) = -\mu Q_{a_S}(t) + \gamma_A T_{a_S}(t) \tag{A.73}$$

$$\begin{aligned}\partial_t A^{\alpha}_{a_S}(t) = & -\mu A^{\alpha}_{a_S}(t) \\ & + 2\lambda(1 - A^{\alpha}_{a_S}(t) - T^{\alpha}_{a_S}(t) - T^{\alpha}_{a_S|M}(t) - Q^{\alpha}_{a_S}(t))\frac{a_S}{\langle b(t)\rangle}T(t) \\ & - 2\lambda\delta A^{\alpha}_{a_S}(t)\frac{a_S}{\langle b(t)\rangle}(\overline{a_S f} - \overline{a_S f P^{\alpha}}(t) - \overline{a_S f I^{\alpha}}(t)) \\ & - 2\lambda\delta A^{\alpha}_{a_S}(t)\frac{a_S}{\langle b(t)\rangle}(\overline{a_S\varepsilon(1-f)} - \overline{a_S\varepsilon(1-f)P}(t) - \overline{a_S\varepsilon(1-f)I}(t))\end{aligned} \tag{A.74}$$

$$\begin{aligned}\partial_t T^{\alpha}_{a_S}(t) = & -(\mu + \gamma_P)T^{\alpha}_{a_S}(t) \\ & + 2\lambda\delta\frac{a_S}{\langle b(t)\rangle}(1 - A^{\alpha}_{a_S}(t) - T^{\alpha}_{a_S}(t) - T^{\alpha}_{a_S|M}(t) - Q^{\alpha}_{a_S}(t))\overline{a_S f P^{\alpha}}(t) \\ & + 2\lambda\delta A^{\alpha}_{a_S}(t)\frac{a_S}{\langle b(t)\rangle}[\overline{a_S f} - \overline{a_S f P^{\alpha}}(t) - \overline{a_S f I^{\alpha}}(t)]\end{aligned} \tag{A.75}$$

$$\begin{aligned}\partial_t T^{\alpha}_{a_S|M}(t) = & -(\mu + \gamma_A)T^{\alpha}_{a_S|M}(t) \\ & + 2\lambda\delta\frac{a_S}{\langle b(t)\rangle}(1 - A^{\alpha}_{a_S}(t) - T^{\alpha}_{a_S}(t) - T^{\alpha}_{a_S|M}(t) - Q^{\alpha}_{a_S}(t))\overline{a_S\varepsilon(1-f)P}(t) \\ & + 2\lambda\delta A^{\alpha}_{a_S}(t)\frac{a_S}{\langle b(t)\rangle}[\overline{a_S\varepsilon(1-f)} - \overline{a_S\varepsilon(1-f)P}(t) - \overline{a_S\varepsilon(1-f)I}(t)]\end{aligned} \tag{A.76}$$

$$\partial_t Q^{\alpha}_{a_S}(t) = -\mu Q^{\alpha}_{a_S}(t) + \gamma_P T^{\alpha}_{a_S}(t) + \gamma_A T^{\alpha}_{a_S|M}(t) \tag{A.77}$$

where:

$$Z(t) = \delta(\overline{a_S f P^\alpha}(t) + \overline{a_S(1-f)P}(t)) + (1-\delta)(\overline{a_S f A^\alpha}(t) + \overline{a_S f T^\alpha}(t) + \overline{a_S f T_M^\alpha}(t) + \overline{a_S(1-f)T}(t) + \overline{a_S(1-f)A}(t)) \tag{A.78}$$

$$T(t) = \delta\overline{a_S(1-\varepsilon)(1-f)P}(t) + (1-\delta)(\overline{a_S f A^\alpha}(t) + \overline{a_S f T^\alpha}(t) + \overline{a_S f T_M^\alpha}(t) + \overline{a_S(1-f)T}(t) + \overline{a_S(1-f)A}(t)) \tag{A.79}$$

$$W(t) = \delta(\overline{a_S(1-\varepsilon)f P^\alpha}(t) + \overline{a_S(1-\varepsilon)(1-f)P}(t)) + (1-\delta)(\overline{a_S f A^\alpha}(t) + \overline{a_S f T^\alpha}(t) + \overline{a_S f T_M^\alpha}(t) + \overline{a_S(1-f)T}(t) + \overline{a_S(1-f)A}(t)) \tag{A.80}$$

Moreover, we define $\overline{g} = \int da_S \rho_S(a_S) g_{a_S}$ and the average attractiveness at time t is $\langle b(t)\rangle = \overline{b_S} - (1-\delta)(\overline{f b_S Q^\alpha}(t) + \overline{(1-f)b_S Q}(t)) - \delta(\overline{f b_S I^\alpha}(t) + \overline{(1-f)b_S I}(t))$. We consider the system in the thermodynamic limit.

Eqs. (A.67)-(A.77) constitute a set of eleven coupled non-linear differential equations and describes the epidemic in the presence of hybrid CT. It admits the absorbing state, in which all individuals are susceptible, as a solution: the epidemic threshold can be obtained by imposing the stability of the absorbing state, through a linear stability analysis.

Similarly to the manual and digital case of Sections A.1 and A.2, we consider the averaged variables (eventually multiplied by combinations of a_S, $\varepsilon(a_S)$ and $f(a_S)$) by averaging (A.67)-(A.77) on the activity. Then we close the equations in analogously to the purely manual and digital case. We obtain a complex closed and complete set of twenty-two coupled non-linear differential equations, which admits the following Jacobian matrix, obtained by linearizing the system around the absorbing state:

$$J = \begin{bmatrix} \mathbb{A}(13\text{x}13) & \mathbb{C}(13\text{x}9) \\ \mathbb{O}(9\text{x}13) & \mathbb{B}(9\text{x}9) \end{bmatrix} \tag{A.81}$$

where $\mathbb{O}$ is the zero matrix.

$$\mathbb{A} = \begin{bmatrix} -\mu_I & \gamma_P & 0 & 0 & 0 & 0 & 0 & 0 & 0 & 0 & 0 & 0 & 0 \\ 0 & -\gamma_P & 0 & 0 & 0 & 0 & 0 & 0 & 0 & 0 & 0 & 0 & 0 \\ 0 & 0 & -\mu_I & \gamma_P & 0 & 0 & 0 & 0 & 0 & 0 & 0 & 0 & 0 \\ 0 & 0 & 0 & -\gamma_P & 0 & 0 & 0 & 0 & 0 & 0 & 0 & 0 & 0 \\ 0 & 0 & 0 & 0 & -\mu & \gamma_A & 0 & 0 & 0 & 0 & 0 & 0 & 0 \\ 0 & 0 & 0 & 0 & 0 & -\omega & 0 & 0 & 0 & 0 & 0 & 2\lambda\delta\frac{\overline{a_S\varepsilon}}{\overline{a_S}} & 0 \\ 0 & 0 & 0 & 0 & 0 & 0 & -\mu & 0 & 0 & 0 & 0 & -2\lambda\delta\frac{\overline{a_S\varepsilon}}{\overline{a_S}} & 0 \\ 0 & 0 & 0 & 0 & 0 & 0 & 0 & -\mu & \gamma_P & \gamma_A & 0 & 0 & 0 \\ 0 & 0 & 0 & 0 & 0 & 0 & 0 & 0 & -\alpha & 0 & 0 & 0 & 2\lambda\delta\frac{\overline{a_S f}}{\overline{a_S}} \\ 0 & 0 & 0 & 0 & 0 & 0 & 0 & 0 & 0 & -\omega & 0 & 0 & C \\ 0 & 0 & 0 & 0 & 0 & 0 & 0 & 0 & 0 & 0 & -\mu & 0 & B \\ 0 & 0 & 0 & 0 & 0 & 0 & 0 & 0 & 0 & 0 & 0 & -\mu & 0 \\ 0 & 0 & 0 & 0 & 0 & 0 & 0 & 0 & 0 & 0 & 0 & 0 & -\mu \end{bmatrix} \tag{A.82}$$

$$\mathbb{C} = \begin{bmatrix} 0 & 0 & 0 & 0 & 0 & 0 & 0 & 0 & 0 \\ 0 & 0 & 2\lambda\delta & 2\lambda\delta & 2\lambda(1-\delta) & 2\lambda(1-\delta) & 2\lambda(1-\delta) & 2\lambda(1-\delta) & 2\lambda(1-\delta) \\ 0 & 0 & 0 & 0 & 0 & 0 & 0 & 0 & 0 \\ 0 & 0 & 2\lambda\delta & 2\lambda\delta & 2\lambda(1-\delta) & 2\lambda(1-\delta) & 2\lambda(1-\delta) & 2\lambda(1-\delta) & 2\lambda(1-\delta) \\ 0 & 0 & 0 & 0 & 0 & 0 & 0 & 0 & 0 \\ 2\lambda\delta & 2\lambda\delta & 0 & 0 & 0 & 0 & 0 & 0 & 0 \\ -2\lambda\delta & -2\lambda\delta & 2\lambda\delta & 2\lambda\delta & 2\lambda(1-\delta) & 2\lambda(1-\delta) & 2\lambda(1-\delta) & 2\lambda(1-\delta) & 2\lambda(1-\delta) \\ 0 & 0 & 0 & 0 & 0 & 0 & 0 & 0 & 0 \\ 0 & 0 & 0 & 2\lambda\delta & 0 & 0 & 0 & 0 & 0 \\ 2\lambda\delta & 0 & 0 & 0 & 0 & 0 & 0 & 0 & 0 \\ -2\lambda\delta & 0 & 2\lambda\delta & 0 & 2\lambda(1-\delta) & 2\lambda(1-\delta) & 2\lambda(1-\delta) & 2\lambda(1-\delta) & 2\lambda(1-\delta) \\ -\Psi\delta & -\Psi\delta & \Psi\delta & \Psi\delta & \Psi(1-\delta) & \Psi(1-\delta) & \Psi(1-\delta) & \Psi(1-\delta) & \Psi(1-\delta) \\ -\theta\delta & 0 & \theta\delta & 0 & \theta(1-\delta) & \theta(1-\delta) & \theta(1-\delta) & \theta(1-\delta) & \theta(1-\delta) \end{bmatrix} \tag{A.83}$$

with $\Psi = 2\lambda\frac{\overline{a_S^2}}{\overline{a_S}} - 4\lambda r\delta\frac{\overline{a_S\varepsilon}}{\overline{a_S}^2}K$, $\theta = 2\lambda\frac{\overline{a_S^2}}{\overline{a_S}} - 4\lambda r\delta\frac{\overline{a_S\varepsilon(1-f)}+\overline{a_Sf}}{\overline{a_S}^2}J$, $K = \frac{\overline{a_S^3}}{1+2ra_S\delta\frac{\overline{a_S\varepsilon}}{\overline{a_S}}}$, $J = \frac{\overline{a_S^3}}{1+2ra_S\delta\frac{\overline{a_Sf}+\overline{a_S\varepsilon(1-f)}}{\overline{a_S}}}$, $\omega = \mu+\gamma_A$, $\alpha = \mu+\gamma_P$, $B = -2\lambda\delta\frac{\overline{a_Sf}+\overline{a_S\varepsilon(1-f)}}{\overline{a_S}}$ and $C = 2\lambda\delta\frac{\overline{a_S\varepsilon(1-f)}}{\overline{a_S}}$.

$$\mathbb{B} = \begin{bmatrix} -\gamma_P & 0 & \Xi\delta & \Xi\delta & \Xi\sigma & \Xi\sigma & \Xi\sigma & \Xi\sigma & \Xi\sigma \\ 0 & -\gamma_P & \Pi\delta & \Pi\delta & \Pi\sigma & \Pi\sigma & \Pi\sigma & \Pi\sigma & \Pi\sigma \\ 0 & 0 & -\gamma_P+\Delta\delta & \Delta\delta & \Delta\sigma & \Delta\sigma & \Delta\sigma & \Delta\sigma & \Delta\sigma \\ 0 & 0 & \beta\delta & -\gamma_P+\beta\delta & \beta\sigma & \beta\sigma & \beta\sigma & \beta\sigma & \beta\sigma \\ \Omega\delta & \Omega\delta & \phi\delta & \phi\delta & -\omega+\phi\sigma & \phi\sigma & \phi\sigma & \phi\sigma & \phi\sigma \\ -\Gamma\delta & 0 & \Gamma\delta & \beta\delta & \Gamma\sigma & -\alpha+\Gamma\sigma & \Gamma\sigma & \Gamma\sigma & \Gamma\sigma \\ \Sigma\delta & 0 & \Phi\delta & 0 & \Phi\sigma & \Phi\sigma & -\omega+\Phi\sigma & \Phi\sigma & \Phi\sigma \\ -\Omega\delta & -\Omega\delta & \Omega\delta & \Omega\delta & \Omega\sigma & \Omega\sigma & \Omega\sigma & -\mu+\Omega\sigma & \Omega\sigma \\ -\Lambda\delta & 0 & \Lambda\delta & 0 & \Lambda\sigma & \Lambda\sigma & \Lambda\sigma & \Lambda\sigma & -\mu+\Lambda\sigma \end{bmatrix} \tag{A.84}$$

with $\sigma = (1-\delta)$, $\Xi = 2\lambda\frac{\overline{a_S^2\varepsilon(1-f)}}{\overline{a_S}}$, $\Pi = 2\lambda\frac{\overline{a_S^2\varepsilon f}}{\overline{a_S}}$, $\Delta = 2\lambda\frac{\overline{a_S^2(1-f)}}{\overline{a_S}}$, $\beta = 2\lambda\frac{\overline{a_S^2f}}{\overline{a_S}}$, $\phi = 4\lambda r\delta\frac{\overline{a_S\varepsilon}}{\overline{a_S}^2}H$, $\Gamma = 4\lambda r\delta\frac{\overline{a_Sf}}{\overline{a_S}^2}Y$, $\Phi = 4\lambda r\delta\frac{\overline{a_S\varepsilon(1-f)}}{\overline{a_S}^2}Y$, $H = \frac{\overline{(1-f)a_S^3}}{1+2r\delta a_S\frac{\overline{a_S\varepsilon}}{\overline{a_S}}}$, $Y = \frac{\overline{fa_S^3}}{1+2r\delta a_S\frac{\overline{a_S\varepsilon(1-f)}+\overline{a_Sf}}{\overline{a_S}}}$, $\Omega = \Delta-\phi$, $\Sigma = \beta-\Phi$ and $\Lambda = -\Gamma-\Phi+\beta$.

The absorbing state is stable if all eigenvalues of the Jacobian matrix are negative. Since the matrix is composed of four blocks, we can consider separately the two blocks on the diagonal: for $\mathbb{A}$ the eigenvalues are $\xi_{1,2} = -\mu_I$, $\xi_{3,4,5,6,7,8} = -\mu$, $\xi_{9,10} = -\gamma_P$, $\xi_{11} = -\mu-\gamma_P$, $\xi_{12,13} = -\mu-\gamma_A$, all negative. Thus the epidemic threshold can be obtained by imposing all eigenvalues of the block $\mathbb{B}$, which is a matrix 9x9, to be negative. The epidemic threshold in the hybrid case is therefore obtained by numerically diagonalizing the matrix $\mathbb{B}$ and imposing all its eigenvalues to be negative: this allows to obtain analytically the epidemic threshold for the hybrid CT for arbitrary activity distribution $\rho_S(a_S)$, recall probability $\varepsilon(a_S)$ and distribution of the app in the population $f(a_S)$.

Appendix B

Continuous-time Gillespie-like algorithm for CT simulations

In this Appendix we describe the scheme of the continuous-time Gillespie-like algorithm implemented to numerically simulate the epidemic dynamics in the active phase and the dynamics of the activity-driven network, which are coupled by the isolation of symptomatic individuals and by manual and digital contact tracing. The model considered is fully described in Chapter 5.

We consider a network of N nodes and each node is initially assigned with two parameters (a_S, b_S) extracted from the joint distribution $\rho_S(a_S, b_S)$. Initially the network evolve in the absorbing state (i.e. all nodes are susceptible) and the pathogen does not spread:

1. At time $t = 0$ each node i is assigned with its activation time extracted from the distribution $\Psi_{a_S^i}(t_i) = a_S^i e^{-a_S^i t_i}$;

2. The time is set at the minimum activation time $t = t_i$: the node i with the lowest activation time t_i is activated and generates m links with m nodes randomly selected with probability proportional to their attractiveness b_S^j;

3. The new activation time $t_i + \tau$ of node i is obtained by drawing the inter-event time τ from the inter-event times distribution $\Psi_{a_S^i}(\tau) = a_S^i e^{-a_S^i \tau}$;

4. All the links are destroyed and the process is iterated from point 2 up to the relaxation time t_0, in which the dynamics of the network is relaxed to equilibrium (i.e. no more aging effects are present).

At this point the epidemic dynamic is implemented:

1. At time $t = t_0$ each node is assigned with an activation time t_i, resulting from the relaxation dynamics, and the system is then initialized in a configuration of susceptible, infected and recovered.

   Digital CT: the app is initially assigned to each node of activity a_S with probability $f(a_S)$;

2. The minimum activation time t_i is considered. Nodes infected at time t recover at time t_i with probability $\left[1 - e^{-\mu(t_i - t)}\right]$ if asymptomatic (A, T, Q) or with probability $\left[1 - e^{-\mu_I(t_i - t)}\right]$ if symptomatic (I): thus they change their activity and attractiveness $(a_X, b_X) \to (a_R, b_R)$, with $X = \{A, T, Q, I\}$;

3. Traced asymptomatic individuals at time t are isolated at time t_i with probability $\left[1 - e^{-(t_i - t)/\tau_C}\right]$, thus they change their activity and attractiveness $(a_T, b_T) \to (a_Q, b_Q) = (0, 0)$.

   Digital CT: $\tau_C = 0$; **Manual CT:** $\tau_C > 0$;

4. Presymptomatic individuals at time t develop symptoms at time t_i with probability $\left[1 - e^{-\gamma_P(t_i - t)}\right]$: thus they change their activity and attractiveness $(a_P, b_P) \to (a_I, b_I) = (0, 0)$ and activate contact tracing.

   Manual CT: contact tracing is enabled for each symptomatic node. Each contact made in the time window T_{CT} is traced with probability $\varepsilon(a_S)$, where a_S is the activity of the symptomatic node. Each node tested and found asymptomatic is traced and changes its activity and attractiveness $(a_A, b_A) \to (a_T, b_T)$;

   Digital CT: contact tracing is enabled only if the symptomatic node has adopted the app. Each contact performed in the time window T_{CT} is traced with probability 1 if the other node involved has downloaded the app or with probability 0 otherwise. Each node tested and found asymptomatic is traced and changes its activity and attractiveness $(a_A, b_A) \to (a_T, b_T)$;

5. The time is then set at the minimum activation time $t = t_i$ and the node i with the lowest activation time t_i is activated. The active node i generates exactly m links with m randomly selected nodes, with probability proportional to their attractiveness b_j. The contacts are collected in the contact list of both the involved nodes.

6. If the nodes involved in an active link are one susceptible and one infected, an infection occurs with probability λ: the susceptible node become presymptomatic with probability δ or asymptomatic with probability $(1 - \delta)$ and changes behaviour $(a_S, b_S) \to (a_X, b_X)$;

7. The new activation time $t_i + \tau$ of node i is obtained by drawing the inter-event time τ from the inter-event times distribution $\Psi_{a_X^i}(\tau) = a_X^i e^{-a_X^i \tau}$, where $X = \{S, A, T, Q, P, I, R\}$ denotes the dynamic status of node i at time t_i. All links are destroyed and the process is iterated from step 2 until the system reaches the configuration without infected individuals.

Appendix C

Mean-field equations and epidemic threshold for simplicial CT

In this Appendix we derive the mean-field equations for the evolution of an epidemic with presymptomatic and asymptomatic transmission on simplicial activity-driven networks, considering the isolation of symptomatic nodes and the implementation of contact tracing on gatherings. Moreover, we analytically derive the epidemic threshold [32]. The detailed epidemic model and the detailed implementation of CT on gatherings are described in Chapter 6.

The epidemic model corresponds to the SIR model with further distinction in the infected state based on the appearance of symptoms, on tracing and isolation. The transitions between the different compartments are shown in Figure 6.7. The CT is implemented on simplices, i.e. gatherings, with its three mechanisms: forward CT, backward CT and sideward CT (see Chapter 6). We consider the manual implementation of the contact tracing [28]: each simplex in which a symptomatic individual participated is traced as a whole with probability $\epsilon(s)$, where s is the size of the simplex.

The infection and forward CT transitions are (considering the minimum conditions for CT to be activated):

$$P + S \xrightarrow{\lambda\delta} P + P \tag{C.1}$$

$$P + S \xrightarrow{\lambda(1-\delta)\epsilon} P + A_T \tag{C.2}$$

$$P + S \xrightarrow{\lambda(1-\delta)(1-\epsilon)} P + A \tag{C.3}$$

A susceptible individual S can be infected by a presymptomatic node P and become presymptomatic (Eq. (C.1)) or asymptomatic (Eqs. (C.2) and (C.3)). In the latter case, the asymptomatic can be traced with probability $\epsilon(s)$ with forward CT, activated by the infector P upon symptoms development, becoming traced asymptomatic A_T (Eq. (C.2)), otherwise it becomes infected asymptomatic A (Eq. (C.3)).

The infection and backward CT transitions are (considering the minimum conditions for CT to be activated):

$$A + S \xrightarrow{\lambda\delta\epsilon} A_T + P \tag{C.4}$$

$$A + S \xrightarrow{\lambda\delta(1-\epsilon)} A + P \tag{C.5}$$

$$A_T + S \xrightarrow{\lambda\delta} A_T + P \tag{C.6}$$

A susceptible individual S can be infected by an asymptomatic node A (Eqs. (C.4)

and (C.5)) or by a traced asymptomatic node A_T (Eq. (C.6)) and become presymptomatic. The asymptomatic A infector can be traced with probability $\epsilon(s)$ with backward CT, activated by the presymptomatic P upon symptoms development, becoming traced asymptomatic A_T (Eq. (C.4)), otherwise it remains infected asymptomatic A (Eq. (C.5)). Also traced asymptomatic A_T infectors could be traced twice with backward CT activated by the new presymptomatic P, but this has no consequences on the nodes status (Eq. (C.6)).

The infection and sideward CT transitions are (considering the minimum conditions for CT to be activated):

$$A + S \xrightarrow{\lambda(1-\delta)\epsilon} A + A_T \qquad \text{if in the same simplex exists} \qquad A + S \xrightarrow{\lambda\delta} A + P \tag{C.7}$$

$$A + S \xrightarrow{\lambda(1-\delta)(1-\epsilon)} A + A \qquad \text{if in the same simplex exists} \qquad A + S \xrightarrow{\lambda\delta} A + P \tag{C.8}$$

$$A + S \xrightarrow{\lambda(1-\delta)} A + A \qquad \text{otherwise} \tag{C.9}$$

$$A_T + S \xrightarrow{\lambda(1-\delta)\epsilon} A_T + A_T \qquad \text{if in the same simplex exists} \qquad A_T + S \xrightarrow{\lambda\delta} A_T + P \tag{C.10}$$

$$A_T + S \xrightarrow{\lambda(1-\delta)(1-\epsilon)} A_T + A \qquad \text{if in the same simplex exists} \qquad A_T + S \xrightarrow{\lambda\delta} A_T + P \tag{C.11}$$

$$A_T + S \xrightarrow{\lambda(1-\delta)} A_T + A \qquad \text{otherwise} \tag{C.12}$$

A susceptible individual S can be infected by an asymptomatic node A (Eqs. (C.7)-(C.9)) or by a traced asymptomatic node A_T (Eqs. (C.10)-(C.12)) and becomes asymptomatic. The whole simplex can be traced with probability $\epsilon(s)$ if in the same simplex a symptomatic infection occurs: in this case the newly infected asymptomatic is traced with sideward CT, becoming traced asymptomatic A_T (Eqs. (C.7) and (C.10)), otherwise if the simplex is not traced (Eqs. (C.8) and (C.11)) or no symptomatic infections occur in the simplex (Eqs. (C.9) and (C.12)) the newly infected asymptomatic remains A. Notice that the asymptomatic infector can be traced with backward CT in the events of Eqs. (C.7)-(C.8), as described in Eqs. (C.4)-(C.5).

Finally, the spontaneous transitions are:

$$P \xrightarrow{\gamma_P} I \qquad A \xrightarrow{\mu} R \qquad I \xrightarrow{\mu_I} R \tag{C.13}$$

$$A_T \xrightarrow{\gamma_P} A_Q \qquad A_T \xrightarrow{\mu} R \qquad A_Q \xrightarrow{\mu} R \tag{C.14}$$

All these transitions consider the necessary and sufficient conditions, i.e. the minimum conditions, for the CT mechanisms to be activated, indeed they describe the first-order mechanisms for CT activation, which require the presence of one infected individual to activate CT, unlike higher-order terms which require the presence of more than one infected individuals. For example, the sideward CT on an asymptomatic infection can be activated even if a presymptomatic individual is present initially in the simplex, without the need for a symptomatic infection, however this is a second-order term, requiring the presence of at least two infected nodes initially in the simplex. We only consider first-order terms, since we focus on the epidemic threshold and all higher-order terms do not survive the linearization procedure for the calculation of the threshold (see Chapter 6).

We consider the homogeneous case, with all nodes featuring the same attractiveness when susceptible $b_S = b$, and we apply a *mean-field approach*, by considering all nodes statistically equivalent. The approach is exact since the model is exactly mean-field, as all local correlations are destroyed by the random selection of participants in the simplices without memory (Markovian dynamics). Furthermore, the mean-field epidemic threshold of the SIS and SIR model are the same, so we can consider the evolution equations of the SIS model [126, 128–130].

As described in Chapter 6, the epidemic is described by the probabilities $X(t)$ for a node to belong to a specific compartment at time t, with $X = \{S, P, I, A, A_T, A_Q\}$. We derive the equations for the temporal evolution of the probabilities by taking into account the network dynamics, the epidemic spreading and the CT protocol.

The network evolves with simplices activations, which occur over time with a Poissonian dynamics with activation rate a and their size distribution is $\Psi(s)$: nodes participate in active simplices with probability proportional to their attractiveness $p_X \propto b_X$. Presymptomatic, infected asymptomatic and traced asymptomatic individuals behave as susceptible $b_P = b_A = b_{A_T} = b_S = b$, while symptomatic or isolated asymptomatic individuals do not participate in simplices $b_I = b_{A_Q} = 0$. Hence, the average attractiveness at time t is $\langle b(t) \rangle = b(S(t) + P(t) + A(t) + A_T(t))$, and we consider the thermodynamic limit. We define $P_X(t)$ the probability that a node participating in a simplex active at time t belongs to compartment X. Thus:

$$P_X(t) = X(t) \frac{b_X}{\langle b(t) \rangle}. \tag{C.15}$$

This means that $P_X(t) = \frac{X(t)}{S(t)+P(t)+A(t)+A_T(t)}$ for $X = S, P, A, A_T$, while $P_I(t) = P_{A_Q}(t) = 0 \, \forall t$.

The temporal evolution of the probability $P(t)$ that a node is infected presymptomatic is governed by the equation:

$$\partial_t P(t) = -\gamma_P P(t) + \int ds \Psi(s) a s P_S(t) Z_s(t) \delta, \tag{C.16}$$

where the first term on the right-hand side is due to the spontaneous symptoms development, while the second term is due to symptomatic contagion in simplices: the infection occurs if a simplex of size s is activated a, a susceptible node participates with probability $sP_S(t)$ in the active simplex and with probability $Z_s(t)$ is infected by at least one of the remaining $(s-1)$ nodes, the infection is symptomatic with probability δ. The infection term is averaged over the simplex size, by multiplying the term for $\Psi(s)$ and integrating over the simplex size.

$Z_s(t)$ represents the probability that at least one of the other $(s-1)$ nodes in the active simplex infects the susceptible node, and therefore it is defined as:

$$Z_s(t) = 1 - \xi(t)^{s-1}, \tag{C.17}$$

where $\xi(t)$ is the probability that a node in the active simplex does not infect the susceptible node. Since the simplex constitutes a fully connected cluster, all the nodes involved in it are connected to the susceptible node, thus $\xi(t)$ is defined as:

$$\xi(t) = P_S(t) + (1-\lambda)[P_P(t) + P_A(t) + P_{A_T}(t)] = 1 - \lambda \frac{P(t) + A(t) + A_T(t)}{S(t) + P(t) + A(t) + A_T(t)}. \tag{C.18}$$

Thus, by substituting Eqs. (C.17) and (C.18) in Eq. (C.16) we get the complete equation for the evolution of $P(t)$:

$$\partial_t P(t) = -\gamma_P P(t) + a\frac{S(t)}{S(t)+Y(t)}\delta\left\langle s\left[1-\left(1-\lambda\frac{Y(t)}{S(t)+Y(t)}\right)^{s-1}\right]\right\rangle, \quad \text{(C.19)}$$

where we define $\langle f(s)\rangle = \int ds\Psi(s)f(s)$ and $Y(t) = P(t) + A(t) + A_T(t)$, i.e. the probability for a node to be infected and contagious participating in simplices.

The probability $I(t)$ that a node is infected symptomatic evolves accordingly to the equation:

$$\partial_t I(t) = -\mu_I I(t) + \gamma_P P(t), \quad \text{(C.20)}$$

where the first and second terms on the right-hand side are respectively due to spontaneous recovery and spontaneous symptoms development.

The temporal evolution of the probability $A(t)$ that a node is infected asymptomatic (not traced nor isolated) is governed by the equation:

$$\begin{aligned}\partial_t A(t) = -\mu A(t) &+ \int ds\Psi(s)asP_S(t)Z_s(t)(1-\delta)\\ &- \int ds\Psi(s)C_s^{Forward}(t)\\ &- \int ds\Psi(s)C_s^{Backward}(t)\\ &- \int ds\Psi(s)C_s^{Sideward}(t),\end{aligned} \quad \text{(C.21)}$$

where the first term on the right-hand side is due to the spontaneous recovery, while the second term is due to asymptomatic infection in simplices: the infection occurs if a simplex of size s is activated a, a susceptible node participates with probability $sP_S(t)$ in the active simplex and with probability $Z_s(t)$ is infected by at least one of the other $(s-1)$ nodes, the infection is asymptomatic with probability $(1-\delta)$. Finally, the third, fourth and fifth terms account respectively for forward, backward and sideward CT. Both infection and CT terms are averaged on the simplex size, by multiplying for $\Psi(s)$ and integrating over the simplex size.

The infection term can be obtained by simply substituting in Eq. (C.21) the definition of $P_S(t)$ and of $Z_s(t)$ as in Eq. (C.17), obtaining:

$$\begin{aligned}\partial_t A(t) = -\mu A(t) &+ a\frac{S(t)}{S(t)+Y(t)}(1-\delta)\left\langle s\left[1-\left(1-\lambda\frac{Y(t)}{S(t)+Y(t)}\right)^{s-1}\right]\right\rangle\\ &- C^{Forward}(t) - C^{Backward}(t) - C^{Sideward}(t),\end{aligned} \quad \text{(C.22)}$$

where $Y(t) = P(t) + A(t) + A_T(t)$ and we define $C^L = \int ds\Psi(s)C_s^L(t)$, with $L = Forward, Backward, Sideward$.

The probability $A_T(t)$ that a node is traced asymptomatic evolves accordingly to the equation:

$$\begin{aligned}\partial_t A_T(t) = -(\mu+\gamma_P)A_T(t) &+ \int ds\Psi(s)C_s^{Forward}(t)\\ &+ \int ds\Psi(s)C_s^{Backward}(t)\\ &+ \int ds\Psi(s)C_s^{Sideward}(t),\end{aligned} \quad \text{(C.23)}$$

where the first term on the right-hand side is due to the spontaneous recovery process and to the isolation of traced asymptomatic, the second, third and fourth terms are respectively due to forward, backward and sideward CT.

Finally, the temporal evolution of the probability $A_Q(t)$ that a node is isolated asymptomatic is:

$$\partial_t A_Q(t) = -\mu A_Q(t) + \gamma_P A_T(t), \tag{C.24}$$

where the first term on right-hand side is due to spontaneous recovery while the second term accounts for isolation of traced asymptomatic nodes.

Hereafter we evaluate separately each CT term for completing the mean-field equations for $A(t)$ and $A_T(t)$.

C.1 Forward CT

Forward CT allows to trace an asymptomatic individual infected by a presymptomatic, who developing symptoms activates the CT on the simplex in which the infection occurred. This tracing mechanism is described in detail in Chapter 6, its term in the mean-field equations is:

$$C^{Forward} = \int ds \Psi(s) a s P_S(t) \epsilon(s) (1-\delta) F_s(t). \tag{C.25}$$

In this term, the activation a of a simplex of size s is considered: $sP_S(t)$ is the probability that a susceptible individual participates in the simplex; $F_s(t)$ is the probability that at least one of the other $(s-1)$ nodes is presymptomatic and infects the susceptible individual; $(1-\delta)$ is the probability that the infection is asymptomatic. The simplex is traced with probability $\epsilon(s)$, which depends on its size.

Since the simplex constitutes a fully connected cluster, all the nodes involved in it are connected to the susceptible node, thus $F_s(t)$ is defined as:

$$F_s(t) = 1 - k(t)^{s-1}, \tag{C.26}$$

where $k(t)$ is the probability that a node in the active simplex is not presymptomatic, or, if presymptomatic, does not infect the susceptible node. Therefore, by definition:

$$k(t) = P_S(t) + P_A(t) + P_{A_T}(t) + (1-\lambda)P_P(t) = 1 - \lambda \frac{P(t)}{S(t) + P(t) + A(t) + A_T(t)}. \tag{C.27}$$

Substituting Eqs. (C.26) and (C.27) in Eq. (C.25) we get:

$$C^{Forward}(t) = a \frac{S(t)}{S(t) + Y(t)} (1-\delta) \left\langle \epsilon(s) s \left[1 - \left(1 - \lambda \frac{P(t)}{S(t) + Y(t)} \right)^{s-1} \right] \right\rangle, \tag{C.28}$$

where we recall that $Y(t) = P(t) + A(t) + A_T(t)$.

C.2 Backward CT

Backward CT allows to trace an asymptomatic individual who is the primary source of infection for a symptomatic individual, who developing symptoms activates the

CT on the simplex in which the infection occurred. This tracing mechanism is described in detail in Chapter 6, its term in the mean-field equations is:

$$C^{Backward}(t) = \int ds\Psi(s)asP_A(t)\epsilon(s)W_s(t). \tag{C.29}$$

In this term, the activation a of a simplex of size s is considered: $sP_A(t)$ is the probability that an asymptomatic individual A participates in the simplex; $W_s(t)$ is the probability that at least one of the other $(s-1)$ nodes is susceptible S and is infected by the asymptomatic node with symptomatic infection. The simplex is traced with probability $\epsilon(s)$, which depends on its size.

Since the simplex constitutes a fully connected cluster, all the nodes involved in it are connected to the asymptomatic node, thus $W_s(t)$ is defined as:

$$W_s(t) = 1 - \phi(t)^{s-1}, \tag{C.30}$$

where $\phi(t)$ is the probability that a node in the active simplex is not susceptible, or, if susceptible, is not infected with a symptomatic infection. Therefore, by definition:

$$\phi(t) = P_P(t) + P_A(t) + P_{A_T}(t) + (1-\lambda)P_S(t) + \lambda(1-\delta)P_S(t) = 1 - \lambda\delta\frac{S(t)}{S(t)+Y(t)}. \tag{C.31}$$

Substituting Eqs. (C.30) and (C.31) in Eq. (C.29) we get:

$$C^{Backward}(t) = a\frac{A(t)}{S(t)+Y(t)}\left\langle \epsilon(s)s\left[1-\left(1-\lambda\delta\frac{S(t)}{S(t)+Y(t)}\right)^{s-1}\right]\right\rangle, \tag{C.32}$$

where we recall that $Y(t) = P(t) + A(t) + A_T(t)$.

C.3 Sideward CT

Sideward CT allows to trace an asymptomatic individual infected by another asymptomatic (or traced asymptomatic) individual, if in the same simplex a symptomatic infection occurs producing a presymptomatic node, who developing symptoms activates the CT on the simplex in which the infection occurred. This tracing mechanism is described in detail in Chapter 6, its term in the mean-field equations is:

$$C^{Sideward}(t) = \int ds\Psi(s)asP_S(t)(1-\delta)H_s(t)\epsilon(s)K_s(t). \tag{C.33}$$

In this term, the activation a of a simplex of size s is considered: $sP_S(t)$ is the probability that a susceptible individual participates in the simplex; $H_s(t)$ is the probability that at least one of the other $(s-1)$ nodes is infected asymptomatic (or traced asymptomatic) and infects the susceptible node; $(1-\delta)$ is the probability that the infection is asymptomatic; $K_s(t)$ is the probability that at least one of the remaining $(s-2)$ nodes is susceptible and is infected in the simplex with a symptomatic infection. The simplex is traced with probability $\epsilon(s)$, which depends on its size.

Since the simplex constitutes a fully connected cluster, all the nodes involved in it are connected to the susceptible node, thus $H_s(t)$ is defined as:

$$H_s(t) = 1 - h(t)^{s-1}, \tag{C.34}$$

where $h(t)$ is the probability that a node in the active simplex does not infect the susceptible, or, if it infects the susceptible one, it is presymptomatic P. Therefore, by definition:

$$h(t) = P_S(t) + (1-\lambda)(P_A(t) + P_{A_T}(t)) + P_P(t) = 1 - \lambda \frac{A(t) + A_T(t)}{S(t) + P(t) + A(t) + A_T(t)}. \tag{C.35}$$

Analogously, since the simplex constitutes a fully connected cluster all the $(s-2)$ nodes involved in it are connected to the asymptomatic node, thus $K_s(t)$ is defined as:

$$K_s(t) = 1 - \phi(t)^{s-2}, \tag{C.36}$$

where $\phi(t)$ is the probability that a node in the active simplex is not susceptible, or, if susceptible, is not infected with a symptomatic infection. Thus, $\phi(t)$ is the same of Eq. (C.31).

Substituting Eqs. (C.34)-(C.36) in Eq. (C.33) we get:

$$\begin{aligned} C^{Sideward}(t) = a \frac{S(t)}{S(t)+Y(t)}(1-\delta) \Bigg\langle \epsilon(s) s \left[1 - \left(1 - \lambda \frac{A(t)+A_T(t)}{S(t)+Y(t)} \right)^{s-1} \right] \\ \times \left[1 - \left(1 - \lambda\delta \frac{S(t)}{S(t)+Y(t)} \right)^{s-2} \right] \Bigg\rangle, \end{aligned} \tag{C.37}$$

where we recall that $Y(t) = P(t) + A(t) + A_T(t)$.

C.4 Complete CT on gatherings

Substituting Eqs. (C.28), (C.32) and (C.37) in Eqs. (C.22) we get the complete equation for the evolution of $A(t)$:

$$\begin{aligned} \partial_t A(t) = -\mu A(t) &+ a \frac{S(t)}{S(t)+Y(t)}(1-\delta) \left\langle s \left[1 - \left(1 - \lambda \frac{Y(t)}{S(t)+Y(t)} \right)^{s-1} \right] \right\rangle \\ &- a \frac{S(t)}{S(t)+Y(t)}(1-\delta) \left\langle \epsilon(s) s \left[1 - \left(1 - \lambda \frac{P(t)}{S(t)+Y(t)} \right)^{s-1} \right] \right\rangle \\ &- a \frac{A(t)}{S(t)+Y(t)} \left\langle \epsilon(s) s \left[1 - \left(1 - \lambda\delta \frac{S(t)}{S(t)+Y(t)} \right)^{s-1} \right] \right\rangle \\ &- a \frac{S(t)}{S(t)+Y(t)}(1-\delta) \Bigg\langle \epsilon(s) s \left[1 - \left(1 - \lambda \frac{A(t)+A_T(t)}{S(t)+Y(t)} \right)^{s-1} \right] \\ &\qquad \times \left[1 - \left(1 - \lambda\delta \frac{S(t)}{S(t)+Y(t)} \right)^{s-2} \right] \Bigg\rangle. \end{aligned} \tag{C.38}$$

where we recall that $Y(t) = P(t) + A(t) + A_T(t)$.

Analogously, substituting Eqs. (C.28), (C.32) and (C.37) in Eq. (C.23) we get the complete equation for the evolution of $A_T(t)$:

$$\begin{aligned}\partial_t A_T(t) = & -(\mu+\gamma_P)A_T(t) \\ & + a\frac{S(t)}{S(t)+Y(t)}(1-\delta)\left\langle \epsilon(s)s\left[1-\left(1-\lambda\frac{P(t)}{S(t)+Y(t)}\right)^{s-1}\right]\right\rangle \\ & + a\frac{A(t)}{S(t)+Y(t)}\left\langle \epsilon(s)s\left[1-\left(1-\lambda\delta\frac{S(t)}{S(t)+Y(t)}\right)^{s-1}\right]\right\rangle \\ & + a\frac{S(t)}{S(t)+Y(t)}(1-\delta)\Bigg\langle \epsilon(s)s\left[1-\left(1-\lambda\frac{A(t)+A_T(t)}{S(t)+Y(t)}\right)^{s-1}\right] \\ & \qquad \times\left[1-\left(1-\lambda\delta\frac{S(t)}{S(t)+Y(t)}\right)^{s-2}\right]\Bigg\rangle\end{aligned} \tag{C.39}$$

We obtain a complete and close set of five coupled non-linear differential equations in the probabilities $X(t)$ that a node belongs to the compartment X:

$$\partial_t P(t) = -\gamma_P P(t) + a\frac{S(t)}{S(t)+Y(t)}\delta\left\langle s\left[1-\left(1-\lambda\frac{Y(t)}{S(t)+Y(t)}\right)^{s-1}\right]\right\rangle \tag{C.40}$$

$$\partial_t I(t) = -\mu_I I(t) + \gamma_P P(t) \tag{C.41}$$

$$\begin{aligned}\partial_t A(t) = & -\mu A(t) + a\frac{S(t)}{S(t)+Y(t)}(1-\delta)\left\langle s\left[1-\left(1-\lambda\frac{Y(t)}{S(t)+Y(t)}\right)^{s-1}\right]\right\rangle \\ & - C^{Forward}(t) - C^{Backward}(t) - C^{Sideward}(t)\end{aligned} \tag{C.42}$$

$$\partial_t A_T(t) = -(\mu+\gamma_P)A_T(t) + C^{Forward}(t) + C^{Backward}(t) + C^{Sideward}(t) \tag{C.43}$$

$$\partial_t A_Q(t) = -\mu A_Q(t) + \gamma_P A_T(t) \tag{C.44}$$

with:

$$C^{Forward}(t) = a\frac{S(t)}{S(t)+Y(t)}(1-\delta)\left\langle \epsilon(s)s\left[1-\left(1-\lambda\frac{P(t)}{S(t)+Y(t)}\right)^{s-1}\right]\right\rangle \tag{C.45}$$

$$C^{Backward}(t) = a\frac{A(t)}{S(t)+Y(t)}\left\langle \epsilon(s)s\left[1-\left(1-\lambda\delta\frac{S(t)}{S(t)+Y(t)}\right)^{s-1}\right]\right\rangle \tag{C.46}$$

$$\begin{aligned}C^{Sideward}(t) = & a\frac{S(t)}{S(t)+Y(t)}(1-\delta)\Bigg\langle \epsilon(s)s\left[1-\left(1-\lambda\frac{A(t)+A_T(t)}{S(t)+Y(t)}\right)^{s-1}\right] \\ & \qquad \times\left[1-\left(1-\lambda\delta\frac{S(t)}{S(t)+Y(t)}\right)^{s-2}\right]\Bigg\rangle\end{aligned} \tag{C.47}$$

where $S(t) = 1 - P(t) - I(t) - A(t) - A_T(t) - A_Q(t)$ and $Y(t) = P(t) + A(t) + A_T(t)$.

Eqs. (C.40)-(C.44) describe the epidemic spreading in the presence of forward, backward and sideward CT on gatherings. The set of equations admits the absorbing state, in which all individuals are susceptible, as a stationary state: the epidemic threshold can be obtained by imposing the stability of the absorbing state, through a linear stability analysis.

As discussed in Chapter 6, the CT terms feature a highly non-trivial dependence

on λ (see Eqs. (C.28),(C.32) and (C.37)): this complicates the calculation of the epidemic threshold and impose to consider the probability of infection λ as the control parameter, describing the critical behaviour in terms of the epidemic threshold λ_C. Indeed, the recovery rate μ is not a simply scaling factor of λ and the conditions for the stability of the absorbing state do not simply depend on the ratio λ/μ.

We linearize Eqs. (C.40)-(C.44) around the absorbing state, obtaining a closed and complete set of five linear coupled differential equations:

$$\partial_t P(t) = -\gamma_P P(t) + \lambda\delta a\langle s(s-1)\rangle[P(t) + A(t) + A_T(t)] \tag{C.48}$$
$$\partial_t I(t) = -\mu_I I(t) + \gamma_P P(t) \tag{C.49}$$
$$\partial_t A(t) = -\mu A(t) + \lambda(1-\delta)a\langle s(s-1)\rangle[P(t) + A(t) + A_T(t)] - C^{Forward}(t) - C^{Backward}(t) - C^{Sideward}(t) \tag{C.50}$$
$$\partial_t A_T(t) = -(\mu + \gamma_P)A_T(t) + C^{Forward}(t) + C^{Backward}(t) + C^{Sideward}(t) \tag{C.51}$$
$$\partial_t A_Q(t) = -\mu A_Q(t) + \gamma_P A_T(t) \tag{C.52}$$

with the linearized CT terms:

$$C^{Forward}(t) = \lambda(1-\delta)a\langle\epsilon(s)s(s-1)\rangle P(t) \tag{C.53}$$
$$C^{Backward}(t) = a\left\langle\epsilon(s)s\left[1-(1-\lambda\delta)^{s-1}\right]\right\rangle A(t) \tag{C.54}$$
$$C^{Sideward}(t) = \lambda(1-\delta)a\left\langle\epsilon(s)s(s-1)\left[1-(1-\lambda\delta)^{s-2}\right]\right\rangle[A(t) + A_T(t)] \tag{C.55}$$

Each node performs on average $\overline{n} = a\langle s(s-1)\rangle$ contacts per unit of time, which are arranged in simplices whose size s is extracted from the distribution $\Psi(s)$. As discussed in Chapter 6, we consider this quantity constant: this allows to compare the effects of CT for different distribution $\Psi(s)$ in the same condition of link formation, i.e. when the same number of contacts is performed through simplices of differently distributed size. We consider the linearized system of equations and make the dependence on $\overline{n}$ explicit, obtaining the following equations:

$$\partial_t P(t) = -\gamma_P P(t) + \lambda\delta\overline{n}[P(t) + A(t) + A_T(t)] \tag{C.56}$$
$$\partial_t I(t) = -\mu_I I(t) + \gamma_P P(t) \tag{C.57}$$
$$\partial_t A(t) = -\mu A(t) + \lambda(1-\delta)\overline{n}[P(t) + A(t) + A_T(t)] - C^{Forward}(t) - C^{Backward}(t) - C^{Sideward}(t) \tag{C.58}$$
$$\partial_t A_T(t) = -(\mu + \gamma_P)A_T(t) + C^{Forward}(t) + C^{Backward}(t) + C^{Sideward}(t) \tag{C.59}$$
$$\partial_t A_Q(t) = -\mu A_Q(t) + \gamma_P A_T(t) \tag{C.60}$$

where the linearized CT terms are:

$$C^{Forward}(t) = \lambda(1-\delta)\overline{n}\frac{\langle\epsilon(s)s(s-1)\rangle}{\langle s(s-1)\rangle}P(t) \tag{C.61}$$
$$C^{Backward}(t) = \frac{\overline{n}}{\langle s(s-1)\rangle}\left\langle\epsilon(s)s\left[1-(1-\lambda\delta)^{s-1}\right]\right\rangle A(t) \tag{C.62}$$
$$C^{Sideward}(t) = \lambda(1-\delta)\frac{\overline{n}}{\langle s(s-1)\rangle}\left\langle\epsilon(s)s(s-1)\left[1-(1-\lambda\delta)^{s-2}\right]\right\rangle[A(t) + A_T(t)] \tag{C.63}$$

The linearized equations can be rewritten as:

$$\begin{bmatrix} \partial_t A_Q(t) \\ \partial_t I(t) \\ \partial_t P(t) \\ \partial_t A(t) \\ \partial_t A_T(t) \end{bmatrix} = J \begin{bmatrix} A_Q(t) \\ I(t) \\ P(t) \\ A(t) \\ A_T(t) \end{bmatrix} \tag{C.64}$$

where J is the Jacobian matrix of this set of coupled equations:

$$\begin{aligned} J &= \begin{bmatrix} -\mu & 0 & 0 & 0 & \gamma_P \\ 0 & -\mu_I & \gamma_P & 0 & 0 \\ 0 & 0 & -\gamma_P + \beta & \beta & \beta \\ 0 & 0 & \Delta\left(1 - \frac{\langle \epsilon(s)s(s-1)\rangle}{\langle s(s-1)\rangle}\right) & -\mu + \Delta - \Gamma - \Phi & \Delta - \Phi \\ 0 & 0 & \Delta\frac{\langle \epsilon(s)s(s-1)\rangle}{\langle s(s-1)\rangle} & +\Gamma + \Phi & -\mu - \gamma_P + \Phi \end{bmatrix} \\ &= \begin{bmatrix} \mathbb{A}(2\text{x}2) & \mathbb{C}(2\text{x}3) \\ \mathbb{O}(3\text{x}2) & \mathbb{B}(3\text{x}3) \end{bmatrix} \end{aligned} \tag{C.65}$$

where $\beta = \lambda\delta\overline{n}$, $\Delta = \lambda(1-\delta)\overline{n}$, $\Gamma = \frac{\overline{n}}{\langle s(s-1)\rangle}\left\langle \epsilon(s)s\left[1-(1-\lambda\delta)^{s-1}\right]\right\rangle$ and $\Phi = \lambda(1-\delta)\frac{\overline{n}}{\langle s(s-1)\rangle}\left\langle \epsilon(s)s(s-1)\left[1-(1-\lambda\delta)^{s-2}\right]\right\rangle$.

The absorbing state is stable if all eigenvalues of the Jacobian matrix are negative. Since the matrix is composed of four blocks, we can consider separately the two blocks on the diagonal: for $\mathbb{A}$ the eigenvalues are $\xi_1 = -\mu$, $\xi_2 = -\mu_I$, all negative. Thus the epidemic threshold can be obtained by imposing all eigenvalues of the block $\mathbb{B}$, which is a matrix 3x3, to be negative.

This analytical approach allows to obtain the epidemic threshold for a general epidemic with asymptomatic and presymptomatic infections, in the presence of CT on gatherings, considered as the combination of forward, backward and sideward CT, for arbitrary simplex size distribution $\Psi(s)$ and for arbitrary distribution of the recall probability on the simplex size $\epsilon(s)$, i.e. for arbitrary tracing strategy.

In general, the epidemic threshold can be obtained by numerically diagonalizing the matrix $\mathbb{B}$ and by imposing all its eigenvalues to be negative. However in some limit cases, it is possible to analytically solve the stability conditions and obtain an explicit form for λ_C, as discussed in Chapter 6.

Appendix D

WiFi data for the University of Parma

In this Appendix we describe the WiFi data of the University of Parma and the preprocessing procedure, which provide the aggregated and anonymized data on the temporal evolution of the number of presences in the University and on the statistics of the gatherings size.

The University of Parma has a unique WiFi network in all its buildings and premises: the network consists of 713 wireless Access Points (APs) and allows users to make more than 10 000 connections per day. All wireless APs, user connection requests and user sessions are recorded and managed by the login management system and are collected by the "ICT services" (ICTs) office of the University.

The staff of the ICTs office can extract a tabular file from the login management system on a daily basis, i.e. the log file, containing all the data for user connections to the University WiFi network. This file contains a line for each connection or disconnection event from the network, i.e. from an AP, with several information on the corresponding event:

- **Username:** the user's email address;
- **Type of user:** distinguishes the user on the basis of the academic role (e.g. student or structured staff) and on the basis of the university origin (e.g. affiliated with the University of Parma or guest);
- **Calling device ID:** the MAC address of the connecting device;
- **Type of device:** distinguishes the type of connecting device (e.g. computers, smartphones or tablets);
- **Called station ID:** the MAC address of the AP to which the user is connected;
- **Status type:** indicates whether the event corresponds to the beginning (Start) or the end (End) of the user service;
- **Date-time:** indicates the day and time of the event;
- **Session ID:** a unique accounting ID that allows to easily match session start and end events in the log file.

Passive data, such as the ones deriving from the management of the WiFi network, require to be preprocessed and to be subjected to appropriate data anonymization and aggregation algorithms, before any data analysis. Indeed, the log files contain personal information and, according to the European regulation on privacy

(GDPR), we cannot access and use them directly: to respect the principles of data minimization and to comply with the latest Regulation on Privacy and Electronic Communications, a Data Protection Impact Assessment has been conducted.

A procedure has been developed, which is performed directly by the ICTs office in its domain: this procedure takes log files as input, completely anonymizes data and computes the aggregate data of our interest, i.e. the temporal dynamics of the total number of users connected to the network and the number of gatherings of a certain size s observed over a specific time window. The access to the log files is allowed only to the ICTs office, which carries out the developed procedure: we have direct access only to the aggregated anonymized data of our interest, i.e. to the two measures.

The procedure is the following:

1. a pseudo-anonymization of the data is performed: all personal information (e.g. username, type of user, calling device ID and device type) are removed and are replaced with random 16-digit hexadecimal strings. The procedure maintains all the correlations between the attributes for all lines of the log files, so that the pseudo-anonymized data are consistent. Whenever a replacement of personal data with a random string occurs, the personal data-string match is saved in a keys file and that match is used each time the specific sensitive data is found. The seed for the generation of the random strings is changed every 24 hours.

2. if two or more connections of the same user are recorded to the same AP and their temporal distance Δt is lower than 5 minutes, a single connection is considered, beginning with the first connection and ending with the last disconnection. Indeed, some connections can be very short due to the weakness of the WiFi signal or because of the device going into standby, and therefore not for a real disconnection of the user;

3. the considered time window is divided into intervals of ΔT minutes. For each interval ΔT the procedure determines the total number of users connected to the entire WiFi network and for each AP the number of users s connected to it in the entire time interval (see Figure 6.16**a**). This procedure estimates the size s of a gathering, i.e. a cluster, in correspondence with an AP active for a time Δt.

4. the procedure provides the two anonymized and aggregated quantities, which are the only ones we can direct access:

   - **the temporal dynamics of attendance,** i.e. the total number of users connected to the University WiFi network within each ΔT time interval;
   - **the statistics of the gatherings size,** i.e. the number of ΔT-clusters of size s present within the University during the observation window.

5. All temporary data are deleted after 24-hours and only aggregate data are kept.

Bibliography

1. Newman, M. *Networks: An Introduction* (Oxford University Press, 2010).
2. Newman, M. E., Barabási, A.-L. E. & Watts, D. J. *The structure and dynamics of networks* (Princeton University Press, 2006).
3. Barrat, A., Barthélemy, M. & Vespignani, A. *Dynamical Processes on Complex Networks* (Cambridge University Press, 2008).
4. Masuda, N. & Lambiotte, R. *A Guide to Temporal Networks* (World Scientific, Europe, 2016).
5. Holme, P. & Saramäki, J. *Temporal Networks* (Springer Berlin Heidelberg, 2013).
6. Holme, P. & Saramäki, J. Temporal networks. *Physics Reports* **519,** 97–125 (2012).
7. Holme, P. Modern temporal network theory: a colloquium. *The European Physical Journal B* **88,** 234 (2015).
8. Gross, T. & Blasius, B. Adaptive coevolutionary networks: a review. *Journal of The Royal Society Interface* **5,** 259–271 (2008).
9. Gross, T. & Sayama, H. *Adaptive networks* (Springer, 2009).
10. Sayama, H. *et al.* Modeling complex systems with adaptive networks. *Computers & Mathematics with Applications* **65,** 1645–1664 (2013).
11. Pastor-Satorras, R., Castellano, C., Van Mieghem, P. & Vespignani, A. Epidemic processes in complex networks. *Reviews of Modern Physics* **87,** 925–979 (2015).
12. Funk, S., Salathé, M. & Jansen, V. A. A. Modelling the influence of human behaviour on the spread of infectious diseases: a review. *Journal of The Royal Society Interface* **7,** 1247–1256 (2010).
13. Perra, N., Gonçalves, B., Pastor-Satorras, R. & Vespignani, A. Activity driven modeling of time varying networks. *Scientific Reports* **2,** 469 (2012).
14. Mancastroppa, M., Burioni, R., Colizza, V. & Vezzani, A. Active and inactive quarantine in epidemic spreading on adaptive activity-driven networks. *Physical Review E* **102,** 020301 (2020).
15. Alfano, V. & Ercolano, S. The Efficacy of Lockdown Against COVID-19: A Cross-Country Panel Analysis. *Applied Health Economics and Health Policy* **18,** 509–517 (2020).
16. Di Domenico, L., Pullano, G., Sabbatini, C. E., Boëlle, P.-Y. & Colizza, V. Impact of lockdown on COVID-19 epidemic in Île-de-France and possible exit strategies. *BMC Medicine* **18,** 240 (2020).
17. Bonaccorsi, G. *et al.* Economic and social consequences of human mobility restrictions under COVID-19. *Proceedings of the National Academy of Sciences* **117,** 15530–15535 (2020).

18. United Nations Development Programme. *COVID-19 Socio-economic impact* , `https://www.undp.org/coronavirus/socio-economic-impact-covid-19`. (2020).
19. Hale, T. *et al.* A global panel database of pandemic policies (Oxford COVID-19 Government Response Tracker). *Nature Human Behaviour* **5,** 529–538 (2021).
20. Pinotti, F. *et al.* Tracing and analysis of 288 early SARS-CoV-2 infections outside China: A modeling study. *PLOS Medicine* **17,** 1–13 (2020).
21. Fraser, C., Riley, S., Anderson, R. M. & Ferguson, N. M. Factors that make an infectious disease outbreak controllable. *Proceedings of the National Academy of Sciences* **101,** 6146–6151 (2004).
22. Hellewell, J. *et al.* Feasibility of controlling COVID-19 outbreaks by isolation of cases and contacts. *The Lancet Global Health* **8,** e488–e496 (2020).
23. Zastrow, M. Coronavirus contact-tracing apps: can they slow the spread of covid-19? *Nature - Technology Feature* (2020).
24. Ferretti, L. *et al.* Quantifying SARS-CoV-2 transmission suggests epidemic control with digital contact tracing. *Science* **368,** eabb6936 (2020).
25. Sapiezynski, P., Pruessing, J. & Sekara, V. The fallibility of contact-tracing apps, Preprint at: `https://arxiv.org/abs/2005.11297` (2020).
26. Braithwaite, I., Callender, T., Bullock, M. & Aldridge, R. W. Automated and partly automated contact tracing: a systematic review to inform the control of COVID-19. *The Lancet Digital Health* **2,** e607–e621 (2020).
27. Davis, E. L. *et al.* Contact tracing is an imperfect tool for controlling COVID-19 transmission and relies on population adherence. *Nature Communications* **12,** 5412 (2021).
28. Mancastroppa, M., Castellano, C., Vezzani, A. & Burioni, R. Stochastic sampling effects favor manual over digital contact tracing. *Nature Communications* **12,** 1919 (2021).
29. Battiston, F. *et al.* Networks beyond pairwise interactions: Structure and dynamics. *Physics Reports* **874,** 1–92 (2020).
30. Iacopini, I., Petri, G., Barrat, A. & Latora, V. Simplicial models of social contagion. *Nature Communications* **10,** 2485 (2019).
31. Althouse, B. M. *et al.* Superspreading events in the transmission dynamics of SARS-CoV-2: Opportunities for interventions and control. *PLOS Biology* **18,** 1–13 (2020).
32. Mancastroppa, M., Guizzo, A., Castellano, C., Vezzani, A. & Burioni, R. Sideward contact tracing and the control of epidemics in large gatherings, Preprint at: `https://arxiv.org/abs/2110.04742` (2021).
33. Vazquez, A., Rácz, B., Lukács, A. & Barabási, A.-L. Impact of Non-Poissonian Activity Patterns on Spreading Processes. *Physical Review Letters* **98,** 158702 (2007).
34. Iribarren, J. L. & Moro, E. Impact of Human Activity Patterns on the Dynamics of Information Diffusion. *Physical Review Letters* **103,** 038702 (2009).
35. Eckmann, J.-P., Moses, E. & Sergi, D. Entropy of dialogues creates coherent structures in e-mail traffic. *Proceedings of the National Academy of Sciences* **101,** 14333–14337 (2004).

36. Holme, P. Network dynamics of ongoing social relationships. *EPL (Europhysics Letters)* **64,** 427–433 (2003).

37. Candia, J. *et al.* Uncovering individual and collective human dynamics from mobile phone records. *Journal of Physics A: Mathematical and Theoretical* **41,** 224015 (2008).

38. Karsai, M. *et al.* Small but slow world: How network topology and burstiness slow down spreading. *Physical Review E* **83,** 025102 (2011).

39. Stehlé, J. *et al.* Simulation of an SEIR infectious disease model on the dynamic contact network of conference attendees. *BMC Medicine* **9,** 87 (2011).

40. Eagle, N. & (Sandy) Pentland, A. Reality Mining: Sensing Complex Social Systems. *Personal and Ubiquitous Computing* **10,** 255–268 (2006).

41. Isella, L. *et al.* Close Encounters in a Pediatric Ward: Measuring Face-to-Face Proximity and Mixing Patterns with Wearable Sensors. *PLOS ONE* **6,** 1–10 (2011).

42. Stehlé, J. *et al.* High-Resolution Measurements of Face-to-Face Contact Patterns in a Primary School. *PLOS ONE* **6,** 1–13 (2011).

43. Isella, L. *et al.* What's in a crowd? Analysis of face-to-face behavioral networks. *Journal of Theoretical Biology* **271,** 166–180 (2011).

44. Cattuto, C. *et al.* Dynamics of Person-to-Person Interactions from Distributed RFID Sensor Networks. *PLOS ONE* **5,** 1–9 (2010).

45. Pan, R. K. & Saramäki, J. Path lengths, correlations, and centrality in temporal networks. *Physical Review E* **84,** 016105 (2011).

46. Przytycka, T. M., Singh, M. & Slonim, D. K. Toward the dynamic interactome: it's about time. *Briefings in bioinformatics* **11,** 15–29 (2010).

47. Lèbre, S., Becq, J., Devaux, F., Stumpf, M. P. & Lelandais, G. Statistical inference of the time-varying structure of gene-regulation networks. *BMC Systems Biology* **4,** 130 (2010).

48. Bullmore, E. & Sporns, O. Complex brain networks: graph theoretical analysis of structural and functional systems. *Nature reviews neuroscience* **10,** 186–198 (2009).

49. Karsai, M., Perra, N. & Vespignani, A. Time varying networks and the weakness of strong ties. *Scientific Reports* **4,** 4001 (2014).

50. Da F. Costa, L., Rodrigues, F. A., Travieso, G. & Boas, P. R. V. Characterization of complex networks: A survey of measurements. *Advances in Physics* **56,** 167–242 (2007).

51. Holme, P. Network reachability of real-world contact sequences. *Physical Review E* **71,** 046119 (2005).

52. Xuan, B. B., Ferreira, A. & Jarry, A. Computing shortest, fastest, and foremost journeys in dynamic networks. *International Journal of Foundations of Computer Science* **14,** 267–285 (2003).

53. Tang, J., Scellato, S., Musolesi, M., Mascolo, C. & Latora, V. Small-world behavior in time-varying graphs. *Physical Review E* **81,** 055101 (2010).

54. Easley, D. & Kleinberg, J. Networks, crowds, and markets: Reasoning about a highly connected world. *Significance* **9,** 43–44 (2012).

55. Rocha, L. E. C. & Masuda, N. Random walk centrality for temporal networks. *New Journal of Physics* **16,** 063023 (2014).
56. Barabási, A.-L. The origin of bursts and heavy tails in human dynamics. *Nature* **435,** 207–211 (2005).
57. Karsai, M., Jo, H.-H. & Kaski, K. *Bursty human dynamics* (Springer, 2018).
58. Vázquez, A. *et al.* Modeling bursts and heavy tails in human dynamics. *Physical Review E* **73,** 036127 (2006).
59. Stehlé, J., Barrat, A. & Bianconi, G. Dynamical and bursty interactions in social networks. *Physical Review E* **81,** 035101 (2010).
60. Goh, K.-I. & Barabási, A.-L. Burstiness and memory in complex systems. *EPL (Europhysics Letters)* **81,** 48002 (2008).
61. Karsai, M., Kaski, K., Barabási, A.-L. & Kertész, J. Universal features of correlated bursty behaviour. *Scientific Reports* **2,** 397 (2012).
62. Jo, H.-H., Karsai, M., Kertész, J. & Kaski, K. Circadian pattern and burstiness in mobile phone communication. *New Journal of Physics* **14,** 013055 (2012).
63. Takaguchi, T., Nakamura, M., Sato, N., Yano, K. & Masuda, N. Predictability of Conversation Partners. *Physical Review X* **1,** 011008 (2011).
64. Ciaperoni, M. *et al.* Relevance of temporal cores for epidemic spread in temporal networks. *Scientific Reports* **10,** 12529 (2020).
65. Lambiotte, R., Delvenne, J.-C. & Barahona, M. Random Walks, Markov Processes and the Multiscale Modular Organization of Complex Networks. *IEEE Transactions on Network Science and Engineering* **1,** 76–90 (2014).
66. Zhao, K., Stehlé, J., Bianconi, G. & Barrat, A. Social network dynamics of face-to-face interactions. *Physical Review E* **83,** 056109 (2011).
67. Kretzschmar, M. & Morris, M. Measures of concurrency in networks and the spread of infectious disease. *Mathematical Biosciences* **133,** 165–195 (1996).
68. Starnini, M. & Pastor-Satorras, R. Topological properties of a time-integrated activity-driven network. *Physical Review E* **87,** 062807 (2013).
69. Starnini, M. & Pastor-Satorras, R. Temporal percolation in activity-driven networks. *Physical Review E* **89,** 032807 (2014).
70. Ubaldi, E. *et al.* Asymptotic theory of time-varying social networks with heterogeneous activity and tie allocation. *Scientific Reports* **6,** 35724 (2016).
71. Alessandretti, L., Sun, K., Baronchelli, A. & Perra, N. Random walks on activity-driven networks with attractiveness. *Physical Review E* **95,** 052318 (2017).
72. Pozzana, I., Sun, K. & Perra, N. Epidemic spreading on activity-driven networks with attractiveness. *Physical Review E* **96,** 042310 (2017).
73. Starnini, M., Baronchelli, A. & Pastor-Satorras, R. Modeling Human Dynamics of Face-to-Face Interaction Networks. *Physical Review Letters* **110,** 168701 (2013).
74. Starnini, M., Frasca, M. & Baronchelli, A. Emergence of metapopulations and echo chambers in mobile agents. *Scientific Reports* **6,** 31834 (2016).
75. Barrat, A., Barthélemy, M., Pastor-Satorras, R. & Vespignani, A. The architecture of complex weighted networks. *Proceedings of the National Academy of Sciences* **101,** 3747–3752 (2004).

76. Ghoshal, G. & Holme, P. Attractiveness and activity in Internet communities. *Physica A: Statistical Mechanics and its Applications* **364,** 603–609 (2006).
77. Dunbar, R. Neocortex size as a constraint on group size in primates. *Journal of Human Evolution* **22,** 469–493 (1992).
78. Stiller, J. & Dunbar, R. Perspective-taking and memory capacity predict social network size. *Social Networks* **29,** 93–104 (2007).
79. Granovetter, M. S. The Strength of Weak Ties. *American Journal of Sociology* **78,** 1360–1380 (1973).
80. Miritello, G., Lara, R., Cebrian, M. & Moro, E. Limited communication capacity unveils strategies for human interaction. *Scientific Reports* **3,** 1950 (2013).
81. Ubaldi, E., Vezzani, A., Karsai, M., Perra, N. & Burioni, R. Burstiness and tie activation strategies in time-varying social networks. *Scientific Reports* **7,** 46225 (2017).
82. Burioni, R., Ubaldi, E. & Vezzani, A. Asymptotic theory of time varying networks with burstiness and heterogeneous activation patterns. *Journal of Statistical Mechanics: Theory and Experiment* **2017,** 054001 (2017).
83. Tizzani, M. *et al.* Epidemic spreading and aging in temporal networks with memory. *Physical Review E* **98,** 062315 (2018).
84. Moinet, A., Starnini, M. & Pastor-Satorras, R. Burstiness and Aging in Social Temporal Networks. *Physical Review Letters* **114,** 108701 (2015).
85. Mancastroppa, M., Vezzani, A., Muñoz, M. A. & Burioni, R. Burstiness in activity-driven networks and the epidemic threshold. *Journal of Statistical Mechanics: Theory and Experiment* **2019,** 053502 (2019).
86. Moinet, A., Starnini, M. & Pastor-Satorras, R. Random walks in non-Poissoinan activity driven temporal networks. *New Journal of Physics* **21,** 093032 (2019).
87. Petri, G. & Barrat, A. Simplicial Activity Driven Model. *Physical Review Letters* **121,** 228301 (2018).
88. Ramasco, J. J., Dorogovtsev, S. N. & Pastor-Satorras, R. Self-organization of collaboration networks. *Physical Review E* **70,** 036106 (2004).
89. Cencetti, G., Battiston, F., Lepri, B. & Karsai, M. Temporal properties of higher-order interactions in social networks. *Scientific Reports* **11,** 7028 (2021).
90. Giusti, C., Pastalkova, E., Curto, C. & Itskov, V. Clique topology reveals intrinsic geometric structure in neural correlations. *Proceedings of the National Academy of Sciences* **112,** 13455–13460 (2015).
91. Battiston, F. *et al.* The physics of higher-order interactions in complex systems. *Nature Physics* **17,** 1093–1098 (2021).
92. Sekara, V., Stopczynski, A. & Lehmann, S. Fundamental structures of dynamic social networks. *Proceedings of the National Academy of Sciences* **113,** 9977–9982 (2016).
93. Hatcher, A. *Algebraic topology* (Cambridge University Press, 2002).
94. Nadini, M. *et al.* Epidemic spreading in modular time-varying networks. *Scientific Reports* **8,** 2352 (2018).
95. Zino, L., Rizzo, A. & Porfiri, M. Modeling Memory Effects in Activity-Driven Networks. *SIAM Journal on Applied Dynamical Systems* **17,** 2830–2854 (2018).

96. Nadini, M., Rizzo, A. & Porfiri, M. Epidemic Spreading in Temporal and Adaptive Networks with Static Backbone. *IEEE Transactions on Network Science and Engineering* **7,** 549–561 (2020).

97. Zino, L., Rizzo, A. & Porfiri, M. Analysis and control of epidemics in temporal networks with self-excitement and behavioral changes. *European Journal of Control* **54,** 1–11 (2020).

98. Hufnagel, L., Brockmann, D. & Geisel, T. Forecast and control of epidemics in a globalized world. *Proceedings of the National Academy of Sciences* **101,** 15124–15129 (2004).

99. Y Piontti, A. P., Perra, N., Rossi, L., Samay, N. & Vespignani, A. *Charting the next pandemic: modeling infectious disease spreading in the data science age* (Springer, 2018).

100. Halloran, M. E. *et al.* Modeling targeted layered containment of an influenza pandemic in the United States. *Proceedings of the National Academy of Sciences* **105,** 4639–4644 (2008).

101. National Science and Technology Council. *Towards epidemic prediction: federal efforts and opportunities in outbreak modeling* , `https://obamawhitehouse.archives.gov/sites/default/files/microsites/ostp/NSTC/towards_epidemic_prediction-federal_efforts_and_opportunities.pdf`. (2016).

102. Lofgren, E. T. *et al.* Opinion: Mathematical models: A key tool for outbreak response. *Proceedings of the National Academy of Sciences* **111,** 18095–18096 (2014).

103. Heesterbeek, H. *et al.* Modeling infectious disease dynamics in the complex landscape of global health. *Science* **347,** aaa4339 (2015).

104. Colizza, V., Barthélemy, M., Barrat, A. & Vespignani, A. Epidemic modeling in complex realities. *Comptes Rendus Biologies* **330,** 364–374 (2007).

105. Pullano, G. *et al.* Novel coronavirus (2019-nCoV) early-stage importation risk to Europe, January 2020. *Eurosurveillance* **25,** 2000057 (2020).

106. Pullano, G. *et al.* Underdetection of cases of COVID-19 in France threatens epidemic control. *Nature* **590,** 134–139 (2021).

107. Chinazzi, M. *et al.* The effect of travel restrictions on the spread of the 2019 novel coronavirus (COVID-19) outbreak. *Science* **368,** 395–400 (2020).

108. Bansal, S., Chowell, G., Simonsen, L., Vespignani, A. & Viboud, C. Big Data for Infectious Disease Surveillance and Modeling. *The Journal of Infectious Diseases* **214,** S375–S379 (2016).

109. Salathe, M. *et al.* Digital epidemiology. *PLoS Computational Biology* **8,** e1002616 (2012).

110. *GLEAM (Global Epidemic and Mobility) Project* , `https://www.gleamproject.org/`.

111. Broeck, W. V. d. *et al.* The GLEaMviz computational tool, a publicly available software to explore realistic epidemic spreading scenarios at the global scale. *BMC Infectious Diseases* **11,** 37 (2011).

112. Holmdahl, I. & Buckee, C. Wrong but useful—what covid-19 epidemiologic models can and cannot tell us. *New England Journal of Medicine* **383,** 303–305 (2020).

113. Wearing, H. J., Rohani, P. & Keeling, M. J. Appropriate Models for the Management of Infectious Diseases. *PLOS Medicine* **2,** e174 (2005).

114. Darbon, A. *et al.* Disease persistence on temporal contact networks accounting for heterogeneous infectious periods. *Royal Society Open Science* **6,** 181404 (2019).

115. Guerra, F. M. *et al.* The basic reproduction number (R0) of measles: a systematic review. *The Lancet Infectious Diseases* **17,** e420–e428 (2017).

116. Delamater, P. L., Street, E. J., Leslie, T. F., Yang, Y. T. & Jacobsen, K. H. Complexity of the basic reproduction number (R0). *Emerging infectious diseases* **25,** 1 (2019).

117. Billah, M. A., Miah, M. M. & Khan, M. N. Reproductive number of coronavirus: A systematic review and meta-analysis based on global level evidence. *PLOS ONE* **15,** 1–17 (2020).

118. Sonabend, R. *et al. Evaluating the Roadmap out of Lockdown: modelling step 4 of the roadmap in the context of B.1.617.2* , `https://www.gov.uk/government/publications/imperial-college-london-evaluating-the-roadmap-out-of-lockdown-modelling-step-4-of-the-roadmap-in-the-context-of-b16172-delta-9-june-2021`. (2021).

119. Mallapaty, S. Delta's rise is fuelled by rampant spread from people who feel fine. *Nature News* (2021).

120. Diekmann, O., Heesterbeek, J. A. P. & Metz, J. A. J. On the definition and the computation of the basic reproduction ratio R0 in models for infectious diseases in heterogeneous populations. *Journal of Mathematical Biology* **28,** 365–382 (1990).

121. Hébert-Dufresne, L., Althouse, B. M., Scarpino, S. V. & Allard, A. Beyond R0: heterogeneity in secondary infections and probabilistic epidemic forecasting. *Journal of The Royal Society Interface* **17,** 20200393 (2020).

122. Livi, R. & Politi, P. *Nonequilibrium Statistical Physics: A Modern Perspective* (Cambridge University Press, 2017).

123. Van Kampen, N. G. *Stochastic processes in physics and chemistry* (North Holland, 1981).

124. Van Mieghem, P. *Performance analysis of complex networks and systems* (Cambridge University Press, 2014).

125. Valdano, E., Ferreri, L., Poletto, C. & Colizza, V. Analytical Computation of the Epidemic Threshold on Temporal Networks. *Physical Review X* **5,** 021005 (2015).

126. Valdano, E., Poletto, C. & Colizza, V. Infection propagator approach to compute epidemic thresholds on temporal networks: impact of immunity and of limited temporal resolution. *The European Physical Journal B* **88,** 341 (2015).

127. Valdano, E., Fiorentin, M. R., Poletto, C. & Colizza, V. Epidemic Threshold in Continuous-Time Evolving Networks. *Physical Review Letters* **120,** 068302 (2018).

128. Shu, P., Wang, W., Tang, M. & Do, Y. Numerical identification of epidemic thresholds for susceptible-infected-recovered model on finite-size networks. *Chaos: An Interdisciplinary Journal of Nonlinear Science* **25,** 063104 (2015).

129. Van Mieghemy, P., Sahnehz, F. D. & Scoglioz, C. An upper bound for the epidemic threshold in exact Markovian SIR and SIS epidemics on networks. *53rd IEEE Conference on Decision and Control* (2014).

130. Sun, K., Baronchelli, A. & Perra, N. Contrasting effects of strong ties on SIR and SIS processes in temporal networks. *The European Physical Journal B* **88,** 326 (2015).

131. Horváth, D. X. & Kertész, J. Spreading dynamics on networks: the role of burstiness, topology and non-stationarity. *New Journal of Physics* **16,** 073037 (2014).

132. Rocha, L. E. C. & Blondel, V. D. Bursts of Vertex Activation and Epidemics in Evolving Networks. *PLOS Computational Biology* **9,** 1–9 (2013).

133. Marceau, V., Noël, P.-A., Hébert-Dufresne, L., Allard, A. & Dubé, L. J. Adaptive networks: Coevolution of disease and topology. *Physical Review E* **82,** 036116 (2010).

134. Bagnoli, F., Liò, P. & Sguanci, L. Risk perception in epidemic modeling. *Physical Review E* **76,** 061904 (2007).

135. Aoki, T., Rocha, L. E. C. & Gross, T. Temporal and structural heterogeneities emerging in adaptive temporal networks. *Physical Review E* **93,** 040301 (2016).

136. Guo, D., Trajanovski, S., van de Bovenkamp, R., Wang, H. & Van Mieghem, P. Epidemic threshold and topological structure of susceptible-infectious-susceptible epidemics in adaptive networks. *Physical Review E* **88,** 042802 (2013).

137. Colizza, V., Barrat, A., Barthelemy, M., Valleron, A.-J. & Vespignani, A. Modeling the Worldwide Spread of Pandemic Influenza: Baseline Case and Containment Interventions. *PLOS Medicine* **4,** 1–16 (2007).

138. Peak, C. M., Childs, L. M., Grad, Y. H. & Buckee, C. O. Comparing nonpharmaceutical interventions for containing emerging epidemics. *Proceedings of the National Academy of Sciences* **114,** 4023–4028 (2017).

139. World Health Organization. *Non-pharmaceutical public health measures for mitigating the risk and impact of epidemic and pandemic influenza. Annex: Report of systematic literature reviews* , `https://apps.who.int/iris/bitstream/handle/10665/329439/WHO-WHE-IHM-GIP-2019.1-eng.pdf`. (2019).

140. Ferguson, N. M. *et al. Report 9: Impact of non-pharmaceutical interventions (NPIs) to reduce COVID-19 mortality and healthcare demand* , `https://www.imperial.ac.uk/media/imperial-college/medicine/sph/ide/gida-fellowships/Imperial-College-COVID19-NPI-modelling-16-03-2020.pdf`. (2020).

141. Hollingsworth, T. D., Klinkenberg, D., Heesterbeek, H. & Anderson, R. M. Mitigation Strategies for Pandemic Influenza A: Balancing Conflicting Policy Objectives. *PLOS Computational Biology* **7,** 1–11 (2011).

142. European Centre for Disease Prevention and Control. *Guidelines for the implementation of nonpharmaceutical interventions against COVID-19* , `https://www.ecdc.europa.eu/sites/default/files/documents/covid-19-guidelines-non-pharmaceutical-interventions-september-2020.pdf`. (2020).

143. Di Domenico, L., Pullano, G., Sabbatini, C. E., Boëlle, P.-Y. & Colizza, V. Modelling safe protocols for reopening schools during the COVID-19 pandemic in France. *Nature Communications* **12,** 1073 (2021).

144. Mazzoli, M. *et al.* Interplay between mobility, multi-seeding and lockdowns shapes COVID-19 local impact. *PLOS Computational Biology* **17,** 1–23 (2021).

145. Anderson, R. M., Heesterbeek, H., Klinkenberg, D. & Hollingsworth, T. D. How will country-based mitigation measures influence the course of the COVID-19 epidemic? *The Lancet* **395,** 931–934 (2020).

146. Bosetti, P. *et al.* Impact of mass testing during an epidemic rebound of SARS-CoV-2: a modelling study using the example of France. *Eurosurveillance* **26,** 2001978 (2021).

147. Fenichel, E. P. *et al.* Adaptive human behavior in epidemiological models. *Proceedings of the National Academy of Sciences* **108,** 6306–6311 (2011).

148. Ferguson, N. Capturing human behaviour. *Nature* **446,** 733–733 (2007).

149. Funk, S., Gilad, E. & Jansen, V. Endemic disease, awareness, and local behavioural response. *Journal of Theoretical Biology* **264,** 501–509 (2010).

150. Triggle, N. *Swine flu parties 'a bad idea'* , BBC News - `http://news.bbc.co.uk/2/hi/health/8125191.stm`. (2009).

151. McNeil Jr., D. G. *Debating the Wisdom of 'Swine Flu Parties'* , The New York Times - `https://www.nytimes.com/2009/05/07/world/americas/07party.html`. (2009).

152. Center for Disease Control and Prevention. *Chichenpox (Varicella) transmission - "Chickenpox Parties" Don't Take the Chance* , `https://www.cdc.gov/chickenpox/about/transmission.html`. (2021).

153. Dillner, L. *The return of the measles party* , The Guardian - `https://www.theguardian.com/lifeandstyle/2001/jul/26/healthandwellbeing.health`. (2001).

154. Giordano, C. *Anti-vaxxer who went to 'corona party' to become infected dies from Covid* , Independent - `https://www.independent.co.uk/news/world/europe/coronavirus-party-death-italy-bolzano-b1962661.html`. (2021).

155. Karimi, F. & Lynch, J. *Young people are throwing coronavirus parties with a payout when one gets infected, official says* , CNN - `https://edition.cnn.com/2020/07/02/us/alabama-coronavirus-parties-trnd/index.html`. (2021).

156. Scarpino, S. V., Allard, A. & Hébert-Dufresne, L. The effect of a prudent adaptive behaviour on disease transmission. *Nature Physics* **12,** 1042–1046 (2016).

157. Pepe, E. *et al.* COVID-19 outbreak response, a dataset to assess mobility changes in Italy following national lockdown. *Scientific Data* **7,** 230 (2020).

158. Ginsberg, J. *et al.* Detecting influenza epidemics using search engine query data. *Nature* **457,** 1012–1014 (2009).

159. Oliver, N. *et al.* Mobile phone data for informing public health actions across the COVID-19 pandemic life cycle. *Science Advances* **6,** eabc0764 (2020).

160. Rüdiger, S. *et al.* Predicting the SARS-CoV-2 effective reproduction number using bulk contact data from mobile phones. *Proceedings of the National Academy of Sciences* **118,** e2026731118 (2021).

161. Paolotti, D. *et al.* Web-based participatory surveillance of infectious diseases: the Influenzanet participatory surveillance experience. *Clinical Microbiology and Infection* **20,** 17–21 (2014).

162. Jones, J. H. & Salathé, M. Early Assessment of Anxiety and Behavioral Response to Novel Swine-Origin Influenza A(H1N1). *PLOS ONE* **4,** 1–8 (2009).

163. Perra, N., Balcan, D., Gonçalves, B. & Vespignani, A. Towards a Characterization of Behavior-Disease Models. *PLOS ONE* **6,** 1–15 (2011).

164. Center for Systems Science and Engineering - Johns Hopkins University. *COVID-19 Dashboard* , `https://coronavirus.jhu.edu/map.html`. (2021).

165. Funk, S., Gilad, E., Watkins, C. & Jansen, V. A. A. The spread of awareness and its impact on epidemic outbreaks. *Proceedings of the National Academy of Sciences* **106,** 6872–6877 (2009).

166. Gross, T., D'Lima, C. J. D. & Blasius, B. Epidemic Dynamics on an Adaptive Network. *Physical Review Letters* **96,** 208701 (2006).

167. Liu, S., Perra, N., Karsai, M. & Vespignani, A. Controlling Contagion Processes in Activity Driven Networks. *Physical Review Letters* **112,** 118702 (2014).

168. Rizzo, A., Frasca, M. & Porfiri, M. Effect of individual behavior on epidemic spreading in activity-driven networks. *Physical Review E* **90,** 042801 (2014).

169. Hu, P., Ding, L. & An, X. Epidemic spreading with awareness diffusion on activity-driven networks. *Physical Review E* **98,** 062322 (2018).

170. Moinet, A., Pastor-Satorras, R. & Barrat, A. Effect of risk perception on epidemic spreading in temporal networks. *Physical Review E* **97,** 012313 (2018).

171. Leitch, J., Alexander, K. A. & Sengupta, S. Toward epidemic thresholds on temporal networks: a review and open questions. *Applied Network Science* **4,** 105 (2019).

172. Mossong, J. *et al.* Social Contacts and Mixing Patterns Relevant to the Spread of Infectious Diseases. *PLOS Medicine* **5,** 1–1 (2008).

173. Ariza, M. *et al.* Healthcare-seeking behaviour in case of influenza-like illness in the French general population and factors associated with a GP consultation: an observational prospective study. *BJGP Open* **1,** 4 (2018).

174. European Centre for Disease Prevention and Control. *Data on country response measures to COVID-19* , `https://www.ecdc.europa.eu/en/publications-data/download-data-response-measures-covid-19`. (2021).

175. Lagorio, C. *et al.* Quarantine-generated phase transition in epidemic spreading. *Physical Review E* **83,** 026102 (2011).

176. Gillespie, D. T. A general method for numerically simulating the stochastic time evolution of coupled chemical reactions. *Journal of Computational Physics* **22,** 403–434 (1976).

177. World Health Organization. *Statement on the meeting of the International Health Regulations (2005) Emergency Committee regarding the outbreak of novel coronavirus (2019- nCoV)* , `https://www.who.int/news/item/23-01-2020-statement-on-the-meeting-of-the-international-health-regulations-(2005)-emergency-committee-regarding-the-outbreak-of-novel-coronavirus-(2019-ncov)`. (2020).

178. World Health Organization. *Coronavirus Disease (COVID-2019) Situation Report 62* , `https://www.who.int/emergencies/diseases/novel-coronavirus-2019/situation-reports`. (2020).

179. World Health Organization. *Report of the WHO-China Joint Mission on Coronavirus Disease 2019 (COVID-19)* , `https://www.who.int/docs/default-source/coronaviruse/who-china-joint-mission-on-covid-19-final-report.pdf`. (2020).

180. Gazzetta Ufficiale della Repubblica Italiana. *Further implementing provisions of the D.L. 6/2020, containing urgent measures regarding the containment and management of the epidemiological emergency of COVID-19, applicable on the whole italian national territory, D.P.C.M. 11 march 2020* , `https://www.gazzettaufficiale.it/eli/id/2020/03/11/20A01605/sg`. (2020).

181. Haug, N. *et al.* Ranking the effectiveness of worldwide COVID-19 government interventions. *Nature Human Behaviour* **4,** 1303–1312 (2020).

182. Horowitz, J. & Bubola, E. *Italy's quarantine leaves locked-down towns feeling 'sacrificed'* , The New York Times - https://www.nytimes.com/2020/02/28/world/europe/italy-coronavirus-quarantine.html. (2020).

183. Horowitz, J. *Italy Announces Restrictions Over Entire Country in Attempt to Halt Coronavirus* , The New York Times - https://www.nytimes.com/2020/03/09/world/europe/italy-lockdown-coronavirus.html. (2020).

184. Boguñá, M., Castellano, C. & Pastor-Satorras, R. Nature of the Epidemic Threshold for the Susceptible-Infected-Susceptible Dynamics in Networks. *Physical Review Letters* **111,** 068701 (2013).

185. Vinceti, M. *et al.* Lockdown timing and efficacy in controlling COVID-19 using mobile phone tracking. *EClinicalMedicine* **25,** 100457 (2020).

186. Pei, S., Kandula, S. & Shaman, J. Differential effects of intervention timing on COVID-19 spread in the United States. *Science Advances* **6,** eabd6370 (2020).

187. Lavezzo, E. *et al.* Suppression of a SARS-CoV-2 outbreak in the Italian municipality of Vo'. *Nature* **584,** 425–429 (2020).

188. Bradshaw, W. J., Alley, E. C., Huggins, J. H., Lloyd, A. L. & Esvelt, K. M. Bidirectional contact tracing could dramatically improve COVID-19 control. *Nature Communications* **12,** 232 (2021).

189. Cencetti, G. *et al.* Digital proximity tracing on empirical contact networks for pandemic control. *Nature Communications* **12,** 1655 (2021).

190. World Health Organization. *The impact of COVID-19 on global health goals* , https://www.who.int/news-room/spotlight/the-impact-of-covid-19-on-global-health-goals. (2021).

191. Buonomo, B. & Della Marca, R. Effects of information-induced behavioural changes during the COVID-19 lockdowns: the case of Italy. *Royal Society Open Science* **7,** 201635 (2020).

192. Nicola, M. *et al.* The socio-economic implications of the coronavirus pandemic (COVID-19): A review. *International Journal of Surgery* **78,** 185–193 (2020).

193. Marziano, V. *et al.* Retrospective analysis of the Italian exit strategy from COVID-19 lockdown. *Proceedings of the National Academy of Sciences* **118,** e2019617118 (2021).

194. Ruktanonchai, N. W. *et al.* Assessing the impact of coordinated COVID-19 exit strategies across Europe. *Science* **369,** 1465–1470 (2020).

195. Rothe, C. *et al.* Transmission of 2019-nCoV Infection from an Asymptomatic Contact in Germany. *New England Journal of Medicine* **382,** 970–971 (2020).

196. Li, R. *et al.* Substantial undocumented infection facilitates the rapid dissemination of novel coronavirus (SARS-CoV-2). *Science* **368,** 489–493 (2020).

197. Wei, W. E. *et al.* Presymptomatic transmission of SARS-CoV-2—Singapore, january 23–march 16, 2020. *Morbidity and Mortality Weekly Report* **69,** 411 (2020).

198. Müller, J. & Kretzschmar, M. Contact tracing – Old models and new challenges. *Infectious Disease Modelling* **6,** 222–231 (2021).

199. Kwok, K. O. *et al.* Epidemic Models of Contact Tracing: Systematic Review of Transmission Studies of Severe Acute Respiratory Syndrome and Middle East Respiratory Syndrome. *Computational and Structural Biotechnology Journal* **17,** 186–194 (2019).

200. Klinkenberg, D., Fraser, C. & Heesterbeek, H. The Effectiveness of Contact Tracing in Emerging Epidemics. *PLOS ONE* **1,** 1–7 (2006).

201. Eames, K. T. D. & Keeling, M. J. Contact tracing and disease control. *Proceedings of the Royal Society B: Biological Sciences* **270,** 2565–2571 (2003).

202. Kojaku, S., Hébert-Dufresne, L., Mones, E., Lehmann, S. & Ahn, Y.-Y. The effectiveness of backward contact tracing in networks. *Nature Physics* **17,** 652–658 (2021).

203. House, T. & Keeling, M. J. The Impact of Contact Tracing in Clustered Populations. *PLOS Computational Biology* **6,** 1–9 (2010).

204. Eames, K. T. D. Contact tracing strategies in heterogeneous populations. *Epidemiology and Infection* **135,** 443–454 (2007).

205. Lewis, D. Why many countries failed at COVID contact-tracing — but some got it right. *Nature* **588,** 384–387 (2020).

206. Wilder-Smith, A., Chiew, C. J. & Lee, V. J. Can we contain the COVID-19 outbreak with the same measures as for SARS? *The Lancet Infectious Diseases* **20,** e102–e107 (2020).

207. Kretzschmar, M. E. *et al.* Impact of delays on effectiveness of contact tracing strategies for COVID-19: a modelling study. *The Lancet Public Health* **5,** e452–e459 (2020).

208. McLean, E. *et al.* Pandemic (H1N1) 2009 influenza in the UK: clinical and epidemiological findings from the first few hundred (FF100) cases. *Epidemiology and Infection* **138,** 1531–1541 (2010).

209. Crook, P. *et al.* Lack of secondary transmission of Ebola virus from healthcare worker to 238 contacts, United Kingdom, December 2014. *Emerging infectious diseases* **23,** 2081 (2017).

210. Bell, D. M. *et al.* Public health interventions and SARS spread, 2003. *Emerging infectious diseases* **10,** 1900 (2004).

211. Firth, J. A. *et al.* Using a real-world network to model localized COVID-19 control strategies. *Nature Medicine* **26,** 1616–1622 (2020).

212. Baumgarten, L. & Bornholdt, S. Epidemics with asymptomatic transmission: Subcritical phase from recursive contact tracing. *Physical Review E* **104,** 054310 (2021).

213. Ahmed, N. *et al.* A Survey of COVID-19 Contact Tracing Apps. *IEEE Access* **8,** 134577–134601 (2020).

214. *Privacy-preserving contact tracing,* - `https://covid19.apple.com/contacttracing`. (2020).

215. Troncoso, C. *et al.* Decentralized privacy-preserving proximity tracing. *IEEE Data Engineering Bulletin* **43,** 36–66 (2020).

216. *Immuni - tracing app (Italy)* , `https://www.immuni.italia.it/`. (2020).

217. *SwissCovid app - tracing app (Switzerland)* , https://www.bag.admin.ch/bag/en/home/krankheiten/ausbrueche-epidemien-pandemien/aktuelle-ausbrueche-epidemien/novel-cov/swisscovid-app-und-contact-tracing.html. (2020).

218. *NHS COVID-19 app - tracing app (UK)* , https://covid19.nhs.uk/. (2020).

219. *Corona-Warn-App - tracing app (Germany)* , https://www.coronawarn.app/en/. (2020).

220. Colizza, V. *et al.* Time to evaluate COVID-19 contact-tracing apps. *Nature Medicine* **27,** 361–362 (2021).

221. López, J. A. M. *et al.* Anatomy of digital contact tracing: Role of age, transmission setting, adoption, and case detection. *Science Advances* **7,** eabd8750 (2021).

222. Almagor, J. & Picascia, S. Exploring the effectiveness of a COVID-19 contact tracing app using an agent-based model. *Scientific Reports* **10,** 22235 (2020).

223. Nielsen, B. F., Sneppen, K., Simonsen, L. & Mathiesen, J. Differences in social activity increase efficiency of contact tracing. *The European Physical Journal B* **94,** 209 (2021).

224. Barrat, A., Cattuto, C., Kivelä, M., Lehmann, S. & Saramäki, J. Effect of manual and digital contact tracing on COVID-19 outbreaks: a study on empirical contact data. *Journal of The Royal Society Interface* **18,** 20201000 (2021).

225. Kelion, L. *Coronavirus: NHS contact tracing app to target 80% of smartphone users* , BBC - https://www.bbc.com/news/technology-52294896. (2020).

226. Alessandro, L. *Immuni è efficace? gli ultimi numeri, le luci e le ombre dell'app per il covid-19* , Il Sole24Ore - https://www.ilsole24ore.com/art/immuni-e-efficace-ultimi-numeri-luci-e-ombre-app-il-covid-19-ADESe1n. (2020).

227. O'Neill, P. H., Ryan-Mosley, T. & Johnson, B. *A flood of coronavirus apps are tracking us. now it's time to keep track of them* , MIT Technology Review - https://www.technologyreview.com/2020/05/07/1000961/launching-mittr-covid-tracing-tracker/. (2020).

228. MIT Technology Review. *Covid Tracing Tracker* , https://docs.google.com/spreadsheets/d/1ATalASO8KtZMx__zJREoOvFhOnmB-sAqJ1-CjVRSCOw/edit#gid=0. (2020).

229. Rizzo, E. COVID-19 contact tracing apps: the 'elderly paradox'. *Public Health* **185,** 127 (2020).

230. Saw, Y. E., Tan, E. Y.-Q., Liu, J. S. & Liu, J. C. Predicting Public Uptake of Digital Contact Tracing During the COVID-19 Pandemic: Results From a Nationwide Survey in Singapore. *Journal of Medical Internet Research* **23,** e24730 (2021).

231. Von Wyl, V. *et al.* Drivers of Acceptance of COVID-19 Proximity Tracing Apps in Switzerland: Panel Survey Analysis. *JMIR Public Health and Surveillance* **7,** e25701 (2021).

232. Wymant, C. *et al.* The epidemiological impact of the NHS COVID-19 app. *Nature* **594,** 408–412 (2021).

233. News, B. *What is the 'pingdemic' and why does it mean empty shelves in the supermarkets?* , https://www.bbc.co.uk/newsround/57926014. (2021).

234. Bradshaw, T., Pickard, J. & Sheppard, D. *UK 'pingdemic' spreads as record 600,000 people told to self-isolate* , Financial Times - https://www.ft.com/content/1bdef6b5-672d-46e0-9502-492a432a51af. (2021).

235. Plummer, R. *'Pingdemic' dents UK economic growth in July* , BBC - https://www.bbc.com/news/business-58502593. (2021).

236. Guan, W.-j. *et al.* Clinical Characteristics of Coronavirus Disease 2019 in China. *New England Journal of Medicine* **382,** 1708–1720 (2020).

237. Keeling, M. J., Hollingsworth, T. D. & Read, J. M. Efficacy of contact tracing for the containment of the 2019 novel coronavirus (COVID-19). *Journal of Epidemiology and Community Health* **74,** 861–866 (2020).

238. Liu, Y. *et al.* Viral dynamics in mild and severe cases of COVID-19. *The Lancet Infectious Diseases* **20,** 656–657 (2020).

239. Centers for Disease Control and Prevention. *Scaling Up Staffing Roles in Case Investigation and Contact Tracing* , https://www.cdc.gov/coronavirus/2019-ncov/php/contact-tracing/contact-tracing-plan/scaling-staff.html. (2020).

240. European Centre for Disease Prevention and Control. *Resource estimation for contact tracing, quarantine and monitoring activities for COVID-19 cases in the EU/EEA* , https://www.ecdc.europa.eu/sites/default/files/documents/COVID-19-resources-for-contact-tracing-2-March-2020.pdf. (2020).

241. Van Kerckhove, K., Hens, N., Edmunds, W. J. & Eames, K. T. D. The Impact of Illness on Social Networks: Implications for Transmission and Control of Influenza. *American Journal of Epidemiology* **178,** 1655–1662 (2013).

242. European Centre for Disease Prevention and Control. *Contact Tracing for COVID-19: Current Evidence, Options for Scale-Up and an Assessment of Resources Needed* , https://www.ecdc.europa.eu/sites/default/files/documents/COVID-19-Contract-tracing-scale-up.pdf. (2020).

243. Visontay, E. *Victoria's contact-tracing effort buckles under the weight of covid-19 cases* , The Guardian - https://www.theguardian.com/australia-news/2020/aug/04/victorias-contact-tracing-effort-buckles-under-the-weight-of-covid-19-cases. (2020).

244. Centers for Disease Control and Prevention. *Contact Tracing for COVID-19* , https://www.cdc.gov/coronavirus/2019-ncov/php/contact-tracing/contact-tracing-plan/contact-tracing.html. (2021).

245. Organisation for Economic Co-operation and Development. *OECD Household Dashboard* , https://stats.oecd.org/Index.aspx?DataSetCode=HH_DASH%20. (2019).

246. De Arruda, G. F., Petri, G., Rodrigues, F. A. & Moreno, Y. Impact of the distribution of recovery rates on disease spreading in complex networks. *Physical Review Research* **2,** 013046 (2020).

247. Bianconi, G. *Higher-Order Networks* (Cambridge University Press, 2021).

248. Nielsen, B. F., Simonsen, L. & Sneppen, K. COVID-19 Superspreading Suggests Mitigation by Social Network Modulation. *Physical Review Letters* **126,** 118301 (2021).

249. Lewis, D. Superspreading drives the COVID pandemic and could help to tame it. *Nature* **590,** 544–546 (2021).

250. Chen, P. Z., Koopmans, M., Fisman, D. N. & Gu, F. X. Understanding why superspreading drives the COVID-19 pandemic but not the H1N1 pandemic. *The Lancet Infectious Diseases* **21,** 1203–1204 (2021).

251. Pinotti, F. *et al. COVID-19 international cases as of Feb 13* , Database available at (accessed on 25 January 2022): `https://docs.google.com/spreadsheets/d/1X_8KaA7l5B_JPpwwV3js1L6lgCRa3FoH-gMrTy2k4Gw/edit?usp=sharing`. (2020).

252. News, B. *Coronavirus: Five Britons in French ski chalet catch virus* , `https://www.bbc.com/news/uk-51425702`. (2020).

253. St-Onge, G., Sun, H., Allard, A., Hébert-Dufresne, L. & Bianconi, G. Universal Nonlinear Infection Kernel from Heterogeneous Exposure on Higher-Order Networks. *Physical Review Letters* **127,** 158301 (2021).

254. Wong, F. & Collins, J. J. Evidence that coronavirus superspreading is fat-tailed. *Proceedings of the National Academy of Sciences* **117,** 29416–29418 (2020).

255. Adam, D. C. *et al.* Clustering and superspreading potential of SARS-CoV-2 infections in Hong Kong. *Nature Medicine* **26,** 1714–1719 (2020).

256. Majra, D., Benson, J., Pitts, J. & Stebbing, J. SARS-CoV-2 (COVID-19) superspreader events. *Journal of Infection* **82,** 36–40 (2021).

257. Frieden, T. R. & Lee, C. T. Identifying and interrupting superspreading events - implications for control of severe acute respiratory syndrome coronavirus 2. *Emerging infectious diseases* **26,** 1059 (2020).

258. Honderich, H. *Coronavirus: What makes a gathering a 'superspreader' event?* BBC - `https://www.bbc.com/news/world-us-canada-53273382`. (2020).

259. Zimmer, C. *One Meeting in Boston Seeded Tens of Thousands of Infections, Study Finds* , The New York Times - `https://www.nytimes.com/2020/08/26/health/covid-19-superspreaders-boston.html`. (2020).

260. Swinkels, K. *SARS-CoV-2 Superspreading Events Database* , `https://kmswinkels.medium.com/covid-19-superspreading-events-database-4c0a7aa2342b`. (2020).

261. Swinkels, K. *SARS-CoV-2 superspreading events from around the world* , Database available at (accessed on 25 January 2022): `https://docs.google.com/spreadsheets/d/1c9jwMyT1lw2POd6SDTno6nHLGMtpheO9xJyGHgdBoco/edit?usp=sharing`. (2020).

262. Our World in Data. *Restrictions on public gatherings in the COVID-19 pandemic, Jan 7, 2022* , `https://ourworldindata.org/grapher/public-gathering-rules-covid`. (2022).

263. St-Onge, G., Thibeault, V., Allard, A., Dubé, L. J. & Hébert-Dufresne, L. Social Confinement and Mesoscopic Localization of Epidemics on Networks. *Physical Review Letters* **126,** 098301 (2021).

264. Endo, A. *et al.* Implication of backward contact tracing in the presence of overdispersed transmission in COVID-19 outbreak. *Wellcome Open Research* **5,** 67 (2020).

265. Saito, T. *Contact-tracing and peer pressure: how Japan has controlled coronavirus* , The Guardian - `https://www.theguardian.com/commentisfree/2020/jun/06/contact-tracing-japan-coronavirus-covid-19-patients-social-etiquette`. (2020).

266. Morelle, R. *Covid test-and-trace: Is backwards contact tracing the way forward?* BBC - https://www.bbc.com/news/health-54648734. (2020).

267. Loh, T. *Contact tracers eye cluster-busting to tackle COVID-19's new surge* , The Japan Times - https://www.japantimes.co.jp/news/2020/11/04/world/contact-tracers-eye-cluster-busting-tackle-covid-19s-new-surge/. (2020).

268. European Centre for Disease Prevention and Control. *Contact tracing in the European Union: public health management of persons, including healthcare workers, who have had contact with COVID-19 cases – fourth update* , https://www.ecdc.europa.eu/sites/default/files/documents/TGU-20211019-1878.pdf. (2021).

269. World Health Organization. *Contact tracing in the context of COVID-19* , https://www.who.int/publications/i/item/contact-tracing-in-the-context-of-covid-19. (2021).

270. Moghadas, S. M. *et al.* The implications of silent transmission for the control of COVID-19 outbreaks. *Proceedings of the National Academy of Sciences* **117,** 17513–17515 (2020).

271. Johansson, M. A. *et al.* SARS-CoV-2 Transmission From People Without COVID-19 Symptoms. *JAMA Network Open* **4,** e2035057–e2035057 (2021).

272. Forster, V. *4,700 People Positive For Covid-19 After Superspreader Music Festival* , Forbes - https://www.forbes.com/sites/victoriaforster/2021/08/24/4700-attendees-positive-for-covid-19-after-superspreader-music-festival/?sh=57aa68dd34cc. (2021).

273. Italian Conference of Regions and Autonomous Provinces. *Guidelines for the reopening of economic activities* , http://www.regioni.it/newsletter/n-3844/del-19-05-2020/linee-guida-per-la-riapertura-delle-attivita-economiche-21233/. (2020).

274. University of Parma. *Coronavirus: all information for the university community updated in real time* , https://www.unipr.it/coronavirus. (2020).

275. González-Cabañas, J., Cuevas, A., Cuevas, R. & Maier, M. Digital Contact Tracing: Large-Scale Geolocation Data as an Alternative to Bluetooth-Based Apps Failure. *Electronics* **10,** 1093 (2021).

276. Al Qathrady, M., Helmy, A. & Almuzaini, K. Infection tracing in smart hospitals. *12th IEEE International Conference on Wireless and Mobile Computing, Networking and Communications (WiMob),* 1–8 (2016).

277. Trivedi, A. *et al.* WiFiTrace: Network-Based Contact Tracing for Infectious Diseases Using Passive WiFi Sensing. *Proceedings of the ACM on Interactive, Mobile, Wearable and Ubiquitous Technologies* **5,** 37 (2021).

278. Shahroz, M. *et al.* COVID-19 digital contact tracing applications and techniques: A review post initial deployments. *Transportation Engineering* **5,** 100072 (2021).

279. Cobb, S. M. *Harvard to Track Affiliates' Wi-Fi Signals as Part of Contact Tracing Pilot* , The Harvard Crimson - https://www.thecrimson.com/article/2020/8/2/tracefi-wifi-contract-tracing-coronavirus/. (2020).

280. Harvard University. *How TraceFi works* , https://covidtech.harvard.edu/howitworks.html. (2020).

281. Harvard University. *Tech to Combat COVID-19* , https://covidtech.harvard.edu/. (2020).

282. Centers for Disease Control and Prevention. *Scientific Brief: SARS-CoV-2 Transmission* , https://www.cdc.gov/coronavirus/2019-ncov/science/science-briefs/sars-cov-2-transmission.html. (2021).

283. European Centre for Disease Prevention and Control. *Transmission of COVID-19* , https://www.ecdc.europa.eu/en/covid-19/latest-evidence/transmission. (2020).

284. Bazant, M. Z. & Bush, J. W. M. A guideline to limit indoor airborne transmission of COVID-19. *Proceedings of the National Academy of Sciences* **118,** e2018995118 (2021).

285. European Centre for Disease Prevention and Control. *Mobile applications in support of contact tracing for COVID-19* , https://www.ecdc.europa.eu/sites/default/files/documents/covid-19-mobile-applications-contact-tracing.pdf. (2020).

286. United Nations Educational, Scientific and Cultural Organization. *Education: From disruption to recovery* , https://en.unesco.org/covid19/educationresponse. (2021).

287. Engzell, P., Frey, A. & Verhagen, M. D. Learning loss due to school closures during the COVID-19 pandemic. *Proceedings of the National Academy of Sciences* **118,** e2022376118 (2021).

288. Volz, E. *et al.* Assessing transmissibility of SARS-CoV-2 lineage B.1.1.7 in England. *Nature* **593,** 266–269 (2021).

289. Davies, N. G. *et al.* Estimated transmissibility and impact of SARS-CoV-2 lineage B.1.1.7 in England. *Science* **372,** eabg3055 (2021).

290. Liu, Y. & Rocklöv, J. The reproductive number of the Delta variant of SARS-CoV-2 is far higher compared to the ancestral SARS-CoV-2 virus. *Journal of Travel Medicine* **28,** 7 (2021).

291. Karim, S. S. A. & Karim, Q. A. Omicron SARS-CoV-2 variant: a new chapter in the COVID-19 pandemic. *The Lancet* **398,** 2126–2128 (2021).

292. World Health Organization. *Tracking SARS-CoV-2 variants* , https://www.who.int/en/activities/tracking-SARS-CoV-2-variants/. (2021).

293. Di Domenico, L. *et al.* Adherence and sustainability of interventions informing optimal control against the COVID-19 pandemic. *Communications Medicine* **1,** 57 (2021).

294. Marziano, V. *et al.* The effect of COVID-19 vaccination in Italy and perspectives for living with the virus. *Nature Communications* **12,** 7272 (2021).

295. European Centre for Disease Prevention and Control. *COVID-19 vaccination* , https://www.ecdc.europa.eu/en/covid-19/prevention-and-control/vaccines. (2021).

296. European Commission. *EU Digital COVID Certificate* , https://ec.europa.eu/info/live-work-travel-eu/coronavirus-response/safe-covid-19-vaccines-europeans/eu-digital-covid-certificate_en. (2021).

297. Italian Ministry of Health. *Certificazione verde COVID-19* , https://www.dgc.gov.it/web/. (2021).